ENERGY ENGINEERING AND CONTROL SYSTEMS

Volume 11, Number 2, 2025

Modeling of Control Processes for Photovoltaic Power Plants

Oleh Maksymuk*

Lviv Polytechnic National University, 12 Stepana Bandery St., Lviv, 79013, Ukraine

Received: October 15, 2025. Revised: November 14, 2025. Accepted: December 16, 2025.

Abstract

The increase in electricity demand and the need for renewable energy are driving the rapid adoption of distributed generation sources, where photovoltaic (PV) generation holds a leading position. While PV systems convert free sunlight into electrical energy, their sensitivity to weather variations and lack of inertia limit widespread application without auxiliary energy storage systems. The variable nature of output power caused by dynamic solar radiation intensity changes is one of the main challenges for PV. In weak electrical grids, PV output power changes could significantly affect voltage levels, leading to electromagnetic compatibility issues and compromising the stability of generation sources and consumers. This paper focuses on studying short-time intensive solar irradiance changes the impact on a PV-rich medium voltage grid. Using the MATLAB/Simulink environment the rapid solar irradiance changes have been modeled to examine output PV power changes and the resulting voltage changes in the point of common coupling, depending on the control mode applied by the PV inverter.

Keywords: solar power plant; photovoltaic panel; reactive power; voltage change; electrical grid.

1. Introduction

While integrating new solar power plants into the existing grids, severe problems could arise due to photovoltaic (PV) output power changes. The dense cloud cover movement is one of the key weather factors. A sudden decrease in solar irradiation on the panels leads to a sharp drop in the PV output power and a voltage reduction at the point of common coupling (PCC). Conversely, overvoltage conditions appear under high power from PV and decreased PCC load. Such voltage changes could negatively impact consumers, particularly constant power load consumers, who restore their previous consumption level by increasing the current. This is especially dangerous for consumers, such as induction motors, as a voltage reduction leads to a decreased electromagnetic torque, potentially causing their disconnection from the grid, increased reactive power consumption, and the risk of voltage collapse.

2. Analysis of publications and research

Early studies on the integration of PV into the power grids [1]–[4] examine the dynamic response of photovoltaic generation systems to rapid changes in solar irradiance under high solar penetration conditions. The authors found that the voltage levels at the PCCs experience significant deviations during the sharp irradiance change periods if PV inverters are not equipped with reactive power control features. These studies also established that with an increasing level of PV penetration, the amplitude of such voltage changes grows substantially. The simulated impact of rapid solar radiation changes on the distribution grid shows that PV power variations pose a potential threat to voltage stability due to the rapid decrease in generated power, delays in transformer on-load tap changer (OLTC) operation, and dynamic

---

* Corresponding author. Email address: oleh.i.maksymuk@lpnu.ua

This paper should be cited as: O. Maksymuk. (2025). Modeling of control processes for photovoltaic power plants. *Energy Engineering and Control Systems*, Vol. 11, No. 2, pp. 99 – 108. https://doi.org/10.23939/jeecs2025.02.099

loads – particularly induction motors – which significantly affect operational stability. The authors emphasize that equipping inverters with reactive power control features brings a positive impact on power quality and voltage stability.

Recent studies focus on inverter control systems improvements for PV power plants [5], [6], particularly the application of smart inverters with extended reactive power control capabilities during the nighttime [7] and the implementation of grid-support functions during voltage sags and LVRT [8]. Some studies analyze dynamic stability and short-term voltage changes caused by cloud transients, load fluctuations, and fault conditions at the PCC [9], [10]. Other studies are devoted to the long-term PV operational stability research [11], [12], where the authors demonstrate that existing PV control techniques have several drawbacks in long-term voltage control efficiency and propose improved systems to address these issues.

3. Goal of the paper

The purpose of this research is to model the impact of the rapid solar irradiance changes on grid voltages under the different inverter control modes applied to the PV power plant; to analyze voltage changes caused by changes in the active power of PV; and to create a parameterized computer model for further research.

4. Initial data

The studied medium voltage (MV) power system diagram with a PV plant, which consists of panels themselves and inverters, and is connected to the external power grid via a 25 km 35 kV overhead transmission line, is shown in Fig. 1. All components of the power plant are connected to the 10 kV buses of a transformer with a rated power of 10 MVA. Local consumers are also connected to the 10 kV buses of the transformer. These buses are the point of common coupling (PCC) for all elements of the system.

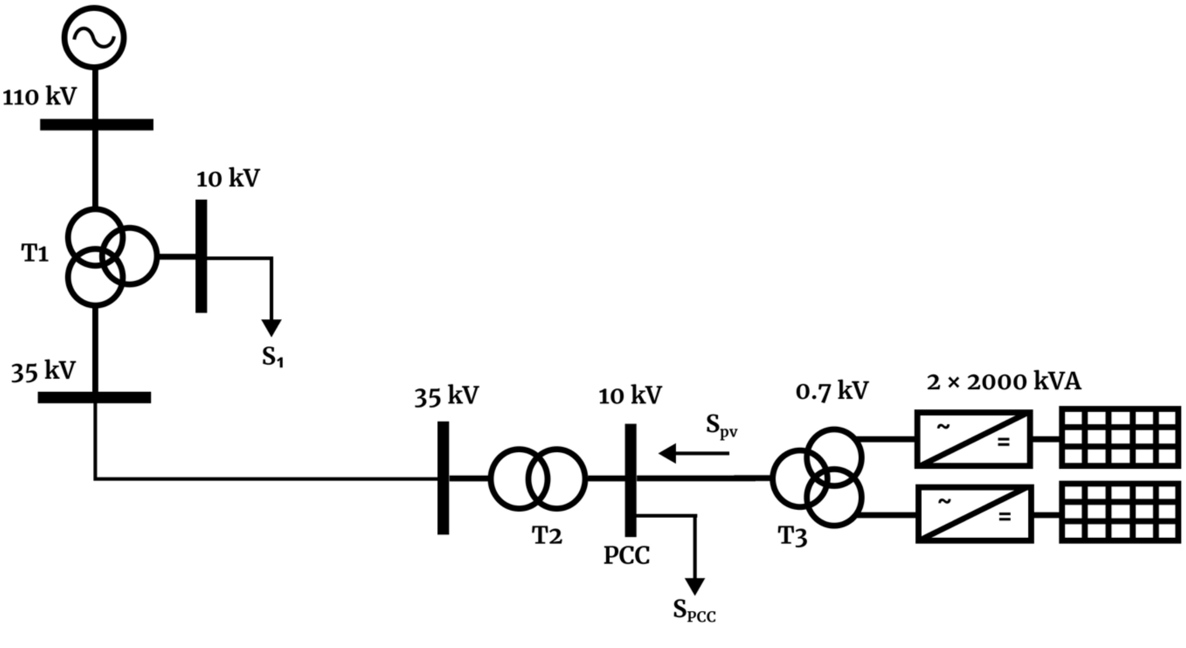

Fig. 1. Schematic diagram of the studied power system.

5. Modeling the inverter control processes

The MATLAB/Simulink environment was used for modeling. To model the power transformers' operation, catalog data and the "Three-Phase Transformer (Two Windings)" and "Three-Phase Transformer (Three Windings)" blocks were used; the parameters for the power transformers are provided in Table 1. The electrical connection between the Point of Common Coupling (PCC) transformer and the main system is established by an overhead power transmission line. The transmission line was modeled based on the catalog data for the AS-70/11 conductor and implemented using the "Three-Phase Series RLC Branch" block; the parameters for the transmission line are presented in Table 2. To create the load at the PCC and at the beginning of the line, the "Three-Phase Series RLC Load" block was used; the parameters for the load are given in Table 3.

Table 1. Power transformer parameters.

Name of parameter	T1	T2	T3
Apparent power S, MVA	25	10	5
Winding 1 voltage V1, kV	115	38.5	10
Winding 2 voltage V2, kV	38.5	10.5	0.7
Winding 3 voltage V3, kV	11	–	0.7
Winding 1 R, p.u.	0.00375	0.00375	0.00465
Winding 2 R, p.u.	0.001343	0.00375	0.0093
Winding 3 R, p.u.	0.0081	–	0.0093
Winding 1 L, p.u.	0.04	0.04	0.0375
Winding 2 L, p.u.	0	0.04	0.075
Winding 3 L, p.u.	0.0675	–	0.075
Magnetization resistance, Rm, p.u.	806	690	544
Magnetization inductance, Lm, p.u.	145	127	114

Table 2. Power transmission lines parameters.

Name of parameter	Value
Length, km	25
R0, Ohms	0.306
X0, Ohms	0.444

Table 3. Load parameters.

Name of parameter	Value
P_l, MW	5
Q_l, MVar	0.5
P_{pcc}, MW	9.5
Q_{pcc}, MVar	1

The “PV Array” block was used to model the set of photovoltaic panels, connected in series to achieve desired voltage and in parallel for desired current, allowing simulation of output power change by causing incoming solar irradiance and temperature changes. The key parameters of the PV array are shown in Table 4. The “Three-Level NPC Converter” was chosen to model DC to AC converter, the inverter parameters are shown in Table 5. The low pass filter parameters are presented in Table 6.

Table 4. PV panels parameters.

Name of parameter	Value
Module data	Solar GS-420KR3
Maximum power, W	420.0526
Open-circuit voltage V_{oc}, V	60.65
Short-circuit current I_{sc}, A	9.12
Voltage at maximum power point V_{mpp}, V	48.73
Current at maximum power point I_{mpp}, A	8.62
Temperature coefficient of V_{oc}, %/deg. C	-0.36
Temperature coefficient of I_{sc}, %/deg. C	0.05
Parallel / Sequential	2 × 31s150p

Table 5. Inverter parameters.

Name of parameter	Value
Model type	Average model U ref controller
Diode on-state resistance, Ohms	0.001
Diode snubber resistance, Ohms	1e6
Diode snubber capacitance, F	inf
Diode forward voltage, V	1e-3
DC side snubber resistance, Ohms	inf

Table 6. Low pass filter parameters.

Name of parameter	Value
L1, mH	150
L2, mH	150
C, μF	500

The inverter control system is implemented based on a phase-locked loop (PLL), achieving inverter voltage synchronization with the measured voltage signal at the point of common coupling (PCC). While the inverter mimics the voltage, the operating modes are controlled by current. To simplify the inverter control system tuning, synchronization with an ideal voltage source has been used, which eliminates undesirable distortions of control signals caused by grid synchronization deviations. The PV system functional diagram is shown in Fig. 2.

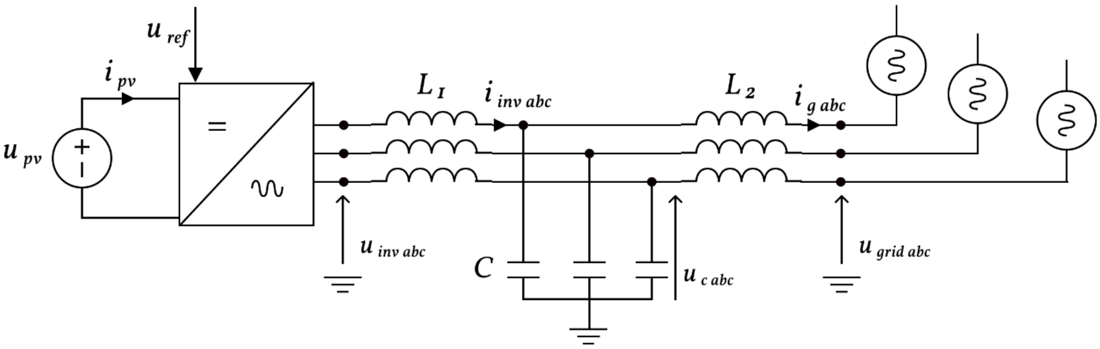

Fig. 2. Functional diagram of the PV system.

The control system was modeled based on Kirchhoff's voltage law for the inverter – filter inductance – filter capacitor loop in the complex-vector form of current and voltage values in the *dq0* coordinate system:

$$\overrightarrow{U_{inv}} = \overrightarrow{U_c} + j\omega L_1 \overrightarrow{I_{inv}}, \tag{1}$$

where $\overrightarrow{U_{inv}}$ is an inverter output voltage vector; $\overrightarrow{U_c}$ is a capacitor voltage vector; $\overrightarrow{I_{inv}}$ is a vector of current from inverter toward filter; L_1 is a filter inductance.

By decomposing the vectors (1) into their real and imaginary parts for each vector, the following expression is obtained:

$$U_{inv\,d} + jU_{inv\,q} = \left(U_{c\,d} + jU_{c\,q}\right) + j\omega L_1\left(I_{inv\,d} + jI_{inv\,q}\right), \tag{2}$$

where $U_{inv\,d}$ is a d-axis component of the inverter voltage; $U_{inv\,q}$ is a q-axis component of the inverter voltage; $U_{c\,d}$ is a d-axis component of the filter capacitor voltage; $U_{c\,q}$ is a q-axis component of the filter capacitor voltage; $I_{inv\,d}$ is a d-axis component of the inverter current; $I_{inv\,q}$ is a q-axis component of the inverter current.

For convenient application in the control system, they have been converted into a system of equations grouped by the values in the real plane and the imaginary plane:

$$\begin{cases} U_{ref\,d} = U_{c\,d} - \omega L_1 I_{inv\,q}; \\ jU_{ref\,q} = jU_{c\,q} + j\omega L_1 I_{inv\,d}. \end{cases} \tag{3}$$

To introduce the reference current values $I_{inv\,d\,ref}$ and $I_{inv\ q\,ref}$ into the system of equations (3), proportional–integral (PI) controllers outputs $(u_{d\,PI}, u_{q\,PI})$ are used, representing the operation of PI controller for the corresponding currents. Thus, the inverter control system takes the form of two control loops – the d-axis current control loop and the q-axis current control loop:

$$\begin{cases} U_{inv\ d\,ref} = u_{d\,PI}\,(I_{inv\,d\,ref} - I_{inv\,d}) - \omega L_1 I_{inv\,q} + U_{c\,d}; \\ U_{inv\ q\,ref} = u_{q\,PI}\,(I_{inv\,q\,ref} - I_{inv\,q}) + \omega L_1 I_{inv\,d} + U_{c\,q}, \end{cases} \tag{4}$$

where $u_{d\,PI}$ is output signal of PI controller for d-axis current; $u_{q\,PI}$ is output signal of PI controller for q-axis current; $I_{inv\,d\,ref}$ is reference current in d-axis; $I_{inv\,q\,ref}$ is reference current in q-axis.

D-q axes currents PI controllers' outputs:

$$u_{d\,PI}(t) = K_p\left(I_{inv\,d\,ref}(t) - I_{inv\,d}\,(t)\right) + K_i\int_0^t \left(I_{inv\,d\,ref}(\tau) - I_{inv\,d}(\tau)\right)d\tau; \tag{5}$$

$$u_{q\,PI}(t) = K_p\left(I_{inv\,q\,ref}(t) - I_{inv\,q}\,(t)\right) + K_i\int_0^t \left(I_{inv\,q\,ref}(\tau) - I_{inv\,q}(\tau)\right)d\tau, \tag{6}$$

where K_p is the proportional gain of the PI controller; K_i is the integral gain of the PI controller; τ is the integration variable.

Since $U_{inv\,d}$ and $U_{inv\,q}$ are large magnitude values, they must be normalized for use in the control systems:

$$\begin{cases} U_{pwm\ d\,ref} = U_{inv\ d\,ref}/(U_{dc}/2); \\ U_{pmw\ q\,ref} = U_{inv\,q\,ref}/(U_{dc}/2), \end{cases} \tag{7}$$

where $U_{pwm\ d\,ref}$, $U_{pmw\ q\,ref}$ are the reference voltage in d-q axes used for PWM generator control; U_{dc} is the DC bus voltage.

Since the variation of solar irradiance directly affects the generated active power, the reference current $I_{inv\,d\,ref}$ value must be carefully adjusted to obtain the maximum power from the solar panels on the one hand, and to maintain the system stability on the other. The d-axis current control equation takes the form of the PI controller output by continuously tracking the difference between the solar panel voltage and reference voltage:

$$I_{inv\,d\,ref} = u_{pv\,PI}\left(U_{pv\,ref} - U_{pv}\right), \tag{8}$$

where $U_{pv\,ref}$ is the reference voltage of the PV panels; U_{pv} is the measured voltage of the PV panels; $u_{pv\,PI}$ is the output signal of PI controller of PV voltage.

PV voltage PI controller output:

$$u_{pv\,PI}(t) = K_p\left(U_{pv\,ref}(t) - U_{pv}(t)\right) + K_i\int_0^t \left(U_{pv\,ref}(\tau) - U_{pv}\,(\tau)\right)d\tau, \tag{9}$$

where K_p is the proportional gain of the PI controller; K_i is the integral gain of the PI controller; τ is integration variable.

To model various techniques of reactive power control, the reference current value $I_{inv\,q\,ref}$ should be continuously adjusted by the control system as a function reacting to external parameters change depending on the specified reactive power control mode, $I_{inv\,q\,ref} = f(\varphi)$ for constant power factor or $I_{inv\,q\,ref} = f\left(U_{pcc}\right)$ for Volt Var control.

To mimic the solar irradiance changes, the results of [13] were used. According to the source, the most probable ramp rate of solar irradiance during dense moving clouds lies in the range of $[-200\ \ldots\ +200]\ (W/m^2)/s$. The solar irradiance variations over 240 seconds used for further modeling are shown in Fig. 3.

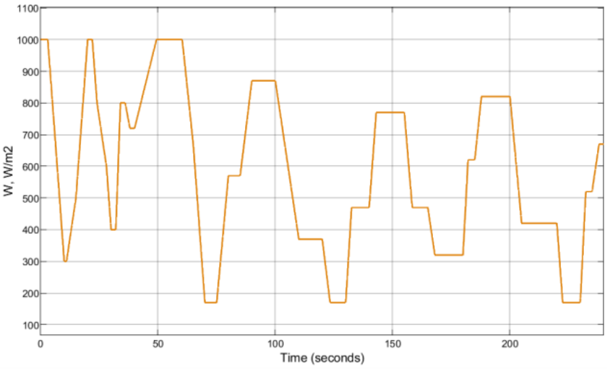

Fig. 3. Solar irradiance variation.

To configure the control system for constant power factor mode the PI controller has been used, which continuously adjusts the q-axis inverter current:

$$I_{inv\,q\,ref} = u_{\varphi\,PI}\left(P_{grid}\mathrm{tg}(\varphi_{ref}) - Q_{grid}\right), \tag{10}$$

where $\mathrm{tg}(\varphi_{ref})$ is a desired power factor for the control system to maintain; Q_{grid} is a measured value of inverter output reactive power injected into the grid; P_{grid} is a measured value of inverter output reactive power injected into the grid; $u_{\varphi\,PI}$ is the output signal of power factor PI controller.

Power factor PI controller output:

$$u_{\varphi\,PI}(t) = K_p\left(P_{grid}(t)\,\mathrm{tg}(\varphi_{ref}(t)) - Q_{grid}(t)\right) + K_i\int_0^t \left(P_{grid}(\tau)\,\mathrm{tg}(\varphi_{ref}(\tau)) - Q_{grid}(\tau)\right)d\tau\,, \tag{11}$$

where K_p is the proportional gain of the PI controller; K_i is the integral gain of the PI controller; τ is integration variable.

Depending on the selected reactive power control technique, a different voltage profile and amplitude of the voltage changes will be observed at the PCC. This is because modern PV inverters are capable not only of converting DC into AC, but also of operating as dynamically controlled devices, generating or consuming reactive power.

Fig.4 presents the simulation results to demonstrate the operating conditions of the PV inverter with a unity power factor. In this case, the inverter generates only active power, while its reactive power equals zero (Fig. 4,*a*). Fig. 4,*c* demonstrates the current component along the q-axis, which corresponds to reactive power, is adjusted by the control system (10) to maintain the inverter's output reactive power, whereas the d-axis component varies according to changes in solar irradiance (8). In this operating mode, the voltage at the PCC (Fig. 4,*b*) increases proportionally to the changes in active power generation. This phenomenon is explained by the fact that the power flow from the PV inverters to the grid reduces the voltage drop across the transmission line impedance, resulting in a voltage increase at PCC.

For comparison, Fig. 5 shows the system controls reactive power maintaining a fixed inductive power factor ($\cos\varphi_{inv} = 0.95$). In this case, in addition to active power generation coming from PV, the inverter consumes reactive power from the grid proportionally to the specified power factor. This is shown in Fig. 5,*c*, where the current component along the q-axis has a negative value. Fig. 5,*b* demonstrates voltage changes are significantly lower compared to the operating mode with $\cos\varphi_{inv} = 1$. This mode serves as an effective method for preventing overvoltage, particularly during periods of peak solar activity and low local demand.

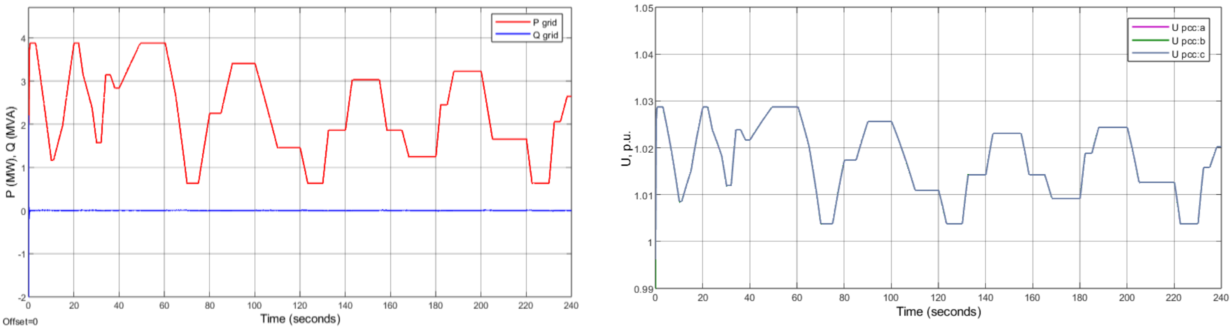

a – the output active and reactive powers of the PV power plant

b – the voltage levels at the PCC

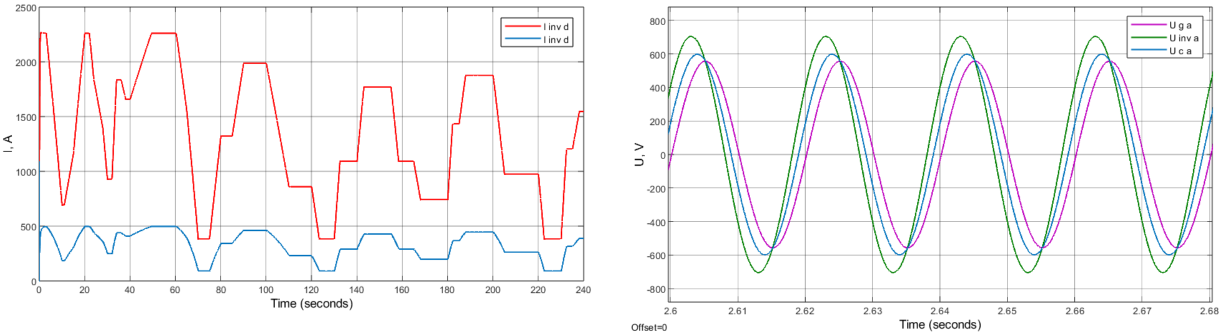

c – the inverter currents' magnitudes along the d and q axes

d – the waveforms of the inverter voltage, filter capacitor voltage, and grid voltage

Fig. 4. Simulation results of the constant power factor $\cos\varphi_{inv} = 1$ reactive power control mode.

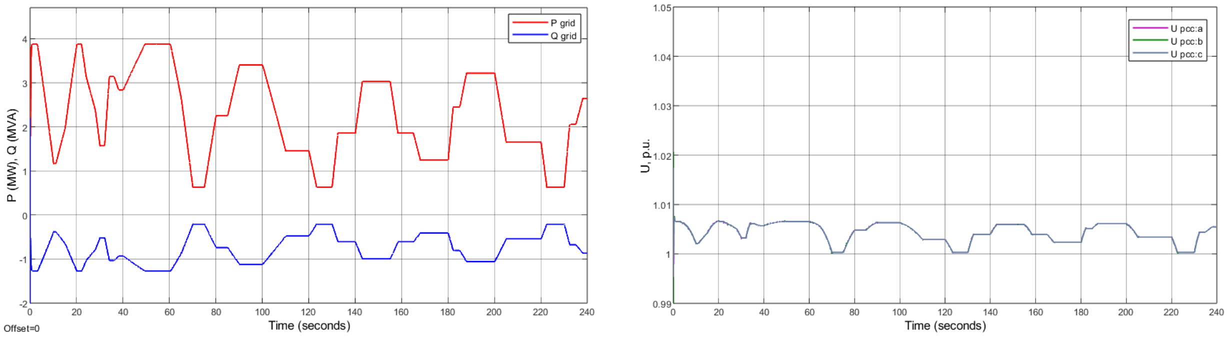

a – the output active and reactive powers of the PV power plant

b – the voltage levels at the PCC

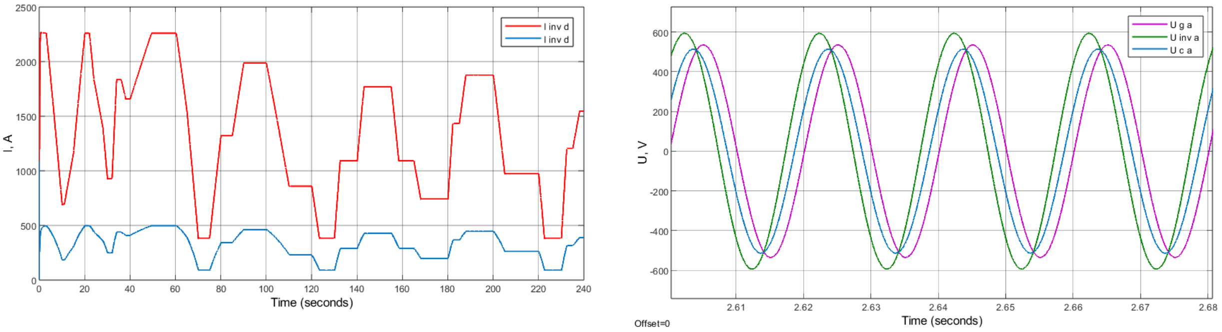

c – the inverter currents' magnitudes along the d and q axes

d – the waveforms of the inverter voltage, filter capacitor voltage, and grid voltage

Fig. 5. Simulation results of the constant power factor $\cos\varphi_{inv} = 0.95$ (inductive) reactive power control mode.

Fig. 6 displays the simulation results for the operating mode with a capacitive power factor, in which the inverter generates reactive power proportionally to the generated active power. In Fig. 6,*c*, the current along the q-axis has the opposite direction and a greater amplitude compared to the inductive mode, which makes it an amplifier of voltage deviations during the active power generation changes caused by irradiance variations.

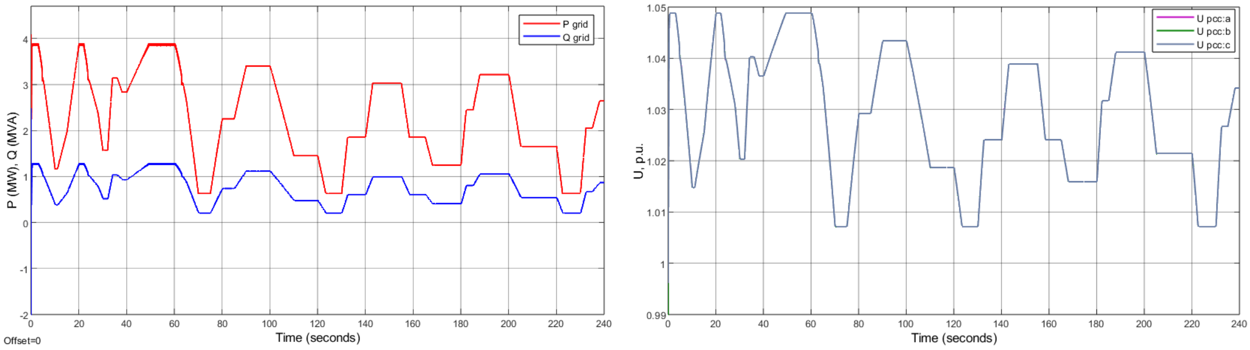

a – the output active and reactive powers of the PV power plant

b – the voltage levels at the PCC

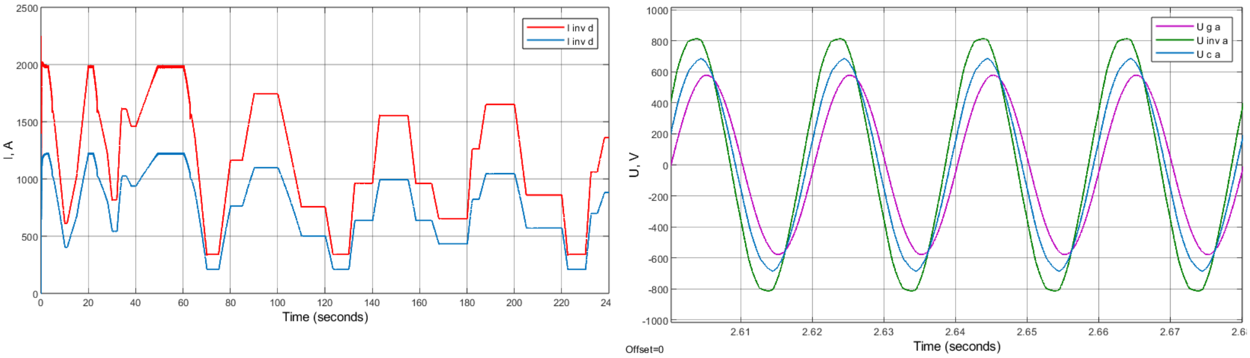

c – the inverter currents' magnitudes along the d and q axes

d – the waveforms of the inverter voltage, filter capacitor voltage, and grid voltage

Fig. 6. Simulation results of the constant power factor $\cos\varphi_{inv} = -0.95$ (capacitive) reactive power control mode.

By analyzing the plots presented in Fig. 4, Fig. 5 and Fig. 6, the common pattern of reactive power control in PV power plants with a constant reactive power factor has been identified and confirmed – a reduction of the amount of reactive power generated into the grid leads to a decrease of voltage changes in the PCC connection with electrical grid [14].

However, this control mode does not provide an adaptive response to variations in grid parameters and does not allow the inverters to maintain the voltage within a specified range, which restricts its application in the grids with a high share of distributed generation.

To implement the Volt Var reactive power control mode, a PI controller was used, whose output adjusts the inverter current magnitude along the q-axis based on measured and reference voltages at the PCC buses:

$$I_{inv\,q\,ref} = u_{vpcc\,PI}\left(U_{ref\,pcc} - U_{pcc}\right), \tag{12}$$

where $U_{ref\,pcc}$ is the reference value of the voltage to maintain at the PCC; U_{pcc} is the measured value of the voltage at the PCC; $u_{vpcc\,PI}$ is the voltage PI controller output.

Voltage PI controller output:

$$u_{vpcc\,PI}(t) = K_p\left(U_{ref\,pcc}(t) - U_{pcc}(t)\right) + K_i\int_0^t \left(U_{ref\,pcc}(\tau) - U_{pcc}(\tau)\right) d\tau\,, \tag{13}$$

where K_p is the proportional gain of the PI controller; K_i is the integral gain of the PI controller; τ is integration variable.

The simulation results of PV operating in the PCC voltage support mode is presented in Fig. 7. The variations of PV output power shown in Fig. 7,*a* indicate that the reactive power increases inversely proportionally to the changes in active power, thereby compensating the variations in solar irradiance. While output power remains the same, Fig. 7,*b* demonstrates a stabilized voltage level at the PCC achieved solely through Volt Var reactive power control technique.

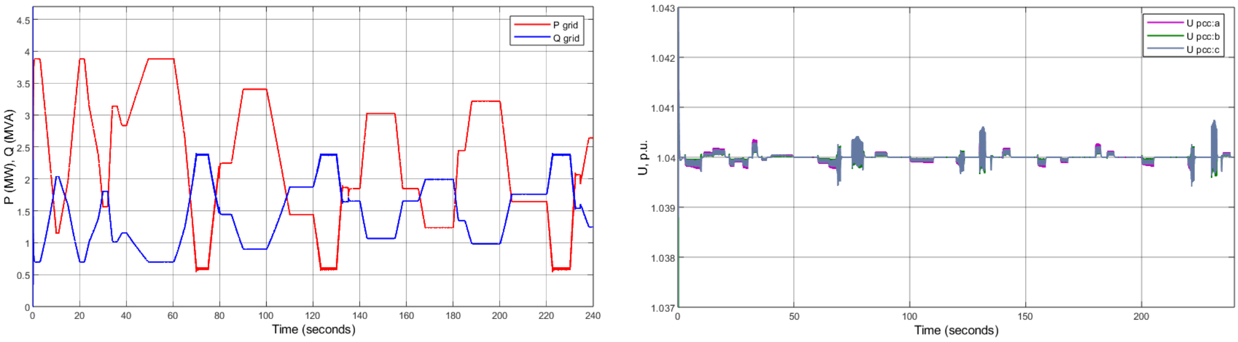

a – the output active and reactive powers of the PV power plant

b – the voltage levels at the PCC

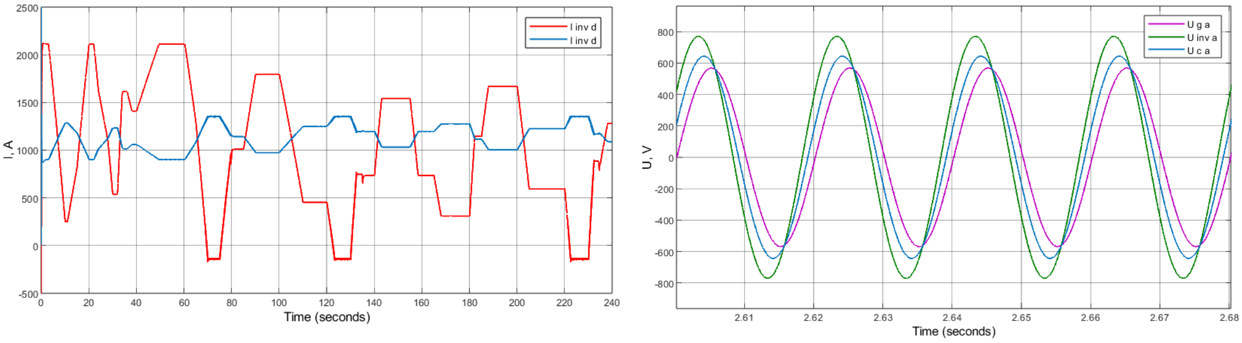

c – the inverter currents' magnitudes along the d and q axes

d – the waveforms of the inverter voltage, filter capacitor voltage, and grid voltage

Fig. 7. Simulation results of the Volt Var voltage support reactive power control mode ($U_{pcc\,ref} = 1.04$).

6. Conclusion

In this study, a control system for a photovoltaic (PV) inverter was modeled, and a comparative analysis was conducted on reactive power control techniques for the PV plant integrated into a medium-voltage grid. The abrupt variations in solar irradiance, causing PV output power changes, were considered as a key factor in voltage changes. Results indicate that in grids featuring a substantial proportion of PV generation, power changes induced by the irradiance changes can cause significant voltage changes at the point of common coupling (PCC). The profiles of the voltage changes at PCC were examined depending on the reactive power control technique. The results show that inverters equipped with the reactive power control features are also effective support devices, maintaining voltage within predefined bounds.

Findings reveal that when incorporating PV power plants into suitably designed grids, voltage control can be performed without the use of expensive energy storage systems, utilizing only the reactive power capabilities of PV inverters. This underscores the role of PV power plants as a grid support asset, especially in scenarios with elevated renewable energy penetration.

References

[1] R. Yan, S. Roediger and T. K. Saha. (2011). Impact of photovoltaic power fluctuations by moving clouds on network voltage: A case study of an urban network. *AUPEC*, Brisbane, QLD, Australia, 2011, pp. 1-6.

[2] R. Yan and T. K. Saha. (2012). Investigation of Voltage Stability for Residential Customers Due to High Photovoltaic Penetrations. *IEEE Transactions on Power Systems*, vol. 27, no. 2, pp. 651-662, May 2012. https://doi.org/10.1109/TPWRS.2011.2180741.

[3] R. Yan and T. K. Saha. (2011). Investigation of voltage variations in unbalanced distribution systems due to high photovoltaic penetrations. *2011 IEEE Power and Energy Society General Meeting*. Detroit, MI, USA, pp. 1-8. https://doi.org/10.1109/PES.2011.6038977.

[4] F. C. L. Trindade, T. S. D. Ferreira, M. G. Lopes and W. Freitas. (2017). Mitigation of Fast Voltage Variations During Cloud Transients in Distribution Systems with PV Solar Farms. *IEEE Transactions on Power Delivery*, vol. 32, no. 2, pp. 921-932, April 2017. https://doi.org/10.1109/TPWRD.2016.2562922

[5] Three-Level Inverter Control Techniques: Design, Analysis, and Comparisons. (2021). *Elektronika Ir Elektrotechnika*, 27(3), 26-37. https://doi.org/10.5755/j02.eie.29015

[6] F. M. Aboshady, I. Pisica, A. F. Zobaa, G. A. Taylor, O. Ceylan and A. Ozdemir. (2023). Reactive Power Control of PV Inverters in Active Distribution Grids with High PV Penetration. *IEEE Access*, vol. 11, pp. 81477-81496, https://doi.org/10.1109/ACCESS.2023.3299351

[7] A. H. Javed, P. H. Nguyen, J. Morren and J. G. H. Slootweg. (2023). Using Smart PV Inverters for Reactive Power Management in Distribution Grids. *2023 IEEE Belgrade PowerTech*, Belgrade, Serbia, pp. 1-6. https://doi.org/10.1109/PowerTech55446.2023.10202681.

[8] Xu, Ke. (2024). Low-Voltage Ride-Through Technology in Photovoltaic Power Generation. Highlights in Science, Engineering and Technology. 81. 176-181. https://doi.org/10.54097/ypyswj45.

[9] A. Amanipoor, M. S. Golsorkhi, N. Bayati and M. Savaghebi. (2023). V-Iq Based Control Scheme for Mitigation of Transient Overvoltage in Distribution Feeders with High PV Penetration. *IEEE Transactions on Sustainable Energy*, vol. 14, no. 1, pp. 283-296, Jan. 2023. https://doi.org/10.1109/TSTE.2022.3211179

[10] K. Kawabe and K. Tanaka. (2015). Impact of Dynamic Behavior of Photovoltaic Power Generation Systems on Short-Term Voltage Stability. *IEEE Transactions on Power Systems*, vol. 30, no. 6, pp. 3416-3424, Nov. 2015, https://doi.org/10.1109/TPWRS.2015.2390649.

[11] Munkhchuluun, Enkhtsetseg & Meegahapola, L.G. & Vahidnia, Arash. (2020). Long-term voltage stability with large-scale solar-photovoltaic (PV) generation. *International Journal of Electrical Power & Energy Systems*. 117. 105663. https://doi.org/10.1016/j.ijepes.2019.105663.

[12] E. Munkhchuluun and L. Meegahapola. (2017). Impact of the solar photovoltaic (PV) generation on long-term voltage stability of a power network. *2017 IEEE Innovative Smart Grid Technologies - Asia (ISGT-Asia)*, Auckland, New Zealand, pp. 1-6, https://doi.org/10.1109/ISGT-Asia.2017.8378456

[13] A. R. Nikolopoulos, E. I. Batzelis, P. Lewin and N. Nikolaou. (2024). Statistical Analysis of Solar Irradiance Variability. *2024 IEEE Power & Energy Society General Meeting (PESGM)*, Seattle, WA, USA, 2024, pp. 1-5, doi: https://doi.org/10.1109/PESGM51994.2024.10689164.

[14] Yu. O. Varetskyy, V. M. Horban, Ya. S. Pazyna. (2016). Voltage variations in electrical microgrid with hybrid power plant. *Bulletin of Lviv Polytechnic National University: Electric Power and Electromechanical Systems*, No. 840, pp. 17-23. (in Ukrainian)

Моделювання процесів керування для фотоелектричних станцій

Олег Максимук

Національний університет «Львівська політехніка», вул. С. Бандери, 12, м. Львів, Україна

Анотація

Збільшення попиту на електроенергію та потреба в відновлюваній енергії сприяють швидкому впровадженню джерел розподіленого генерування, серед яких сонячна енергетика займає провідне місце. Фотоелектричні системи перетворюють енергію сонячного світла на електричну, проте чутливість до змін погодних умов обмежує їх широке застосування без допоміжних систем енергозбереження. Однією з головних проблем під час експлуатації фотоелектричних панелей є змінний характер вихідної потужності, спричинений змінами інтенсивності сонячної радіації. В слабких електричних мережах динамічні зміни активної потужності мають значний вплив на рівні напруги і, як наслідок, на електромагнітну сумісність і стійкість роботи джерел генерування та споживачів. На прикладі мережі з одностороннім живленням, використовуючи програмне середовище MATLAB/Simulink, досліджено вплив змін потужності фотоелектричної станції внаслідок динамічних змін сонячної радіації на рівні напруги в пункті спільного приєднання. Проаналізовано характер змін напруги залежно від способу керування інверторами фотоелектричних станцій.

Ключові слова: сонячна електростанція; фотоелектрична панель; реактивна потужність; зміна напруги; електрична мережа.

ENERGY ENGINEERING AND CONTROL SYSTEMS

Volume 11, Number 2, 2025

Use of Trapezoidal Weirs for Determining Seepage Discharge through Earth Dams

Roman Zaichuk*

National University of Water and Environmental Engineering, 11 Soborna St., Rivne, 33000, Ukraine

Received: October 11, 2025. Revised: November 12, 2025. Accepted: November 19, 2025.

Abstract

The paper presents a comprehensive analysis of the application of trapezoidal weirs coupled with automated measurement systems for the precise determination of seepage flow rates through earth dams at hydroelectric power plants. A key focus is placed on the hydraulic operating modes of these weirs, particularly the distinction between non-submerged and submerged conditions. The paper details the results of extensive laboratory studies conducted to quantify the impact of submergence on the discharge capacity of trapezoidal weirs. These experiments led to the derivation of a submergence coefficient, which is crucial for correcting standard discharge formulas. The findings demonstrate that neglecting this coefficient can lead to significant overestimation of actual flow rates, with errors exceeding 457%. The study proposes a refined formula and a corresponding graphical relationship to ensure accurate seepage monitoring, thereby enhancing the operational safety of hydraulic structures.

Keywords: trapezoidal weirs; laboratory studies; submergence coefficient; discharge capacity; measurement automation.

1. Use of weirs at hydropower plants in Ukraine

In the construction of hydroelectric power plants, earth dams are fundamental structures used to create a hydraulic head. A critical and inherent characteristic of these embankments is the presence of seepage through the dam's body and foundation. According to the U.S. Bureau of Reclamation's Water Measurement Manual [1], the diligent monitoring of this seepage is not merely a procedural task but a cornerstone of dam safety and operational integrity. Uncontrolled or excessive seepage can lead to internal erosion (piping), which compromises the structural stability of the dam and poses a significant risk. Consequently, continuous monitoring is conducted through a network of instruments and observations, tracking key parameters such as soil strength, the position of the phreatic surface (depression curve), seepage velocities, and hydraulic gradients.

To manage and quantify seepage, dams are equipped with special drainage systems designed to intercept and safely divert percolating water. These systems often include internal pipe drains, inspection wells, and collection channels. A crucial aspect of this monitoring program is the accurate measurement of the seepage flow rate at various points within the drainage network. For this purpose, various hydraulic measurement devices are employed, among which weirs are one of the most reliable and widely accepted solutions, as detailed by Ackers et al. in *Weirs and Flumes for Flow Measurement* [2].

For measuring flow in open, non-pressurized channels, thin-plate weirs offer a simple, cost-effective, and accurate method. These structures function by forcing the flow over a crest of a specific shape, creating a direct relationship between the upstream water depth (head) and the discharge. According to their geometry, weirs are classified as rectangular, triangular (V-notch), and trapezoidal, among others (Fig. 1) [3]. The trapezoidal weir, particularly the

---

* Corresponding author. Email address: r.m.zaichuk@nuwm.edu.ua

This paper should be cited as: R. Zaichuk. (2025). Use of trapezoidal weirs for determining seepage discharge through earth dams. *Energy Engineering and Control Systems*, Vol. 11, No. 2, pp. 109 – 114. https://doi.org/10.23939/jeecs2025.02.109

Cipolletti type with sides sloped at 1 horizontal to 4 vertical, is highlighted in the Water Measurement Manual as a standard design that automatically compensates for end contractions. Due to their reliability and robust performance, both trapezoidal and triangular weirs are the most commonly utilized types in field and laboratory settings for hydraulic measurements.

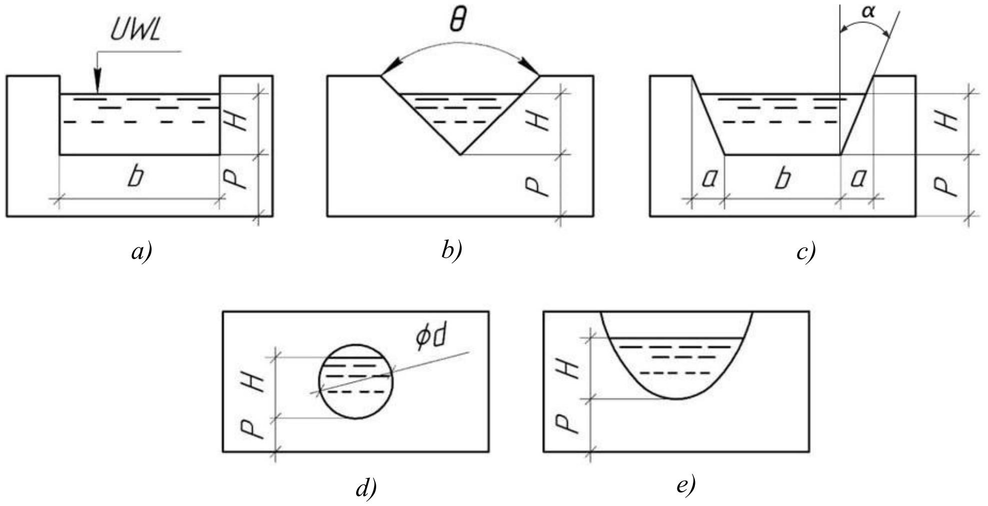

a) *b)* *c)*

d) *e)*

Fig. 1. Types of weirs for non-pressurized flows by cross-sectional shape: *a)* – rectangular, *b)* – triangular, *c)* – trapezoidal, *d)* – circular, *e)* – parabolic (where: UWL is upstream water level; H is the head on the weir crest; P is the weir crest height; b is the crest width; θ is the angle of the V-notch; α is the angle of the side slope; $\o d$ is the diameter)

2. Types of hydraulic regimes for trapezoidal weirs

By the type of hydraulic regime, weirs are divided into submerged and non-submerged (free-flow) [4]. In the presence of a subcritical flow, a thin-plate weir is considered non-submerged if the downstream water level is below the weir crest elevation (Fig. 2). In laboratory settings, weirs are arranged to always operate in a non-submerged mode. In field conditions, efforts are also made to install weirs so that they are non-submerged. The water discharge through a non-submerged symmetric trapezoidal weir can be found using the following formula [5],[6]:

$$Q = m_d(b + 0.8\tan\alpha\, H)H\sqrt{2gH}, \tag{1}$$

where H is the head on the weir crest; m_d is the weir discharge coefficient; b is the crest width; g is the acceleration due to gravity; α is the angle between the vertical and the side of the trapezoid. Here, H and b are expressed in meters, g in m/s², and the discharge Q in m³/s.

If the crest width b and head H are expressed in meters, and we assume $m_d = 0.42$, $m_n = 0.25$ for a trapezoidal thin-plate weir with an angle $\alpha = 14°$, and $g = 9.81$ m/s², the formula (1) takes the following form for discharge Q in m³/s:

$$Q = 1.86(b + 0.2H)H^{3/2}. \tag{2}$$

The calculated discharge values Q, according to formula (2), are presented in Table 1.

The head on the weir crest is measured using sensors, and the discharge is then determined from this head. It must be emphasized that formulas (1), (2), and consequently the results of automatic measurements, are valid only for a non-submerged weir, where the downstream water level (↓DWL) is below the crest elevation (Fig. 2,*a*), $\downarrow DWL < \downarrow weir\ crest$.

In the case of a submerged weir (Fig. 2,*b*), $\downarrow DWL > \downarrow weir\ crest$, the weir is submerged, and formulas (1), (2) contain a certain error due to not accounting for the effect of submergence. The magnitude of this error depends on the degree of submergence, and formulas (1) and (2) significantly overestimate the actual discharge value.

Table 1. Discharge values Q for a trapezoidal weir according to formula (2) with m_d = 0.42, m_n = 0.25, g = 9.81 m/s², b = 0.4 m.

H	*Q*	*H*	*Q*	*H*	*Q*	*H*	*Q*
m	m³/s	m	m³/s	m	m³/s	m	m³/s
0.05	0.009	0.14	0.042	0.26	0.111	0.44	0.265
0.06	0.011	0.15	0.046	0.28	0.126	0.46	0.286
0.07	0.014	0.16	0.051	0.30	0.141	0.48	0.307
0.08	0.018	0.17	0.057	0.32	0.156	0.50	0.329
0.09	0.021	0.18	0.062	0.34	0.173	0.60	0.450
0.10	0.025	0.19	0.067	0.36	0.190	0.70	0.588
0.11	0.029	0.20	0.073	0.38	0.207	0.80	0.745
0.12	0.033	0.22	0.085	0.40	0.226	0.90	0.921
0.13	0.037	0.24	0.098	0.42	0.245	1.00	1.116

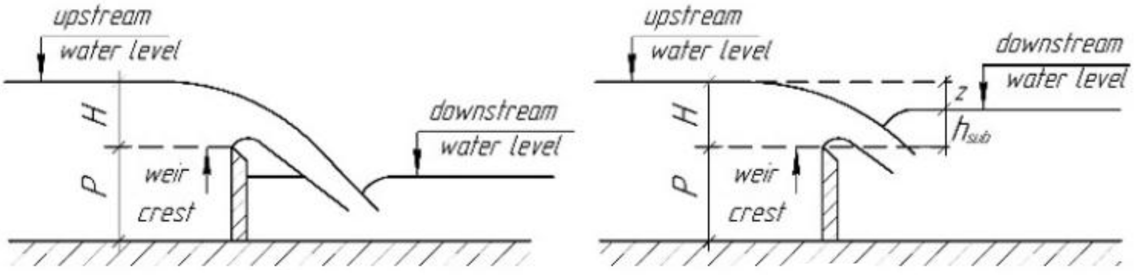

a) *b)*

Fig. 2. Scheme of unsubmerged (*a*) and submerged (*b*) trapezoidal weir.

3. Laboratory investigation of the submergence effect

Formula (2), taking into account the effect of submergence, will take the below form:

$$Q = 1.86(b + 0.2H)\sigma_s H^{3/2}, \tag{3}$$

where σ_s is the submergence coefficient.

Using a symmetric trapezoidal weir with a crest width b = 0.4 m and an angle of inclination of the side relative to the vertical α = 14°, and an automated measurement system, a hydraulic modeling of the operation of trapezoidal weirs in a submerged mode was carried out in the laboratory conditions in the following way.

- The level of weir crest was measured as 20.09 mm.
- The water discharge Q_Δ was supplied to the flume and measured by a triangular weir located at the beginning of laboratory setup.
- The submerged regime was simulated in the downstream of the trapezoidal weir by means of different types of gates.
- The upstream water level (↓UWL) and downstream water level (↓DWL) were measured after the steady flow was formed in the flume.
- The depth downstream the weir was increased several times for the same water discharge in the flume Q_Δ. For each depth, the new values of ↓UWL and ↓DWL were measured.
- The water discharge Q_Δ was changed and all operations were repeated.
- Based on measured data the head H, submerged depth h_{sub} of trapezoidal weir and the flow water rate by formula (2) Q_{f2} were calculated.
- To find the influence from submerged depth on values of water flow rate the difference between the values Q_{f2} and Q_Δ was found.

The results of determining the submergence coefficient are presented in Table 2. Furthermore, there is a comparison of the actual discharge value with the theoretical one, which does not account for the influence of the submergence coefficient.

Table 2. Experimental values of σ_S for a trapezoidal weir.

Actual discharge (from triangular weir), Q_{Δ}, dm^3/s	Head on trapezoidal weir, H, cm	Submergence depth, h_s, cm	h_s / H	Submergence coefficient, σ_S	Theoretical discharge (formula (2)) Q_{f2}, dm^3/s	Deviation of actual from theoretical discharge, ΔQ, %
1	2	3	4	5	6	7
5.00	4.4	0.2	0.045	0.7125	7.02	40.36
13.67	20.5	20	0.976	0.1796	76.13	456.95
	14.8	14	0.946	0.3005	45.50	232.81
	11.6	10.5	0.905	0.4396	31.10	127.50
	7	1.9	0.271	0.9585	14.26	4.33
30.01	24.7	23.7	0.960	0.2925	102.61	241.92
	24.1	23.5	0.975	0.3043	98.63	228.66
	24	22.8	0.950	0.3063	97.97	226.47
	22	20.7	0.941	0.3522	85.22	183.96
	14.7	10.7	0.728	0.6667	45.01	50.00
	12.9	7	0.543	0.8178	36.69	22.27
	11.4	0.8	0.070	0.9914	30.27	0.86
40.75	26.6	25.7	0.966	0.3524	115.64	183.79
	26.4	25.1	0.951	0.3567	114.24	180.35
	24.9	23.1	0.928	0.3920	103.95	155.10
	19.7	15.5	0.787	0.5702	71.46	75.37
	16	9	0.563	0.7924	51.43	26.20
	15.2	6.5	0.428	0.8590	47.44	16.42
	14.5	2	0.138	0.9249	44.06	8.12
50.61	28.6	26.9	0.941	0.3891	130.07	157.00
	27.3	24.4	0.894	0.4196	120.61	138.31
	25.4	21.4	0.843	0.4715	107.34	112.09
	23	17.4	0.757	0.5531	91.50	80.80
	19.7	10	0.508	0.7082	71.46	41.20
	18.1	4.7	0.260	0.8101	62.48	23.45
	17.7	4	0.226	0.8392	60.31	19.16

Table 2 shows that if the influence of the submergence coefficient is not considered, the calculated discharge values using formula (2) will far exceed the actual values. The largest deviation is observed at low flow rates, reaching over 400%. Based on the data from Table 2, a graph of the relationship $\sigma_s = f(h_s/H)$ is plotted and compared with other experimental curves (Fig. 3).

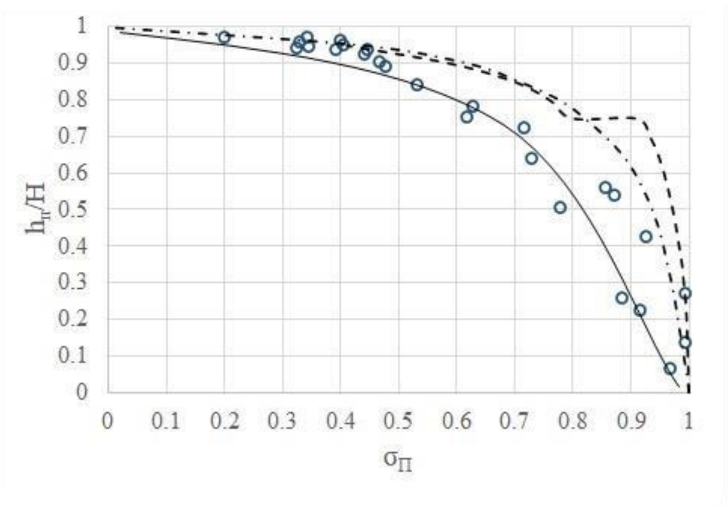

Fig. 3. Graph for determining the submergence coefficient $\sigma_s = f(h_s/H)$: ○ – experimentally obtained values of the submergence coefficient; - - - – submergence coefficient values according to Pavlovsky M.M. [8]; – · – – submergence coefficient values according to TUiN MES [8].

Thus, the general curve $\sigma_s = f(h_s/H)$ for trapezoidal weirs is shown in Fig. 4, and the values of the submergence coefficient are given in Table 3.

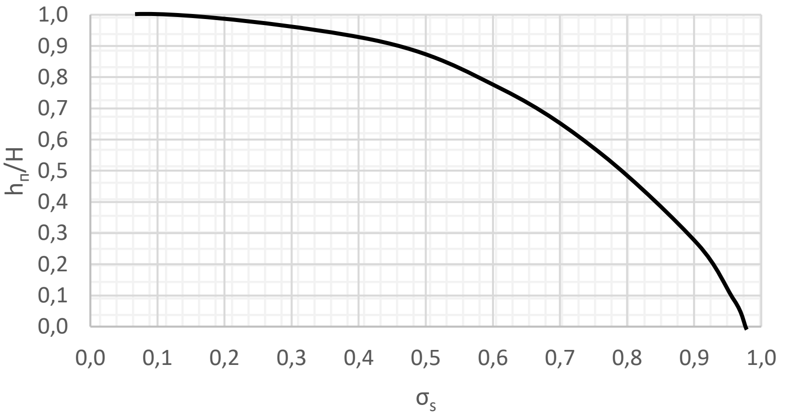

Fig. 4. Curve $\sigma_s = f(h_s/H)$ for trapezoidal weirs with a crest width b = 0.4 m.

Table 3. Submergence coefficient values for trapezoidal weirs with crest width b=0.4 m and side slope angle α=14°.

h_s/H	σ_s	h_s/H	σ_s
1.0	0.000	0.5	0.8
0.95	0.23	0.45	0.83
0.9	0.38	0.4	0.86
0.85	0.47	0.35	0.88
0.8	0.54	0.3	0.9
0.75	0.6	0.25	0.92
0.7	0.66	0.2	0.94
0.65	0.7	0.15	0.95
0.6	0.73	0.1	0.96
0.55	0.77	0.05	0.97
-	-	0	1.000

Taking into account the performed calculations and the obtained results, the final dependencies for determining the discharge capacity of trapezoidal weirs can be defined on the basis of formula (3).

4. Conclusion

The performed research demonstrates that operating trapezoidal weirs in a submerged mode without accounting for the submergence effect leads to significant errors in discharge measurement, reaching up to 457% in the considered range. To obtain reliable data, it is imperative to use the derived submergence coefficient σ_s. The study recommends determining the discharge on trapezoidal weirs with a crest width of $b = 0.4$ m using the corrected formula (3), where the submergence coefficient can be determined from the proposed experimental curve $\sigma_s = f(h_s/H)$. This methodology requires measuring water depths both upstream and downstream of the weirs, but provides a crucial improvement in the accuracy of seepage monitoring for earth dams.

References

[1] U.S. Bureau of Reclamation. (2001). Water Measurement Manual. U.S. Department of the Interior.

[2] P. Ackers, W. R. White, J. A. Perkins, A. J. M. Harrison. (1978). Weirs and Flumes for Flow Measurement. *New York: John Wiley & Sons*, 327 p.

[3] Ali R. Vatankhah, Zahra Amjadian, Mandana Javadi. (2026). Comments on “Numerical modeling and discharge coefficient analysis of semi-elliptical sharp crested weirs” by Parsaie A., BasitNejad M., Bahrami-Yarahmadi M., *Flow Measurement and Instrumentation*, Volume 107, 103118, https://doi.org/10.1016/j.flowmeasinst.2025.103118.

[4] Md. Ayaz, Talib Mansoor. (2018). Discharge coefficient of oblique sharp crested weir for free and submerged flow using trained ANN model. *Water Science*, Volume 32, Issue 2, Pages 192-212, https://doi.org/10.1016/j.wsj.2018.10.002.

[5] Bolshakov, V.A. (Ed.). (1984). Hydraulics Handbook. *Vyshcha shkola*, Kyiv, 343 p. (in Ukrainian)

[6] Havrylenko, I.V., Smyrnov, S.A. (2017). Hydraulics (Part 2): Weirs and Flumes. *LNAU*, Lviv, 120 p. (in Ukrainian)

[7] DSTU B V.2.1-29:2010. (2011). Construction. Hydraulic Structures. Terms and Definitions. *Minrehionbud Ukrainy*, Kyiv. (in Ukrainian)

[8] Pavlovsky, M.M. (1974). Hydraulic Calculations of Thin-Plate Weirs. *Tekhnika*, Kyiv, 185 p. (in Ukrainian)

[9] Riabenko, O.A., Sunichuk, S.V., Zaichuk, R.M. (2022). Modeling of Weir Submergence in Laboratory Conditions. *Bulletin of National University of Water and Environmental Engineering*, No. 4(100), pp. 45–52. (in Ukrainian)

[10] Khilchevsky, V.K., Rudko, H.I., Zabokrytska, M.R. (2012). Fundamentals of Hydrology: Textbook. *Lybid*, Kyiv, 312 p. (in Ukrainian)

[11] Hirin, V.M., Makhynia, M.O. (2010). Dam Structures: Textbook. *ISDO*, Kyiv, 204 p. (in Ukrainian)

Використання трапецієвидних водомірів для визначення фільтраційних витрат земляних гребель

Роман Зайчук

Національний університет водного господарства та природокористування,
вул. Соборна, 11, м. Рівне, 33000, Україна

Анотація

Забезпечення безпечної експлуатації гідроелектростанцій вимагає точного моніторингу фільтраційних процесів у земляних греблях. У статті представлено комплексний аналіз застосування трапецієвидних водомірів, оснащених автоматизованими системами вимірювання, як ефективного інструменту для визначення фільтраційних витрат. Детально розглянуто гідравлічні режими роботи водомірів, зокрема розкрито відмінності між незануреним та зануреним станом. Основну увагу приділено результатам лабораторних досліджень, проведених з метою кількісної оцінки впливу підтоплення на пропускну здатність водомірів. На основі експериментальних даних було виведено коефіцієнт підтоплення, що є ключовим для корекції стандартних розрахункових формул. Дослідження доводить, що ігнорування цього коефіцієнта призводить до значного завищення реальних значень витрати з похибкою, що може перевищувати 457%. У статті запропоновано удосконалену формулу та відповідну графічну залежність для забезпечення точного моніторингу, що суттєво підвищує надійність контролю за станом гідротехнічних споруд.

Ключові слова: трапецієвидні водоміри; лабораторні дослідження; коефіцієнт підтоплення; пропускна здатність; автоматизація вимірювань; фільтраційні втрати.

ENERGY ENGINEERING AND CONTROL SYSTEMS

Volume 11, Number 2, 2025

Public Priorities for the Post-War Reconstruction of Ukraine's Energy Sector

Olena Savchenko[a,*], Khrystyna Kozak[b], Vasyl Zhelykh[a], Omar Al-Hafith[c],
Joao Alencastro[c], Olugbenga Oladinrin[c], Ademola Akinbami[c]

[a]*Lviv Polytechnic National University, 12, S. Bandery St., Lviv, 79013, Ukraine*
[b]*Services Design Solutions LTD, Hembry House, Pynes Hill, Exeter, EX2 5SE, Great Britain*
[c]*University of Plymouth, Roland Levinsky St., 302, Plymouth, PL4 8AA, Great Britain*

Received: October 12, 2025. Revised: November 25, 2025. Accepted: December 02, 2025.

Abstract

The Russian invasion of Ukraine has resulted in the large-scale destruction of many cities across the country. Although the war has not yet ended, there will come a time when the conflict concludes, and reconstruction efforts will begin. Global experiences show that the first step in preparing for post-war reconstruction is to assess the level of destruction. Additionally, it is essential to understand people's needs and priorities. Otherwise, reconstruction activities may fail to address the existing challenges and actual needs of local communities. This study aims to explore post-war reconstruction priorities of Ukrainians, with special focus on the energy sector and particularly the district heating facilities. During hostilities, a significant part of Ukraine's energy infrastructure was damaged or destroyed, which will be an essential sector in the recovery of other sectors. Research work involved undertaking an online survey with questions focusing on Ukrainians' assessment of the importance of the reconstruction of the energy sector. A total of 420 people from different regions of Ukraine, different age groups and professional backgrounds participated in the survey. Results show that a significant number of Ukrainian citizens have a high level of energy awareness. Thus, when asked what measure of post-war reconstruction of the energy sector they consider of high importance, 64% of respondents chose the answer "Reconstruction using energy-saving construction technologies and energy-efficient engineering systems, even if it takes more time". Furthermore, 32% of respondents are ready to pay more for district heating services if alternative energy sources are used to generate heat.

Keywords: online survey; energy infrastructure; district heating systems; post-war reconstruction; priorities; alternative energy sources.

---

1. Introduction

Ukraine's energy system has been under a constant wave of targeted Russian attacks since February 2022. The Russian Federation has occupied more than 18 GW of electricity-generating capacity, including Europe's largest facility, the Zaporizhzhia nuclear power plant (NPP). The Kakhovka and Dniprovska hydropower plants (HPPs), as well as the Zmiivska and Trypilska thermal power plants (TPPs), were completely destroyed. Private thermal power plants suffered critical damage (over 80%), including Ladyzhynska, Burshtynska, Dobrotvirska, Kurakhivska, Kryvyi Rih and Prydniprovska TPPs. In addition, all oil refineries on the territory of Ukraine were destroyed [1]. Nevertheless, with international support, the Ukrainian government managed to restore 3 GW by installing more power generating equipment and making repairs to damaged energy infrastructure. Consumers, mainly businesses, installed distributed generation facilities throughout the country, mainly gas engines, gas turbines and cogeneration

---

[*] Corresponding author. Email address: olena.o.savchenko@lpnu.ua

This paper should be cited as: O. Savchenko, K. Kozak, V. Zhelykh, O. Al-Hafith, J. Alencastro, O. Oladinrin, A. Akinbami. (2025). Public priorities for the post-war reconstruction of Ukraine's energy sector. *Energy Engineering and Control Systems*, Vol. 11, No. 2, pp. 115 – 123. https://doi.org/10.23939/jeecs2025.02.115

units. Thus, by the end of 2024, almost 1 GW of additional power was generated for domestic needs, which allowed reducing the load on the power system. In addition, measures are in place in Ukraine to limit energy consumption for industry, business and ordinary consumers, and calls for energy conservation do not cease even on days with stable power supply. To provide additional electricity, the capacity of electricity imports from the EU increased from 1.7 GW to 2.1 GW by December 1, 2024 [2].

District heating systems are an integral part of the country's energy infrastructure. And ensuring energy security in the field of district heating is an important step towards sustainable development and prosperity of the country. However, district heating systems have also suffered significant damage from shelling. Thus, as of April 2024, 10 thermal power plants were completely destroyed and another 15 were damaged in the territories where hostilities are underway. For example, the destroyed Kremenchuk Combined Heat and Power plant (CHP) (Poltava region) covered about 70% of the city's needs, that is, about 180 thousand residents, who could have been left without heat and hot water for the entire heating season if not for timely repair work. In addition, according to preliminary data, 863 boiler houses were partially damaged or completely destroyed as a result of the fighting, most of them in Kharkiv, Kyiv, Chernihiv, Donetsk and Mykolaiv regions. Also, 183 central substations were partially damaged or completely destroyed, and over 355 kilometres of heating networks were beyond repair [3]. A final assessment of the total damage will only be possible after the end of hostilities, but it is already necessary to consider strategies for rebuilding energy infrastructure, particularly district heating systems.

2. Analysis of recent research

The ways of restoration of Ukraine in the post-war period are a relevant object of research by both Ukrainian and foreign scientists. According to Farenyuk et al. [4], the national priority is to provide housing for people of Ukraine who have lost their homes or have been forced to leave them. This is due to the fact that the largest share in the total loss caused by the Russian military invasion of Ukraine is damage and destruction of residential buildings. As of the end of 2024, these losses amounted to 35.3% of the total, and the total area of damaged and destroyed buildings is 9% of the total area of the housing stock of Ukraine [4]. For the rapid restoration of housing stock, they propose to use the method of large-panel construction, which allows reducing the time of construction, reduce the amount of construction waste, improving the quality of structures through the production of elements in factory conditions. Nazarenko O. at al. [5] suggest that the reconstruction of housing in the post-war years should be carried out on the principles of biosphere compatibility, namely using building materials, which in their composition and characteristics contribute to the minimization of the use of natural resources, do not harm the environment.

In the reconstruction of the industrial sector Deineka et al. [6] see the priorities of the restoration of mechanical engineering and the defense-industrial complex, as well as enterprises of metallurgical, food, chemical, pharmaceutical and woodworking industries, as well as the development of new fields of activity, such as bio- and nanotechnology. The authors [7] consider the transport sector of Ukraine to be one of the most vulnerable sectors of the economy, since its enterprises are in many cases goals for attacks. The authors emphasize the unconditional priority of the post-war reconstruction of the transport sector and offer a comprehensive approach to financing, investing and restoring the transport sector of Ukraine. Simakhova considers the main aspects of the post-war socialization of the Ukrainian economy. She identifies eight aspects: rehabilitation and social support for victims and veterans, employment of the unemployed population, migration processes and return of citizens, education and professional training, social justice and reduction of inequality, health care reform, environmental transformation [8].

The energy sector of Ukraine also suffered significant damage, as mentioned above. Therefore, many studies are devoted to determining the steps and priorities of its post-war reconstruction. So Grand and Svionik [9] have identified eight priority tasks to strengthen the country's energy security: increase in energy production for import substitution; creation of strategic reserves of coal, nuclear fuel, oil and gas; diversification of sources of supply of energy resources; development of alternative energy; ensuring the autonomous operation of the united power system of Ukraine on the basis of the development of energy infrastructure; deepening of Ukraine's international cooperation with partner countries in the field of energy security; providing cybersecurity of energy infrastructure; improvement of the system of state regulation and management of the energy sphere of the state. Sirenko et al. [10], to improve the situation in the energy sector of Ukraine, distinguish the following directions: development of renewable energy, improvement of energy efficiency of components of the power system, modernization of energy infrastructure, promotion of distributed generation, reforming the energy sector. Savchenko proposes the stages of achieving the energy efficiency of centralized heat supply systems both during modernization and in the construction of new centralized heat supply systems, in particular in the post-war reconstruction of Ukraine [11].

The complexity of modernization and restoration of the district heating system of Ukraine is related to the existing condition of facilities of thermal power sector. Thus, most thermal networks and heat generating installations were built in the 1970s and 1980s. Therefore, the main problem of existing district heating systems is the long service life of its equipment, from which the inefficient use of energy resources and significant heat losses from the pipelines of thermal networks.

Since the 2000s, heat-generating enterprises have been implementing measures to modernize district heating systems. The first step in energy savings was the use of pre-isolated polyurethane pipelines during repairs of the existing thermal network. Further steps in the modernization of heating systems included mandatory metering of heat energy and the installation of individual heat points at heat energy consumers. According to the requirements of the Law of Ukraine "On Commercial Accounting of Heat Energy and Water Supply", it is prohibited to connect residential and non-residential buildings to external engineering networks without installing commercial accounting units in them, in particular heat and hot water meters. In Lviv, as of 2021, 98% of houses have house heat meters [12]. Installing individual substations at consumers requires significant capital costs, but to be able to regulate heat supply and save on heat energy bills, consumers can independently look for investors or attract credit funds. For example, in Lviv, 409 individual heat points were installed with funds from the European Bank for Reconstruction and Development from 2019 to 2022. The project covered the entire Sykhiv microdistrict, including residential buildings, schools, and clinics [13]. As of 2022, Lvivteploenergo had 522 individual heat points, which is almost 30% of the buildings served.

After the full-scale invasion of the Russian Federation into Ukraine, the use of cogeneration plants for the simultaneous generation of electric and thermal energy of individual structures was increased. The procedure for the construction or placement of cogeneration plants for the period of martial law was simplified in accordance with the resolution of the Cabinet of Ministers of Ukraine dated May 14, 2024 No. 547. Thus, the construction and placement of gas piston and gas turbine plants with a capacity of 1 MW and more is carried out without the need to obtain a number of permits that are required in peacetime. This allows significantly reducing the time for preparation for construction and responding faster to energy challenges.

Many solutions for using alternative energy sources as energy resources in district heating systems are at the stage of scientific developments. For example, [14] describes the possibility of using wood waste from a woodworking enterprise to produce generator gas, which can then be used to produce thermal energy in a boiler house. The authors of [15] propose using the heat of wastewater to obtain thermal energy. There is also the possibility of using geothermal waters in heating systems. Depending on their composition, they can either be directly fed into the heating system or used to heat the heat carrier of the heating system in an intermediate heat exchanger [16].

In the European Union countries, 4th generation district heating systems (4GDH) are currently being actively promoted and gradually implemented, the main requirements for which are the use of alternative energy sources for heat generation, the use of low-temperature coolant, equipment for heat accumulation, pre-insulated pipelines, heat metering devices, and devices for regulating the release of thermal energy [17].

Therefore, in the post-war reconstruction to increase the energy efficiency of the heat and power sector, the main concept should be geared towards designing new infrastructure using new technologies in compliance with the indicators of the 4th generation heat supply system and the requirements for "efficient district heating". It is clear that most of the proposed measures require significant capital investments and can be postponed in time, so it is important to find out the opinion of Ukrainian citizens, which measures during the reconstruction of district heating systems are a priority for them.

In Ukraine, studies have been conducted that touched the reconstruction, including the energy sector. Thus, in 2023, a sociological research was conducted by the Info sapiens research agency by the Transparency International Ukraine to identify the fears of Ukrainians in reconstruction, as well as to identify approaches and their priorities [18], [19]. The survey received 1012 citizens and business representatives. According to 77% of citizens and 81% of business representatives, corruption is one of the main problems in Ukraine. The main principles of reconstruction, according to the vast majority of respondents, should be: decentralization of funds, early strategy of reconstruction of Ukraine, transparency and openness of rebuilding, attracting citizens and business, quality of work as a priority. Regarding the sector of the reconstruction, 45 % of respondents called the restoration of critical infrastructure. After that, the housing is significant for Ukrainians, for those who lost it, the demining of territories, the restoration of work of hospitals, schools, kindergartens, adaptation of the military to a peaceful life.

In February 2025, Rating Sociological Group conducted a national survey "Energy Situation in Ukraine expectations, challenges and prospects", the results of which were information about how Ukrainians see: they see the situation with energy in general, evaluate the power of power in the energy sphere [20]. The sample included 1200 respondents. Regarding the authorities', measures to improve the energy situation in Ukraine, respondents noted the restoration of destroyed energy (48%), strengthening of protection of energy (38%), raising funds and energy equipment from international partners (37%). 69% of respondents consider the actions of the authorities to improve the situation in energy effective, ineffective actions of the authorities consider 25%.

The cited studies have not identified the opinion of the population of Ukraine on measures to restore the thermal power sector, in particular the district heating systems.

3. Aim of work

The aim of this study is to identify the main priorities of Ukrainian citizens in the post-war reconstruction of district heating systems. This was achieved through an online survey conducted as part of the project by conducting an online survey, which took place as part of the project "Russian-Ukrainian War – Assessment of the Level of Destruction in the Affected Cities of Ukraine".

4. Methodology

In order to evaluate the extent of destruction, as well as the determination of priorities in citizens of Ukraine in the post-war reconstruction, a research project "Russian-Ukrainian War – Assessment of the Level of Destruction in the Affected Cities of Ukraine" was conducted. The results of the research should ensure that the post-war reconstruction efforts align with the priority needs of a particular community. To achieve this goal, a methodology was used on the basis of a survey, which gives priority to broad cover, representativeness and feasibility in difficult conditions. The survey questionnaires were distributed and collected electronically, adhering to recommended practices for remote survey administration. This research approach has proven effective in previous studies, addressing the practical challenges posed by Ukraine's unstable conditions and enabling engagement with respondents across diverse regions [21], [22]. The survey form was produced with help of JISC, a non-profit organization from the United Kingdom that provides IT services and digital resources to support research (Fig. 1). The results of this survey will be able to help develop a strategic reconstruction plan of Ukraine in the future.

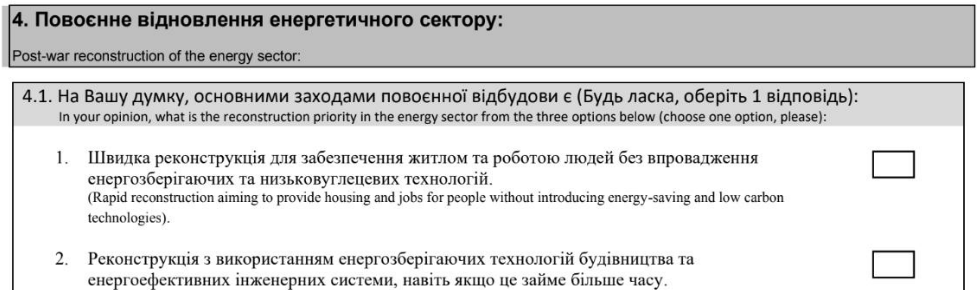

4. Повоєнне відновлення енергетичного сектору:

Post-war reconstruction of the energy sector:

4.1. На Вашу думку, основними заходами повоєнної відбудови є (Будь ласка, оберіть 1 відповідь):

In your opinion, what is the reconstruction priority in the energy sector from the three options below (choose one option, please):

1. Швидка реконструкція для забезпечення житлом та роботою людей без впровадження енергозберігаючих та низьковуглецевих технологій. (Rapid reconstruction aiming to provide housing and jobs for people without introducing energy-saving and low carbon technologies). ☐
2. Реконструкція з використанням енергозберігаючих технологій будівництва та енергоефективних інженерних системи, навіть якщо це займе більше часу. ☐

Fig. 1. Fragment of an online survey form.

Participation in the survey was voluntary for respondents. Even after starting to answer the questions, the respondent could refuse to fill out the survey form and not send their answers at any time. The survey also took into account the principles of confidentiality, so it did not involve the collection of any information that could be used to identify the participants. Before starting the data collection work, the created survey received ethical approval from a leading research institution.

The survey consisted of an introduction and three groups of questions. The introduction described the purpose and objectives of the study, the ethical interpretation of the participants' responses, and the requirements for the confidentiality of the results obtained. The first group of questions concerned some personal data of the survey participants, in particular, it was necessary to provide information about the place of residence before the start of the full-scale Russian invasion of Ukraine and during the survey, the age and field of activity of the survey participant, as well as the level of destruction of the settlement during the hostilities. The second group of questions concerned the primary needs and priorities of the post-war period for the inhabitants of Ukraine. Respondents were asked to identify their first, second, and third priorities for post-war reconstruction from seven options, including demining or rebuilding energy infrastructure, housing, healthcare facilities, education, transport infrastructure, or preserving and restoring cultural heritage sites. The third group of questions concerned post-war reconstruction of the energy sector. All questions used a multiple-choice format, which allowed for the collection of structured quantitative data. In addition, an open-ended question was offered, which allowed respondents to express their own opinion, different from the proposed answers. The online questionnaire was designed so that the respondent would spend no more than 10 minutes on its processing. Ethical approval was obtained from a leading research institution before the start of data collection. Recognizing the importance of cultural and linguistic relevance, the survey was conducted in Ukrainian.

To ensure the reliability of the results obtained, the required sample size was established based on the number of adult Ukrainians, which, according to IMF data, was estimated at approximately 26.2 million people in 2023. The standard sample size formula for proportions [23] was used to calculate the required sample size:

$$n = (z^2 \cdot p \cdot (1 - p))/d^2, \tag{1}$$

where n is the required sample size; z is the value of the normal deviation corresponding to the desired level of confidence; p is the expected proportion of the population that exhibits the characteristic of interest; d is the margin of error.

At a confidence level of 95%, an expected population proportion of $p = 50\%$ and a standard error of $d = 5\%$, the required sample size is 384 residents. Existing studies show that the average response rate in online surveys is 44.1% [23]. In addition, the results obtained may contain certain shortcomings, for example, the absence of some responses. Therefore, it was decided to distribute 2000 questionnaires, which guaranteed that even after taking into account the outflow of poor-quality questionnaires, the required sample size was met, which increased to 420 respondents.

An important task of the survey was to collect questionnaires from as many settlements in Ukraine as possible and, if possible, to cover all regions. People in Ukraine are distrustful of various surveys and therefore very often ignore them. In addition, part of the territory of Ukraine is under temporary occupation, which prevents direct communication with residents. The survey was conducted during May – July 2024, after another massive shelling of rear settlements, which also contributed to the indifference of the population to the proposed survey.

The invitation to participate in the survey was carried out using a link to an online survey form, which was distributed through social media platforms, professional and personal circles of acquaintances of the project co-authors. On social networks, you could get answers from refugees, people from temporarily occupied territories, and territories where active hostilities were taking place. The professional circle of communication of the co-authors included employees of construction educational institutions, companies for the design, sale and installation of equipment for heat and gas supply and ventilation systems, and students of construction specialties.

This paper will present the respondents' answers that relate only to the reconstruction of the energy sector. Information on the damage caused by the war and citizens' priorities in post-war reconstruction will be provided in the authors' subsequent publications.

5. Research results

420 people from different regions of Ukraine took part in the survey. Age distribution of participants: 45% were aged 18 to 30, 24% – from 31 to 40, 20% – from 41 to 50, and 11% were over 51. As for the field of activity, 60% of participants reported that they were working, 5% – pensioners, 27% – students, and 8% – unemployed. Of the surveyed respondents, 65% stated that they did not leave their places of residence due to the war, 10% stated that they

were internally displaced persons in their regions, 1% of participants indicated that they were refugees abroad, 24% did not answer the question about their current place of residence. The geographical location of respondents before the full-scale Russian invasion of Ukraine: 29% of participants were from Lviv, 11% from Kyiv, 5% from Poltava, 3% from Odesa, 3% from Kharkiv, and 49% from approximately ninety cities and towns throughout Ukraine. As for the first priority in post-war reconstruction, approximately 42.7% of participants indicated the reconstruction of energy infrastructure as the main priority, and another 34.7% put it in second place. That is, 77.4% of respondents noted that energy infrastructure, namely electricity, heat, and water in their homes, was extremely important in their lives.

To determine how it is possible to restore the energy infrastructure two questions were proposed. The first question "In your opinion, the main measures of post-war reconstruction are:" had three answers: 1 – "Rapid reconstruction to provide people with housing and work without the introduction of energy-saving and low-carbon technologies", 2 – "Reconstruction using energy-saving construction technologies and energy-efficient engineering systems, even if it takes more time", 3 – "Rapid reconstruction of the housing sector without energy-saving measures, but using energy-saving construction technologies and energy-efficient engineering systems for infrastructure facilities". Figure 2 illustrates the preferences of Ukrainian residents regarding post-war reconstruction of the energy sector.

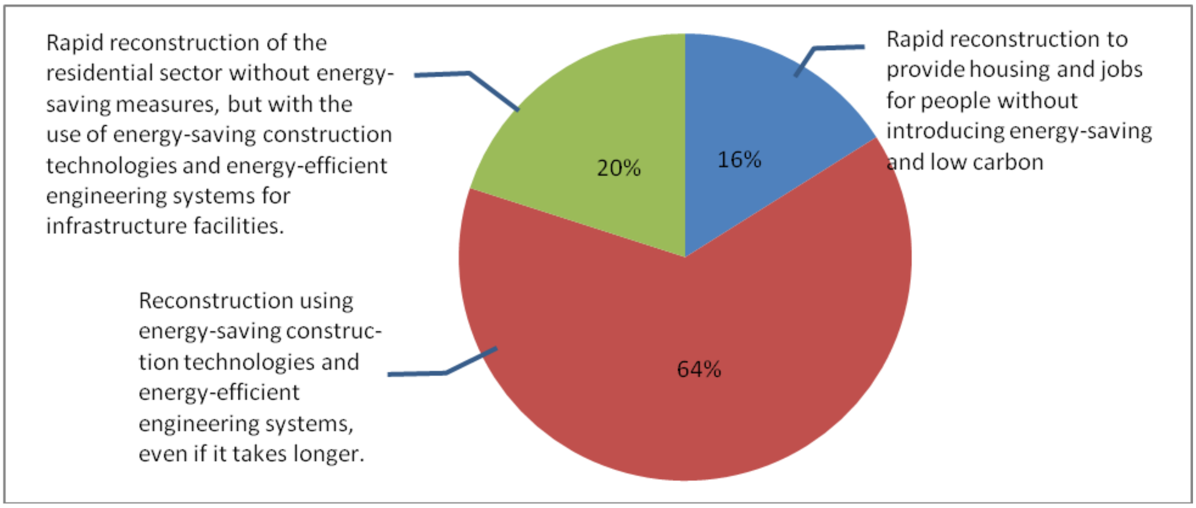

Fig. 2. People's priorities for rebuilding the energy sector

As can be seen from Fig. 2, the majority of respondents (64%) indicated that reconstruction should prioritize the use of energy-saving construction technologies and energy-efficient engineering systems, even if it takes more time. A smaller proportion (20%) supported rapid reconstruction of the residential sector without focusing on energy-saving measures but still incorporating energy-efficient infrastructure. Only 16% preferred rapid reconstruction aimed at providing housing and jobs for people without prioritizing energy-saving or low-carbon solutions. These results suggest that a significant portion of Ukrainian citizens value long-term energy efficiency over speed in reconstruction. One possible explanation for the relatively low selection of the rapid reconstruction option is that many respondents may not have been immediately affected by housing loss or destruction during the hostilities, allowing them to prioritize sustainability rather than urgent shelter needs.

The second question in the third group was worded "Are you willing to pay more for district heating services if…" Respondents were offered five answers: 1 – "Imported natural gas will not be used as fuel", 2 – "Greenhouse gas emissions will be reduced", 3 – "Renewable and/or alternative energy sources will be used (wood waste, agricultural waste, household waste, biogas, etc.)", 4 – "Not willing to pay more for district heating services", 5 – "I have an individual heating system" (Fig. 3).

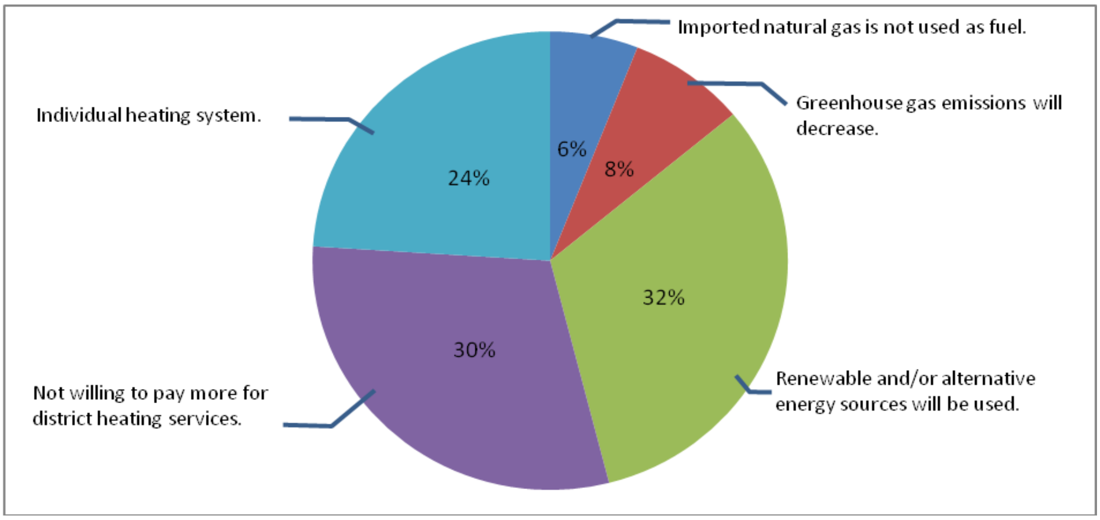

Fig. 3. Respondents' attitude towards increasing the cost of district heating services.

According to the survey data presented in Fig. 3, more than 30% of respondents are not willing to pay more for district heating services, reflecting a notable level of price sensitivity. Among the 76% of participants who currently use district heating, this equates to almost 40% who are unwilling to support a tariff increase. However, there is also a considerable portion of the population open to change. 46% of respondents expressed willingness to accept higher heating tariffs provided certain conditions are met. The most widely supported reason for a potential price increase is the transition to renewable and/or alternative energy sources, with 32% of respondents prioritizing this option. Other motivations include reducing greenhouse gas emissions (8%) and minimizing reliance on imported natural gas (6%). Interestingly, 24% of respondents favor individual heating systems over district heating, signaling a desire for greater autonomy or efficiency in energy use.

The results of the study provide new insights into people's priorities in the reconstruction of the energy sector, in particular district heating systems, which can help in developing an adaptive reconstruction plan for the country. The results obtained are largely consistent with people's priorities presented in the literature. The survey showed that 64% of Ukrainians are ready to wait for the post-war reconstruction of district heating systems, provided that energy-saving construction methods and energy-efficient engineering solutions are implemented. In addition, the data obtained indicate that, although there is resistance to the increase in heating costs, a significant part of the population (32%) is ready to invest in sustainable energy solutions. These results highlight the critical role that renewable energy sources play in the reconstruction of the energy infrastructure, in particular district heating systems, and the energy independence of Ukraine. However, the results of the study demonstrate some differences in the views of the population regarding the priorities for the reconstruction of the energy sector, which also need to be taken into account to meet the needs of local communities in the country.

6. Conclusion

The article presents and analyzes the results of an online survey conducted as part of the project "Russian-Ukrainian War – Assessment of the Level of Destruction in the Affected Cities of Ukraine" which aimed to identify to determine the main priorities of Ukrainian citizens in the post-war reconstruction of energy facilities and directly of district heating systems. The survey consisted of an introduction and three groups of questions, with the third group addressing the restoration of the energy sector after the war.

For the reliability of the results of the online survey, the required sample size was established, namely 420 questionnaires, the value of which was determined based on the number of adult Ukrainians. According to the survey results, 42.7% of respondents indicated that the first priority in post-war reconstruction for them is the restoration of energy infrastructure. This indicates the extreme importance for citizens of energy infrastructure, which allows them to maintain heat and electricity in their homes and have stable job.

When asked what measure of post-war reconstruction of the energy sector they consider the main one, 64% of respondents chose the answer "Reconstruction using energy-saving construction technologies and energy-efficient engineering systems, even if it takes more time" 32% of respondents are willing to pay more for district heating services if alternative energy sources are used for the production of thermal energy. Analysis of the responses received indicates the energy awareness of a significant number of Ukrainian citizens who understand the importance of the energy sector for the national economy. Notably, their readiness to support the transition to alternative energy sources – even at personal financial cost – signals a collective commitment to achieving greater energy independence and sustainability in the post-war period.

7. Acknowledgment

This study was funded by the University of Plymouth in the United Kingdom [Internal Funding 2024].

References

[1] Tarasovsky Yu., Galkin A. Damages and losses of the energy sector of Ukraine due to the war exceeded $56 billion – KSE Institute. [Online]. [Accessed 2025-10-01]. https://forbes.ua/news/zbitki-ta-vtrati-energosektoru-ukraini-cherez-viynu-perevishchili-56-mlrd-kse-institute-10062024-21678 (in Ukrainian)

[2] Attacks on energy infrastructure: updated forecasts and consequences during the 2024-2025 heating season. Thematic Report dated 19 February 2025. [Online]. [Accessed 2025-10-01]. https://www.acaps.org/fileadmin/Data_Product/Additional_resources/20250219_ACAPS_Ukraine_-_Energy_infrastructure_attacks-_Updated_outlook_and_impact_during_the_2024-2025_cold_season_Translation.pdf (in Ukrainian)

[3] Report on direct infrastructure damage from destruction due to Russian military aggression against Ukraine as of early 2024, 2024, 39 p. [Online]. [Accessed 2025-10-01]. https://kse.ua/wp-content/uploads/2024/04/01.01.24_Damages_Report.pdf. (in Ukrainian)

[4] Fareniuk G., Zelenko Ye., Lisenyi O., Slyusarenko Yu. (2025). Prospects of industrial construction for the renovation of housing destroyed as a result of military aggression. *Science and Construction*, **43(1),** 3-17. https://doi.org/10.33644/2313-6679-1-2025-1 (in Ukrainian)

[5] Nazarenko O., Ishchenko O., Ishchenko O., Smykov V. (2022). Post-war housing reconstruction according to the principles of biosheric compatibility. *Resource-Economic Materials of Building Structures and Structures*, **42**, 258-264. https://doi.org/10.31713/budres.v0i42.028 (in Ukrainian)

[6] Deyneko L., Kushnirenko O., Tsyplitska O., Gakhovych N. (2022). Consequences of the full-scale military aggression of the Russian Federation for Ukrainian industry. *Economy of Ukraine*, **5**, 3–25. https://doi.org/10.15407/economyukr.2022.05.003 (in Ukrainian)

[7] Bugayko D., Bonyar S. (2025). Reconstruction of the transport sector of Ukraine: a comprehensive approach to financing, investment and recovery. *Herald of the Economic Sciences of Ukraine*, **1(48)**, 42-48. https://doi.org/10.37405/1729-7206.2025.1(48).42-48 (in Ukrainian)

[8] Simakhova A. (2024). Postwar socialisation of the Ukrainian economy in the conditions of European integration. *Economic scope*, **194**, 128-131. h https://doi.org/10.30838/EP.194.128-131 (in Ukrainian)

[9] Hrand M., & Sviontyk O. (2025). Energy security of Ukraine in the conditions of the Russian-Ukrainian war (2014 – 2024): visions, concepts, priorities. *Axis Europae*, **6**, 89–107. https://doi.org/10.69550/3041-1467.6.326259 (in Ukrainian)

[10] Sirenko Yu., Volvach T., Savoiskyi Yu., Kozin V. (2025). Analysis of the state of Ukraine’s energy system and measures to improve the situation. Bulletin of Kherson National Technical University, **1**, 2(93), 229-237. https://doi.org/10.35546/kntu2078-4481.2025.2.1.30 (in Ukrainian)

[11] Savchenko O. (2023). Increasing the energy efficiency of structures in reconstruction through the use of district heating systems. Science and Construction, **38(4)**, 41-48. https://doi.org/10.33644/2313-6679-4-2023-6 (in Ukrainian)

[12] City heating engineers remind residents of the opportunity to independently regulate the heating supply to the house. [Online]. [Accessed 2025-10-02] https://city-adm.lviv.ua/news/city/housing-and-utilities/284402-teplovyky-mista-nahaduiut-pro-mozhlyvist-dlia-meshkantsiv-samostiino-rehuliuvaty-podachu-opalennia-v-budynok (In Ukrainian)

[13] LCME "Lvivteploenergo" is implementing a project to install ITPs in Sykhiv houses: 380 heat points have already been installed. [Online]. [Accessed 2025-10-02] https://city-adm.lviv.ua/news/city/tsnap/287045-lmkp-lvivteploenerho-realizovuie-proiekt-vstanovlennia-itp-v-budynkakh-sykhova-380-teplovykh-punktiv-vzhe-vstanovleno (In Ukrainian)

[14] Savchenko O., Zhelykh V., Yurkevych Yu., Kozak K., Bahmet S. (2018). Alternative energy source for heating system of woodworking enterprise. *Energy engineering and control systems*, **4 (1),** 27 – 30. https://doi.org/10.23939/jeecs2018.01.027

[15] Basok B., Novitska M., Goncharuk, S. (2020). Technologies, systems, and equipment for wastewater heat utilization (Review). *Thermophysics and Thermal Power Engineering*, **42(3),** 39-46. https://doi.org/https://doi.org/10.31472/ttpe.3.2020.4 (in Ukrainian)

[16] Savchenko O., Yurkevych Y., Zhelykh V., Voznyak O. (2023). Review of schemes of geothermal district heating and recommendations for their use in Lviv region. *Lecture Notes in Civil Engineering*, **290**, 344-354. https://doi.org/10.1007/978-3-031-14141-6_35

[17] Pakere I., Blumberga D., Volkova A., Lepiksaar K., Zirne A. (2023). Valorisation of Waste Heat in Existing and Future District Heating Systems. *Energies*, **16(19),** 6796. https://doi.org/10.3390/en16196796.

[18] Sociological survey on reconstruction. [Online]. [Accessed 2025-10-03] https://www.fid-foundation.com.ua/news/sociologichne-opituvannya-shchodo-vidbudovi (in Ukrainian)

[19] How to rebuild Ukraine, a survey of citizens and business representatives. [Online]. [Accessed 2025-10-03] https://drive.google.com/file/d/1v30npi8x6bK1ghKIoIaSFG9ZxyvNZxqQ/view (in Ukrainian)

[20] How do Ukrainians assess the energy situation in the country? [Online]. [Accessed 2025-10-03] https://www.ratingGroup.ua/news/energy-feb2025 (in Ukrainian)

[21] Al-Hafith O., Satish B.K., Bradbury S., de Wilde, P. (2018). A systematic assessment of architectural approaches for solving the housing problem in Iraq. *Frontiers of Architectural Research*, **7(4),** 561-572. https://doi.org/10.1016/j.foar.2018.07.001

[22] Regmi P., Waithaka E., Paudyal A., Simkhada P., van Teijlingen, E. (2016). Guide to the design and application of online questionnaire surveys. *Nepal J Epidemiol*, **6(4),** 640-644. doi:10.3126/nje.v6i4.17258.

[23] Wu M.-J., Zhao K., Fils-Aime F. (2022). Response rates of online surveys in published research: A meta-analysis. *Computers in Human Behavior Reports*, **7**, 100206. https://doi.org/10.1016/j.chbr.2022.100206

Пріоритети населення щодо повоєнної відбудови енергетичного сектору України

Олена Савченко[a], Христина Козак[b], Василь Желих[a], Омар Аль-Хафіт[c],
Жоао Аленсатро[c], Олугбенга Оладінрін[c], Адемола Акінбамі[c]

[a]*Національний університет «Львівська політехніка», вул. С. Бандери, 12, Львів, 79013, Україна*
[b]*ТзОВ Сервісні дизайнерські рішення, Гембрі Хаус, Паінс Гіл, Екстер, EX2 5SE, Велика Британія*
[c]*Університет Плімута, вул. Р. Левінського, 302, Плімут, PL4 8AA, Велика Британія*

Анотація

Російське вторгнення в Україну призвело до масштабних руйнувань багатьох міст по всій країні. Хоча війна ще не закінчилася, настане час, коли конфлікт завершиться, і розпочнуться зусилля з відбудови. Світовий досвід показує, що першим кроком у підготовці до післявоєнної відбудови є оцінка рівня руйнувань. Крім того, важливо розуміти потреби та пріоритети людей. В іншому випадку, заходи з відбудови можуть не вирішити існуючі проблеми та реальні потреби місцевих громад. Це дослідження має на меті дослідити пріоритети післявоєнної відбудови українців, зосереджуючись на енергетичному секторі та, зокрема, на об'єктах централізованого теплопостачання. Під час бойових дій значна частина енергетичної інфраструктури України була пошкоджена або зруйнована, що буде важливим сектором у відновленні інших секторів. Дослідницька робота включала проведення онлайн-опитування з питаннями, що зосереджувалися на оцінці українцями важливості відбудови енергетичного сектору. В опитуванні взяли участь 420 осіб з різних регіонів України, різних вікових груп та професійного досвіду. Результати показують, що енергетична свідомість значної кількості громадян України висока. Таким чином, на запитання, який захід післявоєнної реконструкції енергетичного сектору вони вважають одним із найважливіших, 64% респондентів обрали відповідь «Реконструкція з використанням енергозберігаючих будівельних технологій та енергоефективних інженерних систем, навіть якщо це потребує більше часу». Крім того, 32% респондентів готові платити більше за послуги централізованого теплопостачання, якщо для виробництва тепла використовуватимуться альтернативні джерела енергії.

Ключові слова: онлайн-опитування; енергетична інфраструктура; системи централізованого теплопостачання; повоєнна відбудова; пріоритети; альтернативні джерела енергії.

ENERGY ENGINEERING AND CONTROL SYSTEMS

Volume 11, Number 2, 2025

Development and Investigation in MATLAB of an Autonomous Induction Generator Model with the Inverter in Rotor Circuit for a Wind Turbine

Bohdan Kopchak*, Andrii Mandiuk, Ihor Dziuba, Ihor Babii

Lviv Polytechnic National University, 12 Stepana Bandery St., Lviv, 79013, Ukraine

Received: October 15, 2025. Revised: December 08, 2025. Accepted: December 15, 2025.

Abstract

The work presents the development and investigation in MATLAB of a model of an autonomous self-excited induction generator with a rotor circuit inverter for a wind turbine. The system employs a scalar-controlled inverter with an independent power supply, and the nonlinear magnetization curve of the induction generator is taken into account. Voltage and frequency regulation are separated. The developed model made it possible to study the self-excitation mode for different rotor supply frequencies. During the simulation of the self-excitation process of the autonomous induction generator, it was found that the optimal parameters for stable self-excitation were achieved at a rotor frequency of 1.8 Hz and a rotor supply voltage of 20 V. The study also examined the effect of applying an active-inductive load and the system's response to changes in the drive shaft speed. When a 40% load of the rated value was connected, a slight voltage drop accompanied by an increase in the rotor phase current was recorded; however, the system remained stable without the need for additional control measures. By increasing the inverter voltage, the generator terminal voltage was restored to its initial level. When the drive shaft speed was suddenly reduced by 10%, a minor voltage decrease and a corresponding increase in rotor current were also observed. This mode remained stable, and the voltage and frequency were successfully leveled again by means of the inverter.

Keywords: model; autonomous induction generator with a wound rotor; inverter; wind turbine.

1. Definition of the problem to be solved

At present, the growing penetration of renewable and distributed energy sources requires the development of reliable and efficient generator systems capable of operating in variable-speed regimes. Among the existing solutions, asynchronous (induction) generators remain attractive due to their simple construction, robustness, low cost, and reduced maintenance requirements. However, their performance under non-standard operating conditions, especially in variable-speed applications, is significantly affected by the control method applied to the rotor circuit. The use of power electronic converters, particularly an inverter connected to the phase rotor winding, makes it possible to control the generator's electromagnetic processes, improve efficiency, and provide stable operation under different load conditions.

Despite the practical significance, comprehensive studies of such systems are still limited. A key challenge is the nonlinear interaction between the machine, the inverter, and the grid or autonomous load. Analytical approaches are often insufficient to capture all transient processes and parameter variations. Therefore, simulation tools are essential for analyzing dynamic behavior and verifying control algorithms. MATLAB Simulink, and in particular the SimPowerSystems (Simpower) library, provides a flexible environment for accurate modeling of electrical machines and power electronic interfaces.

---

[*] Corresponding author. Email address: bohdan.l.kopchak@lpnu.ua

This paper should be cited as: B. Kopchak, A. Mandiuk, I. Dziuba, I. Babii. (2025). Development and investigation in MATLAB of an autonomous induction generator model with the inverter in rotor circuit for a wind turbine. *Energy Engineering and Control Systems*, Vol. 11, No. 2, pp. 124 – 134. https://doi.org/10.23939/jeecs2025.02.124

Developing a reliable model of an induction generator with a rotor-side inverter allows for the investigation of steady-state and transient modes, evaluation of energy efficiency, assessment of control strategies, and prediction of stability margins. Such research is highly relevant for modern energy systems, including wind power plants, microgrids, and autonomous energy complexes, where flexible and efficient generation sources are required.

2. Analysis of the recent publications and research works on the problem

Over the past three decades, a significant number of studies have appeared in periodical literature and conference proceedings devoted to grid-connected and stand-alone doubly-fed induction generators (DFIGs), their modeling, excitation methods, conversion schemes, and control strategies – ranging from classical theoretical works to modern experimental investigations and MATLAB/Simulink-based developments. Below is a detailed review of key sources selected to build the foundation for modeling an autonomous generator and its associated conversion and control systems.

In [1], an experimental analysis of a self-excited induction generator (SEIG) for small autonomous applications is presented. The authors systematically investigated the influence of three critical parameters – excitation capacitance, load and frequency (speed) – on the electrical characteristics of the SEIG. The practical experiments and measurement results in this work are highly valuable for validating MATLAB/Simulink models, as they demonstrate how real nonlinearities and condition variations affect generator behavior and highlight the need for experimental verification of simulation models.

In [2], an "impedance reshaping" approach for DFIG systems is proposed, focused on compensating rotor current dynamics to influence system behavior. This study is important for understanding how controlled inverters and their regulators interact with rotor mechanics and how these interactions should be considered when designing stable configurations for stand-alone operation or during mode transitions.

In [3], the issue of capacitor voltage synchronization in systems where a wind generator fully supplies power through an inverter is considered. The work demonstrates a synchronization control approach and analyzes transient and fault conditions, which are directly relevant to stand-alone systems with fully electronic interfaces where reactive power control and voltage matching are key.

Reference [4] presents a classical review of DFIGs for wind energy systems. The authors emphasized the advantages of a bidirectional converter in the rotor circuit for independent control of active and reactive power and discussed both grid-connected and stand-alone operation capabilities. This work often serves as a theoretical foundation for designing systems with rotor-side inverters.

Reference [5] proposed a detailed model and control strategy for a DFIG, including stand-alone modes under different load conditions. This work is valuable as a methodological resource for building Simulink models with detailed state equations and analysis of excitation and reactive power compensation.

In [6], the dynamic behavior of DFIGs during three-phase voltage dips is analyzed. The results are important for evaluating stand-alone system performance under severe disturbances and for designing protection and recovery strategies.

In [7], the authors presented a real-time analysis of voltage and frequency regulation for a small 2.2 kW SEIG with a dual-loop control structure. The work demonstrates a practical control architecture for a small autonomous system and provides testing scenarios for evaluating transient responses under load conditions.

In [8], a closed-loop ramp-comparison current regulator for an induction machine with a PWM voltage-source inverter is proposed. Although this study concerns motor control, its current control methodology and analysis of PI regulators in closed loops are applicable to controlling a rotor-side inverter in generator systems and help in selecting appropriate current regulation and protection algorithms.

The review shows that the referenced sources cover a wide range of aspects – from classical DFIG architectures and theoretical foundations to modern experimental and simulation implementations of SEIG and DFIG systems with high-performance inverters.

Thus, the necessity of developing a model of an induction generator with a rotor circuit inverter in MATLAB/SimPower Systems can be summarized as follows. First, it provides realistic reproduction of physical processes. The SimPower Systems-based model is not limited to transfer functions or simplified equations but directly simulates electrical and mechanical subsystems (windings, inverter, load, excitation source). This makes it possible to account for magnetic saturation, nonlinear losses, harmonics, and transient effects that cannot be adequately described by linear transfer functions. Second, the integration of the inverter in the rotor circuit enables independent control of active and reactive power in stand-alone operation. Modeling this subsystem in Simulink allows the study of: the influence of various control algorithms; output voltage and current quality (THD, frequency stability); behavior under variable speeds and loads; and the effectiveness of protection algorithms during fault conditions. Third, it enables analysis of the less-studied stand-alone operation mode. Unlike grid-connected operation, stand-alone mode requires the generator to independently maintain voltage and frequency without a "stiff" grid source. The SimPower Systems model allows investigation of self-excitation conditions, load-change stability, as well as power and stability limits of the system.

3. Formulation of the goal of the paper

The combination of an induction generator with an inverter in the phase rotor circuit and modeling in SimPower Systems makes it possible to integrate the classical theory of electrical machines with modern approaches to power conversion technology. This enables the study of operating modes that are difficult to describe analytically, such as harmonic interactions, fast transients, and the influence of control algorithms on real-time stability. MATLAB/Simulink allows for rapid adjustment of machine parameters, excitation circuits, inverter structures and load configurations – something that is practically impossible in a real experiment.

The objective of this work is to develop and investigate in MATLAB a model of a stand-alone induction generator with an inverter in the phase rotor circuit and self-excitation for a wind power installation. The study involves using a two-level inverter with independent power supply and taking into account the nonlinear magnetization curve of the induction generator. In addition, it is necessary to design an active-inductive load block, as well as a voltage regulator of inverter type in the rotor circuit with adjustable transistor firing angle. The investigation should be carried out in self-excitation mode for different rotor supply frequencies. Besides the self-excitation mode from the rotor side at various frequencies, it is also necessary to study the effect of applying an active-inductive load and the system's response to changes in the drive shaft speed.

4. Model Development and Investigation.

The first stage of constructing the MATLAB model of a stand-alone induction generator with self-excitation and an inverter involves selecting and configuring the main generator parameters. Figure 1 shows the induction generator along with data acquisition channels used to monitor key characteristics. This model enables the recording and analysis of parameters such as rotor speed, electromagnetic torque, as well as stator and rotor currents, and the active and reactive power of each individual phase. The figure also illustrates how measurement blocks are integrated into phase A, clearly showing the connection method and data acquisition process. The collected data provide the ability to monitor and adjust the generator's performance, allowing subsequent optimization of the self-excitation process and rotor inverter frequency to ensure stable output voltage.

A 37 kW induction machine was chosen as the main component for modeling. All technical characteristics of this machine were predetermined, allowing for accurate tuning and calibration of the model. Detailed parameterization includes entering such parameters as rated voltage, frequency, number of poles, stator and rotor winding resistances and inductances, as well as other characteristics that determine the dynamic behavior of the machine during operation. This approach allows the model to closely approximate real operating conditions and ensures correct generator performance during start-up, self-excitation, and subsequent loaded operation.

The main feature of the stand-alone induction generator (IG) model is the inclusion of the nonlinear magnetization characteristic, shown in Fig. 2. This characteristic is crucial for accurately reproducing generator operation, as it reflects the real physical properties of the materials used in its construction and directly influences the electromagnetic processes within the machine.

At the next stage, a model of a three-phase active–inductive load was built, allowing the simulation of various operating modes that affect the terminals of the stand-alone IG. This model makes it possible to simulate both purely active loads and combined active–inductive types. Additionally, it provides the ability to connect the load at a specific moment in time using electronic switches that emulate ideal transistors. The diagram shown in Fig. 1 presents the structure of the three-phase active–inductive load with a delayed connection function, enabling control over the timing of load connection to the system. The active resistance in the system is 10 Ω, and the load inductance is 0.001 H, which corresponds to an impedance of 0.314 Ω at the network frequency of 50 Hz. This approach allows for optimal load adjustment, providing effective simulation of various operating modes of the stand-alone generator.

The study implements scalar control of the induction generator through the rotor circuit. The scalar control module of the induction generator is based on maintaining a constant voltage-to-frequency ratio (*V*/*f* or *V*/Hz). The scalar control module determines the voltage applied to the rotor based on the specified reference frequency f_s. The calculation is performed using the following equation:

$$V_s = \left(\frac{V_n - V_{min}}{f_n - f_{min}}\right) \cdot (f_s^* - f_{min}) + V_{min}, \tag{1}$$

where V_n is rated inverter output voltage; V_{min} is minimum inverter output voltage; f_{min} is minimum frequency; f_n is rated frequency.

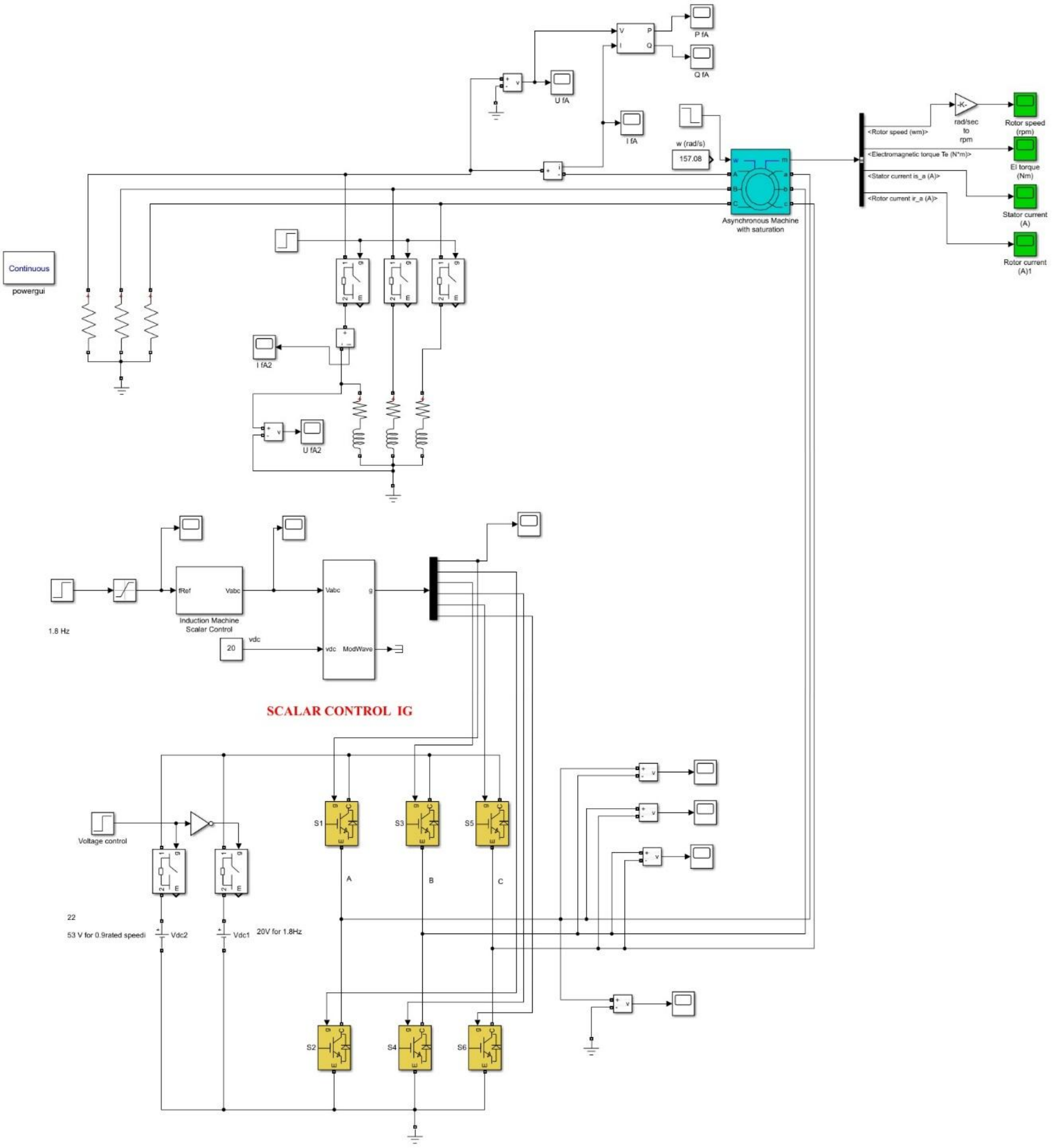

Fig. 1. Model of the stand-alone induction generator with self-excitation and an inverter in the phase rotor circuit.

The scalar control module uses voltage components in a stationary coordinate system. It then computes the phase voltages by performing an inverse Clarke transformation. The inverter is assigned the required frequency f_s, which is used to obtain the desired voltage value in accordance with the V/f principle. The calculated voltage is then transformed into the α–β coordinates. The next step is the conversion from the orthogonal α–β coordinate system to the three-phase abc system, implemented through the inverse Clarke transformation.

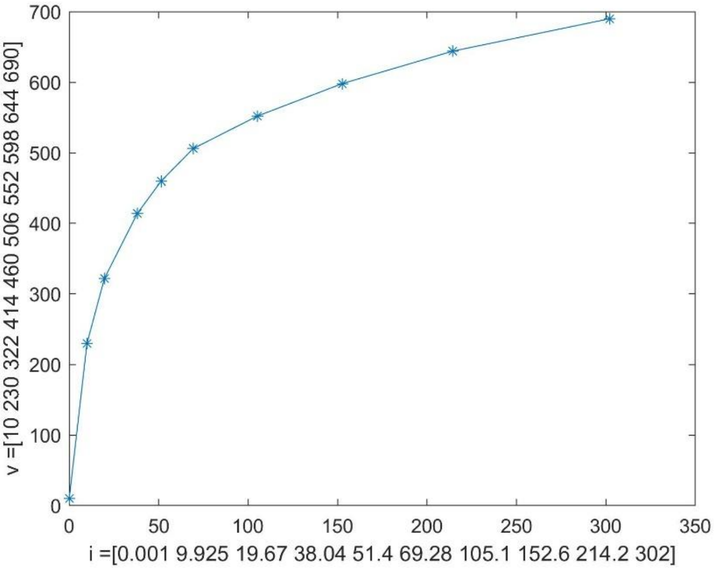

Fig. 2. Nonlinear magnetization curve for the 37 kW induction generator.

The next step after voltage transformation is the generation of a pulse-width modulation (PWM) signal. For this purpose, a specialized PWM generator must be designed. It functions as a three-phase, two-level PWM generator that forms the output signals used to control the inverter. The main task of the PWM generator is to manage the switching of the keys in the three-phase, two-level inverter (also known as a power converter). It determines the switching moments of the transistors based on the input control signals. In addition, the generator forms three sinusoidal reference voltages, each corresponding to one phase of the system. One of the key input parameters is the DC bus voltage, which affects the system's stability. At the output, the PWM generator produces six pulse signals used to control the power transistors of the inverter. Corresponding modulation signals are also generated to shape the desired output characteristics.

A specialized module is used to generate the pulse signals for transistor control. This module receives as input the formed three-phase voltage system V_{abc}, as well as the rectified DC voltage V_{dc}, which can come either from a rectifier or from a battery. To determine the precise switching instants of the transistors, the module uses an integrated MATLAB function that allows for accurate synchronization of the power switches, thereby maximizing the overall efficiency of the conversion system. This method not only provides voltage level control but also optimizes transistor operation, reducing energy losses and increasing the converter's efficiency. As a result, thermal stress on the power components is minimized, ensuring more stable system operation.

Based on the obtained values for the switching periods, the PWM control module generates gating pulse signals for each of the six inverter power transistors. These pulses determine the exact on/off instants of the transistors, ensuring proper operation of the three-phase inverter. This approach enables precise control of switching processes, allowing the inverter output voltage and current levels to be maintained within the desired limits. Such precise control is essential to guarantee the stable and efficient operation of the induction generator or any connected load. The method also contributes to improved energy efficiency and reduced thermal losses, positively affecting the overall system performance.

Fig. 1 presents the schematic diagram of the power inverter, which includes six high-power transistors. This block can be powered either from a three-phase independent rectifier or from a DC battery with a rated voltage of 560 V. This voltage level corresponds to the rectified output voltage generated by a three-phase bridge rectifier. The inverter, powered by a DC voltage source, acts as the key component for converting the DC voltage supplied by the battery or rectifier into a three-phase AC voltage. This enables effective control of the output voltage at the generator terminals and maintains stability under varying load conditions.

Fig. 1 also shows the complete MATLAB model of a household stand-alone induction generator with a phase-wound rotor and self-excitation provided by an inverter in the rotor circuit. The model integrates all the necessary components to ensure reliable power generation and voltage regulation for domestic consumers.

This integrated MATLAB model makes it possible to analyze in detail the operation of the stand-alone induction generator under various operating conditions. In particular, the model allows investigation of the influence of different load types on the generator's performance, evaluating voltage and frequency stability under changes in the active and inductive components of the load. It also enables the analysis of the reactive power compensation system implemented through the rotor-circuit inverter, which maintains the required level of reactive power for optimal generator operation. Thanks to the MATLAB simulation environment, it becomes possible to perform in-depth studies of system dynamics, transient responses, and steady-state performance with high precision.

Advantages of modeling in MATLAB. Creating such a model in MATLAB environment allows one to: conduct multiple simulations of different operating scenarios without the need for physical equipment, significantly reducing research costs; optimize system settings by analyzing generator behavior under various parameter values, thereby improving system efficiency; study the effect of the inverter on reactive power stability, which enables timely detection and correction of possible instabilities under real operating conditions.

For a detailed analysis of the operation of a household autonomous self-excited induction generator with an inverter in the rotor circuit, modeling was carried out based on the developed model. The simulation was performed in MATLAB environment to evaluate system performance under different load conditions and parameters. The purpose of the study was to examine the dynamic characteristics and verify the stability of the system under real operating loads.

The first scenario under investigation is the self-excitation mode. In this mode, the induction generator achieves self-excitation through the use of an inverter connected to the rotor circuit. The rotor circuit voltage frequency is 1.8 Hz, and the inverter voltage is 20 V. The drive shaft rotates at a constant speed of 157 rad/s.

To better understand the dynamics of self-excitation and the stability of the autonomous generator, a series of graphs were constructed to illustrate the transient processes of the system's main electrical parameters. Figure 3,*a* shows the transient graph of the instantaneous values of the phase voltage of the induction generator in phase A during the self-excitation process. This graph illustrates how the voltage rises during the transient state and reaches a stable value of 310 V in instantaneous values. Figure 3,*b* presents the transient process of the reactive power in phase A of the stator. Figure 3,*c* shows the transient process of the active power in phase A. Figure 3,*d* depicts the dynamics of the electromagnetic torque of the induction generator in the self-excitation mode. Figure 3,*e* presents the transient process of the phase current in the rotor, phase A. Measuring the current in the rotor circuit is important for understanding the influence of the inverter on the generator's operation under self-excitation conditions. Figure 3,*f* shows how the instantaneous value of the inverter output phase voltage in phase A changes during the self-excitation process.

Thus, during the study, the optimal self-excitation mode was determined – it occurs when the inverter operating frequency in the rotor circuit is set to 1.8 Hz, which ensures the required voltage levels at the stator terminals. The inverter voltage is 20 V. The reactive power is not drawn from the stator side.

In the no-load mode, the generator receives reactive power from the rotor and consumes a small amount of active power that compensates for its internal losses, including friction and cooling. In this state, the electromagnetic torque is minimal since there is no mechanical load on the shaft. As a result, the power factor is low because most of the energy corresponds to the reactive component.

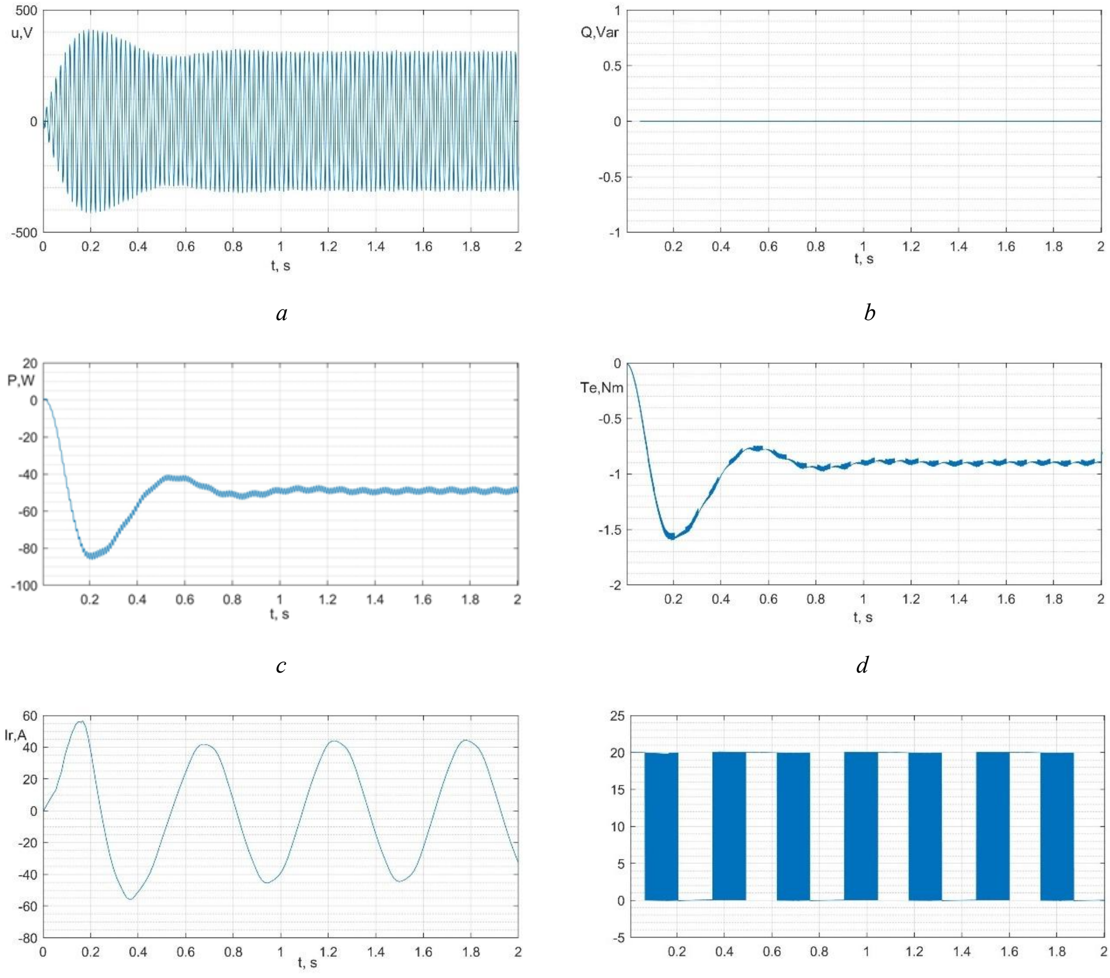

a *b*

c *d*

e *f*

Fig. 3. System diagrams in the self-excitation mode for a rotor circuit voltage frequency of 1.8 Hz.

The next stage of the study involves modeling the operation of the autonomous induction generator under a sudden load application. This mode is critical for assessing the reliability and adaptability of the system to real-time load variations. The simulation was performed for a time interval between 2 and 3 seconds, during which an additional load is connected to the generator.

In this scenario, the rotational speed of the drive shaft is set to 157 rad/s and remains stable throughout the load application. The inverter frequency in the rotor circuit is maintained at 1.8 Hz, ensuring the necessary voltage level during the self-excitation process. The inverter voltage is 20 V. Despite the system being subjected to significant loading between 2 and 3 seconds, the drive shaft speed remains unchanged. At 2.5 seconds, the inverter voltage increases to 22 V to raise the terminal voltage to its nominal value. The 0.5-second delay in increasing the inverter voltage is due to the need to analyze the natural stability of the system.

Figure 4,*a* shows the transient graph of the instantaneous values of the phase voltage of the induction generator in phase A for the time interval from 0 to 3.5 s. Figure 4,*b* presents the transient process of active power in phase A. Figure 4,*c* depicts the dynamics of the electromagnetic torque of the induction generator. Figure 4,*d* illustrates the transient process of the rotor phase current in phase A. Figure 4,*e* shows how the instantaneous value of the inverter output phase voltage in phase A changes. Figure 4,*f* presents the waveform of the instantaneous phase voltage values in phase A for the time interval from 3.4 to 3.46 s.

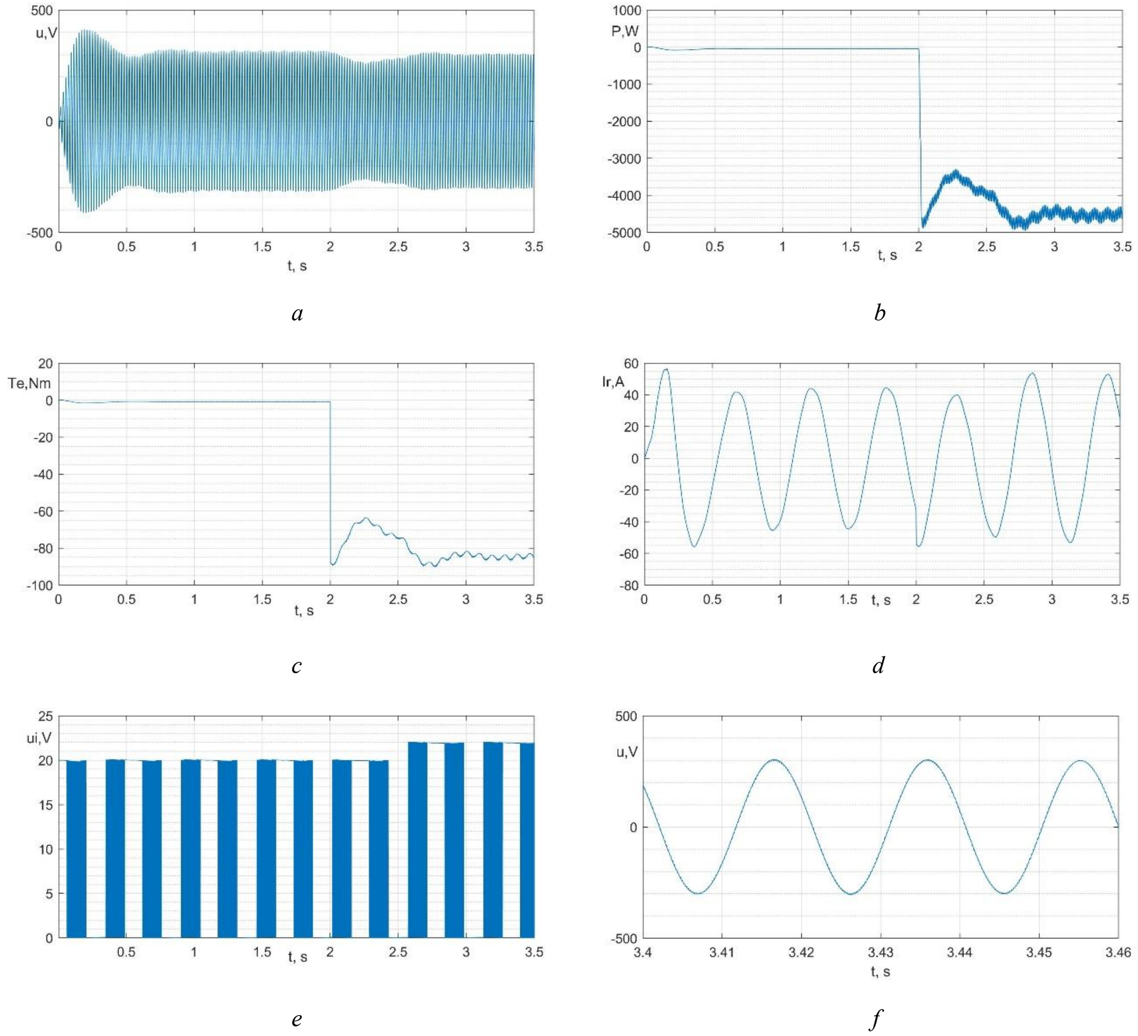

a *b*

c *d*

e *f*

Fig. 4. System diagrams in the load connection mode.

In the load connection mode, a slight voltage drop accompanied by an increase in phase current was recorded (Figure 4,*a*); however, the system remained stable without the need for additional control measures. By increasing the inverter voltage, the generator terminal voltage parameters were restored to their initial level.

This simulation demonstrates the ability of the autonomous induction generator to maintain stable operation during sudden load changes under the condition of independent inverter supply, even for an open-loop system. As a result, the generator retains self-excitation stability, which is crucial for ensuring efficient and uninterrupted power supply to consumers. The obtained results make it possible to evaluate the generator's performance under various operating scenarios and confirm the feasibility of using an autonomous generator for supplying power to household and industrial loads under unstable conditions.

The next stage of the study involves simulating the operation of the autonomous induction generator under a sudden 10% reduction in the drive shaft speed. This mode is also critical for evaluating the reliability and adaptability of the system to real-time variations. The simulation was conducted for the time interval from 2 to 3.5 s.

The inverter operating frequency in the rotor circuit was set to 1.8 Hz to ensure the required self-excitation conditions. The inverter voltage was 20 V. In this mode, as before, the generator relied solely on the inverter for self-excitation. At 2 seconds, the rotational speed of the drive shaft abruptly decreased by 10%, reaching 141.37 rad/s. At 2.5 seconds, the inverter voltage was increased to 53 V to restore the generator terminal voltage to its nominal level. The 0.5-second delay in increasing the inverter voltage was introduced to analyze the natural stability of the system.

This simulation demonstrates the ability of the autonomous induction generator to maintain stable operation under sudden variations in the drive shaft speed, provided the inverter is independently powered, even in an open-loop configuration. Hence, the generator retains self-excitation stability, ensuring effective and continuous power supply. The obtained results confirm the correct system configuration for stable self-excitation and readiness for further experiments under various operating modes. Stable generation of reactive power ensures voltage maintenance within acceptable limits, even under changing load and drive speed conditions.

Figure 5,*a* shows the transient graph of the instantaneous values of the phase voltage of the induction generator in phase A for the time interval from 0 to 3.5 s. Figure 5,*b* presents the transient process of active power in phase A. Figure 5,*c* depicts the dynamics of the electromagnetic torque of the induction generator. Figure 5,*d* illustrates the transient process of the rotor phase current in phase A. Figure 5,*e* shows how the instantaneous value of the inverter output phase voltage in phase A changes. Figure 5,*f* presents the waveform of the instantaneous phase voltage values in phase A for the time interval from 3.4 to 3.46 s.

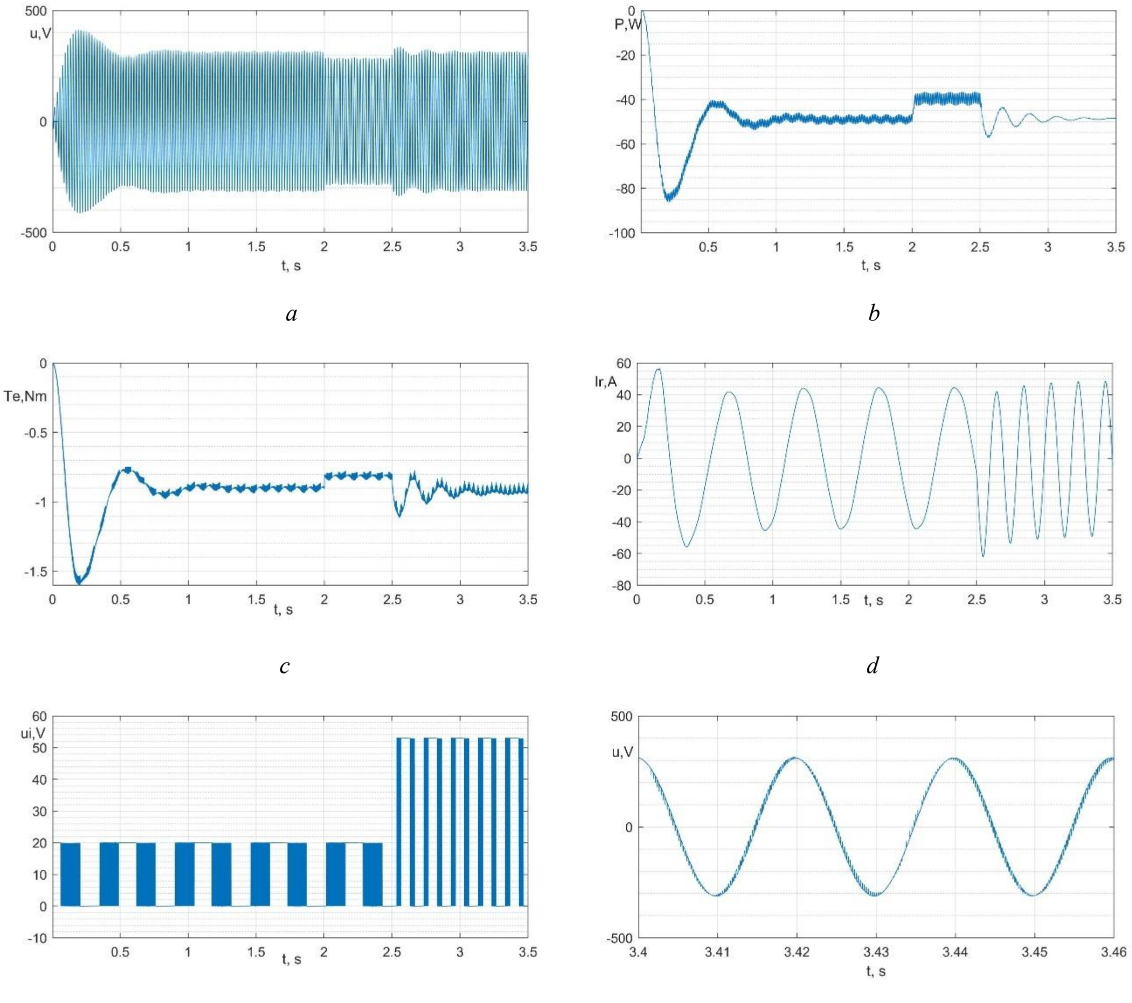

a *b*

c *d*

e *f*

Fig. 5. System diagrams under a sudden speed reduction mode.

When the motor speed was reduced, a slight decrease in voltage and an increase in current were also observed. The system remained stable, and the voltage was restored by the inverter. This simulation confirms the ability of the autonomous induction generator to maintain stable operation during sharp variations in the drive shaft speed under independent inverter supply, even for an open-loop system.

The results indicate that the system configuration ensures stable self-excitation and readiness for further studies. The stable generation of reactive power maintains the voltage within permissible limits, even under variable load and drive speed conditions.

5. Conclusion

In this work, a MATLAB-based model of an autonomous induction generator with a rotor circuit inverter and self-excitation for a wind turbine application was developed and investigated. Voltage and frequency regulation are separated. The implementation of a two-level inverter with an independent DC supply and consideration of the nonlinear magnetization curve of the induction generator significantly improved the model's accuracy.

The developed model enabled the study of self-excitation behavior at different rotor supply frequencies. During the simulation of the self-excitation process, it was found that optimal parameters for stable operation were achieved at a rotor frequency of 1.8 Hz and an inverter voltage of 20 V. As a result, the generator terminal voltage reached 310 V (instantaneous), corresponding to 220 V RMS, which ensures reliable system operation.

The study also investigated the impact of active–inductive load application and the system response to drive shaft speed variations. In the load connection mode (40% of nominal load), a slight voltage drop and an increase in rotor phase current were observed, but the system remained stable without additional regulation. By increasing the inverter voltage, the generator terminal voltage parameters were restored to their nominal levels. Under a sudden 10% reduction of drive shaft speed, a minor voltage decrease and a current increase were recorded, yet the voltage was again stabilized by the inverter.

The developed model serves as a universal tool for: designing autonomous power sources (wind, diesel, or hybrid systems); optimizing control systems for rotor inverters; educational demonstration of induction generator principles for students and engineers.

Developing such a model is crucial for the design of autonomous power supply systems, especially under variable load conditions or in remote areas where connection to the centralized grid is not possible. This approach enables further optimization of system parameters and testing of different operating scenarios in autonomous mode. Therefore, the created model of the autonomous induction generator provides the ability to simulate and analyze its behavior under variable load conditions while ensuring accurate and efficient control of output voltage and frequency.

References

[1] Krishna, V.B.M., Ghosh, S., Rajesh, P., Kiran, T.S.K., Satyanarayana, M. (2023). Experimental Study on Self-Excited Induction Generator for Small-Scale Isolated Rural Electricity Applications. *Results in Engineering*, 18, 101182. doi:10.1016/j.rineng.2023.101182.

[2] Xiong, X., Luo, B., Li, L., Sun, Z., Blaabjerg, F. (2023). Impedance Reshaping Method of DFIG System Based on Compensating Rotor Current Dynamic to Eliminate PLL Influence. *arXiv preprint*, arXiv:2307.10111. https://arxiv.org/abs/2307.10111

[3] Sienkiewicz, Ł., Wilczyński, F., Racewicz, S. (2025). Stand-Alone Operation of Multi-Phase Doubly-Fed Induction Generator Supplied by SiC-Based Current Source Converter. *Energies*, 18(11), 2753. doi:10.3390/en18112753.

[4] Metello, E., Moutinho, I., Véstias, M., Amaral, T., Duque, C., Afonso, J.L. (2024). Study of a Self-Excited Three-Phase Induction Generator. *Energies*, 17(16), 3900. doi:10.3390/en17163900.

[5] Singh, B., Murthy, S.S., Gupta, S. (2002). Analysis and Design of Self-Excited Induction Generators for Renewable Energy Applications. *IEEE Transactions on Energy Conversion*, 17(4), 697–704.

[6] Bansal, R.C. (2005). Three-Phase Self-Excited Induction Generators: An Overview. *IEEE Transactions on Energy Conversion*, 20(2), 292–299.

[7] Khan, M., Iqbal, M.T. (2005). Dynamic Modeling and Simulation of a Small Wind-Fuel Cell Hybrid Energy System. *Renewable Energy*, 30(3), 421–439.

[8] Gupta, S., Murthy, S.S., Singh, B. (2004). Transient Analysis of Self-Excited Induction Generator with Electronic Load Controller. *Electric Power Components and Systems*, 32(10), 927–944.

Розроблення та дослідження в MATLAB моделі автономного асинхронного генератора з інвертором у колі ротора для вітрової установки

Богдан Копчак, Андрій Мандюк, Ігор Дзюба, Ігор Бабій

Національний університет «Львівська політехніка», вул. С. Бандери, 12 , Львів, 79013, Україна

Анотація

В роботі розроблена та досліджена в MATLAB модель автономного асинхронного генератора з інвертором у колі фазного ротора та самозбудженням для вітрової установки. В системі застосований інвертор зі скалярним керуванням та незалежним живленням, а також врахована нелінійна крива намагнічування асинхронного генератора. Регулювання напруги та частоти розділене. Розроблена модель дозволила провести дослідження в режимі самозбудження для різних частот живлення ротора. У ході моделювання процесу самозбудження автономного асинхронного генератора було встановлено, що оптимальні параметри для стабільного самозбудження досягалися при частоті ротора 1,8 Гц та напрузі живлення ротора 20 В. В роботі здійснено дослідження впливу накиду активно-індуктивного навантаження та реакцію системи на зміну швидкості приводного вала. У режимі підключення навантаження 40 % від номінального значення було зафіксовано невелике зниження напруги разом зі зростанням фазного струму ротора, однак система залишалася стабільною без потреби в додаткових засобах регулювання. За допомогою підвищення напруги інвертора параметри напруги на затискачах генератора були повернуті до початкового рівня. При раптовому зниженні швидкості приводного вала на 10 % також спостерігалося незначне зменшення напруги та збільшення струму ротора. Цей режим генератор пройшов стабільно, а напругу і частоту знову вдалося вирівняти завдяки інвертору.

Ключові слова: модель; автономний асинхронний генератор з фазним ротором; інвертор; вітрова установка.

ENERGY ENGINEERING AND CONTROL SYSTEMS

Volume 11, Number 2, 2025

Determination of Critical Values of Parameters for Practical Application of Express Method of Diagnosing the Technical State of Shipboard Diesel Engines

Kostiantyn Boriak*, Oleksandr Ihnatenko

Institute of Naval Forces of National University "Odessa Maritime Academy",
8 Didrikhsona St., Odesa, 65029, Ukraine

Received: September 17, 2025. Revised: October 23, 2025. Accepted: October 30, 2025.

Abstract

This paper substantiates the feasibility and advisability of developing a new express method of diagnosing the state of diesel engines of combat boats based on the analysis of readings through on-board instruments of the information system for controlling and monitoring the boat's powerplant. This express method will enable combat boats' (ships') crews to employ the predictive maintenance of shipboard mechanisms to promptly identify degradation processes during their operation and minimize the risk of unexpected failures (breakdowns) while performing the combat missions. The essence of the new method lies in constructing a model of diagnosing shipboard machinery based on the analysis of empirical criteria for the rates of change of the current values of the determining parameters in singled-out time ranges during engines heating-up. As a result of full-scale tests, the determining parameters were defined and their limiting normalized rates of change were established, exceeding which could lead to emergency situations.

Keywords: shipboard diesel engine; determining parameter; heating-up mode; current values.

1. Statement of the problem in general

The introduction of martial law in Ukraine has not changed the requirements for the operation, maintenance, and repair of ships and their technical equipment. On the contrary, it has imposed additional burdens on the technical operation of the ships and boats of the Ukrainian Navy. At the same time, the conditions for ensuring and maintaining the established technical readiness of the ships and boats have changed. Specifically, the processes for ensuring the trouble-free operation of technical equipment and their timely maintenance have become more complex, and the capabilities of the ship repair and technical support system have deteriorated. Consequently, the requirements placed upon ships' (boats') crews have increased in terms of their specialized training, their ability to make sound decisions and fully perform their duties in difficult conditions, their ability to learn from positive and negative experiences, and their ability to incorporate these lessons into their work.

Under complicated combat conditions of operation, any failure or malfunction of the ship's (boat's) emergency alarm and control systems in combination with the insufficient level of crew's training in the maintenance of powerplants leads to delays in taking timely and adequate measures of responding to changes in technical state of shipboard machinery The crew's insufficient knowledge regarding the methods and techniques for localizing and

---

[*] Corresponding author. Email address: kostya.boryak@gmail.com

This paper should be cited as: K. Boriak, O. Ihnatenko. (2025). Determination of the critical values of parameters for practical application of the express method of diagnosing the condition of marine diesel engines. *Energy Engineering and Control Systems*, Vol. 11, No. 2, pp. 135 – 150. https://doi.org/10.23939/jeecs2025.02.135

repairing combat and emergency damage of technical equipment can lead to serious consequences, including the loss of combat capability by the ship (boat), a death threat to the members of the crew, and, in extreme cases, the wreck of the ship (boat).

In everyday situations, the cost of a belated detection of the values deviation of determining parameters from normalized values or an operational error by crew during the working of a modern ship's (boat's) technical equipment can be very high as well. Accidents can reach such a scale that moderating their consequences will require significantly greater effort and financial expenditures than simply the direct costs of restoring the technical resources and operability of such equipment. In world shipping practice, global environmental disasters as well as serious political consequences by reason of accidents at sea have taken place.

An analysis of technical failures on Ukrainian Navy ships (boats) shows that these failures most often occur as a result of influence of two common factors: (1) design and technological drawbacks (due both to the exhaustion of technical resources and to imperfections in the processes of scheduled inspection and restoration); (2) the accompanying human factor.

The main causes of breakdowns on ships (boats) of the Ukrainian Navy are as follows:

1) The obsolete and exhausted service life of a significant portion of the technical equipment, including equipment received as part of the logistical support.
2) Discrepancy within the chemical compositions of oils, lubricants, and process liquids in comparison with the established reference standards of the manufacturer.
3) Lack of spare parts, special tools, and instruments.
4) Abridged quantity of hours for performing the maintenance of shipboard machinery, and as a result, a low level of quality of work performed by the maintenance and repair department personnel.
5) A low level of quality of repair work and maintenance of watercraft in state-owned and private enterprises (companies).
6) Irregularity of ships' (boats') goings to sea, which leads to the crews losing their practical skills in operating shipboard technical equipment.
7) A low level of quality of incoming inspection of fuels, lubricants, and process liquids by crews.
8) Limited access to modern technical diagnostic tools and their use, as well as an insufficient number of instruments (including auxiliary ones) for technical monitoring.
9) Limited use of nondestructive express diagnostic methods and insufficient qualifications (technical awareness) of crews to carry out routine monitoring and prompt diagnostics of the technical state of shipboard machinery on the high sea.

Thus, the search for ways to further improve the operation of the ships' (boats') powerplants of the Ukrainian Navy under the martial law regime, in particular routine monitoring of the technical state, as well as forecasting and preventing possible failures of marine diesel engines, is an extremely pressing problem given the transition of the Ukrainian Navy to NATO standards for the operation of military equipment.

2. Analysis of recent research and publications

Ensuring the serviceability, reliability, and safe operation of ships (boats) requires the introduction of effective diagnostic tools, among which nondestructive testing (NDT) methods play a leading role. During the operation of technical equipment on the high sea, when maintenance is carried out in limited space and time conditions, and access to specialized laboratories is limited, the correct choice of NDT method becomes a serious condition that directly affects the operability of shipboard machinery.

When deciding on an NDT method for technical diagnostics of machinery, based on ship-repair practice, the following five key areas should be taken into account:

1) Analysis of the physical nature of the defect or property being tested, during which the type of object (hull parts, shafts, gearboxes, pipelines, welds, etc.) and the nature of possible damage as typical for the marine environment (cracks, corrosion, delamination, decompaction, etc.) are determined.

2) Knowledge of the physical principles underlying a specific NDT method. This is necessary to determine the capabilities and limitations when testing steel, aluminum, composite, or anti-corrosion coated objects to be diagnosed.
3) Evaluation of the interaction of a testing medium with the material of a part (assembly). For example, ultrasonic methods require the use of a wetting medium, which may be unacceptable for certain types of ship's equipment (electronics, high-precision components).
4) Analysis of the technical potential of the equipment, the measurement capabilities, and the reliability of the results obtained, taking into account the conditions on shipboard: vibration background, temperature conditions, spatial restrictions of the engine room, the presence of electromagnetic interference, etc.
5) Taking account of regulatory, economic, financial, organizational, and logistical factors for the feasibility of using a specific NDT method, which is related to the cost of maintenance, the speed of inspections, the requirements of marine classification societies (IACS, ABS, DNV, BV, etc.), as well as compliance with environmental requirements (including during stays in port or at anchor).

For example, ultrasonic or magnetic particle testing methods can be used to detect cracks in main engine crankshaft and connecting rod components, such as the crankshaft or connecting rods. Ultrasonic thickness testing is used to check for erosion and corrosion damage in cylinder liner walls, water jackets, or bores. In each of these cases, it is necessary to take into account not only the compliance of an NDT method with the physical characteristics of the object being tested, but also the internal operating conditions of the engine (high temperatures, limited access to components, the presence of lubricant residues, and the possibility of performing the testing without dismantling the components) and external ones (exposure to seawater, high salinity, and corrosive activity).

It should be noted that the equipment sensitivity values specified by manufacturers in their data sheets and operating instructions may differ from the actual parameters under operating conditions of a ship (boat) during a real combat situation. That is the reason why the competence of the personnel performing the testing and adherence to standardized testing procedures are of particular importance.

Thus, the optimization of NDT methods in the maintenance of ships (boats) of the Ukrainian Navy should be based on a deep understanding of physical, technological, and operational factors, which will ultimately allow not only the timely detection of defects and the prevention of emergency situations, but also ensure full compliance with the requirements of international standards for their operation.

It is clear that reliability evaluation of technically complex objects (machinery and their components) using NDT methods plays a significant role both when designing and manufacturing, and when operating and maintaining them. Currently, about a dozen different NDT methods are used: electrical, radio-wave, thermal, acoustic, vibroacoustic, optical, with penetrants, eddy-current, magnetic, radiative. All the NDT methods are categorized by their areas of application, as each has certain technical limitations [1].

At the present time, in the theory of technical diagnostics in relation to shipboard machinery, three groups of methods have received the greatest distribution: (1) the methods of diagnosing by the parameters of working processes (based on determining the technical state of machinery through monitoring the dynamics of changes in their operating parameters); (2) the methods of diagnosing by the parameters of accompanying processes, which indirectly affect the operation of technical equipment (based on the analysis of the indicators of thermal field, noise, vibroacoustics, etc.); (3) the methods of diagnosing by structural (geometric) parameters, which directly characterize the technical state of the units and assemblies of powerplant (based on the evaluation of objective geometric parameters (gaps, backlashes, free plays, displacements, etc.) [2], [3].

Diagnostic objectives, the means and methods for measuring diagnostic parameters, and the physical nature of the processes underlying the operation of the units and components being diagnosed are key factors when choosing a method for diagnosing the technical state of shipboard machinery. For example, when performing a standard technical diagnostics of individual systems and components of a marine diesel engine, as well as its diagnostics as a single unit of equipment, a good deal of diagnostic operations must be performed, which ultimately leads to significant time losses and, therefore, such a diagnostics is lengthy and ineffective.

It is clear that the solution of the problem of early warning of a high probability of failure, whether it is a single complex mechanical system (diesel engine, gearbox, generator, etc.) or individual simple components (injector, bearing, valve, etc.), depends on the availability of possibility to conduct a prompt evaluation of their technical state during operation. One of the key factors that can be singled out among others affecting the reliability of a component (or a mechanism) during operation is the quality level of current monitoring its technical state, which is conducted in the course of its intensive working.

In recent years, several innovations have become known in global practice for the technical diagnostics of complex systems—some enterprises (companies) have introduced so-called deep learning models in production, which ultimately increase the service life of these systems [4]. In dozens of countries, predictive maintenance systems are being added to production, which is associated with the implementation of the so-called smart factory at the Industry 4.0 level [5], [6]. Also highly reasonable is the attempt by Chinese researchers to create standard databases for diagnosing the malfunctions (failures) of technical equipment in order to prevent repetition of their research [7].

According to paper [8], the authors investigated a method for improving the efficiency of parametric diagnostics of marine engines based on the analysis of indicator diagrams and heat release characteristics. The method for diagnosing the quality of the combustion process in a marine internal combustion engine is based on measuring the pressure within cylinder as a function of the crankshaft angle (CA) during engine operation under typical operating conditions. The resulting indicator diagrams allow one to determine a number of indicator parameters (maximum combustion pressure, pressure at the beginning and end of combustion, average indicator pressure, etc.), the analysis of changes in which enables one to identify deviations in the operation of systems that form the combustion process, in particular the fuel injection system, the gas exchange system, and the "piston–piston rings–cylinder" assembly. The advantages of this method are its non-invasiveness (no need to stop the engine), as well as the speed of obtaining results and the ability to directly evaluate the technical state of the engine's functional systems based on physically substantiated indicators of the combustion process.

According to paper [9], the use of new-generation high-performance microcontrollers with wireless interfaces and integrated analog-to-digital converters (given their low overall power consumption) makes it possible to solve the problem of comprehensive diagnostics of marine diesel engines. And this, in turn, makes it possible to develop a portable system for technical diagnostics of the parameters of marine engines, which operates in real time. Such a system can be installed on well-known devices with Android or iOS mobile platforms, which receive information from sensors via Bluetooth system, after which they perform the necessary calculations and display diagrams and data (in real time). The proposed system uses a combination of a gas pressure sensor in the working cylinder and a vibroacoustic sensor, which expands the diagnostic capabilities of marine diesel engines in operating conditions. The presented method allows one to calculate the irregularity indicators of engine working in real time and introduces the integral CII criterion for evaluating the stability of operating cycles, thereby ensuring an accurate determination of the indicated power and providing a possibility of optimizing the settings of engine systems during operation.

Recently, there has been a clear trend in the modernization of marine technical equipment toward the active introduction of artificial intelligence into control and monitoring systems for shipboard machinery. The use of modern machine learning and big data processing technologies significantly improves the reliability of statistical information on the technical state of a ship's powerplant and auxiliary systems. And this, in turn, minimizes the probability of errors when evaluating the parameters of equipment working and ensures the timely detection of process deviations from standard operating modes. For a ship's tending squad, such intelligent solutions become decision support tools that reduce the complexity of understanding complex technical processes and contribute to the transition of the ships' (boats') crews from a reactive approach to the tending of shipboard machinery (i.e., passively responding to external events occurring with machinery) to a proactive approach (i.e., anticipating the failures of machinery in advance through predictive maintenance). In other words, a crew of a modern ship (boat) must have the ability to fully understand technical faults that unexpectedly arise during the operation of shipboard machinery on the high sea, and be able to use their knowledge to take further measures to operate the ship in accordance with the objective reality of the current state of the mechanisms.

In paper [10], the researchers described a new model of artificial intelligence based on a multi-scale attention transformer (MSAT) that can automatically detect faults in marine diesel engines by sensor data (e.g., cylinder pressure). Its unique feature is that it simultaneously recognizes fine signal details (local variations) and the overall picture of engine working (global dependencies). To ensure fast and accurate training of the model, they used an improved optimization algorithm. The testing showed very good results—the model correctly identifies faults even in the presence of significant interference (noise). The study substantiates the advisability of the integration of MSAT into on-board control and monitoring systems of marine engines as a decision support tool for predictive maintenance of ships' powerplants. And this means that such an approach can be applied directly on shipboard to continuously monitor the technical state of an engine and to provide early prevention of potential faults. The authors of this study believe that for developing an express method for diagnosing the diesel engines of fast-moving surface platforms, the method based on the parameters of accompanying processes is the most practicable.

According to paper [11], a passive thermal monitoring method based on the study of bearing heating rates was proposed for the prompt evaluation of the technical state of rolling bearings. A distinctive feature of this approach is the evaluation of the technical state of friction assemblies using the empirical criterion of heating rate as an indirect criterion of bearing operability by thermal state. This paper also took into account the results of bench tests [12], during the analysis of which the issue of shifting the period of prompt evaluation was examined in detail when starting up a unit (mechanism).

Under the conditions of combat operations, the problem of conducting the prompt diagnostics of shipboard diesel engines is particularly pressing. The intensive operation of ships and boats of the Ukrainian Navy at near-maximum operating modes occurs amid active enemy's counteraction and is accompanied by significant physical and psycho-emotional exhaustion of crews. Under such conditions, the known diagnostic methods used, including those based on empirical criteria of accompanying processes (heating rate when shifting the period of prompt evaluation when starting up the units), do not provide complete and reliable information about the actual technical state of the engine precisely at the moment of starting up, as the most critical and vulnerable mode of its operation. And this, in turn, creates the risk of hidden failures and sudden breakdowns, which directly impacts the combat readiness and survivability of ships (boats) [13].

One of the key prerequisites for ensuring the trouble-free operation of the main and auxiliary mechanisms of ships' powerplants during combat and special missions is effective current technical monitoring of critical operating parameters of engines and auxiliary equipment. The possession of reliable information about current changes in the values of these parameters in real time allows the crew to quickly respond to changes in the technical state of the powerplant, duly identify the initial signs of hidden defects and monitor degradation processes, as well as duly warn the maintenance and repair department about potential threats. Based on the data received from the crew, maintenance and repair department specialists can organize unscheduled diagnostic measures (using special instruments and tools) and, based on an analysis of the current values of the measured parameters, make substantiated decisions about the need for unscheduled maintenance or repair of specific assemblies (parts) of the powerplant.

The implementation of express methods of diagnostics based on the analysis of data through the digital display panels of on-board instruments will ensure the timely forestalling of emergency situations while ships are on the high sea. Given the crew's limited access to information about the technical state of shipboard machinery, and having only data coming from standard on-board control and monitoring systems, it is advisable to create an algorithm for the crew's actions and a database with a formalized description of procedures in the event of situations where, during technical diagnostics, an excessive increase in the rate of degradation processes occurs (by extremely high values of the determining parameters). This requires a clear determination of diagnostics objectives, formalization of monitoring procedures, optimization of the selection of critical parameters and establishment of standards for indicators characterizing the oncoming of the technical state of the powerplant to the critical one, as well as taking account of distinction in the use of a direct or indirect mode of measuring the values of the determining parameters.

In paper [14], we described the development of an express method for predicting the development of degradation processes based on a series of full-scale experiments to determine the most informative parameters for the prompt evaluation of the technical state of the diesel engines of boats' powerplants, the values of which vary over time. Using an improved diagnostic technique based on an empirical criterion for the rate of change of determining parameters over a fixed period of time, particularly during the unit heating-up stage, we analyzed data obtained through on-board instruments of the control and monitoring system. This made it possible to establish intermediate values for the rate of change of operating parameters and determine ways to obtain the boundary limits of critical values. As a result of the conducted research, we made a substantiated conclusion that nearing these limits indicates an increased probability of loss of operability of the shipboard diesel engine, which, in turn, increases the risk of the ship (boat) losing her capability to perform combat missions.

Taking into account the aforesaid, there is a need to develop a relatively easy-to-use and physically understandable (for ship's crew) express method of diagnosing the actual technical state of the engine, which allows for the advantages and disadvantages of other methods and provides crews with an effective tool for promptly evaluating the operability of powerplants in real time. Such a method must be technologically simple when introducing, be adaptable to standard technical instruments for measuring the parameters being monitored, ensure rapid acquisition of diagnostic data, and also minimize the influence of human error. Its use will significantly improve the effectiveness of decision-making by the crew under complicated operating conditions (including combat operations), when the combat readiness and survivability of a ship (boat) depend on the failure resistance and timely response to malfunctions.

3. The goal and tasks of the study

The goal of the study is to develop a new express method of diagnosing the technical state of diesel engines of powerplants on shipboard of high-speed combat boats of the Ukrainian Navy directly at the initial stage of engines working, in particular during their heating-up.

Practical application of the new express method by the crews of ships (boats) must ensure the timely detection of early signs of degradation processes in the functional systems of engines, which will enable one to take preventative measures and, consequently, to stave off probable failures in the future. At a later time, this will significantly reduce the probability of operability loss by ships' (boats') powerplants during combat missions on the high sea and will lay the foundation for implementing the concept of predictive maintenance (i.e., maintenance based on actual technical state) into the operational practices of the Ukrainian Navy.

According to paper [14], the model of the express method of diagnosing is based on the evaluation and analysis of the indicators generated by the on-board instruments of the control and monitoring system (with the shifting of period of the prompt evaluation during the engine startup stage and singled-out phases of its heating-up). Taking into account the results of full-scale experimental tests, which were conducted on shipboard diesel engines, and the conclusions from the analysis of the interdependence of the parameters of the on-board instruments of the control and monitoring system, as well as the forecast of the possibility of obtaining the boundary limits of critical values, the following scientific research tasks can be defined that require fulfillment:

1) Calculation of critical values of determining parameters, nearing which increases the probability of loss of engine operability and reduces the combat capability of the ship (boat), taking into account the dynamics of changes during engine startup in heating-up mode.
2) Obtaining confirmation of the specified normalized critical values of determining parameters and the rates of their change within specific time intervals through full-scale experiments on existing diesel engines of ships' powerplants.
3) Development of a new express method of diagnosing the technical state of diesel engines based on the readings through on-board instruments of the control and monitoring system of ship's powerplant, with the possibility of using the method as an auxiliary monitoring tool between scheduled maintenance dates.

4. Materials and methods of the conducted study

Modern military ships and boats are equipped with on-board electronic control and monitoring of the technical state of shipboard machinery with different degrees of informativeness and diagnostic capabilities. Large-displacement ships (frigates, corvettes) are equipped with complicated systems that enable their crews to diagnose the individual mechanisms, autonomous engine groups and the entire propulsion system of the ship (Fig. 1). These systems are distinguished by a wide range of monitoring functions and diagnostic parameters, which is ensured, in particular, by the use of modern diagnostic technologies: sensors and instruments, on-board information and control panels (ECU, EMU, EIM), data collection, storage and display systems (MTS, LOP, LOSDE/GT), software for diagnostic and analysis system, communication and integration modules (CCG, PIMs), information support tools for ships' tending squads [15] with the corresponding visualization of data transmitted to the digital display panel of control and monitoring of the ship's powerplant (Fig. 2).

However, the excessive complexity of up-to-date electronic control and monitoring systems for shipboard machinery, the high cost of their installation and operation, the need for specialized training for ships' tending squads, as well as limited access to spare parts and a small number of maintenance and repair centers, pose significant limitations to their effective use, especially on small military boats of the Ukrainian Navy. In connection with this, there is a need to introduce simpler, more reliable, and more cost-effective control and monitoring systems that provide a sufficient level of monitoring and diagnostics of the technical state of ship machinery, and thereby simplifying tending and reducing operating costs on small vessels.

Fig. 1. Modular hardware for monitoring and diagnostics of modern diesel engines (MTU Co.).

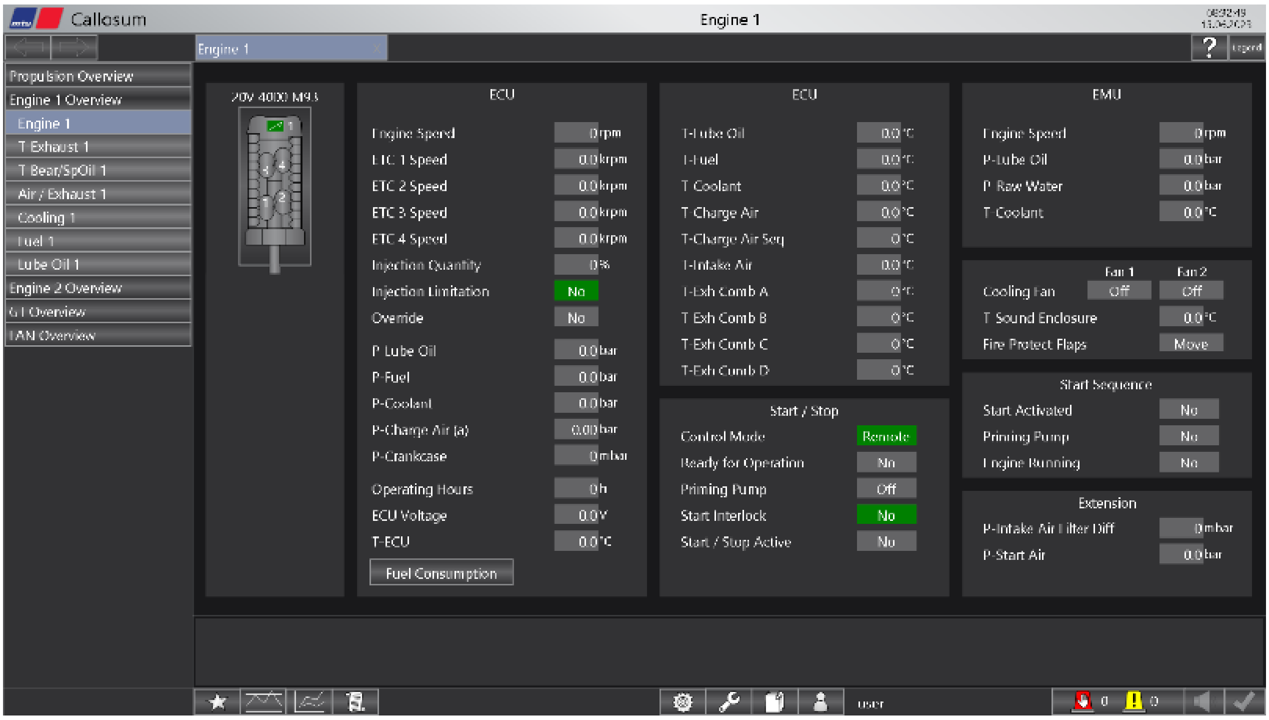

ECU

Engine Speed 0 rpm
ETC 1 Speed 0.0 krpm
ETC 2 Speed 0.0 krpm
ETC 3 Speed 0.0 krpm
ETC 4 Speed 0.0 krpm
Injection Quantity 0 %
Injection Limitation No
Override No
P Lube Oil 0.0 bar
P-Fuel 0.0 bar
P-Coolant 0.0 bar
P-Charge Air (a) 0.00 bar
P-Crankcase 0 mbar
Operating Hours 0 h
ECU Voltage 0.0 V
T-ECU 0.0 °C

ECU

T-Lube Oil 0.0 °C
T-Fuel 0.0 °C
T Coolant 0.0 °C
T-Charge Air 0.0 °C
T-Charge Air Seq 0 °C
T-Intake Air 0.0 °C
T-Exh Comb A 0 °C
T Exh Comb B 0 °C
T-Exh Comb C 0 °C
T-Exh Comb D 0 °C

Start / Stop

Control Mode Remote
Ready for Operation No
Priming Pump Off
Start Interlock No
Start / Stop Active No

EMU

Engine Speed 0 rpm
P-Lube Oil 0.0 bar
P Raw Water 0.0 bar
T-Coolant 0.0 °C

	Fan 1	Fan 2
Cooling Fan	Off	Off
T Sound Enclosure		0.0 °C
Fire Protect Flaps		Move

Start Sequence

Start Activated No
Priming Pump No
Engine Running No

Extension

P-Intake Air Filter Diff 0 mbar
P-Start Air 0.0 bar

Fig. 2. Visualization of current values of determining parameters on the digital display panel.

Currently, small combat and specialized self-propelled marine and river platforms (boats, launches, inflatable boats, etc.) utilize relatively simple control and monitoring systems of powerplants working, which provide the data transmission of minimum necessary but supremely important operating parameters of the main and auxiliary diesel engines to the digital display panels of on-board instruments. The values of these operating parameters indicate the current technical state of the shipboard machinery of powerplant in various operating modes (Fig. 3).

Caterpillar's CAT18 ACERT engines, which were the subject of research in paper [14], exemplify the application of simplified information systems on marine vessels. These engines are equipped with the ADEM A3 control system, which provides a sufficient degree of integration of control, protection, and technical state monitoring functions. The system also supports the functions of diagnostics and fault codes display via the Cat Electronic Technician (ET) interface.

Fig. 3. Types of digital display panels of on-board instruments for controlling and monitoring the powerplant.

The disadvantage of this information system is that the specialists of maintenance and repair department can gain access to information on the state of the machinery only after the ships' return to their home ports. On the high sea, only the ship's (boat's) crew members are present, and they are not sufficiently trained in analyzing and deciphering the coded monitoring results from the ECU (electronic control unit). In addition, in cases where only generally accepted maintenance schedules are in effect on ships, the specialists (of maintenance and repair department) retrieve information from the ECU at fairly long intervals (according to the schedule), or after an emergency situation not provided for by the maintenance schedule has already occurred. It is at preventing and reducing to zero the risk of such unforeseen emergencies on the high sea that the implementation of the new express method is aimed.

At the same time, simple control and monitoring systems of ship's powerplant have certain advantages: (1) the use of simple systems makes it possible to reduce acquisition and maintenance costs, which is critical for military boats with limited funding; (2) reduced complexity of the systems simplifies the procedures of diagnostics and repair, which, in turn, reduces downtime and dependence on specialized personnel; (3) the use of standard components and techniques provides easier access to spare parts and maintenance.

Therefore, adapting simplified on-board electronic control and monitoring systems, such as the CAT18 ACERT™ engine monitoring systems, can be an effective solution for small military boats, which will provide the necessary level of monitoring and diagnostics while reducing the costs and moderating the complexity of maintenance as a whole.

5. Presentation of the main material

As part of the ongoing research, the values of the determining parameters that change their values during the operation of the ship's powerplant in various operating modes with a measurement interval of 3 minutes have already been calculated [14].

Lubricating oil pressure measurements were conducted using a Caterpillar 304-5668 type stationary sensor (Sensor GP-Pressure), which is designed for continuous monitoring of pressure in the lubrication system of a C18 series marine diesel engine. The sensor converts mechanical oil pressure into a standardized electrical signal transmitted to the ECM for indicating and diagnosing the technical state of the system. This sensor has a sealed housing with a threaded connection; it is resistant to vibration and high temperatures, and its operating range of 0–1.8 MPa and fast response time of 5–20 ms ensure instantaneous detection of pressure changes during engine operation and timely activation of automatic protection systems.

Coolant temperature measurements were taken using a Caterpillar 256 6453 type stationary resistive sensor, which is applied on Caterpillar C18 marine diesel engines. The sensor changes its resistance depending on the coolant temperature, transmitting a signal to the ECM to accurately determine the engine temperature, to diagnose and protect the system. This sensor's operating range is 86–99 °C; when the temperature reaches 106 °C, an alarm is activated, preventing overheating. The sensor's response time is 20–100 ms, allowing the ECM to instantly monitor coolant temperature changes and maintain the safe operating mode of engine.

The time interval was recorded using a FLOTT FS 8200 digital stopwatch, a high-precision instrument with an accuracy rating of ±0.01 s. It has a three-line LCD display and memory for 200 readings, which enables one to simultaneously measure and record the current values of all the determining parameters of working engine. The stopwatch ensured reliability under real-world operating conditions, while its resolution and accuracy rating enabled us to precisely monitor the time during experimental measurements of diesel engine operating parameters, in particular when recording rapid changes in operating modes and evaluating the dynamics of powerplant performance.

A preliminary analysis of experimental data showed that the starting mode of heating-up of diesel engine (at no load) is the most informative for forecasting its overall technical state and early detection of faults. This operating mode makes it possible to effectively evaluate the state of engine at the expense of the clearly expressed dynamics of key parameters. On the basis of these circumstances, the following indicators were selected for prompt diagnostics, directly reflecting the thermal and mechanical stress of the engine: (1) coolant temperature (Coolant Temp); (2) oil pressure (Oil Pres); (3) fuel consumption (Fuel Rate). Changes in these three parameters over time during engine heating-up are noticeable indicators, which makes it possible not only to analyze the current state, but also forecast the onset or acceleration of degradation processes, as well as anticipate potential faults before their critical manifestation in the form of a breakdown. This methodology formed the basis for developing an express method as the basic platform for a system for monitoring the current technical state of engines.

Based on experimental data obtained during engines operation in the starting mode of heating-up (the phase of regular heating-up), graphical dependencies were constructed by criteria of the rates of change of the current values of the determining parameters of diesel engines working over time (for two main starboard diesel engines of two boats). These graphical dependencies are presented in Figures 4–7, where the different colors of the jogged lines and the corresponding numbers correspond to the quantity of measurements (tests) performed on two combat boats.

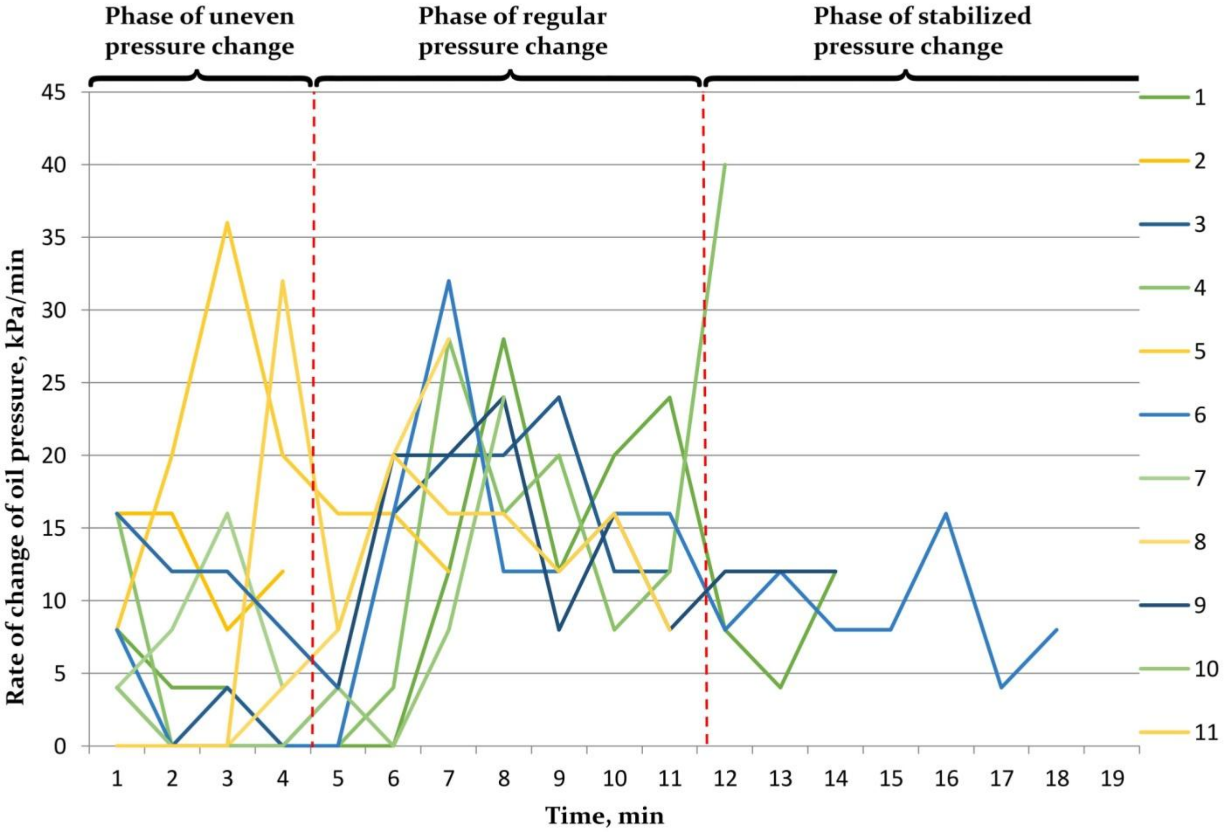

Fig. 4. Boat No. 1: Rate of change in the values of oil pressure in the heating-up mode of engine.

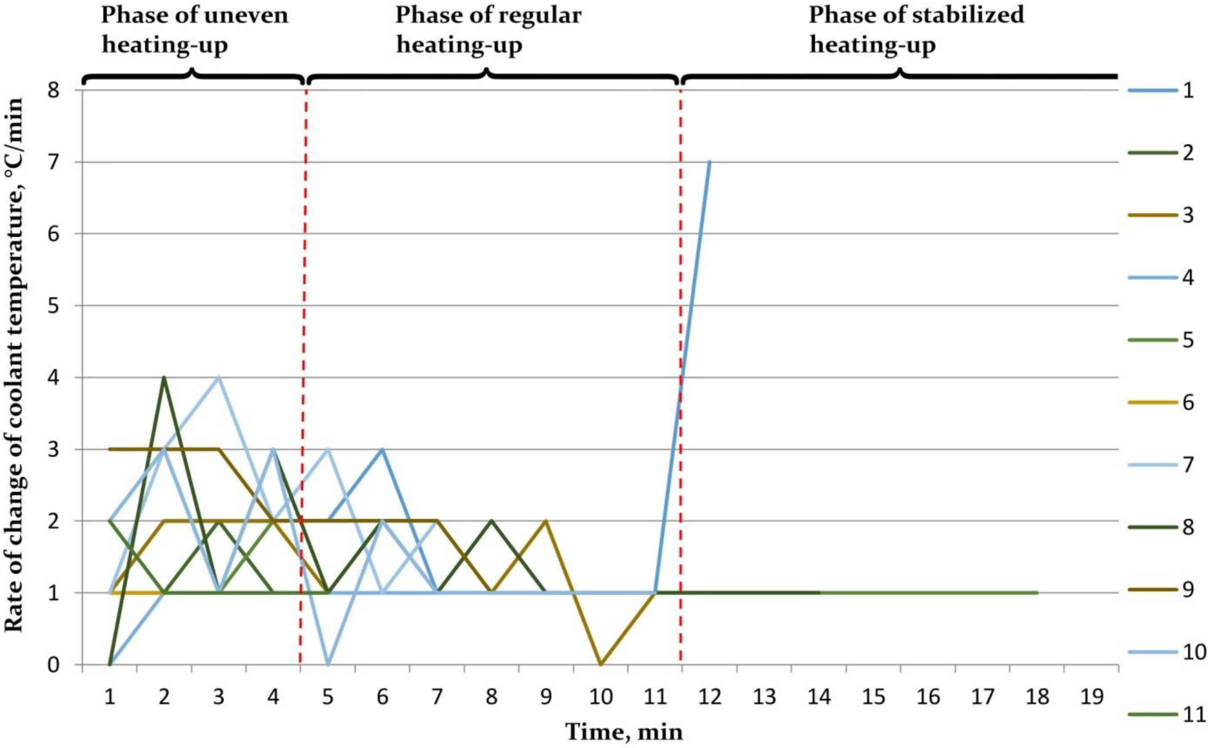

Fig. 5. Boat No. 1: Rate of change in the values of coolant temperature in the heating-up mode of engine.

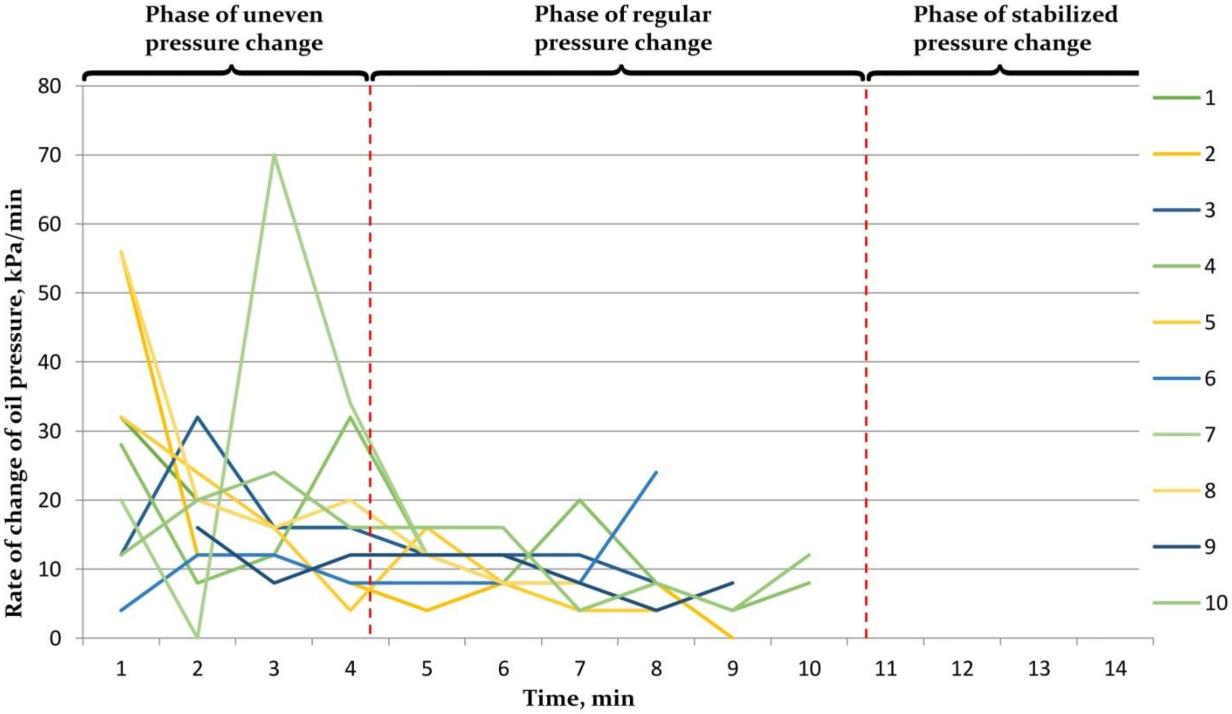

Fig. 6. Boat No. 2: Rate of change in the values of oil pressure in the heating-up mode of engine.

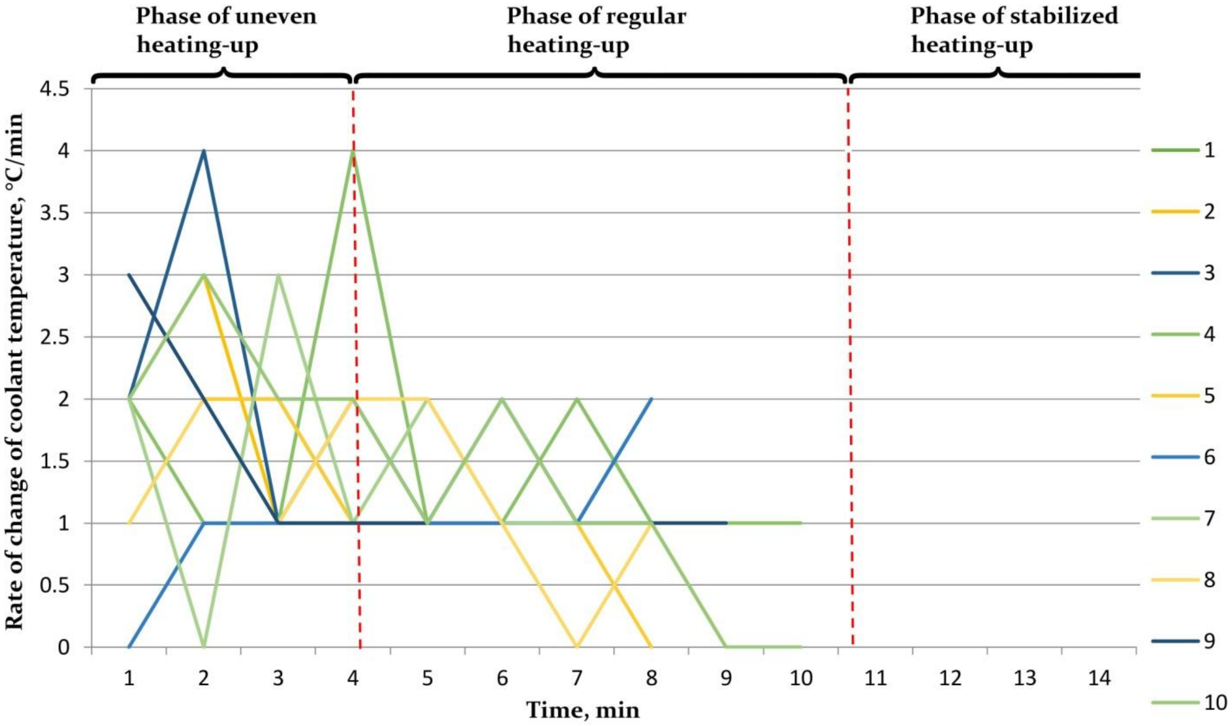

Fig. 7. Boat No. 2: Rate of change in the values of coolant temperature in the heating-up mode of engine.

Further research into the starting mode of the diesel engine showed that, under identical constant loads and rotation speeds of the drive shaft of the engine, the regularities of change in the operating parameters take place, especially the thermal indicator. The cooling mode efficiency of the diesel engine, as a key thermal indicator, has a direct impact on the strength and deformation characteristics of its components, as well as on the quality of lubrication of friction surfaces. Insufficient removal of heat (overheating state) significantly reduces the tensile strength of materials, especially in thermally stressed areas (cylinder heads, pistons, and cylinder liners). This can lead to thermal fatigue, plastic deformation, and, ultimately, breakup of components. An elevated temperature in the cooling system, manifested as engine overheating, is extremely dangerous for the lubrication system and can lead to rapid degradation and sudden failure. At the same time, excessive cooling (low operating temperature) increases engine oil viscosity, which impairs pumpability and lubrication efficiency, increases hydrodynamic friction, and accelerates corrosive wear. Optimal thermal conditions make possible maintaining the necessary oil viscosity to form a strong oil film, and thus minimize friction and wear, and prevent material degradation and structural changes that are critical to engine longevity.

From the moment of starting diesel engines, three time phases of their thermal state can be distinguished: (1) the phase of uneven (chaotic) heating-up; (2) the phase of regular heating-up; (3) the phase of stabilized heating-up. During these phases, changes in the above-mentioned determining parameters (the most informative) occur. From an analysis of the graphical dependencies of the current values of the parameters of diesel engines in the starting mode of heating-up without load (i.e., from the moment of starting a "cold" engine to the phase of stabilized heating-up), it was determined that the main changes in the parameters occur up to the 11th min. of engine operation, which makes it possible to predict engine failure with sufficient probability and quickness, which means to anticipate an imminent emergency situation at the very initial stage of the operation of the ship's powerplant.

Moreover, it can be visually determined that after engine startup, from the first to the fourth minute of operation, a disordered change in all operating parameters is observed, characterized by instability in the thermal and mechanical load conditions on the engine. This time interval is not taken into account when analyzing changes in the values of the determining parameters (for diagnostics).

Between the 4th and 11th min. of engine operation, regular surges take place, and changes in operating parameters have corresponding peak zones, corresponding to a transient state during the increase in operating parameter values.

This phase of engine operation is the most informative (and valuable) component, which is of immediate interest in our study.

The final phase (the 3rd one), from the 11th min. onward, is characterized by a steady increase in operating parameters and indicates stabilization of the engine's operating process. This period of time is also not taken into account when analyzing changes in the values of the determining parameters (for diagnostics).

Further research into the graphical dependencies of the rates of change of oil pressure and coolant temperature parameters within the main diesel engines and analysis of the results showed that the maximum values of these rates in the time interval from the 4th to the 11th min. can be adopted as normalized values for the express method of diagnosing technically faultless engines. All other values of the determining parameters (rates of change of oil pressure and coolant temperature) that exceed the established normalized values can be considered as critical ones for main diesel engines, and which are associated with accelerated degradation processes during the period between scheduled maintenances.

To normalize the critical values of the defining parameters, it is quite appropriate to proceed from the reliability coefficient set by the manufacturer separately for each component of the engine system (lubrication system, coolant system, fuel system). In the technical and operational documentation for CAT18 ACERT engines, which are produced by the famous American company Caterpillar Inc. [16], the minimum and maximum permissible values of the main operating parameters for each separate system are defined. Therefore, to select determining parameters, the excess of which will indicate a deviation from normal operation and signal the presence of a fault, one can use the technical instructions given in Table 1 from the manufacturer.

Table 1. Performance Analysis Report (PAR) data during sea trials (system format) for diesel engine C18 DITASWACTESTSPEC 371-7544 EFFS/NJLE05142ADVPWR 1135 BHP (840 BKW) @ 2300 RPMPERFREFEM0260.

Code Number	Check Parameter	Nominal	Value	Unit
Circulating Water System (of Cooling System)				
922	Circulating water inlet temperature (from cooler)	Max.	92	°C
921	Circulating water pressure from cooling system	Min.	Note 1	kPa
933	Circulating water inlet temperature (to cooling system)	Max.	103	°C
901	Circulating water outlet temperature (before regulator)	Max.	103	°C
918	Circulating water outlet pressure (before regulator)	Min.	Note 1	kPa
902	Circulating water temperature (after water pump)	Max.	103	°C
Delta T	Circulating water (outlet–inlet)	Max.	10	°C
Lubrication System				
914	Oil pressure at low idle	Max.	600	kPa
914	Oil pressure at low idle	Min.	100	kPa
914	Oil pressure at full load	Max.	600	kPa
914	Oil pressure at full load	Min.	275	kPa
927	Oil filter inlet pressure	Min.	Note 15	kPa
928	Oil filter outlet pressure	Min.	Note 15	kPa
Heat Removal				
Overall Cooling System (see Note 5)		Max.	556	kJ/min
Notes				
Note 1	This value is based on an external limitation that is not known during engine manufacturing. This datum is subject to determination during sea trials by a certified expert.			
Note 5	Size the system so that the overload factor is 5 %.			
Note 15	The pressure drop must not exceed 35 kPa across the filter and housing at rated speed.			

The first significant parameter for diagnostics is lubricating oil pressure. The Performance Analysis Report (PAR) during sea trials for a diesel engine contains Note 15 at the very bottom line, which states that at rated speed, the pressure drop across the filter and housing must not exceed 35 kPa. Thus, we have a permissible critical value for the rate of oil pressure change when measured in the time interval from the 4th to the 11th min., which corresponds to the phase of regular rate of change of the first determining parameter, when the oil pressure difference for a faultless engine must not exceed $P/\Delta t \leq 35$ kPa/min. Therefore, the ratio of pressure changes in fixed time intervals should be adopted as the first determining parameter for diagnosing diesel engines, which we have laid down as the basis for constructing a model of our new express method.

The second important parameter for diagnostics is the temperature of the fluid in the circulating water system, along with the overall cooling system. The well-known formula for calculating the amount of heat (Q) required to change the temperature of a body is as follows:

$$Q = c \cdot m \cdot \Delta T \text{ [kJ]} , \tag{1}$$

where *c* is specific heat capacity of the body [coolant] (in kJ/(kg · °C) or kJ/(kg · K)); m is the mass of the body; ΔT is the change in temperature (in °C or K) as the difference between the initial and final temperatures.

Formula (1) allows us to calculate the quantity of heat required to heat or cool a body of a certain mass with a certain specific heat capacity by a certain number of degrees.

Furthermore, the line for Heat Removal of the PAR form states "Overall Cooling System (see Note 5)" and also indicates a maximum value of 556 kJ/min (i.e., maximum heat removal capacity). According to Note 5, the overall cooling system must be sized to provide a 5% overload factor. This is an indicator of the permissible difference in loading when extracting the amount of thermal energy with time (heat removal capacity), and therefore, we have the following condition for the operability of the overall cooling system (i.e, the normalized heat removal capacity):

$$\Delta Q = \frac{Q_{out} - Q_{in}}{\Delta t} \leq 556 \text{ [kJ/min]} , \tag{2}$$

where Q_{in} is the amount of thermal energy that the fluid has in the system at the engine inlet (kJ); Q_{out} is the amount of thermal energy that the fluid has in the system at the engine outlet (kJ); Δt is the time interval (duration) of measurement (min).

According to data of the PAR form for the Circulating Water System (of Cooling System), the maximum circulating water temperatures are 92°C at the inlet (from the cooler) and 103°C after the water pump. The maximum temperature difference ΔT of the circulating water (outlet–inlet) is 10°C. Therefore, the permissible critical value for the circulating water temperature difference is $\Delta T \leq 10$°C. However, the overall cooling system is quite inertial, and therefore such a difference will be characteristic for long-term monitoring of changes in the absolute value of temperature.

It is quite obvious that for a short-term prompt diagnostic interval of 7 minutes (from the 4th to the 11th min.), the derivative of the temperature parameter function with time $\Delta T/\Delta t$ (°C/min) will be more informative, rather than its absolute final value ΔT (°C). On this basis, the second determining parameter for diagnosing diesel engines should be the rate of change of the difference in the temperature of the circulating water in the measurement time interval, which we have laid down as the basis for constructing a model of our new express method.

To clearly define the permissible critical value of the rate of temperature change, it is appropriate to start from the permissible overload factor of the circulation system of 5% and the maximum temperature of the circulating water (after the water pump) of 103 °C, and assign the permissible critical value of the change in temperature difference with time as 5% of 103 °C, i.e., the difference between the measured temperature values in the time interval from the 4th to the 11th min., which corresponds to the phase of regular heating-up of the faultless engine, must meet the condition $\Delta T/\Delta t \leq 4.9$ °C/min.

Thus, based on the readings (current values) through the on-board instruments of the ship's powerplant control and monitoring system and the analysis of these readings, we propose a constructed model of our new express method for diagnosing diesel engines at the initial stage of their heating-up from the 4th to the 11th min., taking into account the monitoring of two determining parameters at fixed time intervals:

1) Change in oil pressure $\Delta P/\Delta t \leq 35$ kPa/min.
2) Change in the temperature difference of the circulating water in the cooling system $\Delta T/\Delta t \leq 4.9$ °C/min.

Based on the information received from the tending squad regarding two determining parameters and normalized criteria, the ship's captain makes a substantiated decision on the possibility of the ship's going to sea to carry out a combat mission or notifies the maintenance and repair department of the presence of a fault, which sends authorized specialists (with specialized equipment and tools) to the ship to find the defective assembly (part) and eliminate the fault by conducting unscheduled maintenance or repair.

The express method being proposed for diagnostics is very simple to use. During the initial heating-up mode of the diesel engines, the ship's tending squad record the current values and the difference in lubrication pressure (ΔP) every minute (Δt) for 7 minutes, starting from the 4th to the 11th min., and compare them with the normalized value $\Delta P/\Delta t \leq 35$ kPa/min. The current values and the difference in temperature of the circulating water in the cooling system ΔT are similarly recorded and compared with the normalized value $\Delta T/\Delta t \leq 4.9$ °C/min. Based on the information received from the tending squad regarding two determining parameters and normalized criteria, the ship's captain makes a substantiated decision on the possibility of the ship's going to sea to carry out a combat mission or notifies the maintenance and repair department of the presence of a fault, which sends authorized specialists (with specialized equipment and tools) to the ship to find the defective assembly (part) and eliminate the fault by conducting unscheduled maintenance or repair.

It is quite obvious that the process of measuring current values, calculating and comparing the results being obtained with the normalized critical values of the determining parameters should preferably be automated using mobile devices (tablet, cellphone, etc.) in order to avoid subjective influence (human factor) on the final results of diagnostics, so we will continue research work in this direction.

As a visual example, it is worth demonstrating the application of the express method being proposed for diagnosing two diesel engines from different boats using empirical data (see Fig. 4–7) for two determining parameters (oil pressure change and circulating water temperature difference in the cooling system). Based on the analysis of the constructed graphical dependencies, several substantiated conclusions can be drawn.

According to ten test measurements of two diesel engines, which were carried out at different times of day and under different ambient temperature values, they did not exceed the permissible normalized values for the determining parameter of oil pressure change with time, namely:

- Engine #1 has maximum values within the range of $\Delta P/\Delta t = 24–32 \Rightarrow < 35$ kPa/min (Fig. 4).
- Engine #2 has maximum values within the range of $\Delta P/\Delta t = 12–20 \Rightarrow < 35$ kPa/min (Fig. 6).

A similar situation was observed in test measurements of changes in the temperature difference of the circulating water with time, namely:

- Engine #1 has maximum values within the range of $\Delta T/\Delta t = 2–3 \Rightarrow < 4.9$ °C/min (Fig. 5).
- Engine #2 has maximum values within the range of $\Delta T/\Delta t = 2 \Rightarrow < 4.9$ °C/min (Fig. 7).

During the comparative analysis of identical experimental diesel engines, for which the first scheduled maintenance period is set at 3,000 hours of operation time, the following was established: main diesel engine #1 with a total operation time of 2,236 hours, which was confirmed by the data of digital display panel of the electronic control unit of the boat's powerplant parameters (photo recording of the "Engine Hours" indicator at the 2,236 hours mark), the service life of which was approaching the first scheduled maintenance, was characterized by a more deteriorated technical state than that of engine #2 due to its operation time of 2,236 hours. In turn, main diesel engine #2 with a total operation time of 3,112 hours, which was confirmed by the data of digital display panel (photo recording of the "Engine Hours" indicator at the 3,112 hours mark), 112 hours of which were operated after the scheduled maintenance, having reached the 3,000 hours mark, showed a better technical state than engine #1.

The conducted comparison of the current technical states of identical diesel engines with different operating hours "before" and "after" maintenance has confirmed the effectiveness of the new express method being proposed of prompt diagnostics, which makes it possible to quickly evaluate the current technical condition of a ship's powerplant in a short period of 7 minutes (from the 4th to the 11th min.) and can serve as an indicator of confirmation of the fact of maintenance fulfillment and the level of its quality. The foregoing example clearly demonstrates the practical value of the new express method for crew members as well as specialists of maintenance and repair department as an additional tool for monitoring changes in the current state of engines, which provides a high degree of technical informativeness during the interim period between the dates of conducting scheduled maintenance.

6. Conclusion

Monitoring the temperature of the circulating water in the cooling system and the lubricating oil pressure is a mandatory and critical requirement for the operation of a shipboard main diesel engine. Deviations from the nominal values of these parameters have a very direct impact on thermal stability, lubrication reliability, fuel efficiency, and the service life of the unit as a whole. A belated detection of deviations in these determining parameters from the normalized values, as well as ignoring such deviations, may lead to unpredictable emergency situations, such as a sudden shutdown (failure, damage) of the ship's powerplant.

Other operational parameters (related to the air intake system, fuel system, exhaust system, engine speed and power, fuel physicochemical properties, etc.) are not critical to the engine's ongoing operation, as changes in these parameters do not result in its unlooked-for shutdown. In this case, if necessary, the ship (boat) can suspend the execution of her combat mission and return to the home port to carry out urgent troubleshooting of these systems by force of the authorized maintenance and repair department.

The express method being proposed should be considered as an auxiliary source for the prompt evaluation of current information, which makes it possible to improve interaction between a ship's (boat's) crew and the maintenance and repair department regarding the current technical state of engines and making appropriate decisions on the possibility of further safe operation of the ship (boat) or the pressing need for performing the unscheduled maintenance and, consequently, her time-urgent return to the home port. In a sense, the constructed model of our express method acts as a kind of "safety net" against unexpected failures, which in practice makes it possible to prevent emergency situations and reduce the risk of sudden breakdowns of the shipboard mechanisms to zero.

The implementation of this express method significantly increases the responsibility of maintenance and repair departments, since the results of their troubleshooting and work as a whole can be quickly verified in practice, which ultimately contributes to an increase in the combat readiness of the ship (boat) before going to sea.

References

[1] Shull, Peter J., ed. (2002). Nondestructive Evaluation: Theory, Techniques, and Applications. *New York: Marcel Dekker, Inc*.

[2] Strelkovskaya, L. A. (2016). Selection of Information for Expert System of the Assessment of Technical Condition of the Ship Internal Combustion Engine in Use. *Information Technologies*, no. 1 (14), 320–328. http://en.crb.com.ua/nvksma/article/view/785/782. (in Russian)

[3] Tymkiv, A. V., and V. G. Denisoff. (2013). Methods and Ways of Diagnosing the Ship's Powerplant. *Ship's Powerplants*, 32, 113–123. http://seu.onma.edu.ua/wp-content/uploads/2020/09/2013_32_32_18_11_13.pdf. (in Russian)

[4] Saufi, S. R, Z. A. B. Ahmad, M. S. Leong, and M. H. Lim. (2019). Challenges and Opportunities of Deep Learning Models for Machinery Fault Detection and Diagnosis: A Review. *IEEE Access*, vol. 7: 122644–122662. https://ieeexplore.ieee.org/document/8819956.

[5] Cerquitelli, T., N. Nikolakis, N. O'Mahony, E. Macii, M. Ippolito, and S. Makris, eds. (2021). Predictive Maintenance in Smart Factories: Architectures, Methodologies, and Use-cases. Singapore: Springer Nature Singapore Pte Ltd.

[6] Budde, L., R. Hänggi, T. Friedli, and A. Rüedy. (2023). Smart Factory Navigator: Identifying and Implementing the Most Beneficial Use Cases for Your Company—44 Use Cases That Will Drive Your Operational Performance and Digital Service Business. Cham: Springer Nature Switzerland AG.

[7] Chen, X., S. Wang, B. Qiao, and Q. Chen. (2018). Basic Research on Machinery Fault Diagnostics: Past, Present, and Future Trends. *Frontiers of Mechanical Engineering*, 13, 264–291. https://link.springer.com/article/10.1007%2Fs11465-018-0472-3.

[8] Wysocki, J., and K. Witkowski. (2023). Increasing the Efficiency of Marine Engine Parametric Diagnostics Based on Analyses of Indicator Diagrams and Heat-Release Characteristics. *Energies*, 16(17): 6240. https://doi.org/10.3390/en16176240.

[9] Varbanets, R., D. Minchev, Y. Kucherenko, V. Zalozh, O. Kyrylash, and T. Tarasenko. (2024). Methods of Real-Time Parametric Diagnostics for Marine Diesel Engine. *Polish Maritime Research*, 3 (123), 71–84. https://doi.org/10.20998/0419-8719.2024.1.09.

[10] Chen, M., H. Gan, and H. Wu. (2024). Research on Fault Diagnosis Method for Marine Diesel Engines Based on Multi-Scale Attention Mechanism Transformer. *Journal of Marine Science and Engineering*, 12(12), 2348. https://doi.org/10.3390/jmse12122348.

[11] Peretiaka, N., K. Boriak, and O. Vatrenko. (2020). Improving the Thermal Method for Assessing the Technical Condition of Rolling Bearings Based on the Heating Rate Criterion. *Eastern-European Journal of Enterprise Technologies*, vol. 5, no. 1 (107): 118–126. https://doi.org/10.15587/1729-4061.2020.212540.

[12] Peretiaka, N. (2017). Analysis of Experimental Tests of Generator Drive Gearboxes from the Middle Part of the Axle of the Wheelset of Passenger Coach. *Collection of Scientific Papers of the Military Institute under Taras Shevchenko National University of Kiev*, no. 55: 81–92, https://miljournals.knu.ua/index.php/zbirnuk/article/view/196. (in Ukrainian)

[13] Oliynyk, K. A. (2021). General Requirements for Designing the Combat Ships and Boats of the Navy of the Ukrainian Armed Forces. *Maritime Strategy of the State. Development and Implementation of the Maritime Potential of Ukraine: Materials of International Scientific Forum*. Kiev: Ivan Cherniahovski National Defence University of Ukraine: 109–112. https://nuou.org.ua/nauka/confi/morska-strategya-derzhavi.-rozvitok-ta-realzaczya-morskogo-poten.html. (in Ukrainian)

[14] Boriak, K., and O. Ihnatenko. (2024). An Express Method of Forecasting the Development of Degradation Processes in Ship's Mechanisms Using Current Information through On-board Instruments. *Proceedings of Odesa Polytechnic University, Issue 2(70), 131-142*. https://doi.org/10.15276/opu.2.70.2024.15.

[15] Operating Instructions: Diesel Engine 20V4000M93x, MS150048/05E. (2018). MTU Friedrichshafen GmbH.

[16] Caterpillar Inc. Website: https://www.caterpillar.com. (Accessed on September 16, 2025)

Визначення критичних значень параметрів для практичного застосування експрес-методу діагностики технічного стану суднових дизельних двигунів

Костянтин Боряк, Олександр Ігнатенко

Інститут Військово-морських сил Національного університету “Одеська морська академія”,
вул. Дідріхсона, 8, м. Одеса, 65029, Україна

Анотація

У цій статті обґрунтовується технічна можливість та доцільність розробки нового експрес-методу діагностики стану дизельних двигунів бойових катерів на основі аналізу показань бортових приладів інформаційної системи керування та стеження за силовою установкою катера. Цей експрес-метод дозволить екіпажам бойових катерів (кораблів) використовувати прогнозне обслуговування суднових механізмів для швидкого виявлення деградаційних процесів під час експлуатації та мінімізації ризику непередбачених відмов (поломок) при виконанні бойових завдань. Суть нового методу полягає в побудові моделі діагностування суднового машинного обладнання на основі аналізу емпіричних критеріїв швидкостей зміни поточних значень визначальних параметрів у виділених часових діапазонах під час прогріву двигунів. В результаті натурних випробувань були визначені визначальні параметри та встановлені їх граничні нормалізовані швидкості зміни, перевищення яких може призвести до аварійних ситуацій.

Ключові слова: судновий дизельний двигун; визначальний параметр; режим прогріву; поточні значення.

ENERGY ENGINEERING AND CONTROL SYSTEMS

Volume 11, Number 2, 2025

Infrared Thermography for Diagnostics of Railway Infrastructure Elements

Maksym Silnyk*, Vasyl Fedynets

Lviv Polytechnic National University, 12 S. Bandery St., Lviv, 79013, Ukraine

Received: October 14, 2025. Revised: November 25, 2025. Accepted: December 02, 2025.

Abstract

The paper presents research results on the application of infrared thermography for diagnostics of machines and devices in railway infrastructure. The theoretical foundations based on Fourier's heat conduction equation are outlined and the principles of designing an automated diagnostic system using thermal cameras, a data processing server, and machine learning algorithms are described. Examples of thermograms and graphs illustrate the detection of defects in cable connections, rail joints and turnout drives. Experimental studies confirmed that infrared diagnostics ensure high accuracy, speed and reliability in detecting hidden faults that remain unnoticed by traditional inspection methods. An economic analysis demonstrated a reduction in maintenance costs by up to 65% and a 67% decrease in train downtime. The obtained results prove the feasibility and effectiveness of implementing infrared thermographic systems in the maintenance practice of Ukrainian railways to enhance operational safety and optimize maintenance expenses.

Keywords: infrared thermography; railway infrastructure; diagnostics; non-destructive testing; thermal imaging camera.

1. Introduction

Infrared thermography (IRT) is a modern non-destructive testing (NDT) method that allows for the evaluation of surface temperature fields of objects in a non-contact manner. Its application in railway transport includes the diagnostics of turnout mechanisms, cable connections, rail joints, and signaling and interlocking (S&C) equipment.

In Ukraine, the relevance of this approach is determined by the high wear of infrastructure, the frequency of failures, and the insufficient level of automation in diagnostics [1], [2], [6]. The main purpose of implementing IRT is the timely detection of defects, reduction of emergency situations and optimization of maintenance costs.

International experience demonstrates that in the Federal Republic of Germany (Deutsche Bahn), infrared control is actively used to prevent overheating in drives and transformers; in Japan (JR East) – to monitor cable routes and high-speed switch mechanisms; and in the United States (Amtrak, BNSF) – to inspect the contact network and power cabinets [4], [8].

2. Analysis of literature and regulatory documents

The topic of infrared thermography is actively covered in international journals. In the Sensors journal, several review papers have been published that systematize the methods of passive and active thermography [6]. Infrared Physics & Technology presents studies on new algorithms for processing infrared camera signals [2]. IEEE Transactions on Instrumentation and Measurement highlights examples of practical applications in transport

---

[*] Corresponding author. Email address: maksym.y.silnyk@lpnu.ua

This paper should be cited as: M. Silnyk, V. Fedynets. (2025). Infrared thermography for diagnostics of railway infrastructure elements. *Energy Engineering and Control Systems*, Vol. 11, No. 2, pp. 151 – 156. https://doi.org/10.23939/jeecs2025.02.151

infrastructure [4], [5]. Additionally, standards such as ISO 18434-1, ISO 18436-7, and ASTM E1933 define the requirements for camera calibration, emissivity measurement, and interpretation of results [9], [10].

3. Purpose of the study

The main objective of implementing IRT is the timely detection of defects, reduction of emergency situations, and optimization of maintenance costs. The method combines speed, safety and high accuracy in identifying hidden defects, making it a promising tool for integration into automated control systems.

4. Theoretical background

The theoretical basis of infrared thermography is the Fourier heat conduction equation [1], [7]:

$$q = -\lambda \cdot \mathrm{grad}(T), \tag{1}$$

where q is the heat flux vector; λ is the thermal conductivity coefficient; $\mathrm{grad}(T)$ is the temperature gradient.

For railway elements (rail joints, cable connections), overheating can be estimated using the simplified formula [1], [7]:

$$\Delta T = (I^2 \cdot R \cdot t) / (m \cdot c), \tag{2}$$

where I is the current; R is the contact resistance; t is time; m is the material mass; c is the heat capacity.

Figure 1 shows an example of temperature field distribution modeling in a node with increased contact resistance.

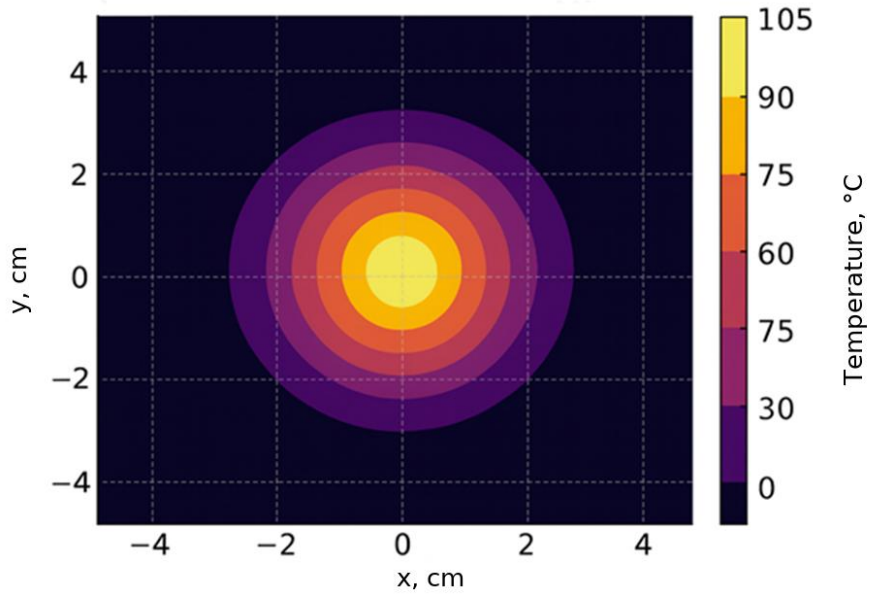

Fig. 1. Temperature field distribution.

5. Methodology

The proposed methodology involves constructing an automated diagnostic system consisting of a thermal imager, a preprocessing unit, a server, and machine-learning algorithms (see Table 1). The general workflow of the system is illustrated in Figure 2.

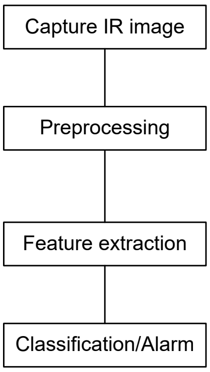

Fig. 2. Algorithm of the diagnostic system operation.

Table 1. Equipment used in the diagnostic system

Component	Model / Characteristics
Thermal imager	FLIR E95, 464×348 pixels, range −20…+650 °C
Optical lens	42° FOV
Server	Intel Xeon, 32 GB RAM, SSD 1 TB
Software	MATLAB, Python (OpenCV, TensorFlow)

6. Research results

Experimental measurements have demonstrated the effectiveness of infrared diagnostics for various objects of railway infrastructure. The obtained thermograms make it possible to detect hidden defects that cannot be identified using traditional methods.

In the thermogram (Fig. 3), localized areas of increased temperature can be observed, indicating the presence of thermal anomalies in the investigated unit. The maximum temperature in the center of the area reaches approximately 100 °C, while the peripheral region has a temperature of about 30 °C.

The color scale on the right illustrates the temperature range from 20 °C (violet tones) to 100 °C (yellow tones). The X-axis represents the geometric position of the element (mm), and the Y-axis shows the height coordinate (mm). Thus, the figure reflects the spatial temperature distribution on the surface of the object.

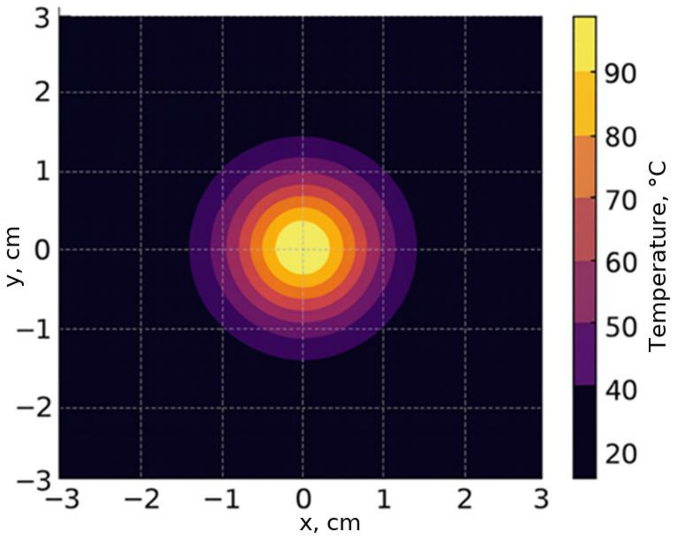

Fig. 3. Thermogram of cable connection.

In the thermogram, local overheating zones are visible, indicating increased contact resistance or insulation defects. Such areas are potentially hazardous and may lead to equipment failures.

The temperature–time dependence for the control point is shown in Fig. 4.

From the graph, it is evident that the temperature changes cyclically: during the first 20 minutes, heating up to approximately 40 °C is observed, followed by cooling down to about 15 °C, and then a subsequent rise again.

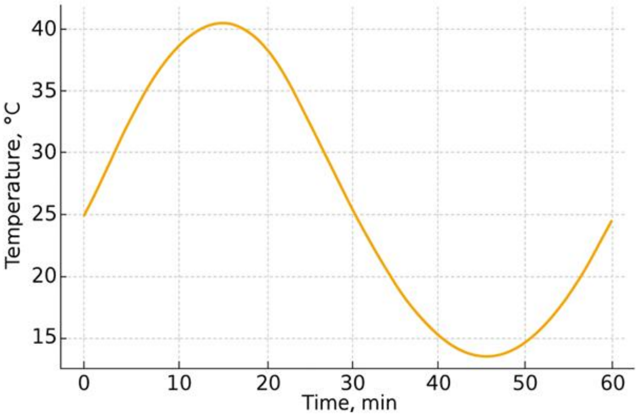

Fig. 4. Temperature vs time dependency during operational testing.

The temperature–time graph shows a gradual increase in the average temperature level with superimposed fluctuations. This indicates the presence of both periodic loads and a long-term trend toward overheating. A comparison of parameters for different objects is presented in Table 2.

Table 2. Comparison of parameters for different objects.

Object	Normal temperature, °C	Anomaly temperature, °C	Comment
Turnout mechanism	up to 40	60–80	Drive overheating
Cable connection	up to 35	55–70	Poor contact
Rail joint	up to 45	65–85	Increased resistance

7. Economic Effect

The results of the economic analysis are given in Table 3, and the graphical representation of the cost difference is shown in Fig. 5.

Economic analysis demonstrates a significant difference between traditional diagnostic methods and the implementation of infrared control [1], [2], [4]. Inspection costs are reduced by 2–3 times, while additional savings are achieved through decreased train downtime and fewer emergency repairs.

Table 3. Comparison of diagnostic methods and cost savings.

Parameter	Traditional methods	IR diagnostics	Savings
Average inspection cost per object (UAH)	2000	700	65 %
Inspection time per object	≈ 3 hours	10–20 min	–
Repair cost per object (UAH)	≈ 50 000	≈ 20 000	60 %
Train downtime due to failures (hours / year)	≈ 120	≈ 40	− 67 %

As shown in Table 3, the application of infrared diagnostics makes it possible to reduce the average inspection costs per object by 65%, decrease rolling stock downtime by more than 67%, and lower repair expenses by over 60%, providing a significant economic effect from the implementation of the method.

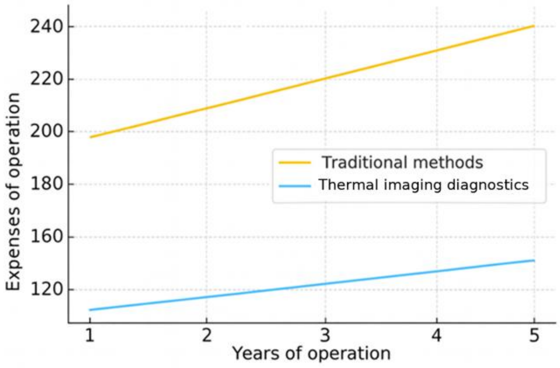

Fig. 5. Comparison of expenses of traditional methods and IR diagnostics.

8. Conclusion

This research substantiates the feasibility of using infrared thermography for the diagnostics of railway infrastructure elements. A methodology for developing an automated monitoring system has been proposed, experimental studies have been conducted, and an economic analysis has been performed.

Key findings:

- IR diagnostics provides high accuracy and speed in defect detection;
- The use of an automated system reduces maintenance and repair costs by 2–3 times;
- Implementation of the system enhances train safety and minimizes downtime;
- The results correspond to the international experience and can be adapted to Ukrainian conditions.

References

[1] X. Maldague. (2001). Theory and Practice of Infrared Technology for Nondestructive Testing. *Wiley*, 704 p. doi:10.1002/9781118211568

[2] A. Bagavathiappan et al. (2013). Infrared thermography for condition monitoring – A review. *Infrared Physics & Technology*, 60, 35–55. doi:10.1016/j.infrared.2013.03.006

[3] S. Vidas, P. Moghadam. (2013). HeatWave: A Hand-Held 3D Thermography System for Energy Auditing. *Energy and Buildings*, 66, 445–460. doi:10.1016/j.enbuild.2013.07.008

[4] Z. Chen et al. (2020). Railway infrastructure defect detection using infrared thermography and deep learning. *IEEE Access*, 8, 128485–128497. doi:10.1109/ACCESS.2020.3008652

[5] G. Rilling, P. Flandrin and P. Goncalves. (2003). On empirical mode decomposition and its algorithms. *IEEE-EURASIP Workshop on Nonlinear Signal and Image Processing*, Grado, Italy. doi:10.1109/NOLISP.2003.1216789

[6] M. Usamentiaga et al. (2014). Infrared thermography for temperature measurement and non-destructive testing. *Sensors*, 14(7), 12305–12348. doi:10.3390/s140712305

[7] P. J. Shull. (2002). Nondestructive Evaluation: Theory, Techniques, and Applications. *CRC Press*, 876 p. doi:10.1201/9780203909133

[8] Y. Park, J. H. Lee and S. Hong. (2017). Application of infrared thermography for railway track inspection. *NDT & E International*, 92, 60–70. doi:10.1016/j.ndteint.2017.08.001

[9] ASTM E1933-14, Standard Test Methods for Measuring and Compensating for Emissivity Using Infrared Imaging Radiometers, ASTM International, 2014. doi:10.1520/E1933-14

[10] ISO 18436-7, Condition Monitoring and Diagnostics of Machines – Requirements for Qualification and Assessment of Personnel – Part 7: Thermography, ISO, 2014.

Інфрачервона термографія для діагностики елементів залізничної інфраструктури

Максим Сільник, Василь Фединець

Національний університет «Львівська політехніка», вул. С. Бандери, 12 , Львів, 79013, Україна

Анотація

В статті представлено результати дослідження ефективності застосування інфрачервоної термографії для діагностики машин і пристроїв залізничної інфраструктури. Розкрито теоретичні основи методу, що базуються на рівнянні теплопровідності Фур'є та описано принципи побудови автоматизованої системи контролю з використанням тепловізійних камер, серверного модуля обробки та алгоритмів машинного навчання. Наведено приклади термограм і графіків, які ілюструють роботу системи під час виявлення дефектів у кабельних з'єднаннях, рейкових стиках і стрілочних переводах. Проведено експериментальні дослідження, результати яких підтвердили, що інфрачервона-діагностика забезпечує високу точність, швидкість обстеження та виявлення прихованих дефектів, недоступних для традиційних методів. Економічний аналіз засвідчив зниження витрат на обслуговування до 65 % і скорочення простоїв поїздів на 67 %. Отримані результати доводять доцільність впровадження інфрачервоних-технологій у практику технічного обслуговування українських залізниць.

Ключові слова: інфрачервона термографія; залізнична інфраструктура; діагностика; неруйнівний контроль; тепловізійна камера.

ENERGY ENGINEERING AND CONTROL SYSTEMS

Volume 11, Number 2, 2025

Fuzzy Control Model with Automated Rule Base Generation for Artillery Systems in Game Simulators

Oleksiy Kozlov[a,*], Oleksiy Maksymov[b], Maksym Maksymov[c], Ruslan Riaboshapka[c]

[a]Petro Mohyla Black Sea National University, 10, 68th Desantnykiv St., Mykolaiv, 54003, Ukraine
[b]National University "Odesa Maritime Academy", 8 Didrikhson St., Odesa, 65029, Ukraine
[c]Odesa Polytechnic National University, Shevchenka Ave., 1 Odesa, 65044, Ukraine

Received: October 07, 2025. Revised: November 12, 2025. Accepted: November 19, 2025.

Abstract

This paper presents the development and validation of a fuzzy control model with automated rule base generation for artillery system actuators in game simulators. The proposed model integrates a bioinspired optimization mechanism based on the ant colony algorithm, enabling the automatic synthesis of efficient rule bases without relying on expert knowledge. This approach ensures adaptability and autonomy under uncertain conditions and provides logical transparency, allowing detailed analysis of control strategies. The model can be employed to simulate the decision-making behavior of virtual allies or adversaries, representing their different skill levels by adjusting reference models and objective functions at the design stage, thereby enhancing the realism in combat scenarios simulation. Experimental studies conducted on the example of an electric drive simulation model responsible for artillery mount barrel elevation demonstrated the superiority of the fuzzy model over a traditional PD controller in terms of robustness, efficiency and accuracy. The methodology presented in this paper can also be applied to hydraulic and other types of actuators.

Keywords: game simulators; artillery systems; fuzzy control model; rule base generation; actuator model.

1. Introduction

In the context of twenty-first century warfare, the rapid proliferation of unmanned aerial vehicles (UAVs) has profoundly transformed reconnaissance, surveillance, and precision strike capabilities. Nevertheless, artillery continues to occupy a central role as one of the most decisive instruments of firepower on the battlefield [1]. Its capacity to deliver sustained, large-scale, and comparatively cost-effective destructive force ensures that it remains indispensable for neutralizing enemy positions, disrupting logistical lines, and providing both offensive and defensive support. Unlike UAVs, which often depend on sophisticated communication infrastructures and are vulnerable to electronic countermeasures, artillery systems maintain their relevance through robustness, operational reliability, and their ability to operate effectively in a wide range of tactical and operational conditions [2].

At the same time, modern high-intensity, technologically advanced combat environments impose exacting demands on artillery employment that transcend traditional paradigms of massed fire [3]. Contemporary operations require pinpoint engagement of threat elements with minimal ammunition expenditure, a significant reduction in time-to-target and in the duration of exposure within firing positions, and the capacity to sustain high sortie rates under contested, degraded conditions. These operational imperatives, compounded by accelerated fatigue and premature wear of mechanical, electromechanical, and electronic subsystems, render conventional, manually tuned

---

[*] Corresponding author. Email address: kozlov_ov@ukr.net

This paper should be cited as: O. Kozlov, O. Maksymov, M. Maksymov, R. Riaboshapka. (2025). Fuzzy control model with automated rule base generation for artillery systems in game simulators. *Energy Engineering and Control Systems*, Vol. 11, No. 2, pp. 157 – 168. https://doi.org/10.23939/jeecs2025.02.157

procedures insufficient. Accordingly, there is an urgent need for novel algorithmic frameworks and mathematical models that provide real-time control, adaptive correction, and predictive diagnostics at multiple hierarchical levels: from sensors, actuators, and individual weapon components to coordinated fire units, batteries, and integrated fire-support systems. Such methods must reconcile stringent constraints on lethality, survivability, and logistical economy while enabling autonomous or semi-autonomous decision-support that is robust to uncertainty, component degradation, and adversarial interference.

A similar tendency can be observed in the field of game simulators development [4]. The demand for achieving maximum realism in the operation of combat vehicles, including artillery systems, under complex and rapidly changing conditions necessitates the application of sophisticated mathematical models and control algorithms. Conventional simplified approaches are no longer adequate to capture the dynamic and uncertain nature of modern battlefield processes. At the same time, the growing role of training, decision support, and operational analysis within virtual environments increases the requirements for accuracy, adaptability, and intelligence in simulation models. In this context, the application of intelligent control models and techniques, encompassing adaptive, data-driven and knowledge-based approaches, emerges as one of the most promising directions [5]. The search for effective approaches to building such models, particularly those based on fuzzy logic and capable of generating and refining rule bases, constitutes the subject of the present study.

2. Literature sources analysis

Contemporary scientific research offers a wide spectrum of advanced computational approaches, mathematical models, and information technologies designed to enhance the precision of artillery fire, improve the prediction of projectile trajectories, and increase the overall reliability of operation, alongside other critical performance characteristics of artillery systems [6], [7]. At the same time, considerable progress has been achieved in the field of verification methodologies, which now make it possible to assess and diagnose the required properties of virtually all essential subsystems of artillery mounts and complexes, ranging from projectiles, charges, and munitions to the supporting logistical infrastructures, across every crucial stage of their life cycle [8], [9]. Furthermore, a significant portion of these methods and models has found successful application in the domain of game-based simulation, where they serve to improve realism and fidelity of virtual representations of artillery processes [10] – [12].

For example, the article [10] examines the tactical use of artillery in counter-amphibious operations across both deep- and shallow-water conditions, with a focus on game-based scenario modeling. Using mathematical models grounded in Markov chains and complementary simulation techniques, the study explores the balance between sustained fire support, resource efficiency, and artillery survivability. Several tactical approaches are analyzed, including ammunition-saving strategies, rapid neutralization methods, and hybrid solutions that adapt to specific battlefield conditions. The results demonstrate the advantages of the mixed method, which ensures operational flexibility and higher effectiveness in countering amphibious assaults.

In turn, the study [11] addresses the critical issue of artillery ammunition quality in modern warfare, with insights drawn from recent conflict experiences. The study develops optimized acceptance sampling algorithms that balance inspection efficiency, resource constraints, and operational reliability, taking into account the impracticality of full inspection. By tailoring sampling plans to different types of artillery missions, the approach ensures both high-quality munitions for destructive fire and efficient use of resources for suppressive operations. The results demonstrate that such strategies not only enhance safety and readiness in real combat but can also be effectively integrated into game-based simulations for greater realism.

The work [12] explores the gap between visual realism and limited scripting in military-themed computer games, focusing on artillery modeling in ARMA 3. The study introduces a shot verification method based on recording projectile flight times at control points and constructing parabolic approximations to predict impact accuracy. Simulation results show that this approach effectively compensates for random disturbances, reducing firing time and ammunition use compared to traditional ranging shots. The findings highlight the potential of integrating advanced artillery verification methods into game simulators for enhanced realism and tactical depth.

At the same time, modern scientific literature devotes comparatively little attention to a rather specific yet critical problem, namely, the control of individual actuators in artillery mounts to ensure precise aiming under the influence of uncertain and variable disturbances. Intensive operational regimes, premature wear, mechanical defects, and environmental factors such as overheating, strong winds, or electromagnetic interference can all lead to significant variations in drive parameters. These fluctuations undermine the effectiveness of conventional control systems with rigidly defined settings, ultimately reducing the accuracy and speed of barrel guidance. The resulting degradation manifests in longer mission execution times, prolonged exposure in firing positions, and increased probable circular error. To address these challenges, a number of studies have proposed the application of fuzzy control models, which have demonstrated the ability to improve both precision and responsiveness of aiming mechanisms [13] – [15]. This methodology also holds considerable promise for game simulators, as the mathematical apparatus of fuzzy logic provides a means of emulating human reasoning and integrating experiential knowledge into the operation of a virtual ally or adversary.

Nevertheless, the issue of generating a reliable fuzzy rule base remains largely unresolved: expert knowledge is not always available, its correct application may be limited, and manual rule formulation is susceptible to subjective bias and errors. In light of this, the present paper proposes an automated approach to rule base generation using a bioinspired optimization algorithm for the fuzzy control models of artillery systems' actuators in game simulators. Such a solution enables the simulator to emulate the presence of an experienced operator, while the ability to adjust the optimization objective function further allows the modeling of varying skill levels of virtual counterparts.

3. Objective and tasks of the research

The central objective of this research is the development of a fuzzy control model with automated rule base generation for the artillery systems' actuators within game simulation environments. In pursuit of this objective, the study sets out to address several key tasks: 1) the conceptual design of the fuzzy control model's structure; 2) the creation of an automated mechanism for rule base formation utilizing a bioinspired optimization algorithm; and 3) the experimental validation and performance assessment of the proposed fuzzy control model.

4. Model and methods

Basic aspects of constructing a fuzzy control model for artillery mount actuators. The principal tasks amenable to resolution with the proposed fuzzy-control architecture are the closed-loop regulation of gun-barrel elevation and the precise steering of azimuth during target engagement. To enact automatic regulation of either angular degree of freedom, the controller must be supplied with a commanded setpoint (e.g., desired elevation) and the corresponding instantaneous feedback measurement. The demanded setpoint is ordinarily computed by the fire-control subsystem on the basis of embedded ballistic models, which obtain target coordinates, the current emplacement position, atmospheric and environmental data, and other mission-relevant inputs. The actual angular state in physical mounts is obtained from position transducers (encoders, resolvers, etc.), whereas in a game simulation environment it is produced by the simulation model of the studied drive.

For generation of the control signal, the fuzzy regulator model operates on the angular error (the difference between commanded and measured angle) and on selected time derivatives or integrals of that error. A review of typical barrel-drive dynamics shows that these subsystems behave as non-self-stabilizing, predominantly integrating plants. Accordingly, effective closed-loop performance can be achieved using the error and its first time derivative alone. Introducing the error integral as an additional input seldom yields commensurate gains in positioning accuracy for such integrating objects, yet it can create undesirable phenomena – most notably integrator windup and degraded transient stability – unless additional anti-windup measures are implemented. Likewise, inclusion of higher-order derivatives amplifies sensitivity to measurement noise and imposes onerous requirements on filtering and signal conditioning. Therefore, a parsimonious input set comprising the angular error and its first derivative provides a pragmatic balance between control precision and robustness for both physical installations and their simulator counterparts. Therefore, the chosen control architecture will achieve significant efficiency and is quite simple to implement.

For the fuzzy inference engine, the Mamdani approach is the most appropriate choice, as it provides a high degree of interpretability and logical transparency [16]. This property is particularly valuable in game simulation environments, where clarity of decision-making is essential for modeling the behavior of virtual allies and adversaries. The Mamdani inference enables the construction of an explicit rule base expressed in the familiar "If–Then" format, where the consequents are formulated in terms of linguistic values assigned to the output variable. For example, for a model of fuzzy control of the barrel elevation angle φ, the rules of the rule base can be defined as follows:

$$\text{IF “}\varepsilon_{\varphi} = A_i\text{” AND “}\frac{d\varepsilon_{\varphi}}{dt} = B_j\text{” THEN “}u_{\varphi} = C_k\text{”,} \tag{1}$$

where ε_{φ} is the angle φ control error; u_{φ} is the calculated control signal; A_i is the i-th linguistic term from the set of terms for control error ε_{φ}, $i \in \{1,...,i_{\max}\}$; B_j is the j-th linguistic term from the set of terms for error's derivative $d\varepsilon_{\varphi}/dt$, $j \in \{1,...,j_{\max}\}$; C_k is the k-th linguistic term from the set of terms for control signal u_{φ}, $k \in \{1,...,k_{\max}\}$.

In this scheme, the number of rules and the structure of their antecedents are determined by the chosen linguistic partitions (the numbers $i_{\max}$ and $j_{\max}$) of the input variables, namely, the control error ε_φ and its time derivative $d\varepsilon_\varphi/dt$ [16]. These partitions can be defined at the initial design stage, which makes the subsequent formulation of the rule base a matter of assigning the most appropriate consequent to each input combination. The diversity of possible consequents depends directly on the number of linguistic terms $k_{\max}$ introduced for the output variable u_φ, also specified in advance. A finer partitioning with a larger number of terms yields greater flexibility and the potential for more sophisticated control strategies. However, it also increases the computational burden and complicates the synthesis process. Conversely, a minimal set of terms simplifies both design and implementation but limits smoothness and adaptability in control responses. Thus, effective model construction requires a balanced compromise, ensuring sufficient expressiveness without imposing excessive complexity on the rule base and its real-time execution.

For the automated synthesis of a fuzzy rule base, the generation mechanism must incorporate several essential stages: 1) the initial creation of the rules antecedents, 2) the assignment of valid consequents to every generated rule, and 3) the evaluation of the correctness and efficiency of the constructed rule base. The formation of the rules antecedents at the first stage can be performed in a straightforward manner by systematically enumerating all possible combinations of the linguistic terms selected for the input variables during the preliminary design phase [16].

The more challenging task lies in assigning suitable consequents to each rule. This can be formulated as a discrete optimization problem, where the set of consequents constitutes the vector of parameters to be optimized [16]. To solve this problem effectively, it is proposed to employ a computationally efficient bioinspired optimization algorithm, capable of navigating the discrete solution space and identifying the most appropriate consequents [17].

The quality of the resulting rule base must then be rigorously evaluated. This requires the definition of an objective function that quantifies the proximity of the control performance obtained from the fuzzy model to the desired performance characteristics. To ensure a comprehensive assessment, it is advisable to compare the examined control system with a reference model, which embodies the target properties such as accuracy, response speed, and stability. The chosen objective function simultaneously serves as a fitness function within the optimization process, being evaluated at each iteration of the bioinspired algorithm. Consequently, once the algorithm converges to a predefined optimal value of this fitness function, the synthesized rule base can be considered sufficiently effective, containing the most appropriate consequents for all generated rules [17].

Building upon the considerations outlined above, it is now possible to address the first key task of this research, namely the development of structure for the fuzzy control model intended for the actuators of artillery mounts.

Structure of the fuzzy control model for artillery mount actuators. Fig. 1 illustrates the structural framework of the fuzzy control model with automated rule base generation for artillery system actuators. The adopted designations and symbols are explained as follows: FCM is the fuzzy control model; FB is the fuzzification block; RB is the rule base; DFB is the defuzzification block; FIB is the fuzzy inference block; AGG, ACT, and ACC are the operators that perform aggregation, activation and accumulation procedures, respectively; MARBG is the mechanism of automated rule base generation; AGB is the antecedents generation block; CGB is the consequents generation block; RM is the reference model; OFCB is the objective function calculation block; BOA is the bioinspired optimization algorithm; SMAAM is the simulation model of the actuator of the artillery mount; DMB is the disturbance modeling block; φ_d and φ_c are the desired and current values of the actuator lifting (rotation) angle; ε_φ is the angle control error; $d\varepsilon_\varphi/dt$ is the error's derivative; u_φ is the FCM output signal; $\mathbf{A}_\varepsilon$, $\mathbf{B}_{d\varepsilon}$, and $\mathbf{C}_u$ are the vectors of linguistic terms used for the variables ε_φ, $d\varepsilon_\varphi/dt$, and u_φ, respectively; $\mathbf{X}_\mathrm{A}$ and $\mathbf{X}_\mathrm{C}$ are the vectors of RB antecedents and consequents; φ_m is the RM output; E_φ is the mismatch between the output of the reference model and the current value of the angle ($E_\varphi = \varphi_m - \varphi_c$); J_φ is the value of the objective function; $\mathbf{\Delta P}$ is the vector of changes in the parameters of the actuator model under the action of parametric disturbances; $\Delta\varphi$ is the change in angle under the action of coordinate disturbances.

In this framework, different types of actuator models, such as electric, hydraulic, or electrohydraulic drives, can be employed as SMAAM, each with its own degree of detail and complexity, depending on the fidelity required in the game simulator environments. To simplify the representation of external and internal disturbances, a dedicated DMB is incorporated. This block enables the emulation of various forms of uncertainty, ranging from parametric variations (vector $\mathbf{\Delta P}$) to fluctuations in the instantaneous coordinate ($\Delta\varphi$). For practical reasons, the control system's main feedback is organized with a coefficient equal to one, ensuring clarity and ease of modeling.

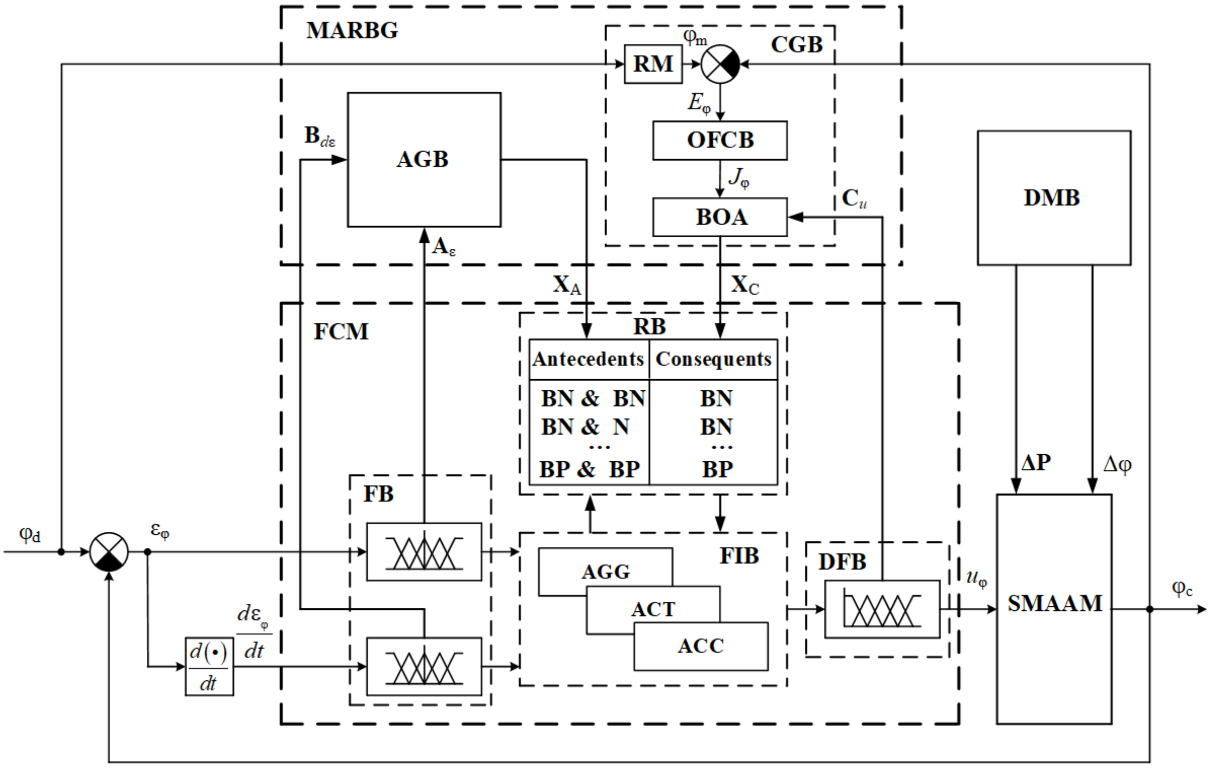

Fig. 1. Structure of the fuzzy control model with automated rule base generation for the artillery systems' actuators.

The FCM itself follows the classical Mamdani-type inference structure, encompassing all essential stages: fuzzification, aggregation, activation, accumulation, and defuzzification. Its rule base consists of conventional "If–Then" rules that connect antecedents with corresponding consequents. To automate the creation of this RB, a specialized mechanism for automated rule base generation is introduced, which is examined in detail below.

Mechanism of automated rule base generation utilizing a bioinspired optimization algorithm. The MARBG process unfolds in four distinct stages. The first stage is preliminary, where essential parameter adjustments and preparatory settings are carried out to ensure correct operation of the subsequent stages. The second stage focuses on generating rule antecedents, while the third stage addresses the generation of corresponding consequents, formulated as a discrete optimization task. Finally, the fourth stage, considered optional, is dedicated to fine-tuning the resulting model, allowing further enhancement of its quality indicators when required. This last step can be omitted if the system already demonstrates satisfactory performance.

Next, a detailed examination of each of the four stages is provided, with particular attention to their functional roles and interrelations within the overall mechanism.

Stage 1. Initial preparatory procedures. At the initial stage, a set of preparatory procedures must be carried out, without which the process of automated rule base generation cannot be initiated. First and foremost, it is necessary to define the linguistic terms for the two input variables ε_φ and $d\varepsilon_\varphi/dt$ of the fuzzy control model and for its output variable u_φ. Based on established methodological recommendations, the number of terms for input variables should generally range from three to seven, while for the output variable it is advisable to select between five and nine terms [18]. Once this choice has been made, the corresponding membership function forms are specified. The most commonly used and practically suitable options include Gaussian, triangular, or trapezoidal functions, depending on the desired trade-off between computational efficiency and approximation accuracy [19].

At the same stage, the selection of operators for the core inference procedures must be carried out. Typically, the "min" operator is employed for aggregation and activation, the "max" operator for accumulation, and the centroid method (center of gravity) for defuzzification, ensuring both transparency and interpretability of the inference process [19]. Additionally, normalizing coefficients are introduced (not shown in Fig. 1) in order to transform all input and output variables into relative units. For convenience, these coefficients are usually defined as the inverse of the maximum possible values of the corresponding variables [20]. Only after completing all these preliminary steps does it become possible to proceed to the subsequent stages, which involve the direct automated generation of the fuzzy rule base.

Stage 2. Generation of rule antecedents. The generation of rule antecedents is carried out in a fully automated manner by means of the AGB module, which operates on the previously defined vectors of linguistic terms $\mathbf{A}_{\varepsilon}$ and $\mathbf{B}_{d\varepsilon}$ for the input variables. At this stage, the structural framework of the rules as well as their antecedents vector $\mathbf{X}_{\mathrm{A}}$ are constructed by systematically generating all possible unique combinations of the selected terms, thereby ensuring complete coverage of the input space. As a result, the total number of rules is explicitly determined as the product of the number of linguistic terms associated with the first and second input variables. Once this exhaustive set of antecedents has been established, the process naturally advances to the subsequent stage, namely, the automated generation of appropriate consequents for each rule.

Stage 3. Generation of rule consequents. The automated generation of rule consequents is performed by the CGB module, which integrates a reference model, a comparison unit, an objective function evaluation block, and a bioinspired optimization algorithm. Within this framework, the entire set of consequents is represented as a vector $\mathbf{X}_{\mathrm{C}}$ of unknown parameters, thereby transforming the task into a discrete optimization problem. The dimensionality of this vector is equal to the total number of rules in the rule base, while each element of the vector is constrained to take values only from the set of linguistic terms $\mathbf{C}_{u}$ defined for the output variable.

For solving this optimization problem, the ant colony algorithm is proposed as an effective bioinspired method, all the details of which, as well as the features of application for rule base optimization are described in [17]. In this context, each iteration of the algorithm simulates the movement of artificial ants across a graph, where the nodes correspond to individual rules of the fuzzy rule base, and the edges represent the potential consequents associated with these rules. The search for the optimal solution is equivalent to identifying the shortest path in this graph, which corresponds to the most suitable vector of consequents yielding the minimal value of the objective function J_{φ}. During the iterative process, the algorithm consistently performs its key operations: traversal of nodes and edges by the ants, deposition of pheromone on the edges, as well as its evaporation and subsequent renewal, gradually decreasing the value of the objective function J_{φ}, ensuring convergence toward the optimal rule configuration. Before running the algorithm, it is also necessary to set the specific values of all its parameters as well as the desired value of the objective function $J_{\varphi\mathrm{d}}$, which serves as the benchmark to be approached throughout the optimization process [17].

In classical shortest-path problems addressed by the ant colony algorithm, the objective function is typically represented as the simple sum of traversed edges. In the present case, however, the situation is far more complex, as the optimization process is tightly coupled with the dynamic performance of the control system under investigation. The first critical step involves selecting an appropriate reference model against which the dynamic characteristics of the fuzzy-controlled system will be compared. Since, in the case of controlling the elevation (or rotational) angle of the gun barrel, the optimal transient response is characterized by an aperiodic nature (without overshoot or oscillations) and by the fastest possible settling time, it is appropriate to adopt transfer function (2) as the RM of the executive mechanism.

$$W_{\mathrm{RM}} = \frac{1}{\left(\tau_{\mathrm{RM}} s + 1\right)^{2}}, \tag{2}$$

where τ_{RM} is the desired time constant for the control process.

It is important to emphasize that, at this stage, by carefully selecting the type of reference model, tuning its parameters, and prescribing the desired value of the objective function, one can flexibly regulate the emulated proficiency level of the virtual operator. Consequently, depending on the intended scenario, whether high, medium, or low expertise, different forms of reference models, along with adjusted parameter values and objective function thresholds, can be employed to reproduce varying degrees of virtual control skill.

At the same time, specific considerations must be made for the modeling of the actuator itself. For instance, in the case of an electric drive, the generalized transfer function (3) can be employed as a representative model for carrying out the calculations.

$$W_{\mathrm{ED}} = \frac{K_{\mathrm{ED}}}{s\left(\tau_{\mathrm{ED1}} s^2 + \tau_{\mathrm{ED2}} s + 1\right)}, \tag{3}$$

where τ_{ED1} and τ_{ED2} are the drive time constants; K_{ED} is the drive gain.

To ensure the synthesis of a complete rule base capable of maintaining robust control performance under diverse conditions, it is essential to conduct simulations across a wide spectrum of operational scenarios. This includes transitions between different initial and final angular positions in both directions, exposure to various types of disturbances (step, impulse, and periodic), as well as systematic parameter variations across iterations. For example, with respect to the time constant τ_{ED1}, the DMB module modifies its value at the beginning of each simulation run in accordance with expression (4), thereby introducing variability into the process and ensuring that the resulting fuzzy control model retains its effectiveness under uncertain and dynamically changing conditions.

$$\tau_{\mathrm{ED1}} = \tau_{\mathrm{ED10}} + r_{\mathrm{ED1}}(n)\delta_{\tau 1}, r_{\mathrm{ED1}}(n) = \mathrm{rand}[-1,1], \tag{4}$$

where τ_{ED10} is the initial value of the time constant τ_{ED1}; r_{ED1} is the random number in the range from – 1 to 1 for the time constant τ_{ED1} at iteration n; $\delta_{\tau 1}$ is the maximum deviation of the time constant τ_{ED1}.

Other parameters of the model should be changed in a similar manner.

With regard to the objective function J_{φ}, its evaluation at each iteration must be performed on the basis of the deviation E_{φ} between the models' outputs, computed in accordance with expression (5).

$$J_{\varphi}(\mathbf{X}_{\mathrm{C}}) = \frac{1}{t_{\max}} \int_0^{t_{\max}} \left[\left(E_{\varphi}\right)^2 + k_1 \left(\frac{dE_{\varphi}}{dt}\right)^2 + k_2 \left(\frac{d^2 E_{\varphi}}{dt^2}\right)^2 \right] dt, \tag{5}$$

where $t_{\max}$ is the total time of all simulations in different modes in one iteration; k_1 and k_2 are the weighting coefficients for the corresponding derivatives of E_{φ}.

Incorporating not only the deviation E_{φ} itself but also its first and second derivatives makes it possible to penalize oscillatory behavior in the transient process, thereby ensuring smoother and more stable system dynamics.

Once the optimization procedure converges to the best vector of consequents $\mathbf{X}_{\mathrm{C}}$ and this solution is embedded into the fuzzy model, the construction of the rule base can be considered complete. At this point, the methodology advances to the final stage of the proposed approach.

Stage 4. Optional fine-tuning procedures. At the final stage, the optimization focuses on refining the parameters of the linguistic terms together with the adjustment of the normalizing coefficients, aiming to enhance the precision and overall efficiency of the control process. This procedure is applied selectively – only when the achieved quality indicators of the model require further improvement. If the system already exhibits stable and satisfactory performance, this step should be omitted.

Conversely, should the results remain inadequate even after completing all stages, including this one, it becomes necessary to return to the initial stage (Stage 1) in order to revise the fundamental settings, such as the number and configuration of linguistic terms, the choice of membership functions, or the selection of fuzzy inference operators.

Thus, the mechanism of automated rule base generation is formed, and the second of the key tasks of this study is solved. Proceeding further, we address the third key task, which involves carrying out a series of computational experiments aimed at substantiating the effectiveness and practical applicability of the proposed fuzzy control model.

5. Experiments

To evaluate the performance of the proposed fuzzy control model with automated rule base generation, a set of computational experiments was carried out in this study. The experiments were implemented on the basis of a simulation model of the gun barrel elevation electric drive, described by basic transfer function (6), which is suitable for using in game simulator environments.

$$W_{\mathrm{ED0}} = \frac{1.5}{s\left(0.21s^2 + 4.3s + 1\right)}. \tag{6}$$

In the course of simulation, both during the automated rule base generation and in subsequent verification experiments, the parameters of the considered transfer function were systematically varied according to the scheme analogous to formula (4). The maximum deviation δ for each parameter reached up to 50% of its nominal value. Additionally, the model incorporated the influence of coordinate disturbances of different types, thereby ensuring a more comprehensive assessment of the control system's robustness under diverse operating conditions.

In the course of synthesizing the fuzzy control model, the initial stage involved the definition of linguistic variables. Specifically, five terms (BN, SN, Z, SP, BP) were assigned to each input variable (ε_φ and $d\varepsilon_\varphi/dt$), while seven terms (VBN, BN, SN, Z, SP, BP, VBP) were chosen for the output variable u_φ. All linguistic terms were represented using triangular membership functions, whose vertices were arranged to guarantee an even partitioning of the full operational interval for all the variables. This configuration provides uniform coverage of the working domain, thereby ensuring consistency and accuracy in subsequent stages of fuzzy inference and rule base generation. Moreover, the "min" operator was employed for aggregation and activation, the "max" operator for accumulation, and the centroid method for defuzzification.

At the second stage of synthesis, the system automatically generated all possible unique pairwise combinations of the linguistic terms corresponding to the two input variables. As a result, a complete set of 25 distinct combinations was obtained, each of which served as the antecedent for one rule within the fuzzy knowledge base.

At the third stage, the consequents for each of the 25 previously generated rules were determined through the application of the ant colony optimization algorithm, configured with the following parameters: colony size – 25 ants; the number of elite ants – 15; pheromone deposition coefficient $\rho = 0.5$; weighting parameters $\alpha = 2$, $\beta = 1$; pheromone quantity factor $Q = 12$. The optimization process was guided by the objective function defined in expression (5). To emulate the behavior of a highly skilled virtual opponent or ally, the desired value of the objective function was set to 10, while expression (2) with a time constant $\tau_{\mathrm{RM}} = 0.5$ s was adopted as the reference model. As a result of the optimization process, by the 73rd iteration an efficient rule base was obtained, for which the value of the objective function reached 8.064, i.e., below the predetermined threshold. The generated rule base, reflecting the most effective set of consequents for all formed rules, is presented in Table 1.

Table 1. Generated rule base of the fuzzy control model for the artillery system's actuator.

		Linguistic terms for the angle error ε_φ				
		BN	SN	Z	SP	BP
Linguistic terms for the derivative of the angle error $d\varepsilon_\varphi/dt$	BN	VBN	VBN	BN	BP	VBP
	SN	VBN	VBN	SN	BP	VBP
	Z	VBN	BN	Z	BP	VBP
	SP	VBN	BN	SP	VBP	VBP
	BP	VBN	BN	BP	VBP	VBP

Since at the third stage the achieved value of the objective function was already lower than the specified threshold, the fourth stage of refinement was not applied in this study. To confirm the efficiency of the developed fuzzy control model, a set of transient response graphs is presented, illustrating its operation under various conditions. For comparative analysis, a conventional PD controller was also employed, with its coefficients optimized through parametric tuning by the gradient method, using the same reference model and objective function as in the proposed approach. The obtained coefficient values of the PD controller were $K_{\mathrm{p}} = 2.13$ and $K_{\mathrm{d}} = 3.42$. However, unlike the fuzzy model, the classical controller demonstrated substantially inferior performance, achieving only a minimal objective function value of 54.56, which is several times higher than the threshold and the result of the proposed solution.

Fig. 2 presents the transient response curves corresponding to the processes of barrel elevation and depression, obtained under the conditions defined by the parameters of transfer function (6). In this experiment, the simulations were performed without the influence of coordinate disturbances, thereby allowing a clearer assessment of the intrinsic dynamic characteristics of the control system.

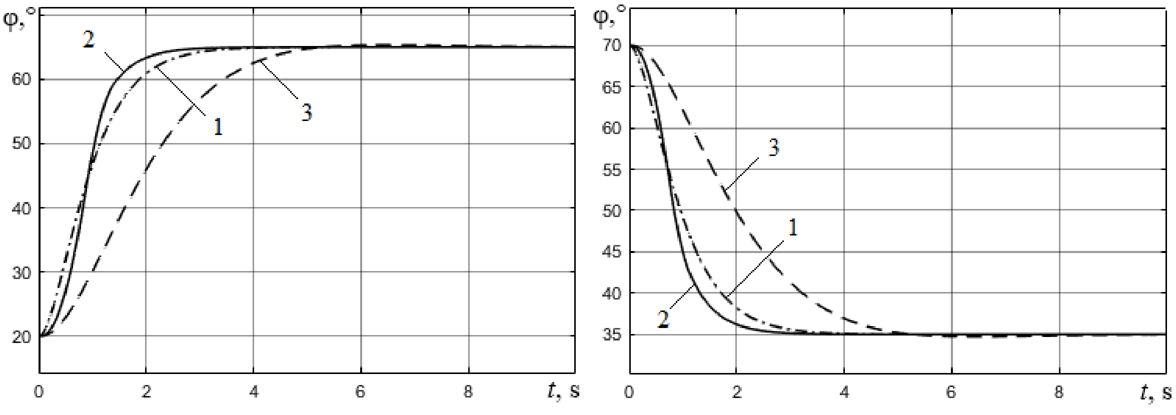

a *b*

Fig. 2. Transient response curves corresponding to the processes of barrel (a) elevation from 20° to 65° and (b) depression from 70° to 35° for: 1 – RM; 2 – proposed FCM; 3 – PD controller.

Subsequently, Fig. 3 illustrates the transient responses of gun barrel elevation obtained using the model parameters defined by transfer function (6), this time under the influence of step-type coordinate disturbances. These results make it possible to evaluate the robustness of the proposed fuzzy control model in conditions where sudden external perturbations affect the dynamics of the actuator. In Fig. 3, the step disturbances began to act at a time of 5 s.

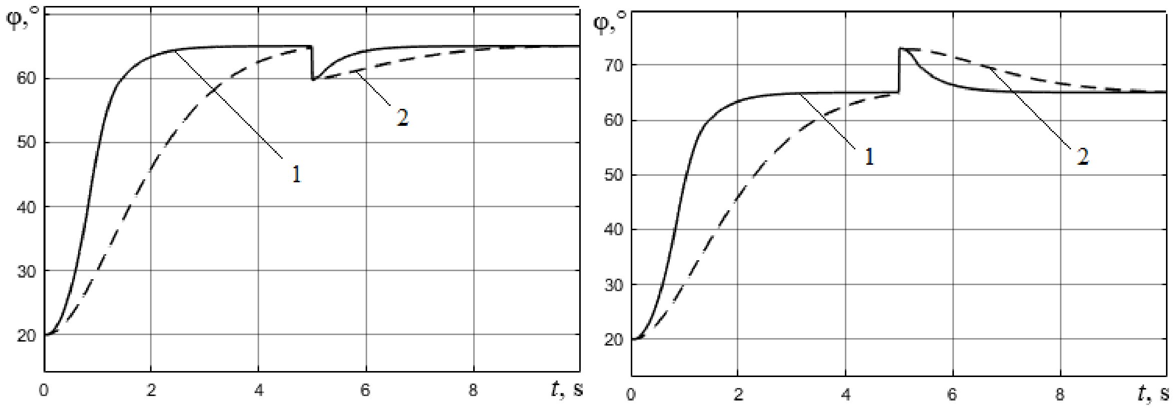

a *b*

Fig. 3. Transient response curves at barrel elevation from 20° to 65° under the action of (a) positive step disturbance of +5° and (b) negative step disturbance of –8° for: 1 – proposed FCM; 2 – PD controller.

In turn, Fig. 4 presents the transient responses of the gun barrel elevation and lowering when time constants of the system model are increased by 50% and the gain is reduced by 50% relative to the nominal values defined in transfer function (6). This experiment demonstrates the adaptability of the proposed fuzzy control model to significant parametric variations, thereby confirming its effectiveness under conditions of pronounced model uncertainty.

Moreover, Fig. 5 presents the transient responses of the gun barrel elevation and lowering when time constants of the system model are reduced by 50% and the gain is increased by 50% relative to the nominal values of the transfer function (6). This experiment also demonstrates the adaptability of the proposed fuzzy control model to parametric disturbances.

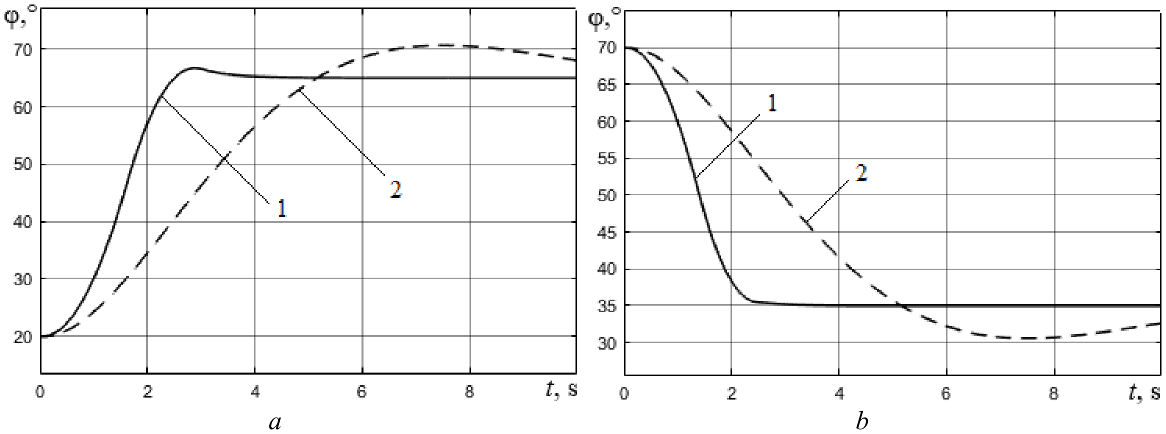

a *b*

Fig. 4. Transient response curves at increasing time constants by 50% and reducing gain by 50% for the processes of barrel (a) elevation from 20° to 65° and (b) depression from 70° to 35° for: 1 – proposed FCM; 2 – PD controller.

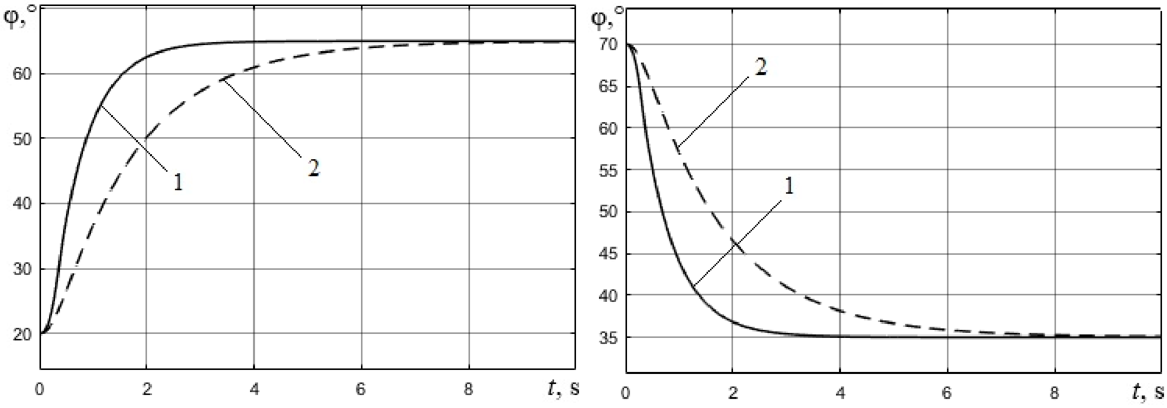

a *b*

Fig. 5. Transient response curves at reducing time constants by 50% and increasing gain by 50% for the processes of barrel (a) elevation from 20° to 65° and (b) depression from 70° to 35° for: 1 – proposed FCM; 2 – PD controller.

Furthermore, in order to explicitly demonstrate the robustness characteristics of the synthesized fuzzy control model, Table 2 summarizes the outcomes of a series of computational experiments performed under variations of the actuator simulation model parameters. In particular, the table reports the response time t_r and overshoot σ values obtained for different parameter configurations, since these indicators represent the most essential criteria for evaluating the quality and reliability of the control process. For brevity, Table 2 provides only the results of simulations for upward barrel movement, as in the case of lowering, the quality indicators were consistently superior across all experimental conditions.

Table 2. Results of computational experiments performed under variations of the actuator simulation model parameters.

Experiment number	Parameters of the actuator simulation model			Quality indicators for FCM		Quality indicators for PD controller	
	τ_{ED1}, s	τ_{ED2}, s	K_{ED}	t_r, s	σ, %	t_r, s	σ, %
1	0.21	4.3	1.5	1.81	0	3.87	0.615
2	0.315	6.45	0.75	2.26	2.615	10.02	8.77
3	0.105	2.15	2.25	1.56	0	4.45	0
4	0.217	3.2	1	1.69	0	4.21	0.32
5	0.3	5.7	0.9	2.08	0	8.24	6.08

As follows from the data presented in Table 2, the fuzzy control model demonstrates a high degree of robustness to parameter variations of the actuator simulation model. Even under the most unfavorable conditions (when the time constants were increased by 50% and the transmission coefficient was reduced by half) the system response time increased by only 25%, with a minor overshoot of 2.615%. In all other scenarios, the performance degradation was negligible, and overshoot remained absent, confirming the stability and reliability of the proposed model. By contrast, the traditional PD controller exhibited substantially inferior performance: in the worst case, the response time nearly tripled and overshoot reached almost 9%, which poses a serious risk in practical artillery guidance scenarios. Moreover, the PD-based system handled step coordinate disturbances far less effectively (Fig. 3).

The obtained results convincingly demonstrate the high efficiency of the proposed fuzzy model in controlling the actuators of artillery mounts within game simulator environments. These findings validate the adequacy of the developed approach and its ability to ensure both stability and robustness under varying operating conditions. Consequently, the third and final research task is successfully solved.

6. Conclusion

In this study, a fuzzy control model with automated rule base generation for artillery system actuators in game simulators has been developed and comprehensively investigated. The proposed architecture incorporates a mechanism for automated rule base synthesis based on a bioinspired optimization approach, namely the ant colony algorithm, which enables the construction of highly efficient rule bases even in the absence of expert knowledge or under conditions where manual rule formulation is impractical or error-prone. This feature ensures adaptability and autonomy of the control system, making it particularly valuable in complex and uncertain environments.

The model demonstrates considerable potential for application in game simulators, where it can be employed to emulate the decision-making logic of virtual allies or adversaries, thereby enhancing the realism of simulated combat scenarios. By adjusting the parameters of the reference model and the objective function during the optimization process, it becomes possible to reproduce different levels of operator proficiency, ranging from novice to expert. This property also highlights the model's value as a training tool, as it allows operators to observe and analyze effective control strategies in diverse tactical situations. Unlike neural network–based player models, fuzzy models possess high degree of logical transparency, enabling direct study and analysis of their control strategies.

Experimental validation, carried out on the example of an electric drive simulation model responsible for artillery barrel elevation, confirmed the practical effectiveness of the approach. When benchmarked against a traditional PD controller, the proposed fuzzy model exhibited superior performance, maintaining robustness under random parameter variations of the drive model as well as under the influence of external disturbances. These results confirm the high efficiency, adaptability, and resilience of the developed model in comparison to conventional control solutions.

Finally, it should be emphasized that the scope of application of the presented model is not limited to electric drives. With appropriate adaptation of simulation models, the proposed fuzzy control model can be effectively extended to other types of artillery actuators, including hydraulic and electrohydraulic systems, thereby broadening its relevance and applicability to a wide range of technical and simulation environments.

References

[1] N. Świętochowski. (2024). Field Artillery in the defensive war of Ukraine 2022-2023. Part II. Methods of task implementation. *SJMULF*, Vol. 211(1), pp. 57-76. https://doi.org/10.5604/01.3001.0054.4136

[2] V. Bartulović, Z. Trzun, M. Hoić. (2023). Use of Unmanned Aerial Vehicles in Support of Artillery Operations. *Strategos*, Vol. 7 (1), pp. 71–92. 10.1007/s00371-023-02940-9

[3] M. Khalil. (2022). Study on modeling and production inaccuracies for artillery firing. *Archive of mechanical engineering*, Vol. 69, No. 1, pp. 165–183. https://journals.pan.pl/Content/121939/PDF/AME_2022_139802_2.pdf

[4] V.E. Demydenko, M.V. Maksymov, V.O. Boltenkov. (2024). Combat operations model of a single self-propelled artillery system for the computer game ARMA 3. *Applied Aspects of Information Technology*, Vol. 7, No. 3, pp. 207–218. https://doi.org/10.15276/aait.07.2024.14

[5] M. Kutyło, M. Pluciński, M. Laskowska. (2015). Application of the reinforcement learning for selecting fuzzy rules representing the behavior policy of units in RTS-type games. *PRZEGLĄD ELEKTROTECHNICZNY*, Vol. 91(2), pp. 142-146. https://doi.org/10.15199/48.2015.02.33

[6] Y. Sun, et al. (2022). Research on a Simulation Algorithm for Artillery Firepower Assignment According to Region. *3rd International Conference on Computer Science and Management Technology (ICCSMT)*, Shanghai, China, pp. 353-356. https://ieeexplore.ieee.org/document/10143885

[7] M. Mady, M. Khalil, M. Yehia. (2020). Modelling and production of artillery firing-tables: case-study. *Journal of Physics: Conference Series*, No. 1507 (8), pp. 082043. https://iopscience.iop.org/article/10.1088/1742-6596/1507/8/082043/meta

[8] V. Boltenkov, et al. (2021). Devising a method for improving the efficiency of artillery shooting based on the Markov model. *Eastern-European Journal of Enterprise Technologies*, Vol. 6, No. 3 (114), pp. 6–17. https://papers.ssrn.com/sol3/papers.cfm?abstract_id=4007265

[9] O.B. Maksymova, et al. (2023). Development and Optimization of Simulation Models and Methods for Controlling Virtual Artillery Units in Game Scenarios. *Herald of Advanced Information Technology*, Vol. 6, No. 4, pp. 320–337. https://doi.org/10.15276/hait.06.2023.21

[10] M. Grishyn, et al. (2025). Development of methods of artillery control for suppression of an enemy amphibious operation in video game simulations. *Technology Audit and Production Reserves*, Vol. 1(2(81), pp. 26–33. https://doi.org/10.15587/2706-5448.2025.321797

[11] O. Toshev, et al. (2025). Optimization of ammunition preparation strategies for modern artillery operations in computer simulation. *Technology Audit and Production Reserves*, Vol. 2(2(82), pp. 50–57. https://doi.org/10.15587/2706-5448.2025.326225

[12] M.V. Maksymov, et al. (2023). Verification of artillery fire under the influence of random disturbances for the computer game ARMA 3. *Applied Aspects of Information Technology*, Vol. 6, No. 4, pp. 362–375. https://doi.org/10.15276/aait.06.2023.24

[13] N. Peng, Y. Bai, H. Luo, J. Bai. (2013). Artillery Position Control through Auto Disturbance Rejection Controller Based on Fuzzy Control. *5th International Conference on Intelligent Human-Machine Systems and Cybernetics*, Hangzhou, China, pp. 496-499, doi: 10.1109/IHMSC.2013.124

[14] J. Y. Bae, Y. Badr, A. Abraham. (2009). A Takagi-Sugeno Fuzzy Model of a Rudimentary Angle Controller for Artillery Fire. *11th International Conference on Computer Modelling and Simulation*, Cambridge, UK, pp. 59-64, doi: 10.1109/UKSIM.2009.105

[15] Y. Zhou, C. Pan. (2010). A control method for the naval artillery servo system based on the grading fuzzy sliding mode control with the interference observer. *2nd International Conference on Advanced Computer Control*, Shenyang, China, pp. 83-87, doi: 10.1109/ICACC.2010.5487053

[16] O.V. Kozlov, Y.P. Kondratenko. (2021). Bio-Inspired Algorithms for Optimization of Fuzzy Control Systems: Comparative Analysis. *"Advanced Control Systems: Theory and Applications", Series in Automation, Control and Robotics*, Yuriy P. Kondratenko, Vsevolod M. Kuntsevich, Arkadiy A. Chikrii, Vyacheslav F. Gubarev (Eds.), River Publishers, Denmark, pp. 83-128. doi: 10.1201/9781003337010-5

[17] Y.P. Kondratenko, O.V. Kozlov. (2019). Generation of Rule Bases of Fuzzy Systems Based on Modified Ant Colony Algorithms. *Journal of Automation and Information Sciences*, Volume 51, Issue 3, pp. 4-25. DOI: 10.1615/JAutomatInfScien.v51.i3.20

[18] O.V. Kozlov, et al. (2022). Fuzzy Systems Design: Optimal Selection of Linguistic Terms Number. *"Recent Developments in Automatic Control Systems", Series in Automation, Control and Robotics*, Yuriy P. Kondratenko, Vsevolod M. Kuntsevich, Arkadiy A. Chikrii, Vyacheslav F. Gubarev (Eds.), River Publishers, Gistrup, Denmark, pp. 197-239. https://doi.org/10.1201/9781003339229-11

[19] Y. Kondratenko, D. Simon. (2018). Structural and parametric optimization of fuzzy control and decision making systems. Recent developments and the new direction in soft-computing foundations and applications. *Selected Papers from the 6th World Conference on Soft Computing*. Berkeley, USA, 2016. Series: Studies in Fuzziness and Soft Computing. 361. Springer International Publishing. pp. 273-289. https://doi.org/10.1007/978-3-319-75408-6_22

[20] O.V. Kozlov, Y.P. Kondratenko, O.S. Skakodub. (2022). Information Technology for Parametric Optimization of Fuzzy Systems Based on Hybrid Grey Wolf Algorithms. *SN Computer Science*, Volume 3, issue 6, 463. https://doi.org/10.1007/s42979-022-01333-4

Модель нечіткого керування з автоматизованою генерацією бази правил для артилерійських систем в ігрових симуляторах

Олексій Козлов[a], Олексій Максимов[b], Максим Максимов[c], Руслан Рябошапка[c]

[a]Чорноморський національний університет ім. П. Могили, вул. 68 Десантників, 10, 54003, м. Миколаїв, Україна
[b]Національний університет «Одеська морська академія», вул. Дідріхсона, 8, 65029, м. Одеса, Україна
[c]Національний університет «Одеська політехніка», пр. Шевченка, 1, 65044, м. Одеса, Україна

Анотація

У даній статті представлено розробку та валідацію нечіткої моделі керування з автоматизованою генерацією бази правил для виконавчих механізмів артилерійських систем у ігрових симуляторах. Запропонована модель інтегрує біоінспірований механізм оптимізації на основі алгоритму мурашиної колонії, що дозволяє автоматично синтезувати ефективні бази правил без використання експертних знань. Такий підхід забезпечує адаптивність та автономність за невизначених умов, а також демонструє логічну прозорість, що дозволяє детально аналізувати стратегії керування. Модель може бути використана для симуляцій поведінки прийняття рішень віртуальними союзниками або противниками, представляючи їхні різні рівні кваліфікації шляхом коригування еталонних моделей та цільових функцій на стадії проєктування, що підвищує реалізм у моделюванні бойових сценаріїв. Експериментальні дослідження, проведені на прикладі імітаційної моделі електроприводу підйому ствола артилерійської установки, продемонстрували перевагу нечіткої моделі над традиційним ПД-контролером з точки зору робастності, ефективності та точності. Представлена методологія також може бути застосована для гідравлічних та інших типів виконавчих механізмів.

Ключові слова: ігрові симулятори; артилерійські системи; нечітка модель керування; генерація бази правил; модель виконавчих механізмів.

ENERGY ENGINEERING AND CONTROL SYSTEMS

Volume 11, Number 2, 2025

Study of the Influence of Optimization Methods on the Efficiency of an Extremal Control System Based on Acoustic Anomaly Detection

Andrii Savula[*], Anton Korotynskyi

National Technical University of Ukraine “Igor Sikorsky Kyiv Polytechnic Institute”,
37 Beresteyskyi Avenue, Kyiv, 03056, Ukraine

Received: October 15, 2025. Revised: November 26, 2025. Accepted: December 16, 2025.

Abstract

The paper investigates the influence of optimization methods on the efficiency of an extremal control system based on acoustic anomaly detection. The proposed system can detect abnormal equipment operating modes by analyzing sound characteristics and automatically adapting control parameters to new operating conditions. Using mathematical modeling, the operation of the system with different optimization algorithms (gradient descent, Momentum, Nesterov and RMSProp) was studied. The results show that RMSProp provides the fastest transition to steady state (103 s) with minimal overshoot (3%), but there are significant oscillations in the control signal. Classic gradient descent demonstrates an acceptable stabilization time (123 s) with moderate overshoot (23%). The Momentum and Nesterov methods are characterized by the longest settling time (173 and 160 s, respectively). The study confirms the feasibility of using extremal control systems with adaptive optimization to improve the reliability and efficiency of technological equipment under variable operating conditions.

Keywords: intelligent control system; optimization; mathematical modeling; transient process.

---

1. Definition of the problem to be solved

Today, in the synthesis and operation of automatic control systems, it is extremely important to consider the technical and operational condition of equipment, as its state directly affects the characteristics of technological processes occurring in the equipment. An example of equipment condition change can be the wear of bearings in rotating mechanisms, which causes additional load on the motor or other system components. Such changes cause alterations in the equipment sound, which can be recorded using a microphone and subsequently used as a trigger for reconfiguring the control system. The sound of equipment operation may not always directly depend on the equipment condition; it can change during operation under incorrect or atypical operating conditions, for example, overloading of a transport conveyor or feeding harder material into a crusher. Atypical operating conditions, in turn, affect the accuracy of the mathematical description of the control object, on the basis of which the synthesis and study of control systems take place.

Currently, there are various methods for determining equipment condition, namely: acoustic, visual, vibration analysis, and analysis using sensor arrays. The application of acoustic anomaly detection approaches allows for the analysis of the current technical and operational state of equipment based on audio data. This approach has a number of advantages, namely:

- relative affordability of sensors for data collection;
- possibility of use in hard-to-reach places and under difficult conditions.

---

[*] Corresponding author. Email address: aasavula@gmail.com

This paper should be cited as: A. Savula, A. Korotynskyi. (2025). Study of the influence of optimization methods on the efficiency of an extremal control system based on acoustic anomaly detection. *Energy Engineering and Control Systems*, Vol. 11, No. 2, pp. 169 – 176. https://doi.org/10.23939/jeecs2025.02.169

The application of the obtained technical and operational state of equipment allows for the identification of anomalous operating modes, which may be new technological regimes, for example, when the load on a motor changes and its characteristic operating sound changes, or potentially emergency situations. Therefore, when a new equipment operating mode is detected, it is necessary to reconfigure the controller according to the system's capabilities to reduce the risk of emergency situations or to return the equipment to a steady-state operating mode.

This work proposes a novel approach to building an extremal control system for solving the problem described above. The fundamental novelty of the proposed system lies in the use of an acoustic sensor unit for detecting an extremal point — the moment of entry into the control optimization algorithm. Unlike traditional approaches, where optimization occurs continuously or on a fixed schedule, the proposed system autonomously makes decisions about the need for reconfiguration based on acoustic data, which significantly reduces computational load and ensures rapid adaptation to changes in the technological object. The practical value of this approach lies in the ability to detect anomalies early and automatically trigger the control optimization procedure only when it is truly necessary, which is critically important for industrial systems with limited computational resources and strict response time requirements. However, for effective application of the proposed control system, it is necessary to conduct a series of studies, one of which is the investigation of the influence of optimization methods on the effectiveness of the proposed approach.

2. Analysis of the recent publications and research works on the problem

The article by Haoqian Wang et al. [1] is devoted to the study of stochastic optimization acceleration for Deep Neural Networks, with a special focus on the theoretical analysis of SGD-Momentum and Nesterov's accelerated gradient methods. The work consists of a mathematical investigation into the stability mechanisms of these algorithms and an evaluation of their convergence properties. The key scientific contribution is the identification and formalization of the "overshoot" phenomenon inherent in momentum-based approaches. The authors prove that because Momentum and Nesterov methods rely on the accumulation of historical gradients to accelerate training, they inevitably suffer from oscillatory behavior where parameters exceed their optimal target values. This discovery highlights a critical limitation in these standard algorithms: the reliance on past error information, while beneficial for speed, can destabilize the optimization path when the gradient direction changes rapidly. The authors further characterize Nesterov's method as a specific variation that applies a higher gain to the current gradient compared to classical Momentum, explaining its distinct convergence behavior.

The dissertation by Olle Trollberg and Elling W. Jacobsen [2] is devoted to the study of extremal control methods with a special focus on the problem of multiple solutions and convergence speed. The work consists of two main parts and contains both theoretical research and practical applications. The key scientific contribution is the identification and investigation of the problem of multiple stationary solutions. The authors prove that even with a convex objective function, the classical ESC method can have multiple stationary points. This discovery refutes previous assumptions about the uniqueness of the solution when the conditions of existence and stability are met. Stationary solutions are characterized by a condition for local phase shift of the process, which can be satisfied at points not related to optimality. The authors show that the observed multiplicity of solutions is related to a certain type of bifurcation and provide conditions for their existence. Using the example of the CANON biochemical reactor process, it is demonstrated that the conditions for phase shift can be satisfied at operating points that are completely unrelated to optimal ones, which can lead to suboptimal system performance. Greedy ESC, a modification of the method for systems with multiscale dynamics, is considered separately. By optimizing only the fast dynamics of the system, significant performance improvements can be achieved while reducing computational complexity.

In the article Vytautas Kaminskas, Kęstutis Šidlauskas and Česlovas Tallat-Kelpša [3] examined a class of dynamic systems in which linear dynamic elements are combined with nonlinear static characteristics, and the output is distorted by random disturbances. Typical examples are fuel combustion and steam condensation processes at thermal power plants. The problem addressed in the article was the constant change in extreme characteristics due to equipment aging, surface contamination and uncontrollable factors. Therefore, a mechanism for automatic adaptation to changes in the system is needed. To solve this problem, the concept of self-tuning control was applied, which combines continuous parameter identification and control synthesis based on current estimates. The implementation includes an optimal predictor that forecasts the future output several steps ahead by decomposing the transfer function of disturbances using the Wiener-Hopf method into future (unpredictable) and past (known) components. The synthesis of the controller is based on the equality of the predicted and desired values, which gives a nonlinear equation with a square root. Periodic sign change before the root provides excitation of the system to improve identification. Constraints are taken into account by projecting the control to the admissible region. Identification uses a recursive least squares method in a component-by-component version. Prediction error updates parameter estimates through a covariance matrix without storing data history. A forgetting factor allows slow parameter changes to be tracked, giving more weight to fresh data.

An analysis of existing approaches shows that gradient-based optimization methods are most often used to solve extremal control problems due to their relative simplicity of implementation, low computational requirements, and ability to operate in real time. However, the literature presents various modifications of gradient methods—from classical gradient descent to adaptive algorithms with inertia (Momentum, Nesterov) and methods with adaptive learning rates (RMSProp, Adam). Each of these methods has specific features of convergence, noise resistance, and speed, which critically affect the efficiency of the control system in the context of anomaly detection. Therefore, it is advisable to investigate the possibility of using gradient-like optimization methods in control systems based on acoustic anomaly detection.

3. Formulation of the goal of the paper

The purpose of this work is to study the influence of optimization methods on the efficiency of an extremal control system based on acoustic anomaly detection. To achieve this goal, an experiment using mathematical modeling methods is proposed. The work will involve mathematical modeling of the operation of an extremal control system under identical conditions, using various optimization methods, namely: gradient-like, momentum, Nesterov, RMSProp.

4. Presentation and discussion of the research results

4.1. Description of the conditions for conducting the experiment

The experiment was conducted using mathematical modeling methods, which are described by a first-order differential equation:

$$\frac{dy}{dt} = -a \cdot y + b \cdot u, \tag{1}$$

where *y* is the output variable of the system; *u* is the control input; *b* is the amplification coefficient of the control input.

This model is typical for a wide class of technical systems, including thermal processes, hydraulic systems, and electrical circuits with capacitive loads.

Anomaly generation model

To simulate the occurrence of defects in the system, a stochastic model based on a normal (Gaussian) distribution was used:

$$\xi(t) \sim \mathcal{N}(\mu, \sigma^2), \tag{2}$$

where μ is the mathematical expectation; σ^2 is the variance of the random variable.

The choice of the normal distribution is justified by its ability to adequately describe the accumulation of small independent random effects, which corresponds to the nature of most technical malfunctions.

Experiment parameters

The parameters that were used for simulation are presented in Table 1. It includes simulation time, expected system output value and control value.

Table 1. Parameters of the experiment.

Parameter	Value
Simulation duration	t∈[0;200] s
Number of discretization points	1000
Anomaly occurrence time	100 s
Target output value (y_target)	1.0
Initial control value (u_init)	0.5

The experimental study was conducted in five stages:

Stage 1. Simulation. The system functioned with nominal parameters ($a = 0.5, b = 0.5$). The adaptive controller learning rate was $\eta_{normal} = 0.01$. This allowed for obtaining the reference characteristics of the transient process and achieving a steady state.

Stage 2. Activation of the anomaly generator. At a defined moment in time, an additive disturbance was introduced into the system to model the occurrence of a defect. The intensity and nature of the disturbance were determined by the parameters of a Gaussian distribution

Stage 3. Anomaly detection. Monitoring of the output variable $y(t)$ was performed, and the deviation from the target value $y_{target} = 1.0$ was recorded. An anomaly was considered detected when the error exceeded the limits of the allowable band $\pm 2\%$.

Stage 4. Transition to a new steady state. The adaptive controller automatically adjusted the control input $u(t)$ to compensate for the changes in system parameters and return the output to the target value.

Stage 5. Analysis of the obtained results. For each optimization algorithm, the transient process quality indicators were calculated:

- settling time;
- overshoot;
- steady-state error.

The modeling time was 200 seconds. During the specified modeling period, an anomaly event was simulated, after which the control optimization procedure was launched. An extremal control system based on control optimization, using a gradient-like adaptation law [4], is considered as the basic control system solution:

$$u(t+1) = u(t) + \eta(y_{target} - y(t)). \tag{3}$$

The error, i.e. deviation from the current setpoint ($y_{target} - y(t)$) was used as the optimization criterion. The paper investigates the operation of the proposed control system based on the following optimization methods: the gradient-like optimization algorithm, the Momentum method, Nesterov (Nesterov Accelerated Gradient) method and RMSProp.

A gradient-like optimization algorithm, in particular gradient descent, is a first-order iterative method for finding the local minimum of a function. The principle of operation is that at each iteration, the gradient of the function at the current point is calculated, after which a step is taken in the direction opposite to the gradient, which contributes to a decrease in the value of the function.

The Momentum method [5] adds inertia to gradient descent. It considers not only the current gradient, but also the accumulated previous direction of movement (velocity). This allows you to speed up movement in stable directions and reduce fluctuations during optimization, especially in narrow “valleys” of the loss function.

Nesterov (Nesterov Accelerated Gradient) [6] is an improvement on Momentum and estimates the future position in advance to make more “far-sighted” steps. The key idea is to first move by inertia (as in Momentum) and then adjust the step based on the new gradient value at the point where inertia “leads.” This provides faster and more stable convergence, especially in convex optimization:

RMSProp (Root Mean Squared Propagation) [7] is an adaptive optimization method that applies different learning rates for each parameter. It uses a moving average of past gradients, which avoids overly small or large steps and stabilizes learning even in tasks with “noisy” or sparse gradients.

4.2. Results of the basic solution

Figure 1 shows the results of the acoustic anomaly detection system. In the figure, during the first 100 seconds, the probability of an anomaly in the equipment's operating mode does not exceed 0.2 (20%). After 100 seconds, the flaw detection system detected an anomaly. Since the anomaly is not peak, it is decided that this is a new operating mode, and the control optimization procedure for the new mode is started. After adaptation is complete, the current operating mode is accepted as the new nominal mode, which is why after 110 seconds, the probability of an anomaly is again below the threshold value.

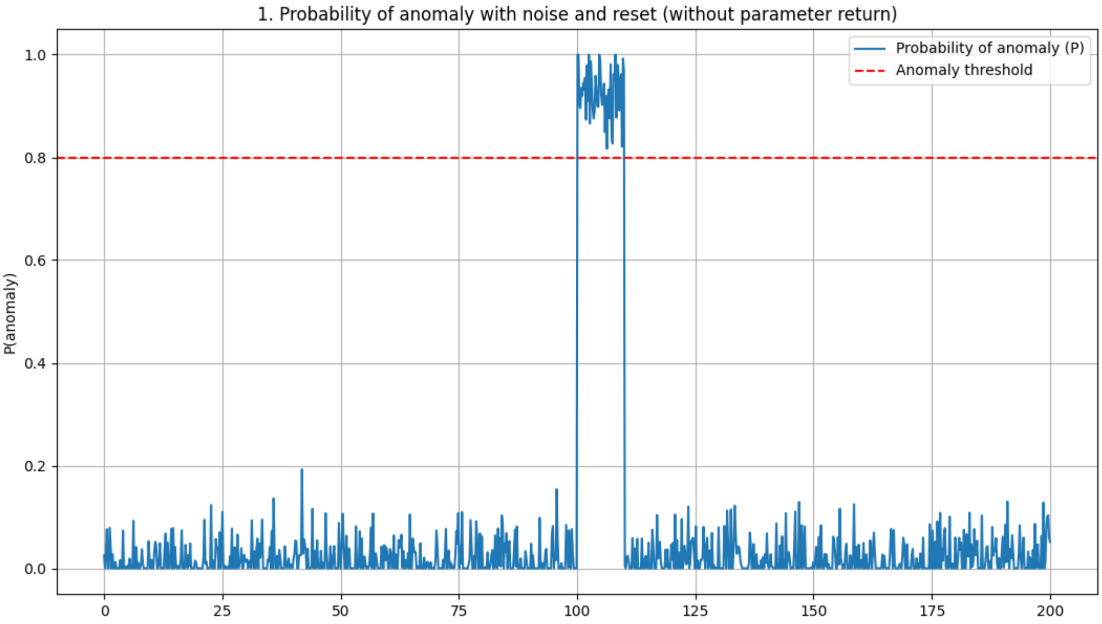

Fig. 1. Graph showing the probability of an audio-based defect.

Figure 2 shows a graph of the deviation from the set value. The time to reach a steady state is approximately 50–60 seconds. After 100 seconds, there is a short-term jump in the error, indicating the presence of an anomaly that requires optimization of the object control under new conditions. In this case, optimization is performed using the gradient descent method. The error after 150 seconds is almost zero, which indicates effective optimization and the ability of the system to adapt.

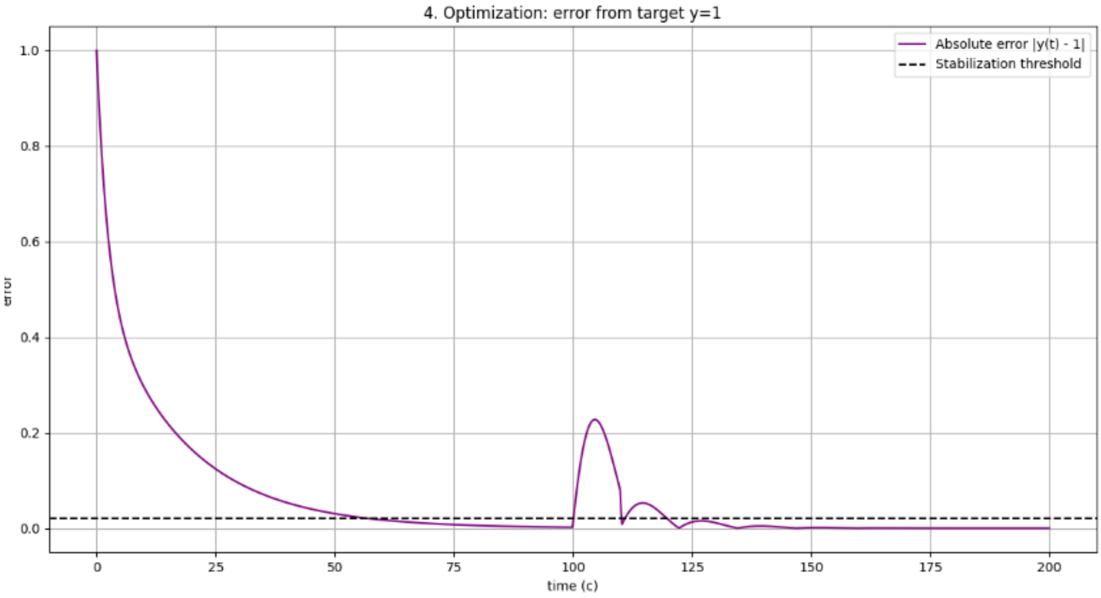

Fig. 2. Graph of deviation from the set value.

The results of the proposed system are shown in Figure 3. The adaptive system quickly reaches the target level *y*=1 and maintains it with high accuracy. When an anomaly occurs, there is a short-term overshoot with an amplitude of about 0.2 and damped oscillations. Thanks to its adaptive properties, the output stabilizes and returns to the set value. This indicates the stability of the system and its ability to compensate for disturbances.

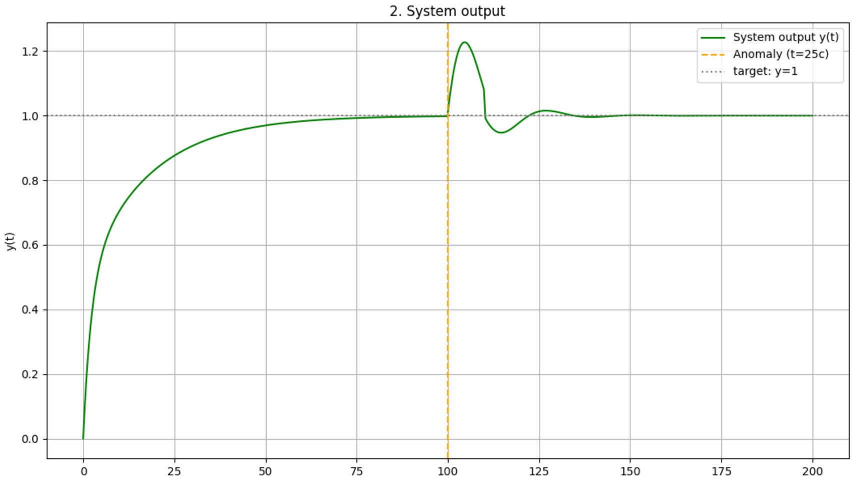

Fig. 3. Transition process of the proposed control system.

4.3. Study of the impact of quality criteria on the efficiency

Figure 4 shows a comparison of the performance of different optimizers in this system. All methods quickly reduce the absolute error to a level close to the target but differ in their response dynamics. RMSProp demonstrates the fastest error reduction and the smallest fluctuations after an anomaly, while Momentum and Nesterov have more pronounced overshoots. Conventional gradient descent (GD) stabilizes more slowly but provides relatively smooth dynamics. In general, all algorithms can return the system within the stabilization threshold (±2%), which, in our case, is reaching a steady state, but the effectiveness of their response to perturbations varies significantly.

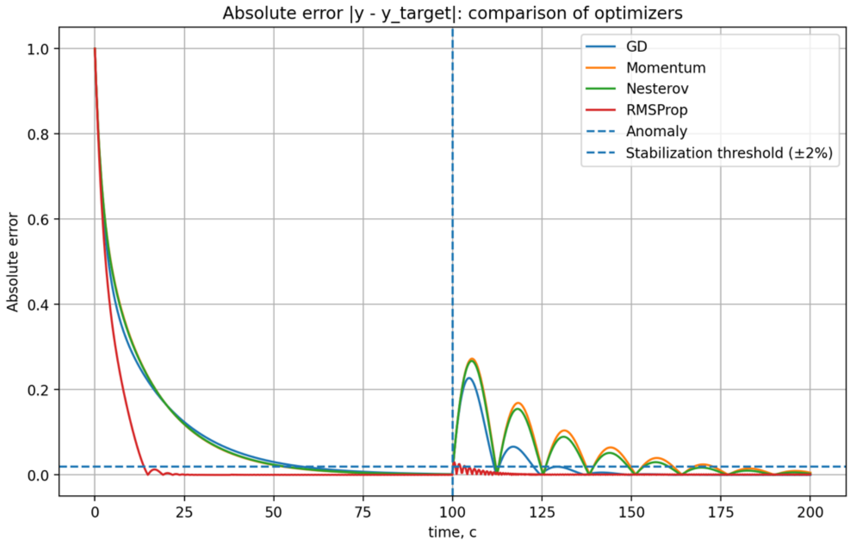

Fig. 4. Transition process of the proposed control system

Figure 5 shows a comparison of control signals obtained using different optimizers. In the initial phase, all methods gradually increase the control influence, but RMSProp forms more pronounced fluctuations even before the anomaly occurs. After the disturbance (t≈100 s), GD, Momentum, and Nesterov provide a smoother response with gradual attenuation of fluctuations, while RMSProp exhibits significant high-frequency fluctuations, indicating its less stable behavior. In conclusion, it can be noted that classical methods (GD, Momentum, Nesterov) provide more stable and predictable control, while RMSProp is fast but unstable in its response to external influences. Figure 6 shows the system output when using different optimization methods. All optimizers achieve the target level, but the dynamics differ. RMSProp reaches steady state faster than other methods, but its response is accompanied by slight fluctuations.

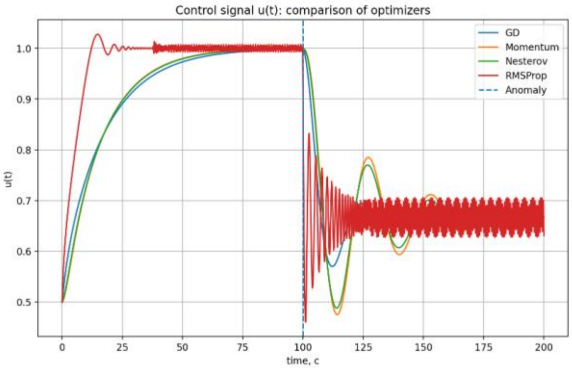

Fig. 5. Control signal.

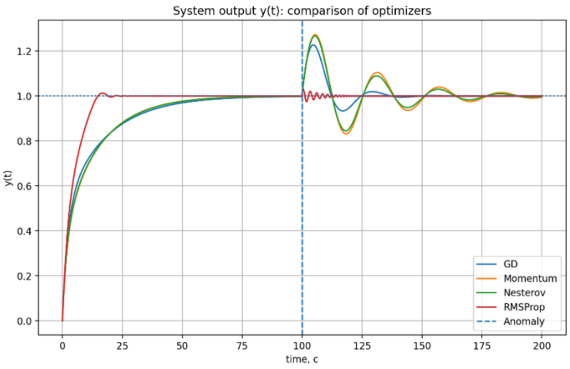

Fig. 6. Comparison of system output.

A comparative description is provided in Table 2. This table shows the time that system needs to reach steady state, the overshoot and the system error across different optimization methods.

Table 2. Optimization methods comparison.

Method	Time, s	Overshoot, %	Steady state error
GD	122.7	22.7	2.05e-05
Momentum	172.7	27.2	0.0069
Nesterov	160.3	26.7	0.0043
RMSProp	103.5	2.9	1.908e-05

5. Conclusion

The extremal control systems using optimization methods have shown high efficiency in achieving and maintaining target values. Despite the presence of disturbances and anomalies, the system stably restores the steady state and keeps the output within the acceptable error threshold. This confirms the feasibility of applying such approaches in real technical objects, where it is important to ensure stability and quick response to changing conditions.

RMSProp demonstrated the best results: minimum time to reach the stabilization threshold (~103 s), very low overshoot percentage (~3%), and virtually no error in steady state. This indicates its high stability and suitability for use in systems of this type. However, this optimization method leads to significant oscillatory processes, which can result in excessive load on the actuator. Gradient Descent (GD) showed acceptable stabilization time (~123 s) and insignificant steady state error, but has a significant overshoot (~23%). It provides relatively smooth dynamics, but is inferior to RMSProp in terms of speed and stability. Momentum and Nesterov are characterized by the longest settling times (173 and 160 seconds) and higher overshoot percentages (~27%), making them less effective for high-speed systems. They also guarantee low steady-state error, so they can be useful in conditions where a longer transition process is acceptable.

References

[1] Wang, H., Luo, Y., An, W., Sun, Q., Xu, J., & Zhang, L. (2020). PID controller-based stochastic optimization acceleration for deep neural networks. *IEEE Transactions on Neural Networks and Learning Systems*, *31*(12), 5079–5091. https://doi.org/10.1109/TNNLS.2019.2963066.

[2] Trollberg, O. (2017). On Real-Time Optimization using Extremum Seeking Control and Economic Model Predictive Control. Doctoral thesis, KTH Royal Institute of Technology.

[3] Kaminskas V, Šidlauskas K, Tallat-Kelpša Č. (1991). Constrained self-tuning control of stochastic extremal systems. Informatica: An International Journal of Computing and Informatics. 2(1):33-52. doi:10.3233/INF-1991-2102.

[4] Mareels, I. M. Y., Anderson, B. D. O., Bitmead, R. R., Bodson, M., & Sastry, S. S. (1987). Revisiting the MIT rule for adaptive control. IFAC Proceedings Volumes, 20(2), 161–166. https://doi.org/10.1016/S1474-6670(17)55954-6

[5] Goh, G. (2017). Why momentum really works. *Distill*. https://doi.org/10.23915/distill.00006

[6] Alexandre d'Aspremont, Damien Scieur and Adrien Taylor. (2021). Acceleration Methods. *Foundations and Trends® in Optimization*, Vol. 5: No. 1-2, pp. 1-245. http://dx.doi.org/10.1561/2400000036

[7] Dauphin, Y., Vries, H., Chung, J., & Bengio, Y. (2015). Equilibrated adaptive learning rates for non-convex optimization. *arXiv*. https://arxiv.org/abs/1502.04390

[8] Saad-Falcon, A., Howard, C., Romberg, J., Allen, K. (2024). Level set methods for gradient-free optimization of metasurface arrays. *Scientific Reports*, 14, 16674. doi: 10.1038/s41598-024-67142-2.

Дослідження впливу методів оптимізації на ефективність екстремальної системи керування на основі аудіальної дефектоскопії

Андрій Савула, Антон Коротинський

Національний технічний університет України «Київський політехнічний інститут імені Ігоря Сікорського»,
Берестейський проспект, 37, Київ, 03056, Україна

Анотація

У роботі досліджується вплив методів оптимізації на ефективність екстремальної системи керування на основі аудіальної дефектоскопії. Запропонована система здатна виявляти аномальні режими роботи обладнання шляхом аналізу звукових характеристик та автоматично адаптувати параметри керування під нові умови експлуатації. Методом математичного моделювання досліджено роботу системи з різними алгоритмами оптимізації: градієнтним спуском, Momentum, Nesterov та RMSProp. Результати показують, що RMSProp забезпечує найшвидший вихід на усталений режим (103 секунди) з мінімальним перерегулюванням (3%), проте супроводжується значними коливаннями керуючого сигналу. Класичний градієнтний спуск демонструє прийнятний час стабілізації (123 секунди) з помірним перерегулюванням (23%). Методи Momentum та Nesterov характеризуються найдовшим часом встановлення (173 та 160 секунд відповідно). Дослідження підтверджує доцільність застосування екстремальних систем керування з адаптивною оптимізацією для підвищення надійності та ефективності роботи технологічного обладнання в умовах змінних режимів експлуатації.

Ключові слова: інтелектуальна система керування; оптимізація; математичне моделювання; перехідний процес.

ENERGY ENGINEERING AND CONTROL SYSTEMS

Volume 11, Number 2, 2025

Definition of Fill Level of Ball Mill Based on Vibration Acceleration Signal

Vasyl Lymych[a, *], Volodymyr Zagraj[b]

[a]*Lviv Polytechnic National University, 12 S. Bandery St., Lviv, 79013, Ukraine*
[b]*Techprylad LLC, 116 V. Antonovycha St., Lviv, 79057, Ukraine*

Received: October 15, 2025. Revised: November 25, 2025. Accepted: December 03, 2025.

Abstract

The paper is devoted to the study of the relationship between the vibration accelerometer signal and the fill level of a ball mill. It was established that there is a direct correlation between the vibration level of the front support of the mill drum and the amount of material being ground in the mill. A low vibration level corresponds to a high fill level of the mill. Two methods of processing the vibration accelerometer signal to obtain a fill level signal using a moving window are proposed. In the first method, the frequency spectrum is built and the maximum is determined in a specific frequency range. The second method consists in calculating the integral of the modulus of the vibration acceleration signal during the time of the moving window. The operation of each method is demonstrated based on the experimental data of vibration acceleration signals during the work of two ball mills at operating conditions.

Keywords: ball mill; vibration acceleration signal; frequency spectrum; moving window; experimental data; fill level.

1. Introduction

A ball mill is a complex control object, since there are mechanical, heat exchange and aerodynamic processes taking place in it with a large number of interrelated parameters. The main production characteristic of the mill is its productivity, namely the amount of ground material per time unit. The productivity of the mill depends on the fill level, i.e. the amount of material in the mill drum during grinding.

For reliable and efficient operation of a ball mill, it is very important to maintain the fill level at an optimal value, since too low a fill level leads to inefficient use of energy consumed by the mill, as well as to rapid wear of the internal armor of the mill [1]. Too high a fill level leads to a blockage of the mill, when a large amount of material rotates in the drum with the balls, but there is no grinding process in the mill. This is an emergency situation when the mill should be stopped in order to clean it and restart it. This situation can be prevented by measuring the fill level and maintaining it at an optimal value. Therefore, measuring the fill level is an extremely important process for ensuring reliable and efficient operation of a ball mill.

There are no direct methods for measuring the fill level of the mill, so indirect measurement methods are used in practice, namely, determining the fill level based on the vibration acceleration signal or the acoustic signal of the mill operation. In addition, during the operation of the ball mill other parameters are also measured, i.e. the air mixture temperature at the mill outlet, the differential pressure across the mill drum and the active power consumed by the mill electric drive. These parameters are used to control the mill operation, as well as to protect against emergency situations.

---

[*] Corresponding author. Email address: vasyl.v.lymych@lpnu.ua

This paper should be cited as: V. Lymych, V. Zagraj. (2025). Definition of fill level of ball mill based on vibration acceleration signal. *Energy Engineering and Control Systems*, Vol. 11, No. 2, pp. 177 – 186. https://doi.org/10.23939/jeecs2025.02.177

2. Goal of the paper

The goal of this paper is to analyze the vibration acceleration signals during the operation of ball drum mills under operating conditions and also to present the methods for processing these signals to determine the variation of the fill level of the mill (filling with the material) with a constant amount of ball charge.

3. Analysis of recent publications

Studies of the acoustic signals of ball mills, as well as vibration acceleration signals during ball mill operation, are presented in publications [2]-[9]. In [2], a method for processing the acoustic signals for determining the grinding fineness of calcined alumina in a small ball mill is presented. In [3], [4], the acoustic signals of a ball mill for different fill levels and rotation speeds are analyzed using a sound signal model and the discrete element method. In [5], the results of processing the acoustic signal of the mill using machine learning models are presented.

Since the acoustic signal, besides the useful information, often contains additional noise and sounds from other equipment, a more effective signal for determining the fill level of the mill is the vibration acceleration signal. In [6], a method for collecting and processing vibration signals using sensors installed on the outer surface of the mill drum, as well as on the supports of the front and rear bearings of the mill drum is presented. In [7], a method for determining the characteristics of the ground material based on the vibration accelerometer signal installed on the surface of the mill drum is presented. In [8], a method for determining the mill load based on the vibration accelerometer signal using the Adaptive Chirp Mode Decomposition (ACMD) method and the Standardized Variable Distance Classifier (SVD) method is presented. And in work [9], a method of processing the signal from an accelerometer using a Hampel filter to eliminate noise, as well as Fast Fourier Transformation (FFT) to construct the spectral density (PSD).

In the publications mentioned above, a great deal of attention is paid to the processing of signals from the operation of ball mills in laboratory conditions and there are no results of signal analysis in operating conditions.

4. Presentation of research results

4.1. Analysis and processing of vibration acceleration signal for the first mill

The vibration acceleration signals were recorded using a sound card for two ball mills under operating conditions. ABC117-03 vibration accelerometer was installed on the front support of the mill. The parameters of the recorded vibration acceleration signal file for the first mill are as follows:

File name:	Mill_1.wav
File size:	64.9 MB
Bit rate:	1536 kbit/s
Sample rate:	96000
Total samples:	34028800
Duration:	354.4667 s
Bits per sample:	16

The vibration acceleration signal was imported into Matlab using the “audioread” command [10]. The results are presented in Fig. 1.

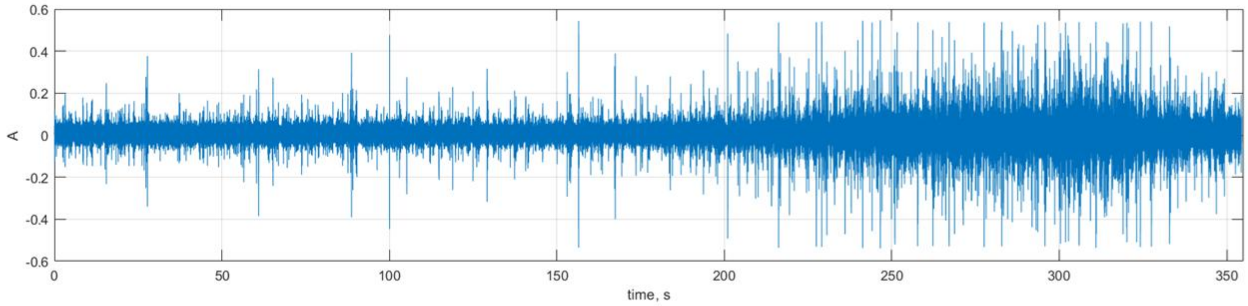

Fig. 1. Imported vibration acceleration signal.

Fig. 1 shows that in the first part of the recorded signal the amplitude is smaller than in the second part of the signal. This means that the fill level of the mill with material is higher for the first part of the recorded signal, and in the second part the fill level (the amount of material in the mill) decreases.

To process the vibration acceleration signal, it is proposed to use a moving window. The signal within the moving window is processed with application of the following two methods:

- fast Fourier transform;
- integral of the modulus of the vibration acceleration.

We need to select the size of the moving window to process the signal. The technique for defining the optimal size of a moving window is presented in [11]. As a result of applying this technique to the signal from the file “Mill_1.wav”, it was found that the optimal value of the moving window size is 400 ms. The window movement step is chosen to be 200 ms.

According to the first method of the vibration acceleration signal processing, the frequency spectrum was built for each position of the moving window with application of “fft” command [12]. The result of building the frequency spectra for the first five positions of the moving window is presented in Fig. 2.

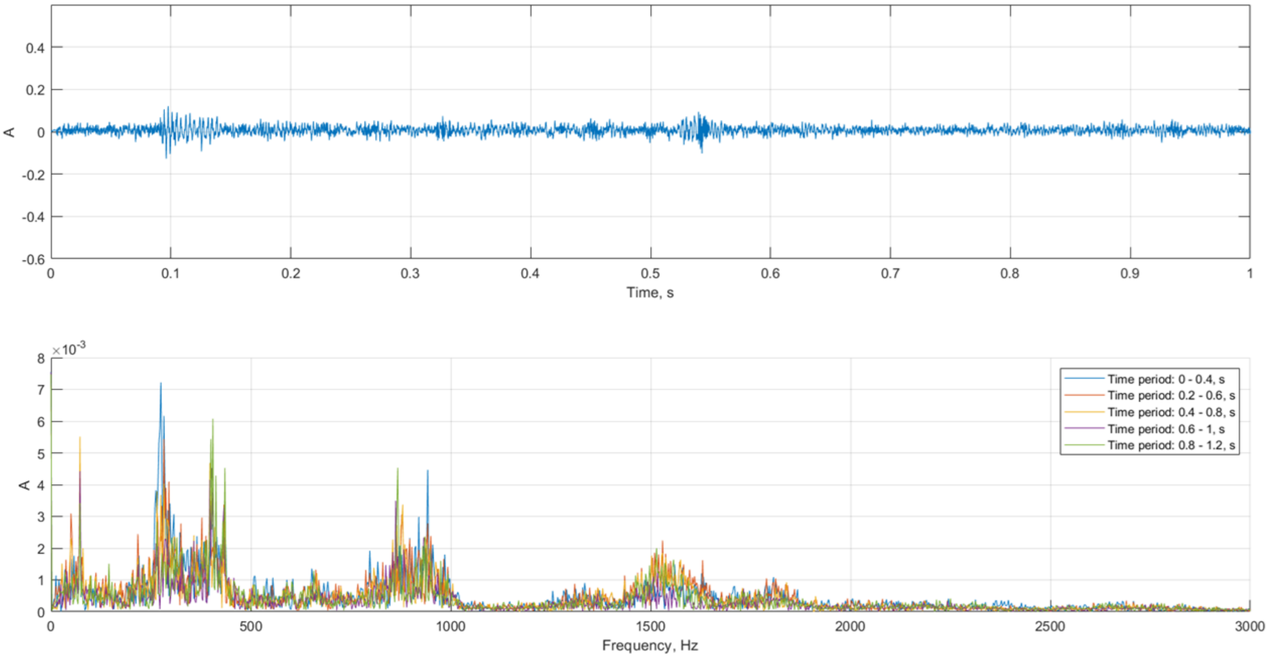

Fig. 2. Beginning of the vibration acceleration signal and the first five frequency spectra.

We can see from Fig.2 that the frequency spectrum has several ranges where there is useful signal. These are the following ranges: from 200 to 500 Hz, from 750 to 1100 Hz and from 1300 to 2000 Hz. To determine the vibration level using the first method, the maximum of the frequency spectrum in the frequency range from 750 Hz to 1100 Hz was selected.

Variation of the vibration level according to the first method of the vibration acceleration signal processing with application of the moving window is presented in Fig. 3. The obtained values were smoothed using a moving average filter (causal) with a smoothing window size of 20 s, which contained 101 samples of the vibration level signal. The delay of the smoothed vibration level signal with respect to the non-smoothed signal is 10 s. A causal filter was chosen to smooth the signal, since this type of filter can be used to process the vibration acceleration signal in real time.

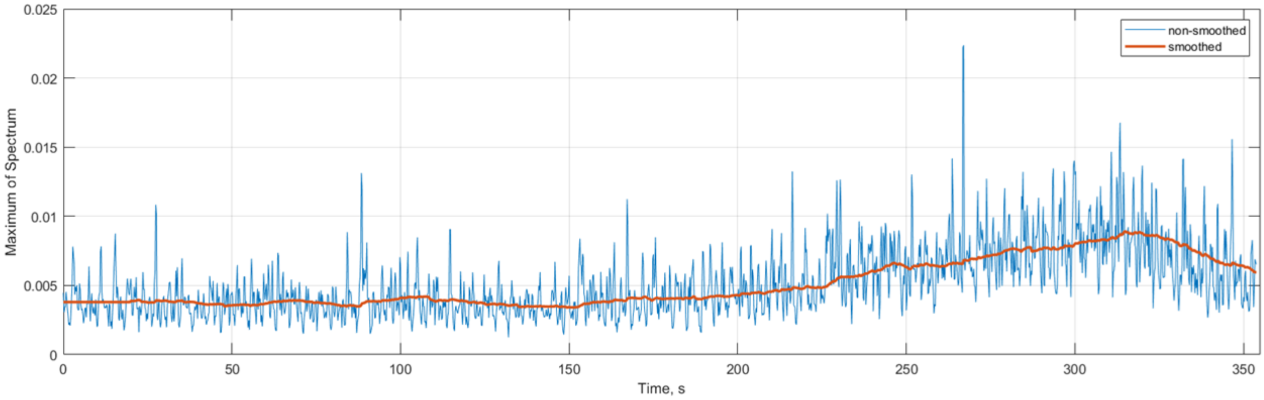

Fig. 3. Variation of the vibration level defined by the first method
(maximum of the frequency spectrum in the frequency range from 750 Hz to 1100 Hz).

To calculate the variation of the fill level of the mill on the basis of the vibration level (smoothed), the following assumptions were made: the fill level signal starts at the value of 90%; the fill level signal decreases to the minimum value of 60%. Calculation of the fill level was made by means of the following formula:

$$y = \frac{(x_0 - x)\cdot\Delta y}{\max(x) - x_0} + y_0, \tag{1}$$

where y is the fill level of the mill; x is the vibration level (smoothed); $x_0 = 0.0038$ is the initial value of the vibration level; $\Delta y = 30$ is the range of fill level variation; $y_0 = 90$ is the initial value of the fill level.

The result of defining the fill level of the mill on the basis of the vibration acceleration signal with application of the first method is presented in Fig. 4. This figure shows that from the beginning to 200 s, the amplitude of the vibration acceleration signal and the fill level of the mill remain approximately at a constant value. Between 200 s and 320 s, the vibration acceleration amplitude increases, and the fill level decreases. After 320 s, the vibration acceleration amplitude decreases, and the fill level increases.

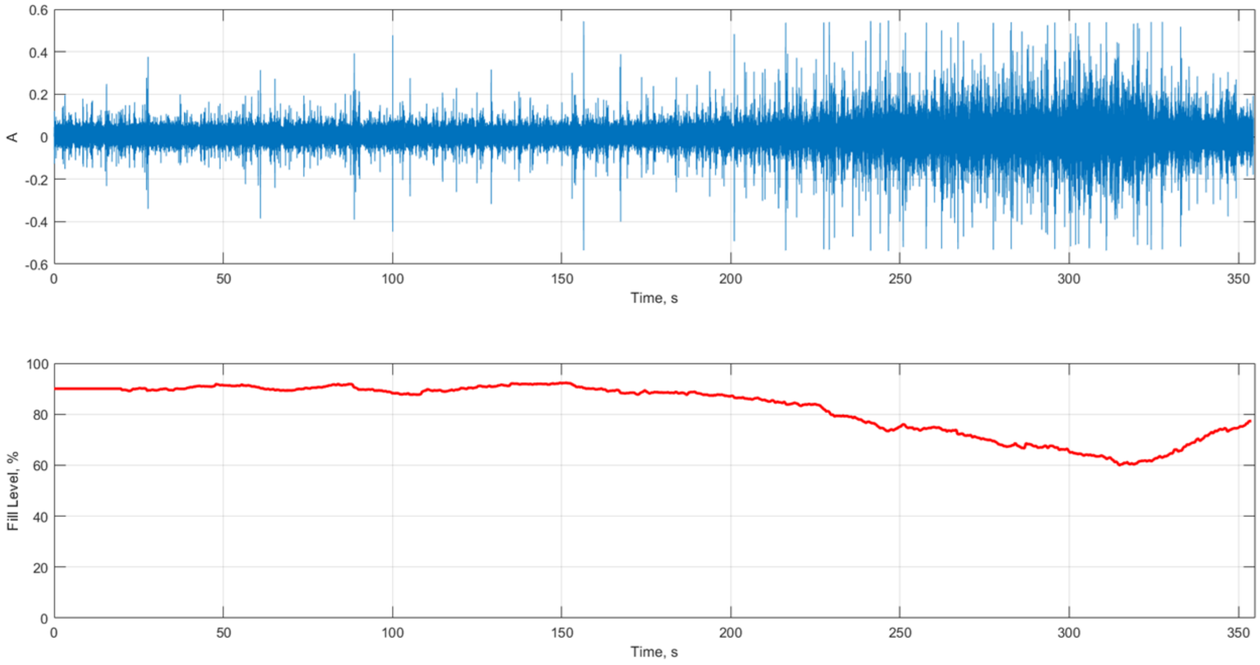

Fig. 4. Vibration acceleration signal and variation of fill level of mill defined by the first method.

Now we will apply the second method of the vibration acceleration signal processing, i.e. the integral of the modulus of the vibration acceleration over the duration of the moving window. The window size is again taken to be 400 ms, the window movement step is 200 ms.

For each position of the moving window, the integral of the modulus of the vibration acceleration signal was calculated using the “cumtrapz” command [13]. The result of calculating the variation of the integral for the first five positions of the moving window is presented in Fig. 5.

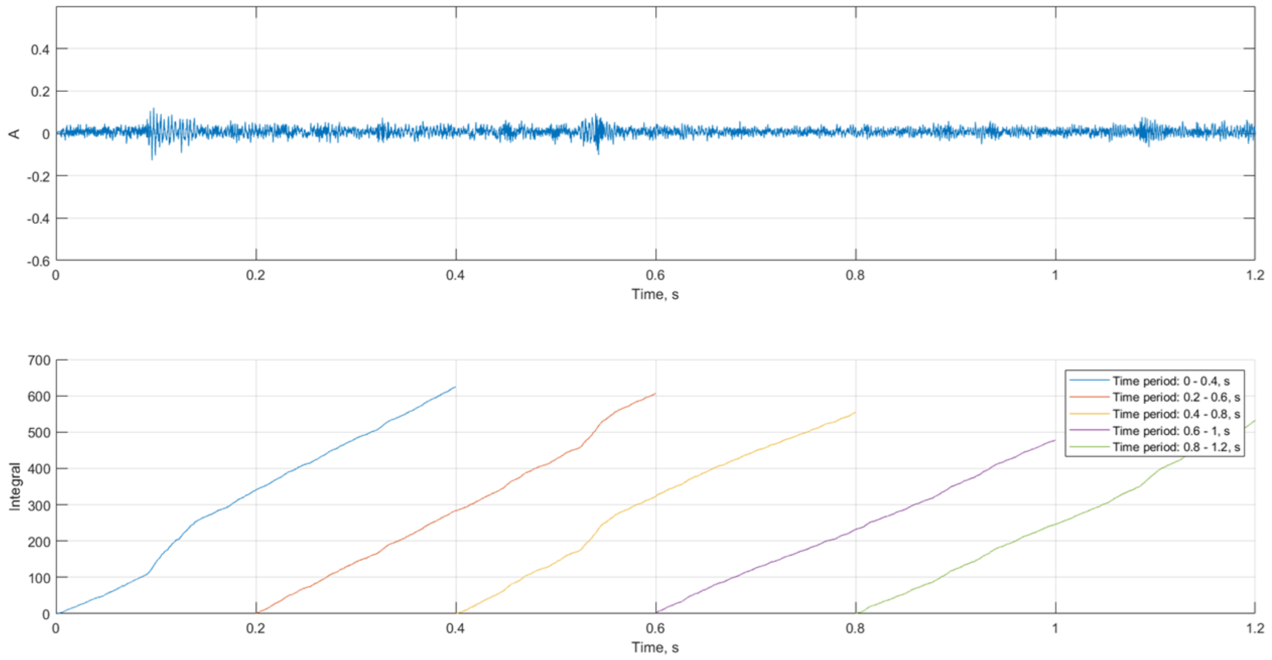

Fig. 5. Beginning of the vibration acceleration signal and variation of the integral for the first five positions of the moving window.

Variation of the vibration level defined by the second method is shown in Fig. 6. The obtained values were smoothed using a moving average filter (causal) with a smoothing window size of 20 s, which contained 101 samples of the vibration level signal. The delay of the smoothed vibration level is 10 s with respect to the non-smoothed vibration level.

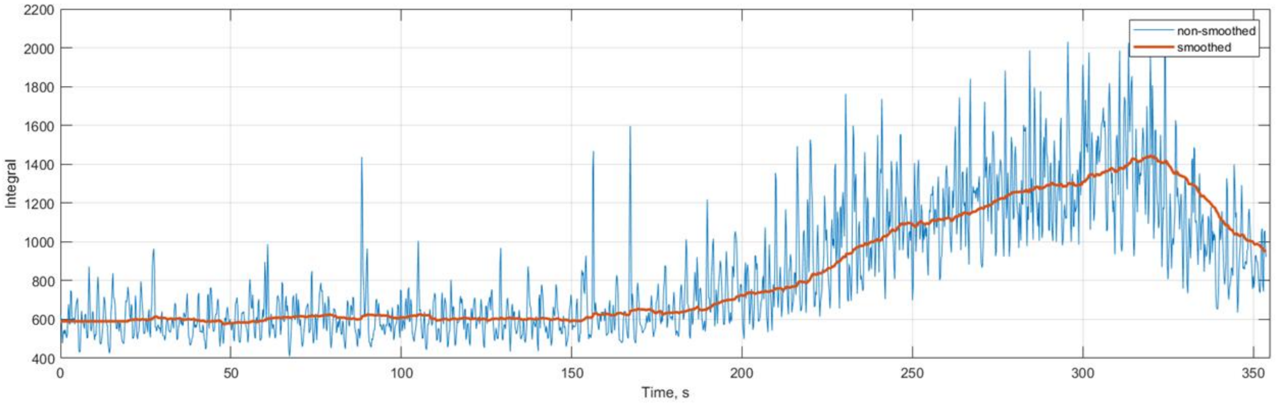

Fig. 6. Variation of the vibration level defined by the second method
(integral of the modulus of the vibration acceleration).

To calculate the variation of the fill level based on the second method, the same assumptions were made as for the first method (initial value of the fill level is 90% and minimum value of the fill level is 60%). Formula (1) was used for calculation. The value of x_0 was taken equal to 590. The result of defining the fill level of the mill on the basis of the vibration acceleration signal with application of the second method is presented in Fig.7.

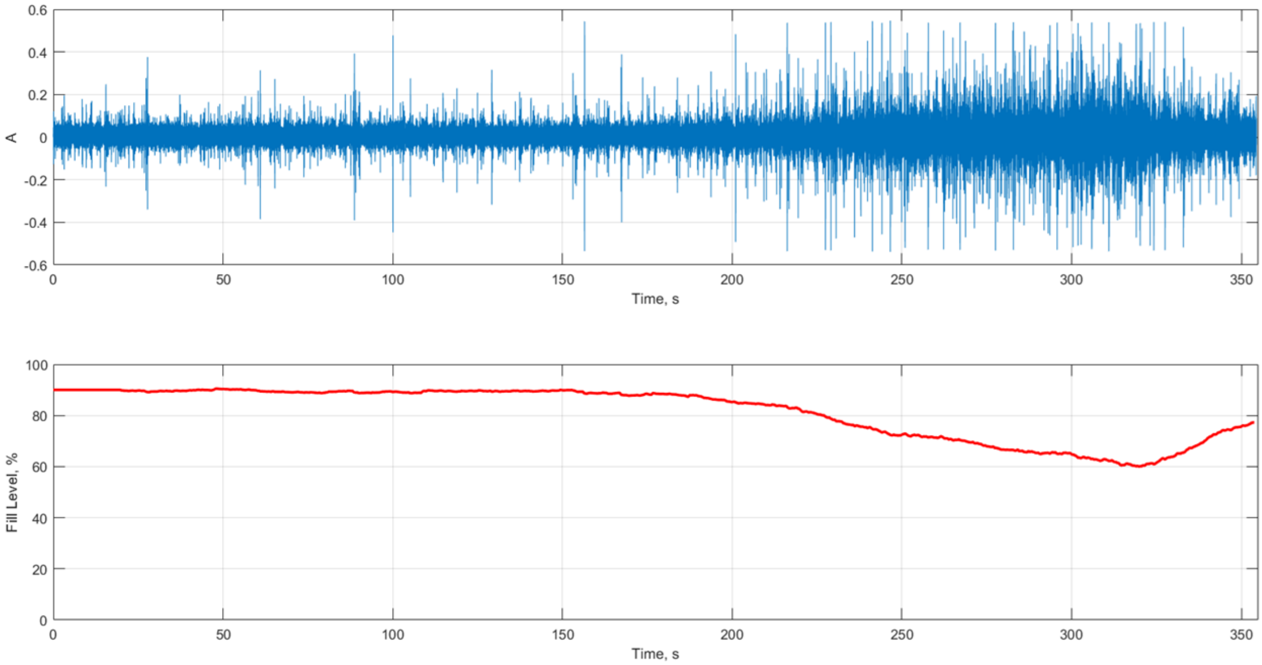

Fig. 7. Vibration acceleration signal and variation of fill level of mill defined by the second method.

We can see from Fig. 7 that from the beginning to 200 s, the amplitude of the vibration acceleration signal and the fill level of the mill remain approximately at a constant value. Between 200 s and 320 s, the vibration acceleration amplitude increases, and the fill level decreases. After 320 s, the vibration acceleration amplitude decreases, and the fill level increases.

Based on the comparison of the fill level signal obtained by the second method with the signal obtained by the first method, it can be concluded that the signal obtained by the second method (Fig. 7) is smoother than the signal obtained by the first method (Fig. 4).

4.2. Analysis and processing of vibration acceleration signal for the second mill

Now we will analyze and process the vibration acceleration signal for the second ball mill. The parameters of the recorded vibration acceleration signal file for the second mill are as follows:

File name:	Mill_2.wav
File size:	77.2 MB
Bit rate:	1536 kbit/s
Sample rate:	96000
Total samples:	40500480
Duration:	421.8800 s
Bits per sample:	16

The file “Mill_2.wav” was processed in the same way as the file “Mill_1.wav”. The size of the moving window was set to be 400 ms, the window step was 200 ms. According to the first method of signal processing, the maximum of the frequency spectrum was calculated in the frequency range from 950 Hz to 1800 Hz. The values of the vibration level were smoothed using a moving average filter (causal) with a smoothing window size of 20 s. The following assumptions were made to calculate the variation of the fill level: the fill level signal starts at the value of 80%; the fill level signal decreases to the minimum value of 10%.

The calculation of the fill level signal with application of the first method (maximum of the frequency spectrum in the frequency range from 950 Hz to 1800 Hz) was made using formula (1), where the following values of constants were taken: $x_0 = 0.0045$, $\Delta y = 70$, $y_0 = 80$. The results of processing “Mill_2.wav” file with application of the first method are presented in Figures 8 – 11.

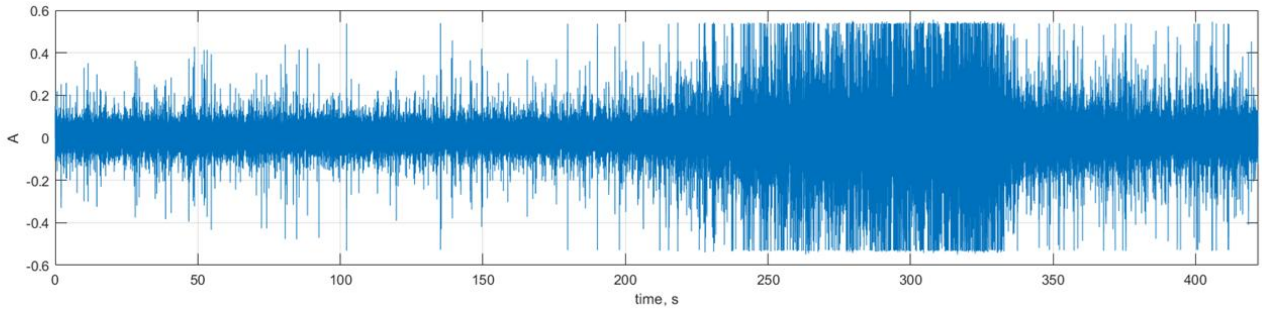

Fig. 8. Imported vibration acceleration signal for the second mill.

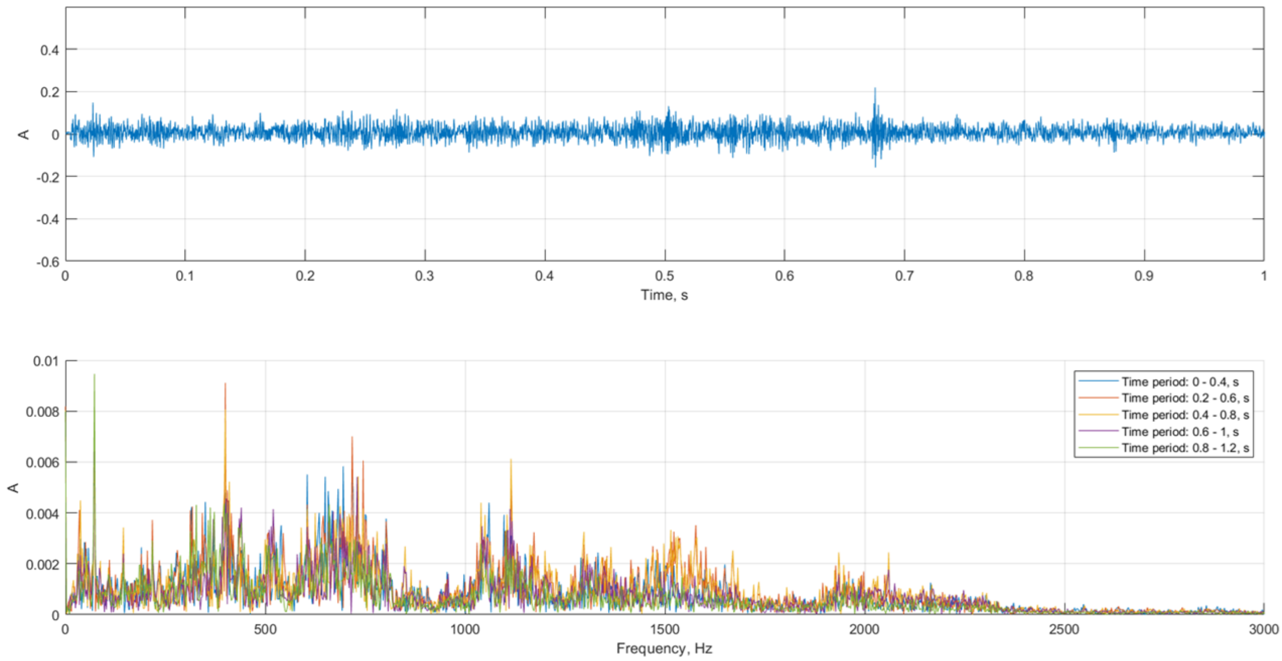

Fig. 9. Beginning of the vibration acceleration signal and the first five frequency spectra.

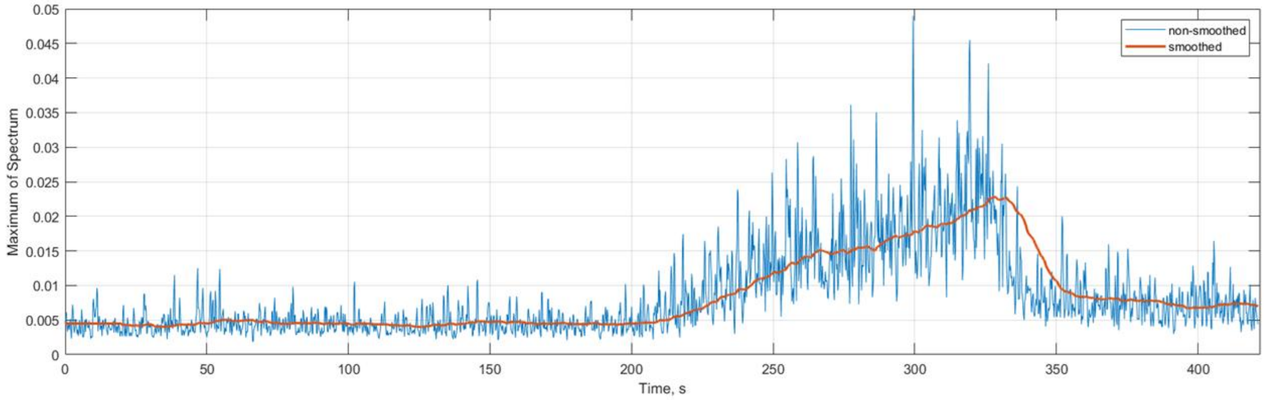

Fig. 10. Variation of the vibration level defined by the first method
(maximum of the frequency spectrum in the frequency range from 750 Hz to 1100 Hz).

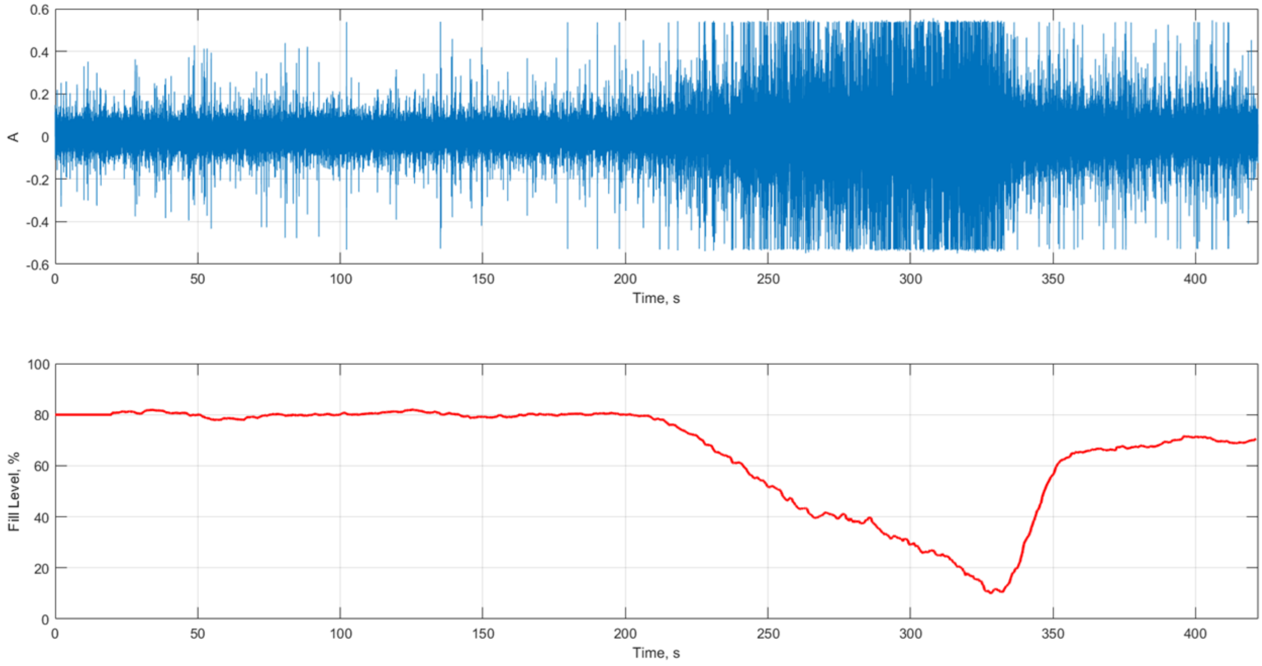

Fig. 11. Vibration acceleration signal and variation of fill level of mill defined by the first method.

The calculation of the fill level signal by the second method (integral of the modulus of the vibration acceleration signal over the time of the moving window) was made using formula (1), where the following values of constants were taken: $x_0 = 885$, $\Delta y = 70$, $y_0 = 80$. The result of processing "Mill_2.wav" file by the second method is presented in Fig. 12.

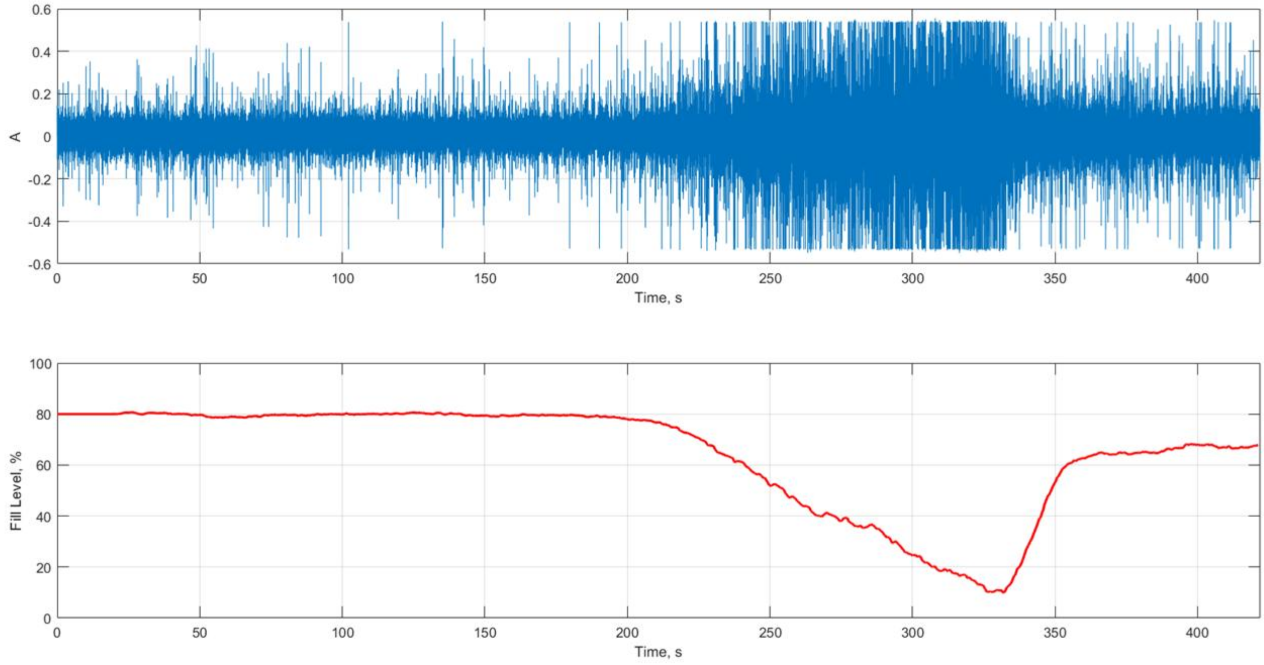

Fig. 12. Vibration acceleration signal and variation of fill level of mill defined by the second method.

Based on the comparison of the results obtained by the first and the second method, for the second mill we can draw a similar conclusion as for the first mill: the fill level signal obtained by the second method (Fig. 12) is smoother than the signal obtained by the first method (Fig. 11). By comparing the results for files "Mill_1.wav" and "Mill_2.wav", the following conclusions can be made:

- the frequency spectra of the signals in these files are slightly different, therefore, for the file "Mill_1.wav" the maximum was calculated in the frequency range from 750 Hz to 1100 Hz, and for the file "Mill_2.wav" – in the frequency range from 950 Hz to 1800 Hz;
- the initial value of the amplitude in the file "Mill_1.wav" is slightly smaller than that in the file "Mill_2.wav", therefore the initial fill level for the first mill was set to a higher value than for the second mill;
- the increase in the amplitude of the vibration acceleration signal in the file "Mill_1.wav" is less significant than in the file "Mill_2.wav", therefore the fill level signal for the file "Mill_1.wav" changes by a smaller amount than for the file "Mill_2.wav".

5. Conclusion

As a result of the study, it was found that the vibration level of the front support of the ball mill is directly correlated with the amount of material being ground in the mill. The higher the vibration level, the less material is in the mill and vice versa. Two methods with application of a moving window are proposed to process the vibration acceleration signal during the operation of the ball mill. The first method consists in building the frequency spectrum using the fast Fourier transform and subsequent determination of the maximum in a specific frequency range. The second method consists in calculating the integral of the modulus of the vibration acceleration signal during the time of the moving window.

Based on the experimental data for two ball mills, each of the two proposed methods was tested. The results show that the fill level signal obtained by the second method is smoother than the signal obtained by the first method. In addition, it should be noted that to obtain the fill level signal by the second method, less computational resources of the controller are needed than for the signal obtained by the first method, since the calculation of the integral of the modulus of vibration acceleration is a simpler algorithm than building the frequency spectrum with subsequent determination of the maximum in a specific frequency range.

References

[1] Fedoryshyn, R.; Nykolyn, H.; Zagraj, V. & Pistun, Y. (2012). The improved system for automation and optimization of solid material grinding by means of ball mills. *Annals of DAAAM for 2012 & Proceedings of the 23rd International DAAAM Symposium*, ISBN 978-3-901509-91-9, ISSN 2304-1382, CDROM version, pp.053-056, Editor B. Katalinic, Published by DAAAM International, Vienna, Austria, EU, 2012

[2] Deng, Jiacheng & Zhang, Yi & Huang, Ao & Wang, Runfeng & Gu, Huazhi & He, Jian. (2020). Monitoring and analysis of ball milling process based on acoustic signal inversion. *IOP Conference Series: Earth and Environmental Science*. 461. 012093. https://doi.org/10.1088/1755-1315/461/1/012093.

[3] Li, Yaoyu & Bao, Jie & Yang, Runyu. (2021). Acoustic signals of rotating drums generated based on DEM simulations. *EPJ Web of Conferences*. 249. 14019. https://doi.org/10.1051/epjconf/202124914019.

[4] P. Hosseini, S. Martins, T. Martin, P. Radziszewski, F.-R. Boyer. (2011). Acoustic emissions simulation of tumbling mills using charge dynamics. *Minerals Engineering*, V. 24, Issue 13, P. 1440-1447, ISSN 0892-6875, https://doi.org/10.1016/j.mineng.2011.07.002.

[5] Owusu, K. B., Skinner, W., & Asamoah, R. K. (2023). Acoustic sensing and supervised machine learning for in situ classification of semi-autogenous (SAG) mill feed size fractions using different feature extraction techniques. *Powders*, 2(2), 299-322. https://doi.org/10.3390/powders2020018

[6] Huang, P., Jia, M. & Zhong, B. (2014) Study on the method for collecting vibration signals from mill shell based on measuring the fill level of ball mill. *Mathematical Problems in Engineering*, Volume 2014, Article ID 472315, 10 pages, http://dx.doi.org/10.1155/2014/472315.

[7] Jeong, H., Yu, J., Lee, Y., Ryu, S. S., & Kim, S. (2022). Real-time slurry characteristic analysis during ball milling using vibration data. *Journal of Asian Ceramic Societies*, 10(2), 430–437. https://doi.org/10.1080/21870764.2022.2068747

[8] Tang, W., Zhang, F., Luo, X., Wan, J., and Deng, T. (2023). Method of vibration signal processing and load-type identification of a mill based on ACMD-SVD. *Mineral Resources Management*, 39(1), pp.217-233. https://doi.org/10.24425/gsm.2023.144626

[9] Zhang, X., Wang, S., Li, W. and Lu, X. (2021). Heterogeneous sensors-based feature optimisation and deep learning for tool wear prediction. *The International Journal of Advanced Manufacturing Technology*, 114, 2651-2675. DOI: 10.1007/s00170-021-07021-6

[10] https://www.mathworks.com/help/matlab/ref/audioread.html (accessed on 26.09.2025)

[11] R. Fedoryshyn, V. Lymych, V. Zagraj, O. Masniak. (2024). Technique for defining the optimal parameters of moving window at vibration accelerometer signal processing. *Energy Engineering and Control Systems*, Vol. 10, No. 2, pp. 142 – 152. https://doi.org/10.23939/jeecs2024.02.142

[12] https://www.mathworks.com/help/matlab/ref/fft.html (accessed on 26.09.2025)

[13] https://www.mathworks.com/help/matlab/ref/cumtrapz.html (accessed on 26.09.2025)

Визначення рівня наповнення кульового барабанного млина на основі сигналу віброприскорення

Василь Лимич[a], Володимир Заграй[b]

[a]*Національний університет «Львівська політехніка», вул. С. Бандери, 12, Львів, 79013, Україна*
[b]*ТзОВ «Техприлад», вул. В. Антоновича, 116, Львів, 79057, Україна*

Анотація

Стаття присвячена дослідженню зв'язку між сигналом віброакселерометра та рівнем наповнення кульового барабанного млина розмелюваним матеріалом. Встановлено, що є пряма кореляція між рівнем вібрації передньої опори млина та кількістю матеріалу, що розмелюється у млині. Низький рівень вібрації відповідає високому рівню наповнення млина. Запропоновано два способи опрацювання сигналу віброакселерометра для отримання сигналу рівня наповнення із застосуванням рухомого вікна. У першому способі виконується побудова частотного спектру та визначення максимуму в певному діапазоні частот. Другий спосіб полягає у розрахунку інтеграла модуля сигналу віброприскорення за час рухомого вікна. Продемонстровано роботу кожного способу на основі експериментальних даних сигналів віброприскорення під час роботи двох кульових барабанних млинів.

Ключові слова: кульовий барабанний млин; сигнал віброприскорення; частотний спектр; рухоме вікно; експериментальні дані; рівень наповнення.

ENERGY ENGINEERING AND CONTROL SYSTEMS

Volume 11, Number 2, 2025

Synthesis of Automatic Control System for Low-Temperature Separator

Mykhailo Horbiychuk, Ihor Yednak*

Ivano-Frankivsk National Technical University of Oil and Gas, 15 Karpatska St., Ivano-Frankivsk, 76019, Ukraine

Received: October 14, 2025. Revised: December 08, 2025. Accepted: December 15, 2025.

Abstract

The gas produced from the well under high pressure is fed to a complex preparation unit, where solid impurities and water are removed. Purified natural gas contains valuable components such as condensate, as well as heavy hydrocarbons, butane and propane. To extract associated components from gas (condensate and heavy hydrocarbons) low-temperature separation is used. The temperature regime in the separator is maintained by the energy of the compressed gas. When the gas passes through the throttle, due to the Joule-Thomson effect, the pressure and temperature decrease. The technological regime in the separator is provided by the single-loop automatic control systems for pressure and condensate level control. As shown by the studies carried out by the authors of the paper, the low-temperature separation as a control object is characterized by internal cross-links. Their presence significantly reduces the efficiency of single-loop control systems. To improve the quality of the control process, an autonomous control system for the low-temperature separation process was synthesized. A cross-coupling compensator was included in the control circuit of such a system, resulting in two independent single-loop automatic control systems. Based on the developed mathematical model, the transfer function of the compensator is synthesized and a method for determining the parameters of PI controllers is developed. The essence of the method is that on the complex plane of the roots of the characteristic equation, the positions of the roots are determined, which should ensure the desired quality of the control process. The placement of the roots is selected from the condition of the minimum of the generalized quadratic criterion of the quality of the control process.

Keywords: low-temperature separation; mathematical model; autonomous system; compensator; PI controller; quadratic criterion.

---

1. Introduction

In the case when the gas extracted from the well under high pressure enters the pre-treatment unit, then low-temperature separation (LTS) is used to separate the condensate from the gas. The decrease in gas temperature, which is below the dew point, occurs due to adiabatic expansion of the gas (Thomson-Joule effect). The effectiveness of the LTS process depends on the degree of compliance with the technological regulations, which are implemented by means of automation. The main technological parameters that affect the technological process are the temperature in the separator, the condensate level and the gas pressure in the low-temperature separator.

The analysis of the dynamic properties of the LTS process showed that there are cross-links between the input and output values. The presence of cross-links significantly complicates the automatic control process, since changing the task on the first control channel will cause an undesirable change in the output value on the second channel. A similar negative event will occur when changing the input value on the second input of the separator control system.

---

[*] Corresponding author. Email address: ihor4698@gmail.com

This paper should be cited as: M. Horbiychuk, I. Yednak. (2025). Synthesis of automatic control system for low-temperature separator. *Energy Engineering and Control Systems*, Vol. 11, No. 2, pp. 187 – 198. https://doi.org/10.23939/jeecs2025.02.187

The quality of the low-temperature separator control process can be significantly improved by compensating for cross-coupling in some way. One possible way to eliminate the negative impact of cross-coupling is to use the autonomous control method.

2. Analysis of literature sources

The current state of automation of technological processes is characterized by the widespread introduction of microprocessor technology for the implementation of complex control algorithms that were inaccessible to traditional automation tools, with the help of which single-loop automatic control systems were implemented. In this regard, the interest of both scientists and practitioners in methods of automatic control of multidimensional objects, which are quite common in oil and gas production, petrochemical, metallurgical, chemical and other industries, has increased.

The use of single-loop systems for automatic control of complex multidimensional objects did not provide the desired quality indicators of the control process [1]. With the advent of microprocessor control tools that can implement complex control algorithms, new methods for controlling multidimensional objects were developed. Such methods should be divided into two groups. The first of them is the synthesis of control systems in the state space; the second is the synthesis in the frequency domain.

The first group consists of methods of analytical design of regulators (modal control [2], Riccati method [2], [4] – [6], H^{∞} optimization [2]). The second group includes analytical synthesis of automatic control systems and separation of control loops [9] (autonomous control). Systems synthesized using methods of analytical controller design, H^{∞}optimization and modal control are static systems in which control errors are nonzero.

The method of analytical synthesis of automatic control systems assumes that the transfer function of the control device is the ratio of two polynomials. The synthesis of such a system is carried out under the condition that the specified location of the zeros and poles of the system is achieved and the necessary indicators of the quality of the control process are provided. The control device synthesized in this way can have a high order of the transfer function. In [4] an example of the synthesis of a control device for an object with a third-order transfer function is given. As a result, a control device is obtained, the transfer function of which is of the sixth order, which significantly complicates the structure of a controller suitable for implementing such a transfer function.

Almost all methods of synthesis of control systems for multidimensional objects solve the problem of finding the so-called consistency matrix, the purpose of which is to compensate for cross-connections, which makes it possible to improve the qualitative and quantitative indicators of the control process.

The aim of the work is to synthesize an autonomous control system for the LTS process to increase the efficiency of condensate separation from produced gas from the well. To achieve the goal, it was necessary to solve the following tasks:

- synthesize a cross-coupling compensator and determine the parameters of its matrix transfer function.
- for the two obtained independent control loops, find the PI controller tuning parameters and evaluate the quality of the low-temperature separator control process.

3. Synthesis of cross-link compensator

The synthesis of an autonomous control system involves the inclusion of a cross-coupling compensator with the transmission circuit in the control loop $W_{eq}(p)$ (Fig. 1). The matrix transfer function of the controller $W_{cl}(p)$ is a diagonal matrix whose elements are the transfer functions of the controllers. The matrix transfer function of the system, which is depicted in Fig. 1, will be as follows:

$$W_{yu_d}(p) = \left(I + W(p)\right)^{-1} W(p), \tag{1}$$

where $W(p) = W_{yu}(p)W_{eq}(p)W_{cl}(p)$ is the matrix transfer function of the open system; $W_{yu}(p)$is the matrix transfer function of the low-temperature separator.

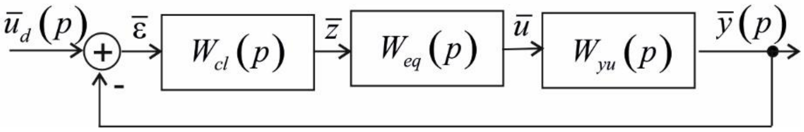

Fig. 1. Block diagram of an autonomous control system.

In [1] it is shown that the matrix transfer function for the low-temperature separator problem is as follows:

$$W_{yu} = (Ip - A)^{-1}B,$$

where $A = \begin{bmatrix} a_{11} & a_{12} \\ a_{21} & a_{22} \end{bmatrix}$; $B = \begin{bmatrix} 0 & b_{12} \\ b_{21} & b_{22} \end{bmatrix}$.

Since $(Ip - A)^{-1} = \frac{1}{\Delta(p)}\begin{bmatrix} p - a_{22} & -a_{12} \\ -a_{21} & p - a_{11} \end{bmatrix}$, then

$$W_{yu}(p) = \frac{1}{\Delta(p)}\begin{bmatrix} -a_{12}b_{21} & (p - a_{22})b_{12} - a_{12}b_{22} \\ (p - a_{11})b_{21} & (p - a_{11})b_{22} - a_{21}b_{12} \end{bmatrix}. \tag{2}$$

The elements of the matrix transfer function (2) determine the dynamic properties of the transmission channels of the effects of input quantities on the outputs of the object. Therefore,

$$W_{yu}(p) = \begin{bmatrix} w_{11}(p) & w_{12}(p) \\ w_{21}(p) & w_{22}(p) \end{bmatrix},$$

where $w_{11}(p) = -\frac{a_{12}b_{21}}{\Delta(p)}$; $w_{12}(p) = \frac{b_{12}p - (a_{22}b_{12} + a_{12}b_{22})}{\Delta(p)}$; $w_{21}(p) = \frac{b_{21}p - a_{11}b_{21}}{\Delta(p)}$;
$w_{22}(p) = \frac{b_{22}p - (a_{11}b_{22} + a_{21}b_{12})}{\Delta(p)}$; $\Delta(p) = p^2 - (a_{11} + a_{22})p + a_{11}a_{22} - a_{12}a_{21}$.

For the control system to be autonomous, it is necessary to have a diagonal transfer matrix of the open system. It is known that the sum and product of diagonal matrices also give a diagonal matrix, and the operation of inverting a diagonal matrix also generates a diagonal matrix. Indeed, if the matrix $W(p)$is diagonal, then the matrix will also be diagonal $W_{yu_d}(p)$.

It was assumed that $W_{cl}(p)$is a diagonal matrix. For the matrix $W(p)$to be also diagonal, the following condition must be met [2]:

$$W_{yu}(p)W_{eq}(p) = \mathrm{diag}W_{yu}(p),$$

where $\mathrm{diag}W_{yu}(p)$is the diagonal matrix obtained from the matrix $W_{yu}(p)$after zeroing off-diagonal elements.

From the last equation we find

$$W_{eq}(p) = W_{yu}^{-1}(p)\mathrm{diag}W_{yu}(p). \tag{3}$$

Formula (3) defines the matrix transfer function of the compensator and shows that the value $W_{eq}(p)$ depends only on the matrix transfer function of the object.

Let us calculate the matrix transfer function of the compensator. First, we find

$$W_{yu}^{-1}(p) = \frac{1}{\Delta_W(p)}\begin{bmatrix} w_{22}(p) & -w_{12}(p) \\ -w_{21}(p) & w_{11}(p) \end{bmatrix},$$

where $\varDelta_w(p) = w_{11}(p)w_{22}(p) - w_{12}(p)w_{21}(p)$; $diagW_{yu}(p) = \begin{bmatrix} w_{11}(p) & 0 \\ 0 & w_{22}(p) \end{bmatrix}$.

Then

$$W_{eq}(p) = \frac{1}{\varDelta_w(p)} \begin{bmatrix} w_{22}(p) & -w_{12}(p) \\ -w_{21}(p) & w_{11}(p) \end{bmatrix} \cdot \begin{bmatrix} w_{11}(p) & 0 \\ 0 & w_{22}(p) \end{bmatrix}.$$

After multiplying the matrices, we get

$$W_{eq}(p) = \frac{1}{\varDelta_w(p)} \begin{bmatrix} w_{11}(p)w_{22}(p) & -w_{12}(p)w_{22}(p) \\ -w_{11}(p)w_{21}(p) & w_{11}(p)w_{22}(p) \end{bmatrix}. \tag{4}$$

From the matrix equation (4) we find the transfer functions of individual signal transmission channels from the compensator input to its output, i.e.

$$w_{11}^{(eq)}(p) = \frac{w_{11}(p)w_{22}(p)}{\varDelta_w(p)};\ w_{12}^{(eq)}(p) = -\frac{w_{12}(p)w_{22}(p)}{\varDelta_w(p)};$$

$$w_{21}^{(eq)}(p) = -\frac{w_{21}(p)w_{11}(p)}{\varDelta_w(p)};\ w_{22}^{(eq)}(p) = w_{11}^{(eq)}(p).$$

Let's find the order of the compensator's transfer functions. To do this, we write the object's transfer functions in the following form: $w_{ij}(p) = \frac{r_{ij}(p)}{\varDelta(p)}$, $i, j = 1,2$. Then $w_{11}^{(eq)}(p) = w_{22}^{(eq)}(p) = \frac{1}{\varDelta_w(p)} \cdot \frac{r_{11}(p)r_{22}(p)}{\varDelta^2(p)}$; $w_{12}^{(eq)}(p) = -\frac{1}{\varDelta_w(p)} \cdot \frac{r_{12}(p)r_{22}(p)}{\varDelta^2(p)}$; $w_{21}^{(eq)}(p) = -\frac{1}{\varDelta_w(p)} \cdot \frac{r_{21}(p)r_{11}(p)}{\varDelta^2(p)}$.

Since $\varDelta_w(p) = \frac{1}{\varDelta^2(p)}\big(r_{11}(p)r_{22}(p) - r_{12}(p)r_{21}(p)\big)$, then

$$w_{11}^{(eq)}(p) = w_{22}^{(eq)}(p) = \frac{r_{11}(p)r_{22}(p)}{D(p)};\ w_{12}^{(eq)}(p) = -\frac{r_{12}(p)r_{22}(p)}{D(p)};\ w_{21}^{(eq)}(p) = -\frac{r_{21}(p)r_{11}(p)}{D(p)}, \tag{5}$$

where $D(p) = r_{11}(p)r_{22}(p) - r_{12}(p)r_{21}(p)$.

Thus, the order of the transfer functions of the compensator is determined by the order of the products of the polynomials $r_{ij}(p)r_{kl}(p)$, $i, j, k, l \in \{1,2\}$. Since the order of each of the polynomials $r_{ij}(p)$ is not more than one, the order of the product of two polynomials $r_{ij}(p)r_{kl}(p)$ does not exceed number two. The analysis allows us to state that for each transfer function $w_{ij}^{(eq)}(p)$, $i, j = 1,2$ the condition $M \leq N$ is satisfied. Here M is the order of the polynomial of the numerator and N is the order of the polynomial of the denominator of the corresponding transfer function. Then the condition of the physical implementation of the cross-coupling compensator is satisfied.

For the transfer functions of the cross-coupling compensator, we have the following values: $M = 1$ for $w_{11}^{(eq)}(p)$, $w_{22}^{(eq)}(p)$ and $w_{21}^{(eq)}(p)$; $M = 2$ for $w_{12}^{(eq)}(p)$; $N = 2$ for all transfer functions $w_{ij}^{(eq)}(p)$, $i, j = 1,2$.

Conducted research [1] on modeling the NTS process as an automatic control object made it possible to obtain the following transfer functions:

$$w_{11}(p) = \frac{0.1106}{p^2+49.42p+0.8282};\ w_{12}(p) = \frac{0.2484p+12.27}{p^2+49.42p+0.8282};$$

$$w_{21}(p) = \frac{1994p+36.05}{p^2+49.42p+0.8282};\ w_{22}(p) = \frac{4.396p+289.9}{p^2+49.42p+0.8282}.$$

So, we have: $r_{11}(p) = 0.1106$; $r_{12}(p) = 0.2484p + 12.27$; $r_{21}(p) = 1994p + 36.05$;
$r_{22}(p) = 4.396p + 289.9$.

Using software developed in the Matlab environment, the transfer functions of the cross-coupling compensator were obtained, i.e.

$$w_{11}^{(eq)}(p) = w_{22}^{(eq)}(p) = -\frac{0.9812\cdot10^{-3}p+0.064711}{p^2+49.42p+0.8282};\ w_{12}^{(eq)}(p) = \frac{0.2204\cdot10^{-2}p^2+0.2543p+7.1811}{p^2+49.42p+0.8282};\ w_{21}^{(eq)}(p) = \frac{0.4451p+0.0080462}{p^2+49.42p+0.8282}.$$

Let us now find the transfer function of the closed-loop automatic control system of the LTS process, considering the transfer function of the compensator (3). To do this, first we find the transfer function of the open-loop system

$$W(p) = \mathrm{diag}W_{yu}(p)W_{cl}(p).$$

We substitute $W(p)$ into formula (1). As a result, we obtain

$$W_{yu_d}(p) = \left(I + \mathrm{diag}W_{yu}(p)W_{cl}(p)\right)^{-1}\mathrm{diag}W_{yu}(p)W_{cl}(p).$$

The resulting matrix equation in expanded form will be as follows:

$$W_{yu_d}(p) = \begin{bmatrix} 1 + w_{11}(p)w_{11}^{(cl)}(p) & 0 \\ 0 & 1 + w_{22}(p)w_{22}^{(cl)}(p) \end{bmatrix}^{-1} \begin{bmatrix} w_{11}(p)w_{11}^{(cl)}(p) & 0 \\ 0 & w_{22}(p)w_{22}^{(cl)}(p) \end{bmatrix}.$$

After performing the operations of rotating the diagonal matrix and multiplying the matrices, we obtain

$$W_{yu_d}(p) = \begin{bmatrix} \frac{w_{11}(p)w_{11}^{(cl)}(p)}{1+w_{11}(p)w_{11}^{(cl)}(p)} & 0 \\ 0 & \frac{w_{22}(p)w_{22}^{(cl)}(p)}{1+w_{22}(p)w_{22}^{(cl)}(p)} \end{bmatrix}.$$

Thus, we obtained the matrix transfer function of the closed-loop system, which is diagonal, which means that the two-dimensional system can be considered as two independent systems with the following transfer functions:

$$w_{11}^{(yu)}(p) = \frac{w_{11}(p)w_{11}^{(d)}(p)}{1+w_{11}(p)w_{11}^{(d)}(p)}; \tag{6}$$

$$w_{22}^{(pu)}(p) = \frac{w_{22}(p)w_{22}^{(c)}(p)}{1+w_{22}(p)w_{22}^{(cl)}(p)}. \tag{7}$$

Since the transfer functions $w_{11}(p)$ and $w_{22}(p)$ of the object (separator) are known, the synthesis of an autonomous control system is reduced to determining the transfer function of the compensator, choosing the control law (PI or PID law) and determining the tuning parameters for the regulators.

4. Calculation of the tuning parameters for the regulators of the autonomous control system

For the first and second control loops, we will choose PI control laws

$$w_{11}^{(cl)}(p) = \frac{C_0^{(1)}p+C_1^{(1)}}{p}, \tag{8}$$

$$w_{22}^{(c)}(p) = \frac{C_0^{(2)}p+C_1^{(2)}}{p}, \tag{9}$$

where $C_0^{(i)}$, $C_1^{(i)}$ are the controller settings ($i = 1, 2$).

In formulas (6) and (7) the transfer functions of the object are known. Considering the transfer functions of the regulators of the first and second circuits (8) and (9), we write the transfer function of the closed-loop system for the first and second circuits

$$w_{11}^{(yu)}(p)=\frac{b_1^{(1)}C_0^{(1)}p+b_1^{(1)}C_1^{(1)}}{p^3+a_1p^2+(b_1^{(1)}C_0^{(1)}+a_2)p+b_1^{(1)}C_1^{(1)}}, \tag{10}$$

$$w_{22}^{(yu)}(p)=\frac{b_0^{(2)}C_0^{(2)}p^2+(b_0^{(2)}C_1^{(2)}+b_1^{(2)}C_0^{(2)})p+b_1^{(2)}C_1^{(2)}}{p^3+(a_1+b_0^{(2)}C_0^{(2)})p^2+(b_0^{(2)}C_1^{(2)}+b_1^{(2)}C_0^{(2)}+a_2)p+b_1^{(2)}C_1^{(2)}}. \tag{11}$$

The parameters for setting the controllers will be determined by the combined method [7], [8], the essence of which is that on the p -plane (on the plane of poles) certain values of the poles in the left part of the p -plane are selected to achieve the desired properties of the automatic control system.

Vieta's theorem establishes the relationship between the roots of the characteristic equation of the system and its coefficients. Since for the first and second circuits the characteristic equations of the closed system have the same orders ($n = 3$), we will have [7]:

$$\begin{cases} p_1+p_2+p_3=-\frac{\alpha_1}{\alpha_0}, \\ p_1p_2+p_1p_3+p_2p_3=\frac{\alpha_2}{\alpha_0}, \\ p_1p_2p_3=-\frac{\alpha_3}{\alpha_0}. \end{cases} \tag{12}$$

The coefficients of the characteristic equation for the first circuit are as follows: $\alpha_0=1$, $\alpha_1^{(1)}=a_1$, $\alpha_2^{(1)}=a_2+b_1^{(1)}C_0^{(1)}$, $\alpha_3^{(1)}=b_1^{(1)}C_1^{(1)}$, where $b_1^{(1)}=a_{12}b_{21}$, $a_1=-(a_{11}+a_{22})$, $a_2=a_{11}a_{22}-a_{12}a_{21}$. For the second circuit: $\alpha_0=1$, $\alpha_2^{(2)}=b_0^{(2)}C_1^{(2)}+b_1^{(2)}C_0^{(2)}+a_2$, $\alpha_3^{(2)}=b_1^{(2)}C_1^{(2)}$.

Since $\alpha_0=1$, we have the following system of equations for the first circuit:

$$\begin{cases} p_1+p_2+p_3=-\alpha_1, \\ p_1p_2+p_1p_3+p_2p_3=\alpha_2, \\ p_1p_2p_3=-\alpha_3. \end{cases}$$

Let the roots of the characteristic equation of the first circuit be as follows: $p_1=-\pi_1+j\zeta_1$, $p_2=-\pi_1-j\zeta_1$.

From the first equation of the system of equations (12) we find $p_3=-(p_1+p_3)-\alpha_1$. Considering the values of p_1 and p_2 we have $p_3=2\pi_1-\alpha_1^{(1)}$.

Considering the value of p_3, the second and the third equation of system (12) will take the following form:

$$\pi_1^2+\zeta_1^2-2\pi_1(2\pi_1-\alpha_1^{(1)})=\alpha_2^{(1)},$$
$$(\pi_1^2+\zeta_1^2)(2\pi_1-\alpha_1^{(1)})=-\alpha_3^{(1)}.$$

Let us determine the degree of oscillation of the first circuit of the system $\mu_1=\frac{\zeta_1}{\pi_1}$. From the last equality we find $\zeta_1=\pi_1\mu_1$. Considering the values of ζ_1, $\alpha_1^{(1)}$, $\alpha_2^{(1)}$and $\alpha_3^{(1)}$, we will have

$$\pi_1^2r_1-2\pi_1(2\pi_1-a_1)=b_1^{(1)}C_0^{(1)}+a_2,$$
$$\pi_1^2r_1(2\pi_1-a_1)=-b_1^{(1)}C_1^{(1)},$$

where $r_1=\mu_1^2+1$.

From the resulting system of equations, we find

$$C_0^{(1)} = \frac{1}{b_1^{(1)}}(\pi_1^2 r_1 - 2\pi_1(2\pi_1 - a_1) - a_2), \tag{13}$$

$$C_1^{(1)} = -\frac{1}{b_1^{(1)}}\pi_1^2 r_1(2\pi_1 - a_1), \tag{14}$$

where $b_1^{(1)} = a_{12}b_{21}$.

Therefore, the tuning parameters of the primary circuit regulator will be calculated using formulas (13) and (14), which are functions of the real part of the roots $p_1$and p_2

For the stability of a closed system, the condition $p_3 < 0$ must be fulfilled or considering the value of p_3 we will have

$$0 < \pi_1 < \frac{a_1}{2}. \tag{15}$$

In addition to condition (15), it is necessary that the PI controller tuning parameters be positive numbers, i.e. $C_0^{(1)} > 0$ and $C_1^{(1)} > 0$.

Now we will find the tuning parameters of the PI controller as a function of the real part $\pi_2$of the characteristic equation of the second closed loop. We have

$$\begin{cases} p_1 + p_2 + p_3 = -\alpha_1^{(2)}, \\ p_1p_2 + p_1p_3 + p_2p_3 = \alpha_2^{(2)}, \\ p_1p_2p_3 = -\alpha_3^{(2)}. \end{cases}$$

where $p_1 = -\pi_2 + j\zeta_2$; $p_2 = -\pi_2 - j\zeta_2$; $\mu_2 = \frac{\zeta_2}{\pi_2}$.

From the first equation of the obtained system of equations we find $p_3 = 2\pi_2 - \alpha_1^{(2)}$. Considering the value of $\alpha_1^{(2)}$ we have

$$p_3 = 2\pi_2 - a_1 - b_0^{(2)}C_0^{(2)}, \tag{16}$$

If we now consider the roots of the characteristic equation p_1, p_2 and the root p_3, which is determined by formula (16), and the values of $\alpha_2^{(2)}$and $\alpha_3^{(2)}$, we obtain the following result:

$$\begin{cases} (2\pi_2 b_0^{(2)} - b_1^{(2)})c_0^{(2)} - b_0^{(2)}c_1^{(2)} = a_2 - \pi_2^2(r_2 - 4) - 2\pi_2 a_1, \\ \pi_2^2 r_2 b_0^{(2)}C_0^{(2)} - b_1^{(2)}C_1^{(2)} = \pi_2^2 r_2(2\pi_2 - a_1), \end{cases} \tag{17}$$

where $b_0^{(2)} = b_{22}$; $b_1^{(2)} = a_{21}b_{12} - a_{11}b_{22}$; $r_2 = \mu_2^2 + 1$.

The system of linear algebraic equations (17) can be represented in the following form:

$$\begin{cases} \chi_{11}C_0^{(2)} + \chi_{12}C_1^{(2)} = q_1, \\ \chi_{21}c_0^{(2)} + \chi_{22}c_1^{(2)} = q_2. \end{cases} \tag{18}$$

From (18) we find

$$C_0^{(2)} = \frac{\chi_{22}q_1 - \chi_{12}q_2}{\Delta}, \tag{19}$$

$$C_1^{(2)} = \frac{\chi_{11}q_2 - \chi_{21}q_1}{\Delta}, \tag{20}$$

where $\chi_{11} = 2\pi_2 b_0^{(2)} - b_1^{(2)}$; $\chi_{12} = -b_0^{(2)}$; $\chi_{21} = \pi_2^2 r_2 b_0^{(2)}$; $\chi_{22} = -b_1^{(2)}$;
$q_1 = a_2 - \pi_2^2(r_2 - 4) - 2\pi_2 a_1$; $q_2 = \pi_2^2 r_2(2\pi_2 - a_1)$; $\Delta = \chi_{11}\chi_{22} - \chi_{12}\chi_{21}$.

The stability of the second circuit of the autonomous control system will occur when the following conditions are met: $C_0^{(2)} > 0$, $C_1^{(2)} > 0$ and $p_3 < 0$. From formula (16) we find that

$$0 < \pi_2 < \tfrac{1}{2}(a_1 + b_0^{(2)} C_0^{(2)}). \tag{21}$$

Therefore, for both the first and second circuits, the tuning parameters of the PI controllers are functions of the real part $\pi_1$and π_2 the roots $p_1$and p_2.

The values of $\pi_1$and π_2 shall be defined in such a way that the generalized integral criterion takes a minimum value. Therefore, we will minimize

$$J = \int_0^\infty (\varepsilon^2(t) + \tau^2 \dot{\varepsilon}^2(t))\, dt, \tag{22}$$

where $\varepsilon(t)$ is the amount of inconsistency (control error); τ is a constant value that determines the influence of the component $\dot{\varepsilon}^2(t)$ on the quality of the control process.

We can rewrite criterion (22) in the following form:

$$J = J_1 + \tau^2 J_2, \tag{23}$$

where $J_1 = \int_0^\infty \varepsilon^2(t)dt$; $J_2 = \int_0^\infty \dot{\varepsilon}^2(t)dt$.

The values of the components $J_1$and J_2can be calculated using tables [7] if the transfer functions of the control error and its derivative with respect to the controller task are known.

The control error transfer function for the first loop was calculated using the following formula:

$$W_{\varepsilon\mu}^{(1)}(p) = \frac{1}{1+W_{os}^{(1)}(p)},$$

where $W_{os}^{(1)}(p)$ is the transfer function of the open system.

Considering formula (6), we can write $W_{os}^{(1)}(p) = w_{11}(p) w_{11}^{(el)}(p)$. Considering the values of $w_{11}(p) = \frac{b_1^{(1)}}{a_0^{(1)}p^2 + a_1^{(1)}p + a_2^{(1)}}$ and $w_{11}^{(el)}(p) = \frac{C_0^{(1)}p + C_1^{(1)}}{p}$, we obtain

$$W_{Eu}^{(1)}(p) = \frac{(a_0^{(1)}p^2 + a_1^{(1)}p + a_2^{(1)})p}{a_0^{(1)}p^3 + a_1^{(1)}p^2 + (a_2^{(1)} + b_1^{(1)}C_0^{(1)})p + b_1^{(1)}C_1^{(1)}}. \tag{24}$$

With a single step input $u_d^{(1)}$ (Fig. 1), the Laplace representation of the control error will be as follows:

$$\mathrm{E}_1^{(1)}(p) = \frac{a_0 p^2 + a_1 p + a_2}{\alpha_0^{(1)}p^3 + \alpha_1^{(1)}p^2 + \alpha_2^{(1)}p + \alpha_3^{(1)}}, \tag{25}$$

where $\alpha_0^{(1)} = a_0 = 1$.

Now we find the Laplace representation of the derivative of the control error: $\mathrm{E}_1^{(1)}(p) = L[\dot{\varepsilon}(t)]$.

Since $L[\dot{\varepsilon}(t)] = p\mathrm{E}^{(1)}(p) - \varepsilon(0)$, then, using the theorem on the initial value of the function, we obtain: $\varepsilon(0) = \lim_{p\to\infty} p\mathrm{E}^{(1)} = 1$.

Considering the found value of $\varepsilon(0)$, we obtain

$$E_2^{(1)}(p) = \frac{\beta_0 p^2 + \beta_1 p + \beta_2}{\alpha_0^{(1)} p^3 + \alpha_1^{(1)} p^2 + \alpha_2^{(1)} p + \alpha_3^{(1)}}, \tag{26}$$

where $\beta_0 = 0$; $\beta_1 = -b_1^{(1)} C_0^{(1)}$; $\beta_2 = -b_1^{(1)} C_1^{(1)}$.

For the second circuit, using the same algorithm, we determined the Laplace representation of the control error and its derivative. Therefore,

$$\mathrm{E}_1^{(2)} = \frac{a_0 p^2 + a_1 p + a_2}{\alpha_0^{(2)} p^3 + \alpha_1^{(2)} p^2 + \alpha_2^{(2)} p + \alpha_3^{(2)}}, \tag{27}$$

$$\mathrm{E}_2^{(2)} = \frac{\varphi_0 p^2 + \varphi_1 p + \varphi_2}{\alpha_0^{(2)} p^3 + \alpha_1^{(2)} p^2 + \alpha_2^{(2)} p + \alpha_3^{(2)}}, \tag{28}$$

where $\varphi_0 = a_1 - \alpha_1^{(2)}$, $\varphi_1 = a_2 - \alpha_2^{(2)}$, $\varphi_2 = -\alpha_3^{(2)}$.

The analysis of formulas (24) – (28) shows that the difference between the polynomials of the numerators and denominators is equal to one. Therefore, using the known values of $\mathrm{E}_1^{(i)}$, $\mathrm{E}_2^{(i)}$, $\mathrm{i} = 1{,}2$ from the table in [7], for the first circuit we find:

$$J_{N,1}^{(1)} = a_0^2 \alpha_2^{(1)} \alpha_3^{(1)} + (a_1^2 - 2a_0 a_2) \alpha_0^{(1)} \alpha_3^{(1)} + a_2^2 \alpha_0^{(1)} \alpha_1^{(1)}, \tag{29}$$

$$J_{N,2}^{(1)} = \beta_0^2 \alpha_2^{(1)} \alpha_3^{(1)} + (\beta_1^2 - 2\beta_0 \beta_2) \alpha_0^{(1)} \alpha_3^{(1)} + \beta_2^2 \alpha_0^{(1)} \alpha_1^{(1)}, \tag{30}$$

$$J_D^{(1)} = 2\alpha_0^{(1)} \alpha_3^{(1)} (\alpha_1^{(1)} \alpha_2^{(1)} - \alpha_0^{(1)} \alpha_3^{(1)}). \tag{31}$$

Since $\beta_0 = 0$, then

$$J_{N,2}^{(1)} = \beta_1^2 \alpha_0^{(1)} \alpha_3^{(1)} + \beta_2^2 \alpha_0^{(1)} \alpha_1^{(1)}. \tag{32}$$

For the second control circuit we find

$$J_{N,1}^{(2)} = a_0^2 \alpha_2^{(2)} \alpha_3^{(2)} + (a_1^2 - 2a_0 a_2) \alpha_0^{(2)} \alpha_3^{(2)} + a_2^2 \alpha_0^{(2)} \alpha_1^{(2)}, \tag{33}$$

$$J_{N,2}^{(2)} = \varphi_0^2 \alpha_2^{(2)} \alpha_3^{(2)} + (\varphi_1^2 - 2\varphi_0 \varphi_2) \alpha_0^{(2)} \alpha_9^{(2)} + \varphi_2^2 \alpha_0^{(2)} \alpha_1^{(2)}, \tag{34}$$

$$J_D^{(2)} = 2\alpha_0^{(2)} \alpha_3^{(2)} (\alpha_1^{(2)} \alpha_2^{(2)} - \alpha_0^{(2)} \alpha_3^{(2)}). \tag{35}$$

Formulas (27) – (35) determine the generalized quadratic criterion for both the first and second control loops, which we present in the following form:

$$J^{(i)} = \frac{1}{J_D^{(i)}} (J_{N,1}^{(i)} + \tau_i^2 J_{N,2}^{(i)}), \ \ i = 1{,}2 \tag{36}$$

The analysis of formulas (27) – (35) shows that the generalized quadratic criterion (36) for both the first and second control loops is a function of the position of the roots P_1 and P_2 on the p -plane, which is determined by the values of π_1 and π_2.

Let us set the following problem: find such values of π_1 and π_2 that minimize the generalized quadratic criteria $J^{(1)}$ and $J^{(2)}$, that is

$$\min_{\pi_1^{(1)} \le \pi_i \le \pi_1^{(2)}} : J^{(i)}(\pi_i), \ i = 1{,}2, \tag{37}$$

where $\pi_i^{(1)}$, $\pi_i^{(2)}$, are the beginning and end of the interval of the local minimum of the functions $J^{(i)}(\pi_i)$, $i = 1{,}2$.

The interval of the local minimum of the functions $J^{(i)}(\pi_i)$ is chosen based on the stability requirement of the control system, which is determined by the conditions $C_0^{(i)} > 0$ and $C_1^{(i)} > 0,\ i = 1{,}2$, as well as relations (15) and (26).

Using the developed method, software was created in the Matlab environment, with the help of which graphs of the dependences $J^{(1)}(\pi_1)$ and $J^{(2)}(\pi_2)$ were constructed (Fig. 2).

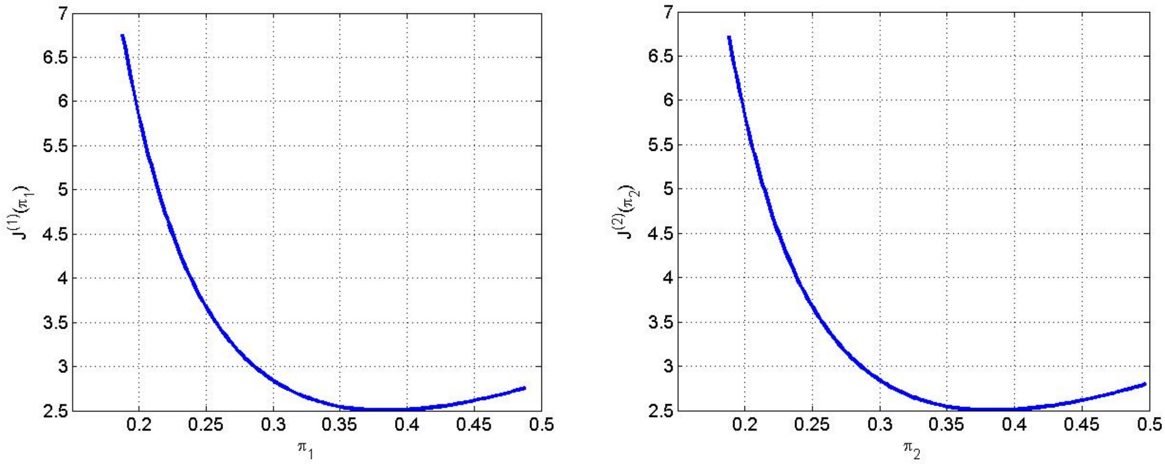

Fig. 2. Dependence graphs of $J^{(1)}(\pi_1)$ and $J^{(2)}(\pi_2)$.

From the graphs (Fig. 2) we found the intervals of local minima $\pi_1 \in [0.3; 0.45]$ and $\pi_2 \in [0.3; 0.45]$, which contain the minima of the functions $J^{(1)}(\pi_1^*)$ and $J^{(2)}(\pi_2)$. The solution of problem (37) gave the following results: $\pi_1^* = 0.38389$, $J^{(1)}(\pi_1^*) = 2.5007$; $\pi_2^* = 0.3880$, $J^{(2)}(\pi_2^*) = 2.5071$. The values of π_1^* and π_2^* made it possible to determine the optimal tuning parameters $C_1^{(i)}$ and $C_0^{(i)}$, $i = 1{,}2$ of the PI controllers for the first control loop according to formulas (13), (14) and for the second control loop according to formulas (19), (20) (Table 1).

To assess the quality of the control process, using formulas (10) and (11), graphs of transient processes were constructed for the first and second control loops (Fig. 3), from which the quality indicators of the control process were determined (Table 1).

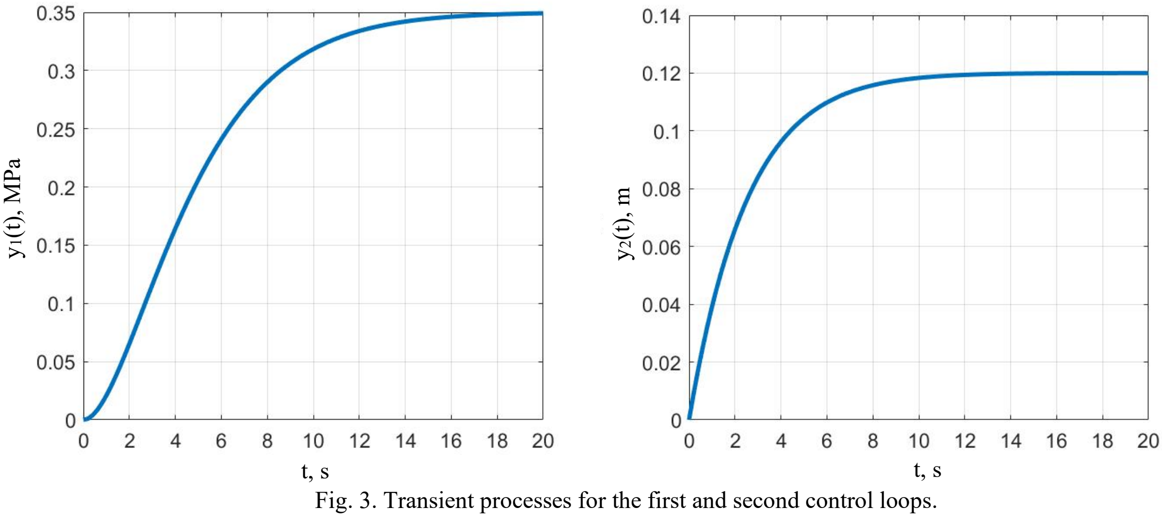

Fig. 3. Transient processes for the first and second control loops.

Table 1. Results of calculations of PI controller tuning parameters and control process quality indicators for the first and second control loops.

	C_0	C_1	t_c, s	σ, %
First circuit	12.901	5.0406	15.6	0
Second circuit	0.33871	0.13233	10.6	0

The calculation of the controller tuning parameters and the quality indicators of the control process were performed using software developed in the Matlab environment. Thus, the obtained indicators of the quality of the control process are satisfactory, since there is no overshoot in both the first and second circuits, and the control time is 15.6 and 10.6 s, respectively.

5. Presentation and discussion of research results

As a result of mathematical modeling of the low-temperature separation process as an object of automatic control, it was established that there are cross-links between control actions and output values (pressure and liquid level in the separator). The presence of cross-links reduces the efficiency of single-loop systems for automatic control of the low-temperature separation process.

The synthesized compensator makes it possible to eliminate cross-coupling and obtain two single-loop independent automatic control systems with PI regulators.

The tuning parameters of the PI controllers of both the first and second control loops of the autonomous system are determined using the developed method of placing the roots of the characteristic equations on the complex p -plane, provided that the stability and minimum of the generalized quadratic control criterion are ensured.

Computer simulation of the autonomous system for automatic control of the low-temperature separation process confirmed the high quality of the control process. There is no overshoot in the system. The control time is 15.6 s for the first circuit and 10.6 s for the second one.

The direction of future research will be aimed at determining the structure of the cross-coupling compensator with the aim of its implementation on industrial microprocessor automation equipment.

6. Conclusion

The transfer functions of the cross-link compensator are determined, based on the condition that the matrix transfer function of the closed-loop control system must be diagonal. This condition makes it possible to "eliminate" cross-links and obtain two independent control loops with respect to the task influences.

A method for determining the tuning parameters of PI controllers of an autonomous control system for the low-temperature separation process by placing the roots of the characteristic equation on the p-plane has been developed. The choice of the placement of the roots of the characteristic equations of closed-loop systems of the first and second control loops was carried out by minimizing the generalized quadratic criterion of the quality of the control process and under the condition of the stability of the autonomous control system.

Based on the software developed in Matlab environment, the PI controller tuning parameters were calculated (using the combined method) and quality indicators of the control process were defined. There is no overshoot in the system. The control time is 15.6 s for the first circuit and 10.6 s for the second one.

References

[1] Horbiychuk M.I. Yednak I.S. Skrypka O.A. (2023). Mathematical modeling of the low-temperature separation process. *Modern engineering and innovative technologies*. Issue #27. Part 1. pp. 101-121. URL: https://www.moderntechno.de/index.php/meit/issue/view/meit27-01/meit27-01

[2] Ray W.H. (1981). Advanced Process Control. *New York: McGraw-Hill Company*. 385p.

[3] Louis C. Westphal. (2001). Handbook of Control Systems Engineering. 2nd edition. *The Springer International Series in Engineering and Computer Science. Springer*, 1063

[4] Bhattacharyya Shankar P., Keel Lee H. (2022). Linear Multivariable Control Systems. *Cambridge UniversityPress*. 698 p.

[5] Zozulya V.A., Osadchy S.I. (2024). Stewart Platform Multidimensional Tracking Control System Synthesis. *Radio Electronics, Computer Science, Control.* No. 3. P. 233-245. https://doi.org/10.15588/1607-3274-2024-3-20

[6] Newton G.C. Jr., Gould L.A., Kaiser J.F. (1957). Analytical design of linear feedback controls. *New York, J. Wiley and Sons, Inc*. 419 p.

[7] Gorbiychuk, M., Lazoriv, N., Chyhur, L., Chyhur, I. (2021). Determining configuration parameters for proportionally integrated differentiating controllers by arranging the poles of the transfer function on the complex plane. *Eastern-European Journal of Enterprise Technologies*, 5 (2 (113)). 80-93. https://doi.org/10.15587/1729-4061.2021.242869

[8] Horbiichuk M., Vasylenchuk M., Yednak I., Lahoida A. (2025). Devising a combined method for setting pi/pid controller parameters for oil and gas facilities. *Eastern-European Journal of Business Technologies.* 1 (2) (133), 85–95. https://doi.org/10.15587/1729-4061.2025.322424

[9] Popovych M. G., Kovalchuk O. V. (1997). Theory of Automatic Control. *Kyiv: Lybid*. 544 p. (in Ukrainian)

Синтез автоматичної системи керування низькотемпературним сепаратором

Михайло Горбійчук, Ігор Єднак

Івано-Франківський національний технічний університет нафти і газу,
вул. Карпатська, 15, м. Івано-Франківськ, Україна, 76019

Анотація

Добутий газ із свердловини під високим тиском поступає на установку комплексної підготовки, де відбувається вилучення твердих домішок і води. Очищений природний газ має у своєму складі такі цінні компоненти як конденсат, а також важкі вуглеводні бутан і пропан. Для вилучення із газу попутних компонентів (конденсату і важких вуглеводнів) використовують низькотемпературну сепарацію Температурний режим в сепараторі підтримується за рахунок енергії стисненого газу. При проходженні газу через дросель внаслідок ефекту Джоуля-Томсона відбувається зниження тиску і температури. Технологічний режим в сепараторі забезпечується одноконтурними системами автоматичного керування – тиску і рівня конденсату. Як показали дослідження, виконані авторами статті, низькотемпературній сепарації як об'єкта керування притаманні внутрішні перехресні зв'язки. Їх наявність значно знижує ефективність одноконтурних систем керування. З метою підвищення якості процесу керування в роботі синтезована автономна система керування процесом низькотемпературної сепарації. У контур керування такої системи включений компенсатор перехресних зв'язків, внаслідок чого отримали дві незалежні одноконтурні системи автоматичного керування. На основі розробленої математичної моделі синтезована передавальна функція компенсатора та розроблений метод визначення параметрів ПІ-регуляторів. Суть методу у тому, що на комплексній площині коренів характеристичного рівняння визначається положення коренів, які повинні забезпечити бажану якість процесу керування. Розміщення коренів вибирається із умови мінімуму узагальненого квадратичного критерію якості процесу керування.

Ключові слова: низькотемпературна сепарація; математична модель; автономна система; компенсатор; ПІ-регулятор; квадратичний критерій.

ENERGY ENGINEERING AND CONTROL SYSTEMS

Volume 11, Number 2, 2025

Remote Monitoring System for Microclimate Parameters of Smart Home and Industrial Premises Based on ESP8266 Microcontroller

Pavlo Skibel, Fedir Matiko*, Ihor Demkiv

Lviv Polytechnic National University, 12 S. Bandery St., Lviv, 79013, Ukraine

Received: October 15, 2025. Revised: November 25, 2025. Accepted: December 18, 2025.

Abstract

The paper analyzes developments in the field of environmental parameter monitoring using microcontrollers and Internet of Things technologies, with results that justify the use of ESP8266 microcontroller. A monitoring system for microclimate parameters (temperature, humidity and atmospheric air pressure) in smart homes and industrial premises based on ESP8266 microcontroller has been developed, which demonstrated its effectiveness through a combination of hardware and software tools. The integration of BMP280 and AHT10 sensors ensured the accurate measurement of temperature, humidity and atmospheric air pressure. The asynchronous web server integrated into the ESP8266 allows for displaying the results as interactive, real-time graphs. In the developed system, users access data directly from the local network, ensuring functionality even without Internet access. Furthermore, the cost of the hardware (ESP8266 controller, BMP280 and AHT10 sensors) remains minimal, making the system accessible for widespread use. The implementation of a user notification system via WhatsApp Messenger using CallMeBot service became an important addition, allowing for the prompt notification of users about exceeding parameter limit values, even without logging into the web application. This approach increases the level of automation, convenience and reliability of microclimate control, making the system suitable for a wide range of tasks in domestic and industrial applications.

Keywords: microclimate parameters; smart home; monitoring system; microcontroller; Internet of Things; web application.

1. Definition of the problem to be solved

In the modern world, there is a rapidly growing interest in process automation across all spheres of human activity. In particular, the task of automating parameter monitoring in industrial and residential premises often arises. This task is relevant for production facilities in the food and processing industries, pharmaceutical manufacturing, warehouses, greenhouses, server rooms, and smart homes. In such environments, even a slight error in temperature, humidity or atmospheric pressure can lead to reduced product quality, spoilage of goods, disruption of technological processes or discomfort for people.

Internet of Things (IoT) technologies are widely used for remote monitoring of parameters in industrial and residential premises, enabling the creation of intelligent systems for collecting, transmitting, and processing data in real time. One of the most popular solutions in this field is ESP8266 microcontroller, which combines low cost, compact size, and a built-in Wi-Fi module. Thanks to these advantages, it is widely used for building wireless sensor networks, home automation, environmental monitoring, and many other tasks. The platform is supported in the

---

* Corresponding author. Email address: fedir.d.matiko@lpnu.ua

This paper should be cited as: P. Skibel, F. Matiko, I. Demkiv. (2025). Remote monitoring system for microclimate parameters of smart home and industrial premises based on ESP8266 microcontroller. *Energy Engineering and Control Systems*, Vol. 11, No. 2, pp. 199 – 209. https://doi.org/10.23939/jeecs2025.02.199

Arduino IDE development environment, which significantly simplifies firmware writing, and the ability to use the LittleFS file system allows for the implementation of an autonomous web server without the need for external hosting. Combining ESP8266 with BMP280 barometric-temperature sensor and AHT10 humidity sensor provides the capability to measure microclimate parameters – temperature, barometric pressure, humidity – and transmit them in real time to a web interface. The use of standard web technologies (HTML, CSS, JavaScript) along with the Highcharts library ensures convenient and interactive visualization of the measured data, allowing the user to dynamically select graphs, adjust the update period and monitor instantaneous values. This approach not only demonstrates the practical capabilities of ESP8266 in the IoT sphere but also creates a flexible, adaptive, and easily scalable system for further development and application in automating processes in daily life and industry.

2. Analysis of recent publications and research

In recent years, many developments and studies have been carried out in the field of environmental parameter monitoring using ESP8266 microcontrollers and IoT technologies, which indicates a steady trend towards the use of inexpensive and compact solutions for real-time data collection and processing.

Publication [1] presents an algorithm for the functioning of a monitoring system for technological process parameters based on mobile communication networks. Publication [2] develops the concept of a "smart system" for monitoring and protecting power equipment, which allows for timely response to dangerous parameter deviations. These works present monitoring systems developed based on programmable logic controllers, communication modules, and HMI tools from leading automation manufacturers. The disadvantage of the presented systems is the high cost of equipment, software, and, consequently, these monitoring systems themselves.

Publication [3] proposes a portable IoT station for measuring temperature, humidity, pressure, and air quality indicators based on ESP8266 microcontroller with AHT10 and BMP280 sensors. A similar approach is used in publication [4], which developed a system for monitoring air pollution in urban conditions using ESP8266, ensuring real-time data transmission to a server. The disadvantage of both approaches is the dependence on external servers or cloud services, which reduces the system's autonomy and complicates its use in conditions of unstable Internet connection.

Publication [6] presents a portable sensor node for robotic systems, which can integrate ESP8266 or ESP32 with many environmental sensors. The authors in publications [7] and [8] emphasize the role of IoT solutions in the "smart city" concept, where monitoring atmospheric parameters is a basic element of infrastructure management.

Publications [9]–[11] propose architectures for low-cost systems for environmental monitoring using ESP8266, Arduino, and cloud platforms. The authors in publications [13], [15], and [17] demonstrate practical skills in using IoT devices for data collection and analysis, which confirms the high level of interest in creating accessible solutions in this area.

Publications [16], [18] and [19] examine advanced approaches to forecasting and the educational use of IoT monitoring systems, indicating their potential for practical implementation. Publication [21] compares ESP8266 with other popular platforms (Arduino, Raspberry Pi), confirming its advantages in building compact and wireless systems.

In general, the review shows that ESP8266 remains one of the most promising solutions for implementing IoT environmental monitoring systems due to its low cost, support for wireless data transmission and ease of programming in the Arduino IDE environment. The task of developing IoT monitoring systems for each specific application remains relevant, as it provides the opportunity to develop simple and inexpensive monitoring systems with a set of functions adapted specifically for that application.

3. Purpose of the work

The purpose of this article is to create a prototype of an IoT monitoring system for microclimate parameters based on ESP8266 microcontroller, which ensures sensor integration, autonomous data collection and processing, organization of access to results via a built-in web server, and the possibility of their further visualization and analysis. The work involves creating the hardware part, developing software in the Arduino IDE environment and implementing a web interface for the operational display of environmental parameter dynamics.

4. Development and testing of the monitoring system

ESP8266 (WEMOS D1 mini module) microcontroller serves as the central component of the developed hardware–software environmental-parameter monitoring system. In addition to the built-in microcontroller, this module contains a flash-memory chip for program storage of 1, 2 or 4 MB and a CP2104 interface chip for converting the USB control signal to UART. The ESP8266 microcontroller has no built in on-chip non-volatile user memory; program execution is performed from external ROM through dynamic loading of required program fragments into the instruction cache. The ESP8266 consists of a 32-bit Tensilica Xtensa L106 processor with a clock frequency of up to 80 MHz, a Wi-Fi 802.11 b/g/n module, 14 input/output pins, SPI, I²C, I²S and UART interfaces, and a 10-bit ADC. General view and pin assignment of the ESP8266 microcontroller (WEMOS D1 mini module) are presented in Fig. 1.

Digital sensors BMP280 and AHT10 are connected to the ESP8266 (WEMOS D1 mini) to measure ambient temperature, barometric pressure and humidity. Both sensors are placed on the same board. The connection diagram of the board with BMP280 and AHT10 sensors to the microcontroller is presented in Fig. 2.

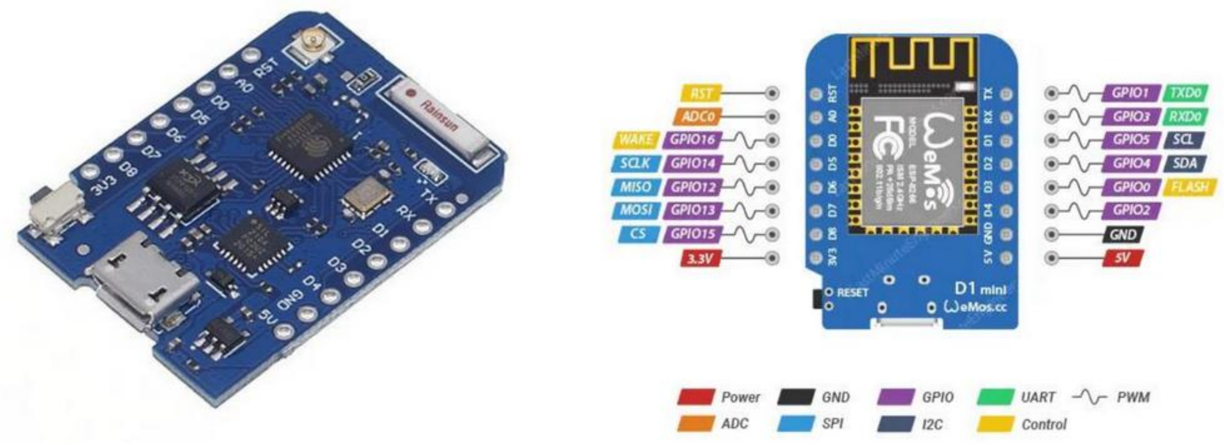

a) *b*)

Fig. 1. ESP8266 microcontroller (WEMOS D1 mini module) with CP2104 converter:
(*a*) general view; (*b*) pin assignment of the microcontroller.

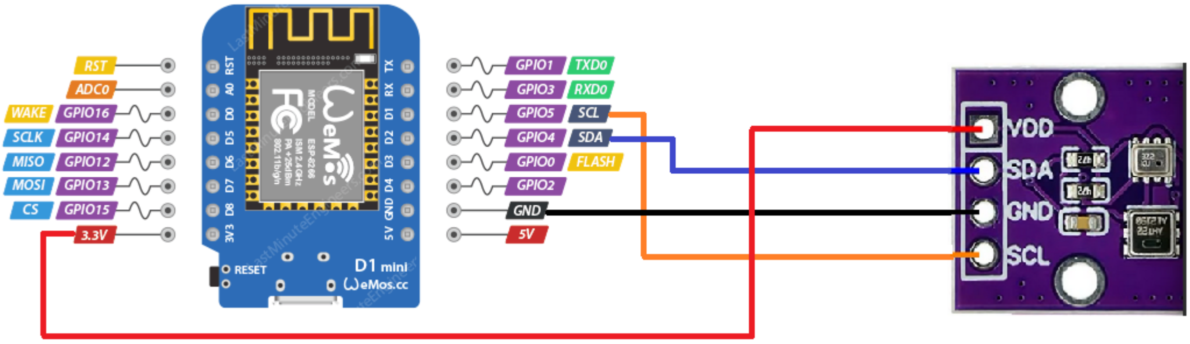

Fig. 2. Connection diagram of BMP280 and AHT10 sensors to WEMOS D1 mini module via the two-wire I²C interface.

These sensors offer significant advantages at low cost. The measurement error for BMP280 is about ±1 hPa for pressure and ±1 °C for temperature; for AHT10 the relative humidity error is only ±2 % RH. Both sensors feature low power consumption, fast response, and compact size, and are connected to the board through the I²C bus. Such a hardware combination ensures compactness and low cost of the solution. Thanks to the Wi-Fi module integrated on the ESP8266 board, wireless communication is provided, allowing implementation of an autonomous local web server for remote access to the measured values within a single local network. The LittleFS file system is used to store web-interface files (HTML/CSS/JS), enabling frontend hosting directly on the controller without any external servers or hosting services.

A functional algorithm of the monitoring system based on WEMOS D1 mini module has been developed, including the following steps (see Fig. 3). At the initial stage, network parameters (SSID and Wi-Fi password) are initialized, followed by mounting of the LittleFS file system that stores web pages and configuration files. Next, the I²C interface is initialized and the functionality of BMP280 and AHT10 sensors is checked to ensure correct measurement of temperature, humidity and barometric pressure. ESP8266 connects to the Wi-Fi network, obtains a local IP address, and launches an asynchronous web server based on the AsyncWebServer and LittleFS libraries, which enables user interaction through a web browser. After the web interface is started, initial limit values of the parameters are set; they can be adjusted in a dedicated settings section. The microcontroller periodically reads data from BMP280 and AHT10 sensors, compares them with the preset limit values, and updates the values on the web interface in real time. If any parameter exceeds the permissible range, the system automatically sends a notification to WhatsApp via the CallMeBot API, which improves responsiveness and user awareness of critical environmental changes. This algorithm ensures autonomous operation of the device, continuous data acquisition, and reliable information delivery through a user-friendly web interface and mobile application.

The software implementation of the functional algorithm was performed in the Arduino IDE environment using the ESPAsyncWebServer, ESPAsyncTCP and LittleFS libraries, as well as sensor drivers such as Adafruit_BMP280 and Thinary_AHT10. During initialization, the serial port is launched for diagnostics, the LittleFS file system is mounted, the I²C interface is initialized and sensor availability is checked, followed by connection to Wi-Fi and startup of an asynchronous HTTP server. After a successful connection, the controller outputs to the serial monitor the local IP address at which the web interface can be accessed (see Fig. 4).

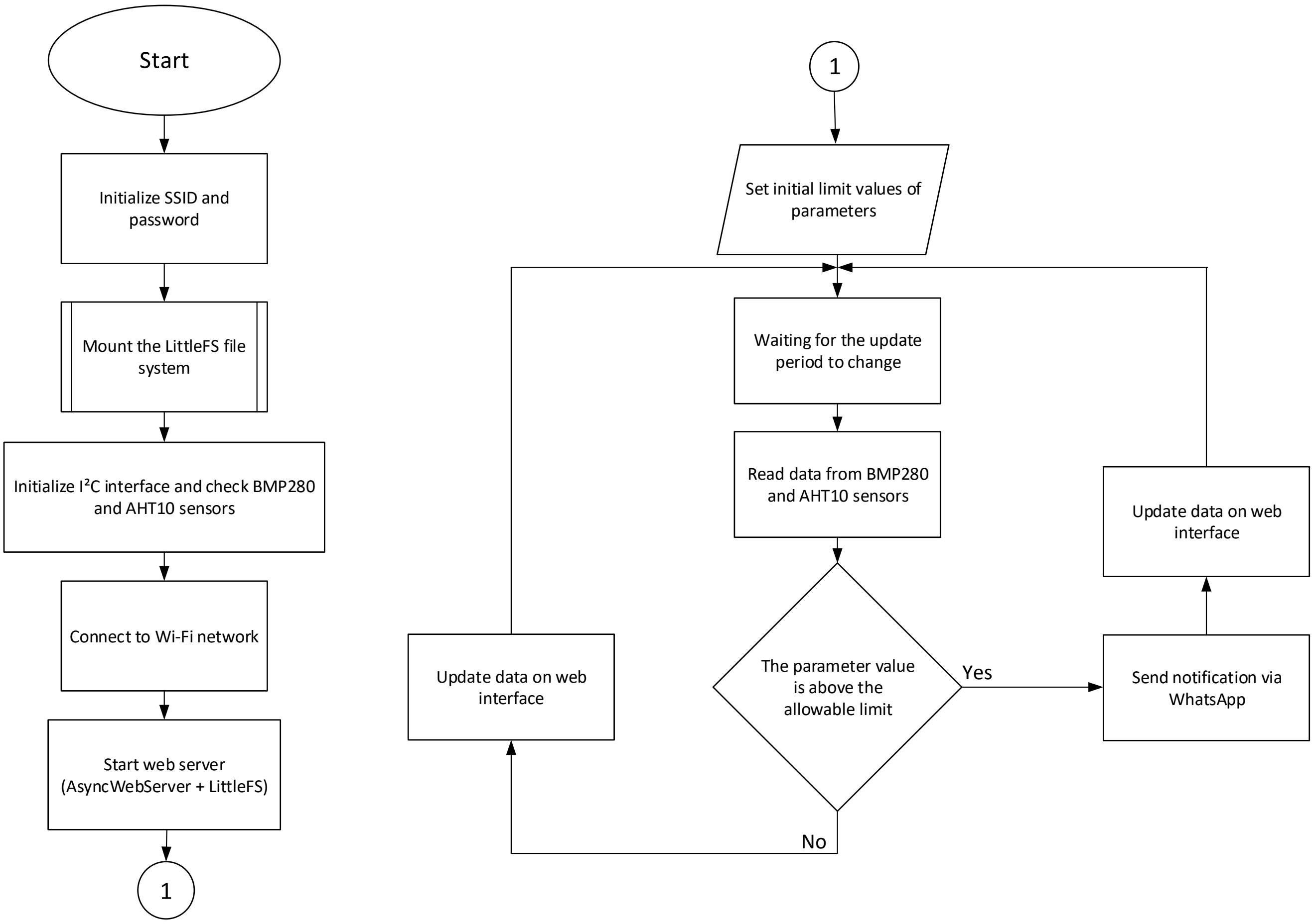

Fig. 3. Block diagram of ESP8266 microcontroller functional algorithm.

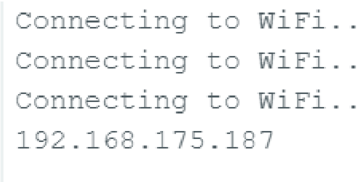

```
Connecting to WiFi..
Connecting to WiFi..
Connecting to WiFi..
192.168.175.187
```

Fig. 4. Obtaining a local IP address to access the web page.

The process of establishing Wi-Fi connection and reading the local IP address is implemented using WiFi.begin(ssid, password) and while (WiFi.status() != WL_CONNECTED) instructions in the controller program.

The asynchronous web server defines routes for the main page (/), for individual trend pages (/temp, /hum, /pres, /all) and for API endpoints returning current parameter values in plain-text format (/temperature, /humidity, /pressure). This enables the web server to perform periodic AJAX requests at specified intervals and retrieve updated data for trend plotting. An example of an API endpoint that returns the temperature value as unformatted data is:

```
server.on("/temperature", HTTP_GET, [](AsyncWebServerRequest *request){
    request->send_P(200, "text/plain", readBMP280Temperature().c_str());
  });
```

Sensor-reading functions include validation of measurements: if a NaN value is received or no response is detected, an error message is displayed in the Serial Monitor and an empty string or error message is returned to the HTTP request. This minimizes incorrect readings and helps to diagnose hardware issues during debugging. If a sensor (such as BMP280) is not initialized, the controller's operation is blocked to prevent further errors.

The user web application interface is implemented entirely with HTML/CSS/JavaScript and stored as files on the controller's flash memory formatted with the LittleFS file system, ensuring autonomous operation. On the main page, the user can select a window to monitor a specific parameter, view all parameters simultaneously, or open a settings page to adjust limit values (Fig. 5).

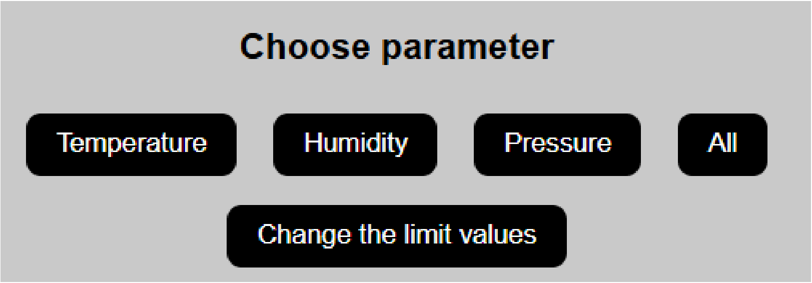

Fig. 5. Main page of the user web application.

Each trend page contains an interactive chart built with the Highcharts library, a field showing the current parameter value, a slider to set the update period (1 to 10 s), and a confirmation button to apply changes. When the page loads, the program automatically sets a timer that executes an AJAX call to the corresponding API endpoint every *N* seconds. The update period is user-defined. Each received value is displayed both on the chart and in the instant value field. Fig. 6 shows the examples of web-application windows displaying temperature, humidity, and air-pressure changes, each with its own instant value field, update-interval slider and "Confirm interval change" button.

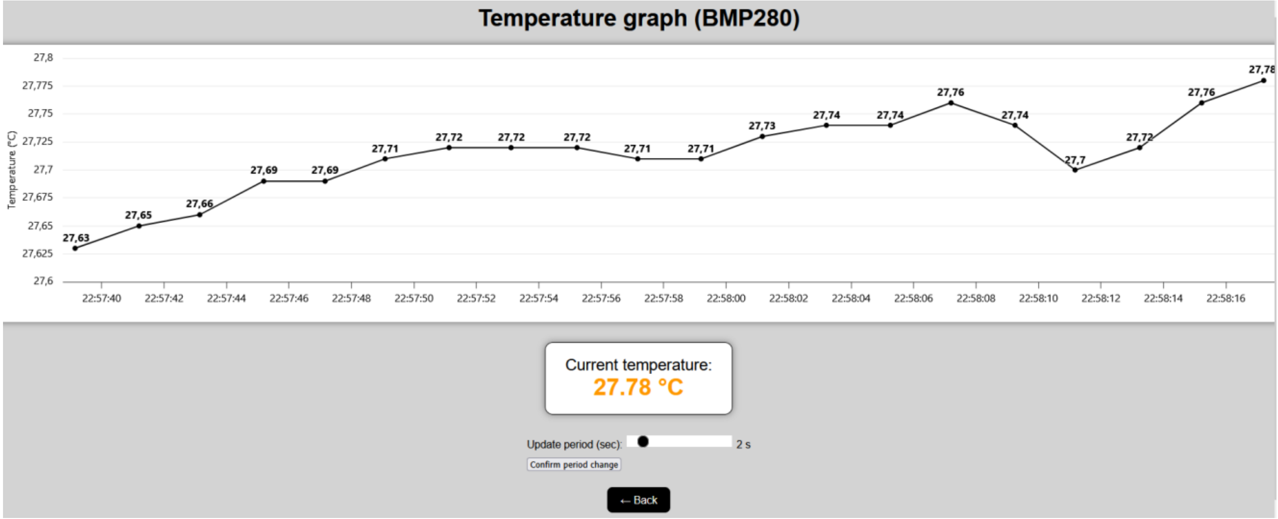

Current temperature:
27.78 °C

Update period (sec): 2 s

a)

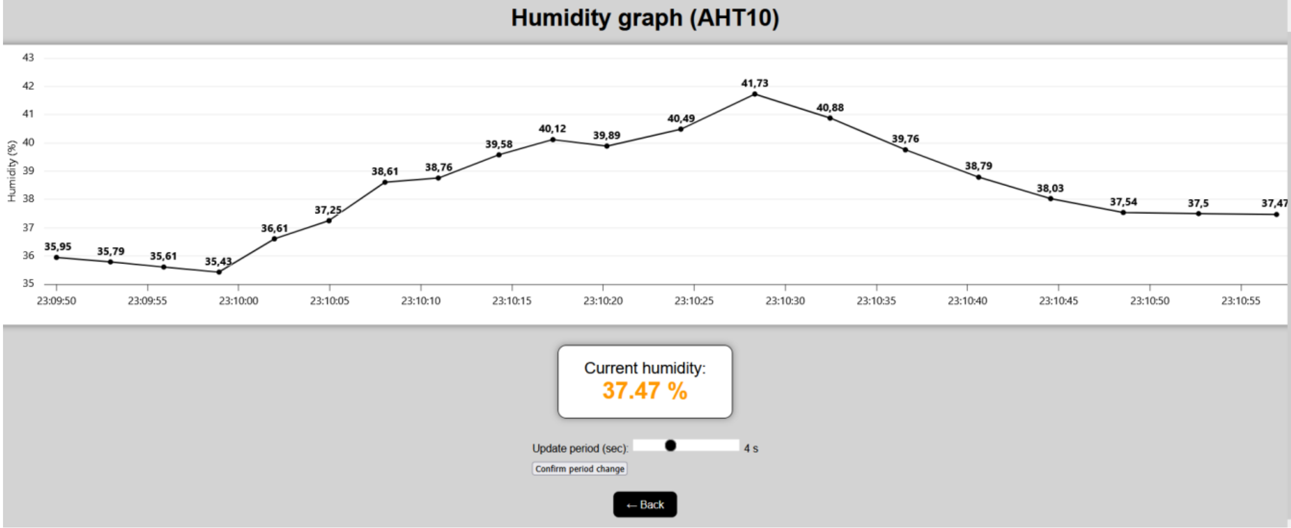

Current humidity:
37.47 %

Update period (sec): 4 s

b)

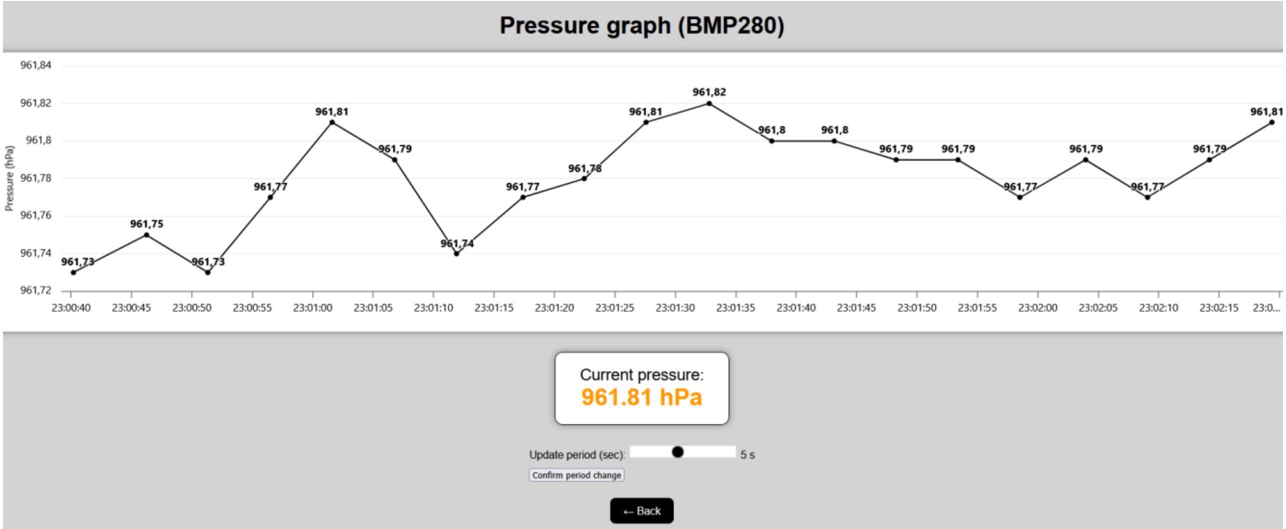

Current pressure:
961.81 hPa

Update period (sec): 5 s

c)

Fig. 6. Web-application windows for monitoring: (*a*) temperature; (*b*) humidity; (*c*) air pressure.

To save the graph data after page reloads, the browser's built-in localStorage mechanism is used, allowing storage of trend point arrays in JSON format and restoration upon reload. Thus, the user can view measurement history without continuous connection to a server or database.

For the page displaying all the graphs, createChart(...) set of functions has been implemented to standardize appearance and behavior. Data updates are handled by a timer responsible for temperature, humidity and pressure, while the update period for all three parameters is controlled by a single slider element (Fig. 7).

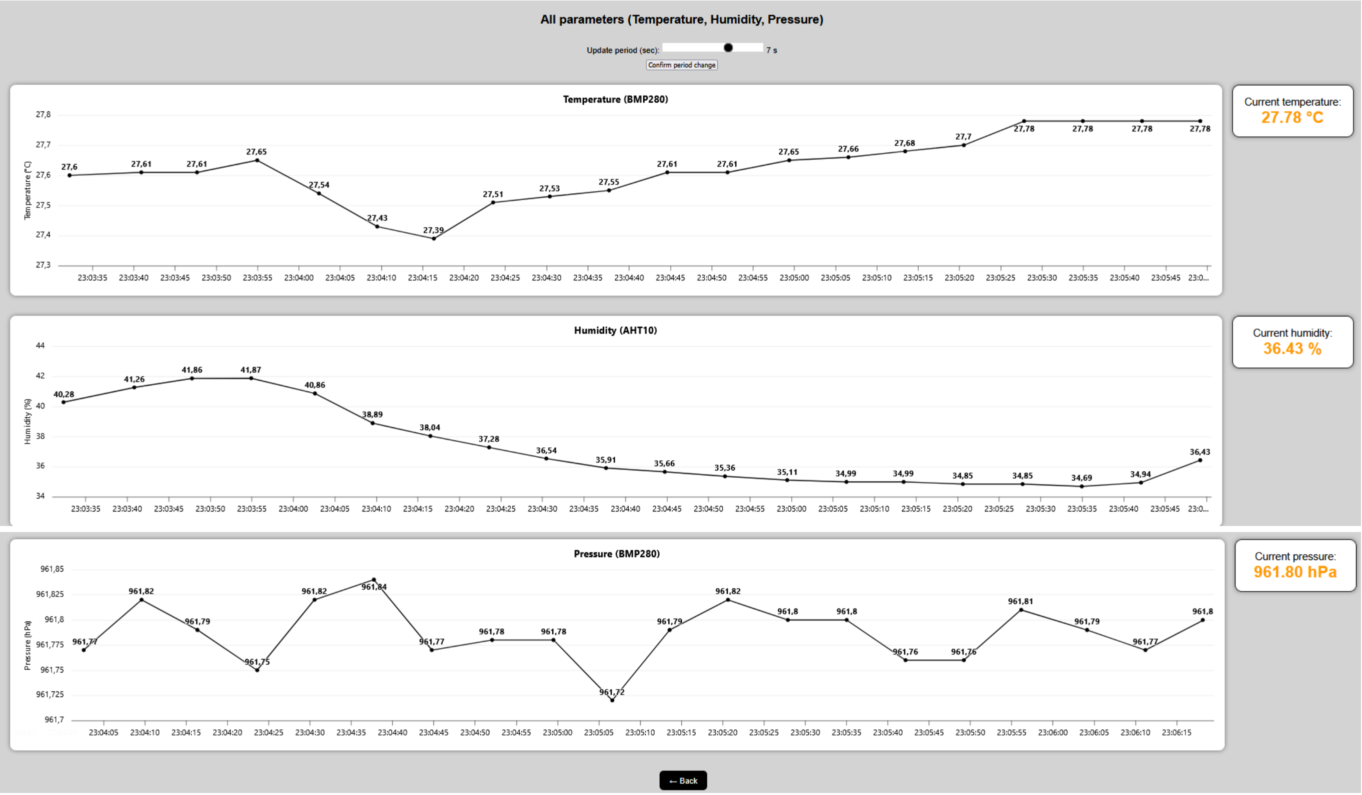
All parameters (Temperature, Humidity, Pressure)

Update period (sec): 7 s

Current temperature: 27.78 °C

Current humidity: 36.43 %

Current pressure: 961.80 hPa

Fig. 7. Monitoring window of all parameters at initial update period of 5 s.

To enhance responsiveness to critical environmental changes, the developed system includes an alert algorithm via WhatsApp messenger. This feature complements the local web interface and enables the user to receive notifications of exceeded limit values of temperature, humidity and pressure directly on a smartphone, even without local-network access. The functionality is implemented through the CallMeBot API, which sends HTTP requests from ESP8266 microcontroller. sendWhatsAppMessage() function forms the request based on the current Wi-Fi connection status and message content.

Within the controller program, the loop() cycle periodically reads data from BMP280 and AHT10, analyzes them and automatically generates WhatsApp alerts when set limit values are exceeded (see Fig. 8). This allows the user to respond promptly to parameter errors without opening the web application.

To set limit values, the user can open the "Change the limit values" page in the browser (see Fig. 9) and adjust them as needed.

The update periods for the bot and AJAX frontend updates should be selected conservatively to avoid connection interruptions. It is also important to keep the token and chat_id confidential and test the system with an active Internet connection, since WhatsApp notifications function only online.

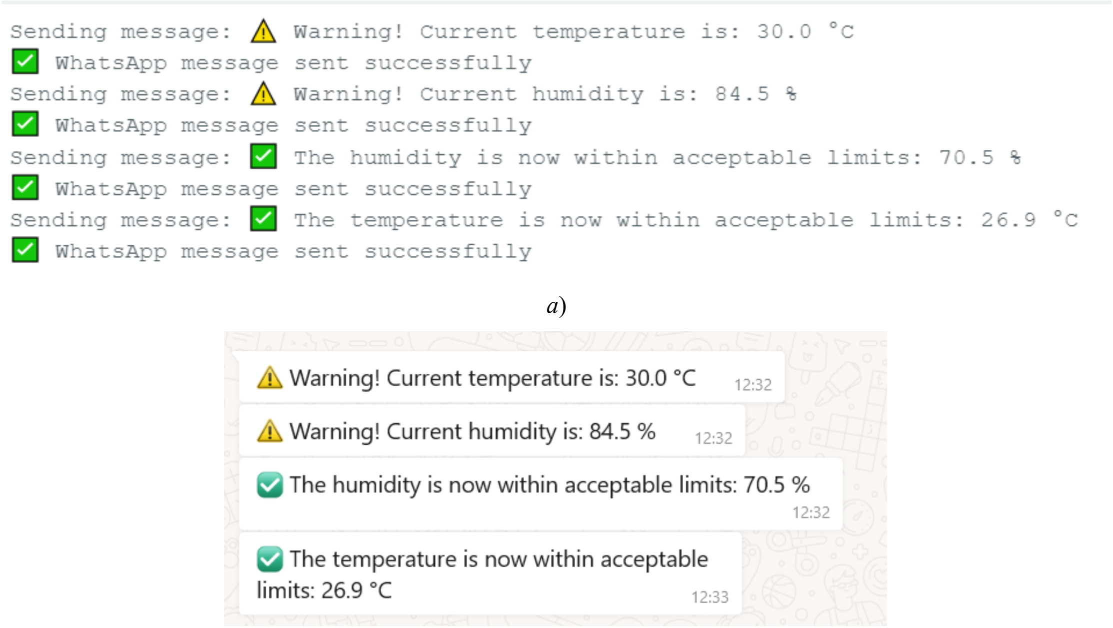

```
Sending message: ⚠️ Warning! Current temperature is: 30.0 °C
✅ WhatsApp message sent successfully
Sending message: ⚠️ Warning! Current humidity is: 84.5 %
✅ WhatsApp message sent successfully
Sending message: ✅ The humidity is now within acceptable limits: 70.5 %
✅ WhatsApp message sent successfully
Sending message: ✅ The temperature is now within acceptable limits: 26.9 °C
✅ WhatsApp message sent successfully
```

a)

⚠️ Warning! Current temperature is: 30.0 °C 12:32

⚠️ Warning! Current humidity is: 84.5 % 12:32

✅ The humidity is now within acceptable limits: 70.5 % 12:32

✅ The temperature is now within acceptable limits: 26.9 °C 12:33

b)

Fig. 8. Example of messages in Arduino IDE Serial Monitor (*a*) and in WhatsApp messenger (*b*) when limit values are checked.

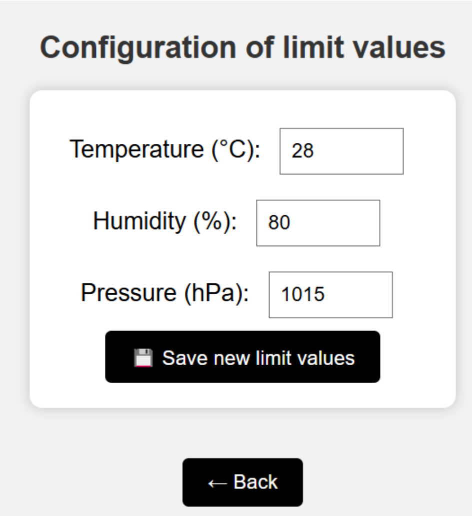

Configuration of limit values

Temperature (°C): 28

Humidity (%): 80

Pressure (hPa): 1015

Fig. 9. Configuration of parameters limit values in the browser window.

During the work, the sensor initialization and data validity were verified, Wi-Fi connection and web interface availability were checked, the update period behavior was evaluated at different intervals (1–10 s) and system stability was assessed under moderate load with multiple LAN clients. It was found that at a 5-second update interval the system operates stably: charts update correctly, and current values are displayed with two decimal places accuracy. When the update period is changed, timers are restarted and frontend behavior is adjusted accordingly. At the minimum polling interval (1 s) and with many simultaneous clients, occasional chart-point skips or increased server response latency may occur.

Both the controller firmware and frontend include basic data-validation mechanisms: check of NaN, control of trend-series length, and limits of maximum message-buffer size. Use of the asynchronous web server (AsyncWebServer) prevents blocking of the main loop and enables parallel request handling, improving multitasking and allowing simultaneous operation of multiple browser tabs within one local network.

Integration of the WhatsApp bot significantly expanded the functionality of the developed monitoring system: it provides real-time remote alerts on out-of-range temperature, humidity and pressure, allows querying of current values, and enables dynamic limit values adjustment without re-flashing the controller. This communication method improves operational convenience and reaction speed while reducing the need for constant web-interface monitoring.

A comparison was made between the developed monitoring system and those presented in other publications. For example, publication [1] proposed an algorithm for generating and sending SMS messages about technological-process status implemented in a PLC program – a solution aimed at integration with existing automation systems using mobile networks for operator notification. Publication [2] describes a smart system for monitoring and protecting energy equipment based on a distributed PLC SIMATIC S7-1200 architecture with message-queue algorithms and SCADA/HMI integration. Both systems offer good industrial scalability but require complex and costly hardware and qualified personnel.

Publication [3] presents a portable station for measuring temperature, humidity, pressure and air quality based on NodeMCU ESP8266. However, its implementation is limited to simple data reading and server transmission, unlike the system proposed here, which provides an interactive web interface with flexible update period settings and real-time visualization, significantly improving functionality.

A similar approach is in publication [4], where an air-pollution monitoring system for urban environments is developed, but its architecture depends on an external data-processing server. In contrast, the implementation presented here, based on ESP8266 with the LittleFS file system, ensures complete autonomy: the web interface is hosted directly on the microcontroller, eliminating the need for external hosting.

Table 1. Comparison results of microclimate parameter monitoring systems.

Source	Advantages of the proposed system	Disadvantages	Brief description
[1] Shaleva et al., 2021	1) Integration with PLC and SCADA; 2) Use of mobile networks for notifications; 3) Focus on industrial applications.	1) Implementation complexity; 2) High system cost.	Monitoring system for technological process parameters using mobile communication networks.
[2] Shaleva et al., 2022	1) Scalability; 2) Application in industrial energy systems; 3) Integration capability with SCADA/HMI.	1) Implementation complexity; 2) High system cost.	Smart system for monitoring technological parameters and protecting energy equipment.
[3] Aashiq et al., 2023	1) Compactness; 2) Portability.	1) Limited web interface functionality, including lack of trend charts and update-frequency settings.	Portable environmental parameter monitoring station based on ESP8266.
[4] Gueye et al., 2024	1) Real-time data transmission to the server; 2) Suitable for urban environments.	1) Dependence on external server and Internet access.	Air-pollution monitoring system.
[6] Al-Okby et al., 2024	1) Integration with robotic platforms; 2) Support for ESP8266/ESP32 and various sensors.	1) Not intended for local visualization; 2) Requires integration with other systems.	Portable sensor node for robot-based monitoring systems.
[7] Anjali & Sukhada, 2022	1) Focus on scalability and urban applications; 2) Integration into the smart city environment.	1) High architectural complexity; 2) Dependence on external services.	IoT-based monitoring system for smart city applications.
[9]-[11] Gupta et al., 2019; Patil & Deshmukh, 2018; Shah & Memon, 2020	1) Low hardware cost; 2) Ease of implementation.	1) Dependence on Internet connectivity; 2) Reduced reliability in case of network failure.	IoT-based monitoring systems using ESP8266 and Arduino with cloud data transmission.

Publications [9]–[11] proposed low-cost models for environmental monitoring using ESP8266, Arduino and cloud platforms. Their main drawback is dependence on stable Internet connections and third-party services. In the proposed system, the user accesses data directly from the local network, ensuring operation even without Internet access. At the same time, the hardware cost (ESP8266 controller and BMP280/AHT10 sensors) remains minimal, making the system affordable for a wide range of applications – from educational projects to domestic and industrial use. This implementation demonstrates an efficient practical approach for building an autonomous ESP8266-based monitoring system combining simple hardware, flexible software architecture, and an intuitive web interface with interactive visualization. The developed system is suitable for educational laboratories, household microclimate control, IoT prototyping, and small local applications, and can serve as a foundation for further scaling to industrial or scientific tasks with additional data-collection and storage integration. The results of the comparison of the analyzed monitoring system characteristics are presented in Table 1.

5. Conclusion

The developed environmental parameter monitoring system based on ESP8266 microcontroller has demonstrated its effectiveness through the combination of hardware and software tools to create an affordable and reliable solution. The integration of BMP280 and AHT10 sensors ensured accurate measurement of temperature, humidity, and atmospheric pressure, while the built-in asynchronous web server enables real-time visualization of results as interactive graphs. An important enhancement of the system is the implementation of a user notification mechanism via the WhatsApp messenger using the CallMeBot service, which allows prompt alerts when limit values are exceeded – even without accessing the web application. This approach increases the level of automation, convenience, and safety of microclimate control, making the system suitable for a wide range of applications.

In the proposed system, the user can access the data directly from the local network, ensuring operability even in the absence of Internet connection. At the same time, the hardware cost (ESP8266 controller and BMP280 and AHT10 sensors) remains minimal, making the system accessible for broad use – from educational projects to household and industrial applications. The developed system is suitable for educational laboratories, household microclimate monitoring, prototyping of small-scale IoT applications and can also serve as a foundation for further scaling to industrial or research tasks through additional integration with data collection and storage services.

References

[1] Shaleva Volodymyr, Matiko Fedir, Krykh Hanna. (2021). Algorithm for operating the system of monitoring the technological process parameters using mobile communication networks. *Selected issues of electrical engineering and electronics : 16th International conference*, Rzeszów 13-15 September, 2021. – p. 1–4.

[2] Shaleva V., Matiko F., Krykh H., Roman V. (2022). Smart system for monitoring technological process parameters and energy equipment protection. *2022 IEEE 8th International Conference on Energy Smart Systems (ESS)* : proceedings (Kyiv, 12–14 October 2022). – p. 216–220.

[3] Aashiq, M.N.M.; Kurera, W.T.C.C.; Thilekaratne, M.G.S.P.; Saja, A.M.A.; Rouzin, M.R.M.; Neranjan, N.; Yassin, H. (2023). An IoT-Based Handheld Environmental and Air Quality Monitoring Station. *Acta IMEKO 2023*, 12, 1–9.

[4] Gueye A, Drame M.S., Niang S.A.A. (2024). A low-cost IoT-based real-time pollution monitoring system using ESP8266 NodeMCU. *Measurement and Control*. 58(10):1337-1345. doi:10.1177/00202940241306690

[5] Huang, Y., Zhao, Q., Zhou, Q., Wanchang, J. (2018). Air Quality Forecast Monitoring and Its Impact on Brain Health based on Big Data and Internet of Things. *IEEE Access*. PP. 1-1. 10.1109/ACCESS.2018.2885142.

[6] Al-Okby, M. F. R., Junginger, S., Roddelkopf, T., Huang, J., Thurow, K. (2024). Ambient Monitoring Portable Sensor Node for Robot-Based Applications. *Sensors*, 24(4), 1295. https://doi.org/10.3390/s24041295

[7] Anjali, D. G., Sukhada, S. (2022). IoT Based Environmental Monitoring System for Smart City. *Proceedings of the 2022 International Conference on Smart Technologies in Computing, Electrical, and Electronics*. IEEE. pp. 175-180.

[8] Dhananjay, K. B., Sandeep, K. S. (2020). IoT-Based Smart Environmental Monitoring System: Design and Implementation. *Proceedings of the 2020 International Conference on Communication and Electronics Systems (ICCES)*. IEEE. pp. 23-27.

[9] Gupta, H., Kumar, S. (2019). Environmental Monitoring System Using IoT. *International Journal of Computer Applications*, 975, 8887. https://doi.org/10.5120/ijca2019918820

[10] Patil, M. S., Deshmukh, S. P. (2018). Smart Environmental Monitoring System Using IoT. *International Journal of Science and Research*, 7(2), 113-117. https://www.ijsr.net/archive/v7i2/ART20192563.pdf

[11] Shah, A. M., Memon, S. (2020). Design of a Smart Environmental Monitoring System Using IoT. *International Journal of Computer Applications*, 975, 8887. https://doi.org/10.5120/ijca2020910665

[12] BMP280 - Ultra-Low Power Sensor for Barometric Pressure and Temperature. https://www.bosch-sensortec.com/media/boschsensortec/downloads/product_flyer/bst-bmp280-fl000.pdf

[13] S. Zafar, G. Miraj, R. Baloch, D. Murtaza, K. Arshad. (2018). An IoT Based Real-Time Environmental Monitoring System Using Arduino and Cloud Service. *Eng. Technol. Appl. Sci. Res.*, vol. 8, no. 4, Aug. 2018, pp. 3238–3242.

[14] Manisalidis, I., Stavropoulou, E., Stavropoulos, A., Bezirtzoglou, E. (2020). Environmental and Health Impacts of Air Pollution: A Review. *Frontiers in public health*, *8*, 14. https://doi.org/10.3389/fpubh.2020.00014

[15] J. Jo, B. Jo, J. Kim, S. Kim, W. Han. (2020). Development of an IoT-Based Indoor Air Quality Monitoring Platform. *J. Sens.*, vol. 2020, 1-14. 10.1155/2020/8749764.

[16] A. Kulkarni, D. Mukhopadhyay. (2018). Internet of Things Based Weather Forecast Monitoring System. *Indones. J. Electr. Eng. Comput. Sci.*, vol. 9, no. 3, pp. 555–557.

[17] N. A. Zakaria, Z. Zainal, N. Harum, L. Chen, N. Saleh, F. Azni. (2018). Wireless Internet of Things-Based Air Quality Device for Smart Pollution Monitoring. *Int. J. Adv. Comput. Sci. Appl.*, vol. 9, no. 11, pp. 65–69

[18] Gryech, I., Ben-Aboud, Y., Guermah, B., Sbihi, N., Ghogho, M., Kobbane, A. (2020). MoreAir: A Low-Cost Urban Air Pollution Monitoring System. *Sensors*, 20(4), 998. https://doi.org/10.3390/s20040998

[19] Carlos-Mancilla, M. A., Luque-Vega, L. F., Guerrero-Osuna, H. A., Ornelas-Vargas, G., Aguilar-Molina, Y., González-Jiménez, L. E. (2021). Educational Mechatronics and Internet of Things: A Case Study on Dynamic Systems Using MEIoT Weather Station. *Sensors*, 21(1), 181. https://doi.org/10.3390/s21010181

[20] Santos R. (2024) Getting Started with ESP8266 NodeMCU Development Board. *Random Nerd Tutorials*. https://randomnerdtutorials.com/projects-esp8266/.

[21] Patnaikuni D. (2017). A comparative study of Arduino, Raspberry Pi and ESP8266 as IoT development board. *Int. J. Adv. Res. Comput. Sci.*; 8(9): 2350–2352. https://doi.org/10.26483/ijarcs.v8i5.3959

Система віддаленого моніторингу параметрів мікроклімату для розумного будинку та виробничих приміщень на основі мікроконтролера ESP8266

Павло Скібель, Федір Матіко, Ігор Демків

Національний університет «Львівська політехніка», вул. С. Бандери, 12, Львів, 79013, Україна

Анотація

У статті виконано аналіз розробок у сфері моніторингу параметрів навколишнього середовища із застосуванням мікроконтролерів та технологій Інтернету речей, за результатами якого обґрунтовано застосування мікроконтролера ESP8266**.** Розроблено систему моніторингу параметрів мікроклімату (температури, вологості та атмосферного тиску повітря) у розумному будинку та виробничих приміщеннях на базі мікроконтролера ESP8266, яка продемонструвала ефективність завдяки поєднанню апаратних і програмних засобів. Інтеграція сенсорів BMP280 та AHT10 забезпечила точне вимірювання температури, вологості та атмосферного тиску, а інтегрований в ESP8266 асинхронний web-сервер дозволяє відображати результати у вигляді інтерактивних графіків у реальному часі. У розробленій системі користувач отримує доступ до даних напряму з локальної мережі, що гарантує працездатність навіть за відсутності доступу до Інтернету. При цьому вартість апаратної частини (контролер ESP8266 і сенсори BMP280 та AHT10) залишається мінімальною, що робить систему доступною для широкого використання. Важливим доповненням стало впровадження системи сповіщень користувача через месенджер WhatsApp із використанням сервісу CallMeBot, що дало змогу оперативно інформувати користувача про перевищення граничних значень параметрів навіть без входу у web-додаток. Такий підхід підвищує рівень автоматизації, зручності та надійності контролю мікроклімату, роблячи систему придатною для широкого кола задач у побуті та промисловості.

Ключові слова: параметри мікроклімату; розумний будинок; система моніторингу; мікроконтролер; Інтернет речей; web-додаток.

ENERGY ENGINEERING AND CONTROL SYSTEMS

Volume 11, Number 2, 2025

Transformer-Based Network for Robust 3D Industrial Environment Understanding in Autonomous UAV Systems

Oleksii Kuchkin, Artem Sazonov*, Iryna Cherepanska, Anatoliy Zhuchenko

National Technical University of Ukraine "Igor Sikorsky Kyiv Polytechnic Institute",
37 Peremohy Ave., Kyiv, 03056, Ukraine

Received: October 15, 2025. Revised: December 11, 2025. Accepted: December 18, 2025.

Abstract

Autonomous navigation of unmanned aerial vehicles (UAVs) in unstructured industrial environments remains challenging due to irregular geometry, dynamic obstacles and sensor uncertainty. Classical Simultaneous Localization and Mapping (SLAM) systems, though geometrically consistent, often fail under poor initialization, textureless areas or reflective surfaces. To overcome these issues, this work proposes a hybrid transformer-geometric framework that fuses learned scene priors with keyframe-based SLAM. A TinyViT encoder and lightweight multi-task decoder jointly estimate inverse depth, surface normals and semantic segmentation, providing dense geometric and semantic cues that stabilize localization and mapping. These priors are incorporated into the SLAM optimization to enhance convergence, reject dynamic objects and improve relocalization. The system operates near real-time (~1 FPS) on a Raspberry Pi 5 CPU, suitable for keyframe-level inference. Experiments show robust localization and consistent mapping in cluttered, reflective and dynamic industrial scenes, confirming that transformer-based dense perception effectively complements classical SLAM for resource-efficient UAV navigation.

Keywords: UAV robust control; computer vision; SLAM; transformer-based neural network; autonomous navigation; 3D environment understanding.

1. Introduction

Autonomous navigation of unmanned aerial vehicles (UAVs) i.e. quadcopters in unstructured industrial environments remains a vital task for modern mobile robotics. In such settings, the surrounding scene is typically characterized by irregular geometry, varying illumination, dynamic obstacles and sensor noise. These factors lead to incomplete or inconsistent sensory data, making real-time localization, mapping, and trajectory planning highly uncertain. Moreover, the limited computational resources available on embedded systems further constrain the use of computationally intensive algorithms for reliable navigation.

Conventional Simultaneous Localization and Mapping (SLAM) methods, though widely used, remain limited when applied to stochastic and unstructured environments. Traditional feature-based or keyframe-based SLAM approaches rely heavily on precise initial conditions and accurate sensor calibration. Without sufficiently accurate initialization, the optimization problem behind SLAM may diverge or converge to suboptimal local minima. Furthermore, these methods typically assume static or near-static environments, while industrial spaces often contain reflective, transparent or dynamic objects that produce unstable key-points and degrade the quality of the generated map. As a result, the robustness and reliability of autonomous navigation are significantly reduced under real-world conditions.

---

* Corresponding author. Email address: a.sazonov@kpi.ua

This paper should be cited as: O. Kuchkin, A. Sazonov, I. Cherepanska, A. Zhuchenko. (2025). Transformer-based network for robust 3D industrial environment understanding in autonomous UAV systems. *Energy Engineering and Control Systems*, Vol. 11, No. 2, pp. 210 – 216. https://doi.org/10.23939/jeecs2025.02.210

To address these challenges, recent developments in neural scene understanding offer a promising alternative. Transformer-based neural architectures demonstrate exceptional capabilities when capturing long-range dependencies and global spatial relationships in both two-dimensional and three-dimensional data. Unlike convolutional networks, transformers process visual information through self-attention mechanisms, enabling them to model context and uncertainty across the entire visual field. This property is extremely beneficial for unstructured scenes, where local geometric cues alone are insufficient for reliable understanding and further autonomous navigation.

In this work, we propose a transformer-based approach for predicting 3D scene parameters – such as depth, surface normal orientation, semantic segmentation, and object class distributions – directly from visual observations. The predicted scene structure serves as a prior for keyframe-based SLAM, providing an informed initialization that improves convergence stability and reduces localization errors. Additionally, semantic segmentation allows the system to exclude points associated with reflective or dynamically moving objects from the optimization process, preventing instability in pose estimation. When trained on large-scale datasets encompassing diverse visual contexts, including segmentation supervision derived from EfficientSAM, the model demonstrates robust generalization across a wide range of industrial environments and illumination conditions.

The integration of transformer-based scene prediction with traditional SLAM approaches enables a hybrid navigation framework that combines the interpretability of geometric methods with deep learning adaptiveness. Such a hybrid approach enhances localization robustness, reduces computational overhead and enables more efficient decision-making for autonomous quadcopter control in stochastic and dynamically changing unstructured industrial environments.

2. Analysis of related works

Autonomous UAV navigation in unstructured and visually challenging industrial environments lies at the convergence of geometric SLAM, learning-based perception, and resource-constrained onboard control. Classical geometric SLAM-both key-frame and feature-based pipelines (e.g., ORB-style systems, direct dense methods)-remains widely used due to well-understood models of camera geometry, principled optimization, and interpretability. However, such systems exhibit characteristic failure modes under real-world conditions: poor or ambiguous initialization, reflective or transparent surfaces, dynamic obstacles, or high sensor noise [1], [2]. Critically, bundle adjustment and pose-graph optimization depend on reasonably accurate initial poses and reliable correspondences. When these prerequisites are violated, the resulting non-linear optimization may diverge or converge to incorrect local minima, producing tracking dropouts or severely distorted maps [2], [3].

To alleviate these limitations of purely geometric pipelines, a second class of approaches augments SLAM with learned priors. These hybrid geometric-neural methods integrate compact depth codes, CNN-based dense prediction models, or latent scene representations into the optimization loop [3], [4]. By providing coarse but globally consistent scene structure, such priors improve robustness in weakly textured or ambiguous regions and regularize dense mapping. Yet the majority of these approaches still rely on convolutional backbones or low-dimensional latent codes, which inherently limit the ability to model long-range spatial dependencies and global context – an important aspect of complex industrial scenes with clutter, large structures, and variable lighting.

A third category, neural SLAM and neural-implicit mapping, replaces explicit geometric representations with learned continuous fields. Neural radiance field (NeRF)-inspired methods, neural implicit mapping (e.g., NICE-SLAM) and end-to-end learned tracking-mapping architectures [5], [6] can recover high-fidelity scene geometry and demonstrate resilience to noise or partial observations. Nevertheless, because these systems typically maintain dense neural fields or multi-level feature grids, they suffer from scalability constraints and are difficult to deploy on resource-limited UAV platforms that require strict real-time guarantees. Although hierarchical latent grids and local implicit representations partially mitigate this overhead, integrating these dense neural structures with real-time control pipelines and onboard estimation remains an open challenge [7].

A more recent lineage of SLAM-relevant research investigates transformer-based perception and multimodal fusion as a means to enhance mapping inputs. Vision Transformers (ViTs), hierarchical variants such as Swin, as well as transformer-based dense predictors and point-cloud transformers (e.g., DPT, Point Transformer) demonstrate strong global reasoning capabilities for depth estimation, surface normal prediction, and semantic segmentation [8]–[11]. Furthermore, multimodal transformers-such as BEV/3D fusion models (e.g., BEVFormer, TransFusion)-leverage global cross-attention to align heterogeneous inputs (RGB, depth, LiDAR, inertial cues) and temporal information, which directly aligns with UAV sensing conditions under calibration uncertainty [12]. For tasks central to SLAM, transformer-augmented depth and segmentation networks (e.g., AdaBins, DPT, BinsFormer) provide improved accuracy and uncertainty estimation, while large pre-trained models such as SAM and EfficientSAM supply reliable masks that enable filtering of dynamic or reflective objects during geometric optimization [13]–[16].

Finally, learned optimization frameworks represent a distinct category that reinterprets tracking and mapping as differentiable iterative refinement. Systems such as DROID-SLAM show that learned, recurrent update rules can improve resilience to poor initialization and reduce catastrophic failures without fully replacing the geometric pipeline [16]. These frameworks highlight an emerging direction: using learned modules not as end-to-end replacements, but as components that supply robust priors or corrections to traditional SLAM optimization.

Across these SLAM paradigms-geometric, hybrid geometric–neural, neural-implicit, transformer-based perception, and learned optimization – emerges a common insight: geometric SLAM remains efficient, explainable, and suited to real-time UAV deployment, but its performance degrades in visually challenging conditions; meanwhile, fully neural alternatives offer richer scene understanding but often impose prohibitive computational and scalability costs. This motivates a balanced strategy in which learning contributes high-level global scene priors while geometric optimization maintains accuracy and real-time reliability. The approach proposed in this work follows precisely this principle: a transformer-based dense perception module is executed only on keyframes to predict depth, surface normals, semantic masks, and uncertainty maps, which then provide informed initialization and robust correspondence selection for a conventional key-frame SLAM backend. By restricting learned inference to keyframes and leveraging segmentation-aware rejection of unstable points, the system preserves the efficiency and interpretability of geometric SLAM while substantially improving convergence stability and robustness in industrial UAV environments characterized by reflective materials, dynamic objects and variable lighting.

3. Algorithms and methods

This section outlines the proposed hybrid perception and mapping framework, which integrates transformer-based dense prediction with traditional keyframe-based SLAM for robust autonomous navigation in unstructured industrial environments. The overall system comprises a lightweight transformer encoder-decoder network for multi-task scene understanding and a tightly coupled SLAM module that exploits the predicted geometric and semantic priors to improve localization stability and mapping fidelity.

3.1. Overview

In this work, we propose a hybrid perception and mapping framework designed for autonomous UAV navigation in unstructured industrial environments. The framework leverages a transformer-based encoder-decoder architecture to generate dense predictions of inverse depth, surface normals, and semantic segmentation from monocular RGB inputs. These dense priors are subsequently integrated into a keyframe-based VIO backend to enhance robustness and reduce the risk of divergence during bundle adjustment. The high-level architecture is depicted in Fig. 1. A TinyViT backbone serves as the lightweight visual encoder, providing multi-scale features to a multi-head decoder.

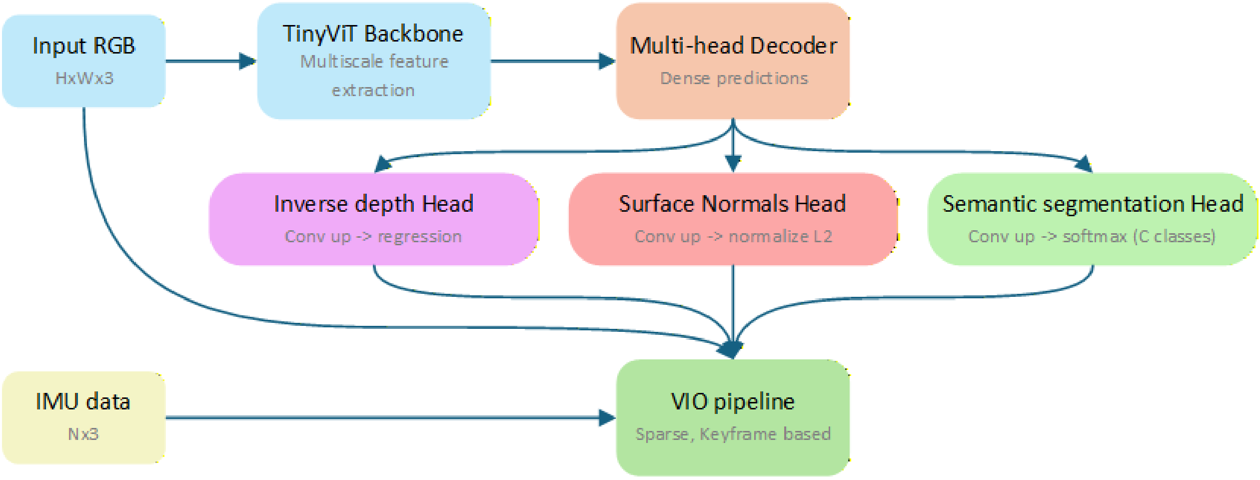

Fig. 1. High-level architecture of the proposed framework.

The decoder outputs three complementary modalities:

1) Inverse depth maps, providing scene geometry cues even in textureless regions.

2) Surface normals, enforcing local geometric consistency.

3) Semantic segmentation masks, facilitating the rejection of dynamic or reflective surfaces.

The predicted outputs are fused into the SLAM module to guide pose-graph optimization and improve convergence reliability.

3.2. TinyViT backbone and decoder design

The TinyViT backbone [1] was selected for its balance between representational capacity and computational efficiency, enabling deployment on resource-constrained UAV hardware. It processes monocular RGB images to extract hierarchical feature representations at multiple spatial resolutions.

The decoder, shown in Fig. 2, adopts a multi-task structure with three dedicated output branches for inverse depth, surface normals, and semantic segmentation. Each branch employs convolutional upsampling with skip connections from the corresponding TinyViT layers, thereby maintaining high-resolution spatial information while minimizing computational cost.

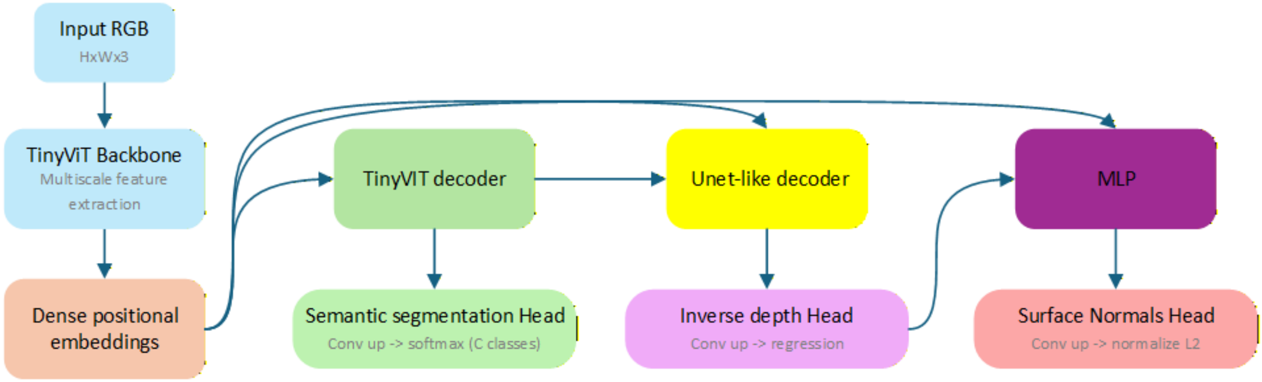

Fig. 2. Transformer-based network architecture.

This design enables joint optimization across complementary geometric and semantic cues, which has been shown to improve prediction stability and cross-task consistency in dense scene understanding.

3.3. Data and training

The model is trained on widely used 3D perception datasets that provide synchronized RGB, depth, normal, and semantic labels:

- NYUv2 [17]: indoor scenes with dense depth and semantic labels.
- ScanNet [18]: large-scale indoor scans with rich geometry and object classes.
- TUM-RGBD [19]: sequences suitable for evaluating SLAM performance in dynamic and cluttered environments.

To improve generalization, data augmentations include random cropping, photometric distortion, and horizontal flipping. The total loss function is defined as:

$$L = \lambda_d L_{depth} + \lambda_n L_{normals} + \lambda_s L_{segmentation}, \tag{1}$$

where L_{depth} is the L1 loss on inverse depth; $L_{normals}$ is the cosine distance between predicted and ground-truth normals; $L_{segmentation}$ is the standard cross-entropy loss; $\lambda_d, \lambda_n, \lambda_s$ are the weights (they are tuned empirically to balance geometric and semantic supervision).

3.4. Integration with SLAM

The integration between the transformer-based predictor and the geometric SLAM module is central to the proposed system. The predicted priors are incorporated at multiple stages of the SLAM pipeline:

1) Depth and normal priors are used to initialize 3D landmarks in each keyframe, providing improved geometric consistency for bundle adjustment.
2) Segmentation masks filter out features corresponding to reflective, transparent, or dynamic objects (e.g., machinery in motion or operator presence), preventing them from corrupting the optimization process.
3) Uncertainty weighting is introduced by leveraging per-pixel confidence maps from the network to modulate residuals in the optimization objective, effectively guiding the solver toward reliable measurements.
4) Pose refinement employs a modified cost function:

$$E = \sum_i w_i \|r_i(T)\|^2, \tag{2}$$

where w_i are confidence weights derived from the neural priors; $r_i(T)$ are photometric and geometric residuals.

By combining learned priors with geometric optimization, the hybrid system achieves improved convergence from poor initial conditions, enhanced map consistency, and increased robustness in the presence of environmental uncertainty. An illustration of the fused predictions-depth, normals, and segmentation is shown in Fig. 3, highlighting how geometric and semantic cues complement each other to produce reliable scene representations even under challenging lighting and cluttered conditions.

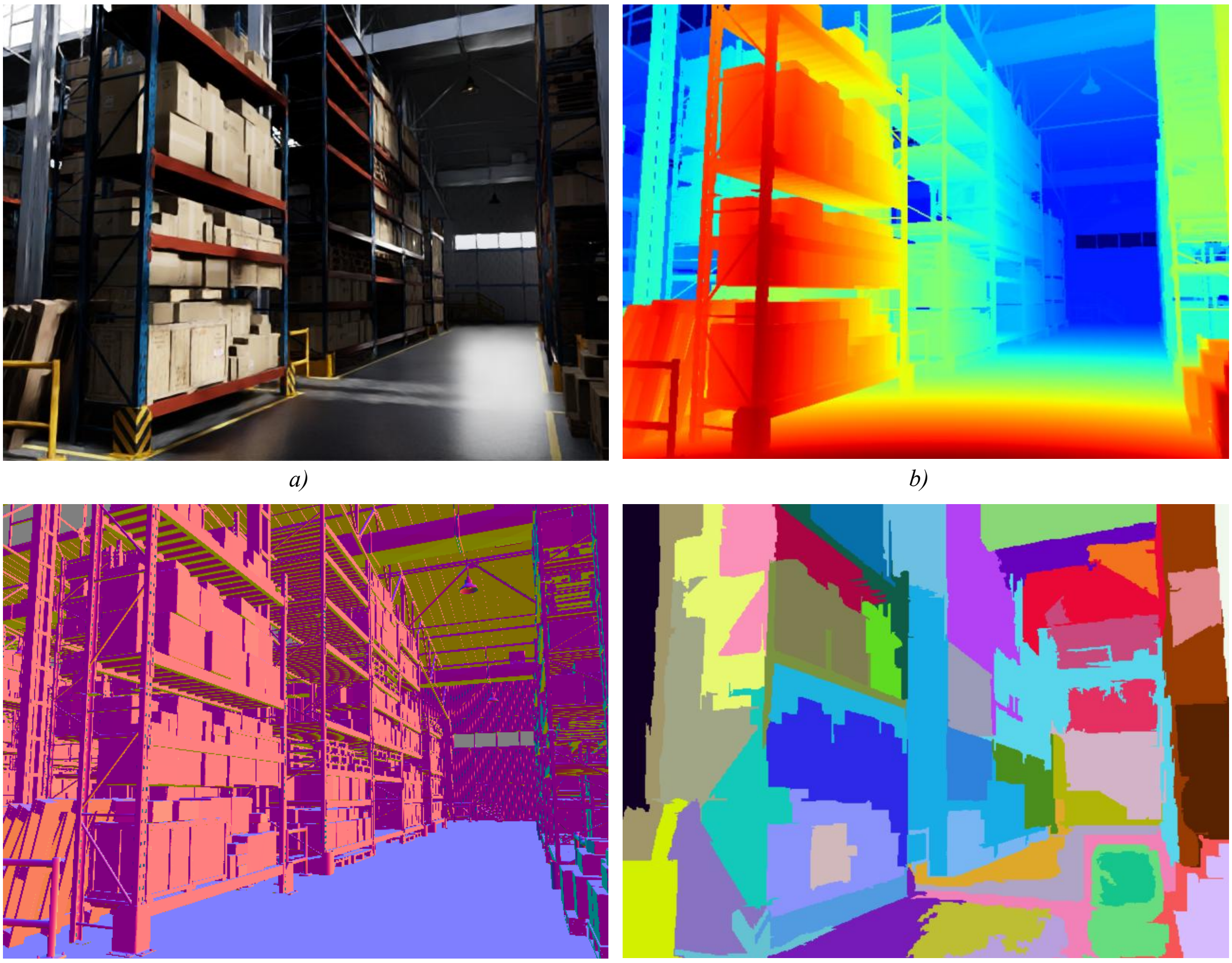

a) *b)*

c) *d)*

Fig. 3. Example predictions from the multi-task decoder: (*a*) input RGB image, (*b*) inverse-depth map, (*c*) surface-normal map, and (*d*) semantic segmentation.

3.5. Computational considerations

The proposed architecture is designed with the computational limitations of embedded onboard systems in mind. In particular, the entire inference pipeline is capable of running on a Raspberry Pi 5 using CPU-only processing, without the need for any dedicated GPU accelerator. Despite the modest computational resources, the transformer-based predictor achieves an average throughput of approximately one frame per second.

Although this frame rate might appear low compared to high-performance computing setups, it remains entirely adequate for the target application. The model is invoked exclusively on keyframes, primarily during relocalization or loop-closure events within the SLAM pipeline – operations that typically occur at a temporal frequency close to one second. Consequently, the computational burden imposed by the neural predictor does not hinder real-time navigation or control.

The TinyViT encoder ensures efficient feature extraction through a compact hybrid convolution-attention design, while the multi-task decoder reuses shared feature hierarchies to minimize redundant computation across depth, normal and segmentation outputs. As a result, the overall system maintains a favorable trade-off between semantic richness, geometric reliability, and energy efficiency, enabling practical onboard deployment on resource-constrained aerial platforms.

4. Conclusion

This paper introduced a hybrid perception-localization framework designed for UAV navigation in unstructured industrial environments, where classical geometric SLAM systems often fail due to poor initialization, textureless regions, reflective surfaces or dynamic elements. By combining a lightweight transformer-based encoder (TinyViT) with a shared multi-task decoder predicting inverse depth, surface normals and semantic segmentation, the proposed method provides rich geometric and semantic priors that guide and stabilize subsequent keyframe-based SLAM optimization.

Unlike purely geometric pipelines, the presented system maintains reliable localization even under partial occlusions, illumination changes or non-Lambertian surfaces – conditions common in industrial halls, workshops or storage areas. The learned priors supply accurate depth and normal structure in regions where visual features are sparse, while segmentation enables selective rejection of unstable or dynamic regions during bundle adjustment. This synergy between learned perception and geometric optimization significantly enhances map consistency, pose convergence, and relocalization reliability.

Despite being executed on a low-power embedded platform (Raspberry Pi 5, CPU-only), the neural module achieves approximately 1 frame per second, which is fully sufficient given its role in keyframe-level correction rather than per-frame tracking. This makes the overall system practical for onboard deployment, satisfying real-time constraints while preserving robustness and interpretability.

In summary, the proposed hybrid approach demonstrates that combining transformer-based dense perception with traditional SLAM backends enables robust localization in highly unstructured, cluttered and noisy environments, bridging the gap between data-driven scene understanding and precise geometric mapping. This line of research opens the way toward fully autonomous UAV systems capable of long-term, stable operation in complex industrial scenarios without dependence on external infrastructure or high-end hardware.

References

[1] Pistun, Y. , Lesovoy, L. , Matiko, F., Fedoryshyn, R. (2014). Computer Aided Design of Differential Pressure Flow Meters. *World Journal of Engineering and Technology*, **2**, 68-77. doi: 10.4236/wjet.2014.22009.

[2] A. Dosovitskiy, L. Beyer, A. Kolesnikov, D. Weissenborn, X. Zhai, T. Unterthiner, M. Dehghani, M. Minderer, G. Heigold, S. Gelly and J. Uszkoreit. (2020). An Image is Worth 16×16 Words: Transformers for Image Recognition at Scale. *arXiv preprint* arXiv:2010.11929.

[3] Z. Liu, Y. Lin, Y. Cao, H. Hu, Y. Wei, Z. Zhang, S. Lin and B. Guo. (2021). Swin Transformer: Hierarchical Vision Transformer using Shifted Windows. *Proc. IEEE/CVF International Conference on Computer Vision (ICCV)*, Montreal, QC, Canada, Oct. 10-17 2021, pp. 10012-10022.

[4] Z. Teed and J. Deng. (2021). DROID-SLAM: Deep Visual SLAM for Monocular, Stereo, and RGB-D Cameras. *Advances in Neural Information Processing Systems (NeurIPS)*, vol. 34/35. arXiv:2108.10869

[5] Z. Zhu, S. Peng, et al. (2022). NICE-SLAM: Neural Implicit Scalable Encoding for SLAM. *Proc. IEEE/CVF Conference on Computer Vision and Pattern Recognition (CVPR)*. arXiv:2112.12130

[6] J. Czarnowski, T. Laidlow, R. Clark and A. J. Davison. (2020). DeepFactors: Real-Time Probabilistic Dense Monocular SLAM. *IEEE Robot. Autom. Lett.* arXiv:2001.05049

[7] X. Zhai, J. Wu, Y. Wang, K. Ye, S. Ruan, et al. (2021). Scaling Vision Transformers. *arXiv preprint* arXiv:2106.04560.

[8] Y. Chen, C.–F. Chen, Z. Dong, T. Wu, et al. (2021). CrossViT: Cross-Attention Multi-Scale Vision Transformer for Image Classification. *Proc. IEEE/CVF International Conference on Computer Vision (ICCV)*. https://doi.org/10.48550/arXiv.2103.14899

[9] X. Dong, J. Bao, D. Chen, W. Zhang, N. Yu, L. Yuan, D. Chen and B. Guo. (2021). CSWin Transformer: A General Vision Transformer Backbone with Cross-Shaped Windows. *arXiv preprint* arXiv:2107.00652.

[10] X. Zhang, Y. Tian, W. Huang, Q. Ye, L. Xie and Q. Tian. (2022). HiViT: Hierarchical Vision Transformer Meets Masked Image Modeling. *arXiv preprint* arXiv:2205.14949.

[11] A. Hassani and H. Shi. (2022). Dilated Neighborhood Attention Transformer. *arXiv preprint* arXiv:2209.15001.

[12] X. Yu, et al. (2023). Mix-ViT: Mixing Attentive Vision Transformer for Ultra-Fine-Grained Visual Classification. *Signal Processing*, vol. 215. https://doi.org/10.1016/j.patcog.2022.109131

[13] X. Bai, Z. Hu, X. Zhu, et al. (2022). TransFusion: Robust LiDAR-Camera Fusion for 3D Object Detection with Transformers. *Proc. IEEE/CVF Conference on Computer Vision and Pattern Recognition (CVPR)*. arXiv:2203.11496

[14] Z. Li, W. Wang, E. Xie, et al. (2022). BEVFormer: Learning Bird's-Eye-View Representation from Multi-Camera Images via Spatio-Temporal Transformers. *Proc. European Conference on Computer Vision (ECCV)*. arXiv:2203.17270

[15] A. Kirillov, E. Mintun, N. Ravi, et al. (2023). Segment Anything (SAM). *arXiv preprint* arXiv:2304.02643.

[16] Y. Xiong, B. Varadarajan, et al. (2024). EfficientSAM: Leveraged Masked Image Pretraining for Efficient Segment Anything. *Proc. IEEE/CVF Conference on Computer Vision and Pattern Recognition (CVPR)*. arXiv:2312.00863

[17] N. Silberman, D. Hoiem, P. Kohli, and R. Fergus. (2012). NYU Depth Dataset V2. [Online]. Available: https://cs.nyu.edu/~silberman/datasets/nyu_depth_v2.html

[18] A. Dai, A. X. Chang, M. Savva, et al. (2017). ScanNet: Richly-annotated 3D Reconstructions of Indoor Scenes. [Online]. Available: http://www.scan-net.org/

[19] J. Sturm, N. Engelhard, F. Endres, W. Burgard, and D. Cremers. (2012). A Benchmark for the Evaluation of RGB-D SLAM Systems. [Online]. Available: https://vision.in.tum.de/data/datasets/rgbd-dataset

Нейромережа трансформерного типу для робастного розуміння тривимірного промислового середовища в автономних системах БПЛА

Олексій Кучкін, Артем Сазонов, Ірина Черепанська, Анатолій Жученко

Національний технічний університет України «Київський політехнічний інститут імені Ігоря Сікорського»,
просп. Перемоги, 37, м. Київ, 03056, Україна

Анотація

Автономна навігація безпілотних літальних апаратів (БПЛА) в неструктурованих промислових середовищах залишається складним завданням через нерегулярну геометрію, динамічні перешкоди та невизначеність сенсорних даних. Класичні системи SLAM, попри геометричну узгодженість, часто виявляються нестійкими за умов поганої ініціалізації, відсутності текстури або наявності віддзеркалювальних поверхонь. Щоб подолати ці обмеження, у роботі запропоновано гібридний трансформерно-геометричний підхід, який поєднує навчальні апріорні уявлення сцени з ключовим SLAM-конвеєром. Енкодер TinyViT та легковаговий мультизадачний декодер спільно оцінюють зворотну глибину, нормалі поверхні та семантичну сегментацію, формуючи густі геометричні й семантичні підказки, що стабілізують локалізацію й побудову карти. Ці апріорні дані інтегруються в оптимізацію SLAM для прискорення збіжності, відкидання динамічних об'єктів та покращення релокалізації. Система працює майже в реальному часі (~1 FPS) на CPU Raspberry Pi 5, що робить її придатною для покадрового інференсу. Експерименти демонструють стійку локалізацію та консистентне картографування у захаращених, віддзеркалювальних і динамічних промислових сценах, підтверджуючи, що трансформерна густинна перцепція ефективно доповнює класичний SLAM для ресурсоощадної навігації БПЛА.

Ключові слова: робастне керування БПЛА; комп'ютерний зір; SLAM; нейронна мережа на основі трансформера; автономна навігація; тривимірне розуміння середовища.

ISSN 2411-8028

Editor-in-Chief
Yevhen Pistun

Energy Engineering and Control Systems

Енергетика та системи керування

Volume 11 • Number 2

Founder and Publisher
Lviv Polytechnic
National University
2 0 2 5

ENERGY ENGINEERING AND CONTROL SYSTEMS

Volume 11, Number 2, 2025

Integrated Approach to Energy Certification and Quality Control of Microclimate Formation in Modern Construction

Oleksandr Pryimak[a], Yurii Burda[b,*], Ihor Redko[c], Yurii Pivnenko[b], Oleksandr Gvozdetskii[b]

[a]*Kyiv National University of Construction and Architecture, Povitroflotskyi Avenue, 31, Kyiv, 03680, Ukraine*
[b]*O.M. Beketov National University of Urban Economy in Kharkiv, 17, Chornoglazivska St., Kharkiv, 61002, Ukraine*
[c]*Ukrainian State University of Railway Transport, Feuerbach Square 7, Kharkiv, 61050, Ukraine,*

Received: September 03, 2025. Revised: October 12, 2025. Accepted: October 20, 2025.

Abstract

This study presents an integrated approach to energy certification and quality control of ventilation systems in modern construction, emphasizing the role of energy efficiency in building performance. The research investigates current methods for evaluating ventilation effectiveness, compliance with energy standards, and the impact of system design on indoor environmental quality. Comprehensive analysis of regulatory frameworks and practical assessment techniques highlights the interconnection between certification processes and construction quality management. Case studies illustrate how systematic monitoring and optimization of ventilation systems can reduce energy consumption while maintaining comfort for people in the building. The findings provide a foundation for improving energy certification protocols and quality assurance practices, promoting sustainable construction strategies, and supporting the development of high-performance, energy-efficient buildings.

Keywords: energy certification; quality control; ventilation systems; energy efficiency; modern construction; sustainable buildings; performance assessment.

1. Introduction

The construction sector is undergoing a significant transformation driven by the growing need for energy efficiency, environmental sustainability, and enhanced indoor environmental quality. Modern buildings are expected not only to minimize energy consumption but also to maintain optimal air quality, thermal comfort, and operational reliability. Ventilation systems play a crucial role in achieving these objectives, as they directly influence indoor air circulation, pollutant removal, and energy demand. Energy certification has emerged as a critical instrument to evaluate the performance of buildings and ensure compliance with increasingly stringent energy regulations. This process involves the systematic assessment of building energy use, insulation effectiveness, and the operational efficiency of mechanical systems, including ventilation. Despite the recognized importance of energy certification, challenges persist in integrating these assessments with comprehensive quality control mechanisms during construction. Ensuring that ventilation systems meet both design specifications and functional performance requirements is essential for achieving sustainable building objectives. This study adopts an integrated approach, combining energy certification protocols with rigorous quality control measures to enhance the effectiveness of ventilation systems in modern construction. By analyzing regulatory frameworks, practical implementation strategies, and case studies of contemporary projects, the research highlights the interdependence between certification processes

---

[*] Corresponding author. Email address: science.yurii.burda@gmail.com

This paper should be cited as: O. Pryimak, Y. Burda, I. Redko, Y. Pivnenko, O. Gvozdetskii. (2025). Integrated approach to energy certification and quality control of microclimate formation in modern construction. *Energy Engineering and Control Systems*, Vol. 11, No. 2, pp. 79 – 84. https://doi.org/10.23939/jeecs2025.02.079

and quality management practices. The findings provide evidence that a systematic approach to energy evaluation and performance monitoring can lead to substantial reductions in energy consumption while maintaining occupant comfort and safety. This research contributes to the development of strategies for optimizing ventilation systems, improving building energy performance, and supporting the advancement of sustainable construction practices in line with global energy efficiency standards.

2. Analysis of recent research and publications

Recent studies highlight the growing importance of integrating thermodynamic and thermophysical analyses into the design and operation of heat and gas supply systems, as well as ventilation networks, to achieve higher energy efficiency and operational reliability. Comprehensive monographs have established theoretical foundations for understanding the complex interactions within these systems, emphasizing the necessity of systematic engineering solutions for modern buildings [1]. Research on coal-fired power plants has focused on peak-shaving strategies, flexible carbon capture, and wastewater treatment to optimize energy consumption while maintaining environmental compliance [2]. The enhancement of operational flexibility through multi-scale utilization of turbine energy storage further demonstrates the potential for energy-efficient management [3]. Investigations into near-critical fluid behaviors under parameter scaling and chemically reactive flows underline the critical role of accurate thermophysical characterization in modeling and system optimization [4], [5].

In the context of ventilation, intelligent control strategies have been explored using neural networks and non-dimensional modeling to regulate airflow and indoor temperature effectively [6], [7]. Additionally, the economic evaluation of energy efficiency measures and the implementation of renewable technologies has been facilitated by artificial intelligence, providing a data-driven framework for sustainable construction practices [8]. Combined heat and power units have been analyzed to improve operational flexibility while simultaneously supplying electricity and two-pressure steam, emphasizing the significance of integrated system design [9]. Advanced studies on thermophysical properties of material systems provide essential data for improving heat exchange components in building services engineering [10]. Collectively, these studies demonstrate a trend towards holistic approaches that couple theoretical, computational, and practical methodologies to optimize energy performance, ventilation quality, and sustainability in modern construction.

Furthermore, the drive for sustainability is materializing through the assessment of regional renewable resources, such as the prospects for geothermal energy development [11]. These initiatives are complemented by foundational research aimed at enhancing the performance of essential building services, including methods for improving the energy efficiency of heating systems [12].

3. Goal and task setting

The primary goal of this study is to develop an integrated approach to energy certification and quality control of ventilation systems in modern construction, aiming to enhance building energy performance, ensure optimal indoor environmental conditions, and promote sustainability. Achieving this goal requires a holistic understanding of the interconnections between system design, operational efficiency, and regulatory compliance.

The tasks of the research include analyzing current methods of energy certification and quality control, evaluating the performance of ventilation systems through practical and theoretical assessment, and identifying key indicators that influence energy efficiency and occupant comfort. Additionally, the study aims to propose strategies for optimizing system design and management, integrating advanced technologies and monitoring tools to ensure consistent compliance with energy standards. The paper seeks to provide actionable recommendations that support sustainable construction practices and improve the overall effectiveness of energy management within modern buildings.

4. The main part of the study

In modern construction, the concepts of energy certification and quality control are fundamental for ensuring the efficiency, reliability, and sustainability of building systems. Energy certification can be defined as a structured evaluation process that quantifies a building's energy performance, including the efficiency of its structural components, insulation, and mechanical systems such as heating, cooling, and ventilation. This process establishes benchmarks for energy consumption, identifies areas of inefficiency, and provides guidance for optimizing energy use, thereby supporting compliance with regulatory standards and sustainability objectives.

Quality control in construction refers to the systematic procedures implemented to verify that design specifications, materials, and installation practices meet established performance standards. It ensures that building systems, particularly ventilation and HVAC networks, operate as intended, delivering adequate indoor air quality, thermal comfort, and energy efficiency. This process encompasses continuous monitoring, testing, and validation at multiple stages of construction, from material selection to system commissioning.

The investigation of energy certification and quality control has become increasingly critical in contemporary construction due to rising energy costs, stricter regulatory requirements, and the growing emphasis on sustainable urban development. Effective implementation of these processes enables the reduction of energy consumption, mitigation of environmental impacts, and improvement of occupant comfort and health. Technical analysis and research in these areas allow engineers and designers to develop optimized solutions for energy-efficient buildings, ensuring that ventilation and other building systems function reliably under variable operational conditions.

Energy conservation plays a pivotal role in the design, operation, and management of modern ventilation systems. Ventilation is one of the most energy-intensive components of building operation, as it involves the continuous movement, heating, or cooling of air to maintain indoor air quality and thermal comfort. Implementing energy-saving strategies within these systems directly impacts overall building efficiency, reducing operational costs and environmental footprint.

Modern energy-efficient ventilation systems incorporate advanced technologies such as variable air volume (VAV) control, heat recovery ventilators (HRV), energy recovery systems, and intelligent sensors that regulate airflow according to occupancy and indoor environmental conditions. By optimizing air distribution, minimizing unnecessary airflow, and recovering energy from exhaust air, these systems significantly reduce electricity and heating demands.

Moreover, energy conservation in ventilation systems contributes to sustainable building performance by lowering greenhouse gas emissions and supporting compliance with energy standards and certification requirements. It enhances the reliability of mechanical systems, prolongs equipment lifespan, and improves indoor comfort levels without compromising air quality. Research and practical implementation of energy-saving measures in ventilation are therefore essential for achieving high-performance, cost-effective, and environmentally responsible building operation in contemporary construction.

An integrated approach to energy certification of buildings involves the comprehensive assessment of all factors influencing a building's energy performance, combining theoretical analysis, practical evaluation, and regulatory compliance into a unified framework. Unlike traditional energy audits, which often focus on isolated components or systems, the integrated approach considers the building as a complex, interdependent system in which structural elements, insulation, heating, cooling, and ventilation collectively determine energy efficiency.

This methodology begins with a detailed evaluation of architectural and structural characteristics, including thermal insulation, glazing, and orientation, which directly affect heat transfer and energy demand. Mechanical systems, particularly ventilation and HVAC networks, are analyzed for their operational efficiency, airflow distribution, and control strategies.

Adopting an integrated energy certification strategy is increasingly essential in contemporary construction, as it aligns with global sustainability objectives, facilitates compliance with stringent energy codes, and provides a scientific basis for improving the energy management and operational reliability of modern buildings. (Table 1).

Table 1. Influence of ventilation system parameters on building energy efficiency.

Parameter	Unit	Value Range	Impact on Energy Efficiency
Heat transfer coefficient of ductwork	$W/m^2 \cdot K$	0.5 – 2.0	Higher coefficient reduces heat losses
Efficiency of heat recovery unit	%	60 – 90	Higher efficiency decreases heating/cooling demand
Average air flow rate	m^3/h	500 – 2000	Increased flow can raise energy consumption
Supply air temperature	°C	15 – 25	Higher temperature reduces heating requirements
Supply air humidity	%	40 – 60	Optimal humidity enhances indoor comfort
Air changes per hour (ACH)	ACH	1 – 6	Higher ACH may increase energy use

This table illustrates the relationship between different ventilation system parameters and their impact on building energy efficiency. It demonstrates how variations in each parameter influence overall energy consumption and indoor comfort.

Table 2 presents a set of experimental nonlinear data illustrating the interdependent behavior of key ventilation system parameters and their impact on building energy efficiency. The heat transfer coefficient of ductwork reflects thermal losses in the ventilation network, while the heat recovery efficiency indicates the proportion of energy reclaimed from exhaust air to precondition incoming supply air. The average air flow rate represents the volume of ventilated air necessary to maintain indoor air quality and thermal comfort. (Table 2).

Table 2. Experimental data of ventilation system parameters and energy efficiency.

No.	Heat Transfer Coefficient ($W/m^2 \cdot K$)	Heat Recovery Efficiency (%)	Average Air Flow Rate (m^3/h)
1	0.5	60	520
2	0.7	65	680
3	0.9	70	850
4	1.1	72	1020
5	1.3	75	1180
6	1.5	78	1350
7	1.7	81	1530
8	1.8	84	1700

This table presents experimental nonlinear data for three key ventilation system parameters: heat transfer coefficient of ductwork, heat recovery efficiency, and average air flow rate. The values illustrate how variations in duct insulation and heat recovery performance correlate with changes in airflow, showing a nonlinear trend. These data points can be used to analyze energy efficiency, as improvements in heat recovery efficiency and optimization of duct characteristics affect the required airflow to maintain comfort, thus reducing or increasing energy consumption depending on system tuning.

Below is the 3D graph illustrating the nonlinear relationship between ventilation system parameters and building energy efficiency, showing how the heat transfer coefficient, heat recovery efficiency, and average air flow rate interact to influence energy consumption (Fig. 1).

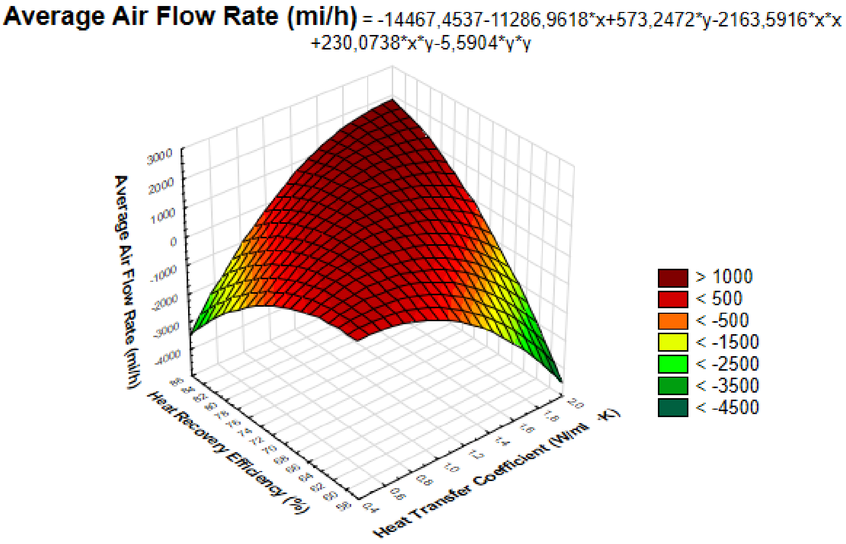

Fig. 1. Nonlinear interaction of ventilation system parameters affecting energy efficiency.

The 3D graph also includes a fitted regression surface that models the nonlinear relationship among the three parameters. This regression equation represents how changes in the heat transfer coefficient and heat recovery efficiency influence the required average air flow rate, providing a predictive tool for estimating energy consumption under varying ventilation system configurations. The surface highlights the complex, nonlinear interactions between duct thermal performance, heat recovery, and airflow, allowing engineers to optimize system design and operational efficiency.

5. Conclusion

The conducted study demonstrates the critical role of energy certification and quality control in modern ventilation systems and building energy efficiency. Analysis of the first table, which presents key ventilation parameters and their general influence on energy consumption, indicates that optimizing the heat transfer coefficient of ductwork, heat recovery efficiency, and airflow characteristics is essential for minimizing energy losses while maintaining indoor comfort. The data highlights that even small improvements in duct insulation or recovery efficiency can lead to significant reductions in energy demand.

The second table, containing experimental nonlinear data, provides a more precise and quantitative understanding of these interactions. The observed nonlinear relationships among the heat transfer coefficient, heat recovery efficiency, and average air flow rate confirm that energy efficiency cannot be addressed through isolated adjustments of individual parameters. Instead, a holistic, integrated approach is necessary to predict and control energy consumption accurately. The regression surface derived from these data serves as a predictive tool for estimating system performance under varying operational conditions.

Overall, the results of this study emphasize that energy-efficient ventilation design requires simultaneous consideration of multiple interdependent parameters. Implementing integrated energy certification practices and continuous quality control allows for optimized airflow, reduced operational costs, and improved environmental performance. These findings provide actionable insights for engineers and designers, supporting sustainable building practices and ensuring compliance with contemporary energy standards.

References

[1] Burda Y. (2025). Comprehensive analysis of thermodynamic and thermophysical processes in heat and gas supply and ventilation systems: theoretical foundations and engineering solutions: monograph / Y. Burda; Kharkiv. O. M. Beketov National University of Urban Economy in Kharkiv. – *Kharkiv: O. M. Beketov NUUE*. – 130 p. URL: https://eprints.kname.edu.ua/68140/

[2] Tiancheng Ouyang, Shutao Xie, Mingming Pan, Peijia Qin. (2022). Peak-shaving scheme for coal-fired power plant integrating flexible carbon capture and wastewater treatment. *Energy Conversion and Management*. Volume 256, 15 March 2022. https://doi.org/10.1016/j.enconman.2022.115377

[3] Di Wang, Deying Liu, Chaonan Wang, Yunlong Zhou, Xiaoli Li, Mei Yang. (2022). Flexibility improvement method of coal-fired thermal power plant based on the multi-scale utilization of steam turbine energy storage. *Energy*. Volume 239, Part D, 15 January 2022. https://doi.org/10.1016/j.energy.2021.122301

[4] Rui Zhang, Xu, Lin Chen. (2024). Asymptotic thermophysical behaviors of near-critical fluid under parameter scaling. *International Journal of Heat and Fluid Flow*. Volume 108, September 2024, 109442. https://doi.org/10.1016/j.ijheatfluidflow.2024.109442

[5] Sohail A. Khan, T. Hayat, A. Alsaedi. (2024). Chemically reactive flow beyond constant thermophysical characteristics. *Case Studies in Thermal Engineering*. Volume 61, September 2024, 104980. https://doi.org/10.1016/j.csite.2024.104980

[6] Rong Liu, Yi He, Yunfeng Zhao, Xiang Jiang, Song Ren. (2020). Tunnel construction ventilation frequency-control based on radial basis function neural network. *Automation in Construction*, Volume 118, October 2020, 103293, https://doi.org/10.1016/j.autcon.2020.103293

[7] Chen Ren, Shi-Jie Cao. (2021). Construction of linear temperature model using non-dimensional heat exchange ratio: Towards fast prediction of indoor temperature and heating, ventilation and air conditioning systems control. *Energy and Buildings*, Volume 251, 15 November 2021, 111351, https://doi.org/10.1016/j.enbuild.2021.111351

[8] Cheng Chen, Yuhan Hu, Marimuthu Karuppiah, Priyan Malarvizhi Kumar. (2021). Artificial intelligence on economic evaluation of energy efficiency and renewable energy technologies. *Sustainable Energy Technologies and Assessments*, Volume 47, October 2021, https://doi.org/10.1016/j.seta.2021.101358

[9] Miaomiao Liu, Ming Liu, Weixiong Chen, Junjie Yan. (2023). Operational flexibility and operation optimization of CHP units supplying electricity and two-pressure steam. *Energy*, Volume 263, Part E, 15 January 2023, https://doi.org/10.1016/j.energy.2022.125988

[10] Bo Jin, Shuhong Liu, Kai Xu, Qiang Lu b, Yong Du. (2023). Thermophysical properties in the Al-Cu-Ag system: A combined CALPHAD and first-principles study. *Journal of Molecular Liquids*. Volume 370, 15 January 2023, 121001. https://doi.org/10.1016/j.molliq.2022.121001

[11] O. Savchenko, Y. Yurkevych, I. Liubuska. (2023). Spatial analysis of renewable energy sources in Lviv region. *Energy Engineering and Control Systems*, Vol. 9, No. 1, pp. 22 – 30. https://doi.org/10.23939/jeecs2023.01.022

[12] Yu. Yurkevych, O. Savchenko, Z. Savchenko. (2022). Prospects for development of geothermal energy in Lviv region. *Energy Engineering and Control Systems*, Vol. 8, No. 1, pp. 1 – 6. https://doi.org/10.23939/jeecs2022.01.001

Інтегрований підхід до енергетичного сертифікування та контролю якості формування мікроклімату в сучасному будівництві

Олександр Приймак[a], Юрій Бурда[b], Ігор Редько[c], Юрій Півненко[b], Олександр Гвоздецький[b]

[a]Київський національний університет будівництва і архітектури, просп.Повітряних Сил, 31, Київ, 03037, Україна
[b]Харківський національний університет міського господарства імені О.М. Бекетова,
вул. Чорноглазівська, 17, Харків, 61002, Україна
[c]Український державний університет залізничного транспорту, майдан Фейєрбаха 7, Харків, 61050, Україна

Анотація

У статті представлено інтегрований підхід до енергетичного сертифікування та контролю якості вентиляційних систем у сучасному будівництві, що підкреслює роль енергоефективності у забезпеченні експлуатаційних характеристик будівель. Досліджено сучасні методи оцінки ефективності вентиляції, відповідності енергетичним стандартам та вплив конструктивних рішень на внутрішнє середовище приміщень. Комплексний аналіз нормативно-правових вимог та практичних методів контролю демонструє взаємозв’язок між процесами сертифікації та управління якістю будівництва. На прикладі сучасних проектів показано, що систематичний моніторинг і оптимізація вентиляційних систем дозволяють значно зменшити енергоспоживання, водночас забезпечуючи комфорт та безпеку перебування людей у будівлях. Отримані результати створюють наукову основу для вдосконалення процедур енергетичного сертифікування та контролю якості, сприяють впровадженню стійких будівельних стратегій та розвитку високоефективних енергоощадних споруд.

Ключові слова: енергетичне сертифікування; контроль якості; вентиляційні системи; енергоефективність; сучасне будівництво; стійкі будівлі; оцінка ефективності.

Analysis of Cation Resins for WWER-1000 Reactor Coolant Purification Filters

Halyna Matiko[*], Nazar Zosymchuk

Lviv Polytechnic National University, 12 S. Bandera St., Lviv, 79013, Ukraine

Received: October 15, 2025. Revised: December 08, 2025. Accepted: December 16, 2025.

Abstract

The paper considers filtration equipment used for coolant purification in WWER-1000 reactors, which plays an important role in providing an optimal water-chemical regime, reducing radioactive contamination of equipment and extending the service life of reactor components. The operating features of ion-exchange filters are investigated and directions for their modernization are determined. The design and characteristics of cation exchange filters are analyzed and key factors affecting their efficiency are highlighted, including the replacement of ion-exchange resins and optimization of the regeneration process. A comparative analysis of nuclear-grade ion-exchange resins, such as Lewatit MonoPlus S 108 H, Purolite® NRW100 and DIAION™ SKN1, is carried out, and their suitability for cation exchange filters modernization is evaluated. Cation exchange filter parameters are calculated for different ion-exchange resins, such as operational exchange capacity, intervals between regenerations and acid amount for filter regeneration. It was determined that Lewatit MonoPlus is the optimal resin for cation exchange filters due to its higher exchange capacity (2 g-eq/L), longer intervals between regenerations (22 regenerations per year) and lower cost.

Keywords: WWER-1000 reactor; coolant; purification system; cation exchange filter; regeneration; ion exchange resin.

1. Definition of the problem to be solved

Nowadays, nuclear power units with WWER-1000 reactors play an important role in electricity production in Ukraine. The efficiency and safety of their operation largely depend on providing an optimal water-chemical regime. The primary circuit of the power unit, where the coolant circulates, operates under conditions of high temperature and pressure, as well as ionizing radiation, which creates significant technical challenges, including corrosion of structural materials, wear of mechanical equipment, formation of deposits in the core, damage to fuel rod cladding, and contamination of reactor systems [1], [2]. Consequently, the urgent tasks are preventing corrosion, minimizing the radioactive deposits, and ensuring the stable reactor performance. The water-chemical regime solves these challenges while reducing radiation exposure to personnel by limiting the formation of radioactive aerosols and deposits. This simplifies equipment maintenance, lowers radiation doses, minimizes radioactive emissions, and supports environmental protection [3], [4].

At Ukrainian nuclear power plants with WWER-1000 reactors, a mildly alkaline, reducing, ammonia-potassium water-chemical regime with boric acid regulation is used. The water in WWER reactors serves a dual purpose: it acts as a coolant, transferring heat from the reactor core, and as a neutron moderator for nuclear fission reactions. Boric acid (H_3BO_3) is used to ensure reactor controllability. The acid content in the coolant depends on the core neutron physical characteristics. The primary reagent for maintaining the required pH level in the primary circuit is potassium hydroxide

---

[*] Corresponding author. Email address: halyna.f.matiko@lpnu.ua

This paper should be cited as: H. Matiko, N. Zosymchuk. (2025). Analysis of cation resins for WWER-1000 reactor coolant purification filters. *Energy Engineering and Control Systems*, Vol. 11, No. 2, pp. 85 – 92. https://doi.org/10.23939/jeecs2025.02.085

(KOH), which creates a mildly alkaline medium to minimize corrosion of the primary circuit metal. To establish a reducing medium, ammonia (NH_3) is added to the coolant to provide an optimal content of dissolved hydrogen, which appears as a result of its radiolytic decomposition. This helps suppress the formation of radiolytic oxygen and prevents corrosion of stainless steel [3]–[6]. Consequently, the feedwater for the primary circuit is prepared by deionization, degassing and removing residual oxygen by dosing hydrazine hydrate ($N_2H_4 \cdot H_2O$).

Special attention is given to providing the concentration of corrosive impurities (oxygen, chloride, fluoride, and sulfate ions) below permissible levels. Reactor water treatment systems SVO-1 and SVO-2 are used to purify the coolant from dispersed corrosion products and radionuclides, and to promptly adjust the water-chemical regime parameters in case of deviations from specified values [3]. These systems must be appropriately designed and operated to ensure effective coolant purification.

2. Analysis of recent publications and research works on the problem

Issues related to preventing corrosion in primary circuit equipment and coolant treatment are the subject of numerous studies [5]–[12]. Significant attention is given to the system for purifying the organized leakages and blowdown water from the primary circuit of WWER-1000 reactors, as well as improving the performance of its main components – ion-exchange filters, which are responsible for deep removal of dissolved ionic impurities, elimination of excess alkalinity, and some colloidal and finely dispersed suspended solids [6]–[8].

The productivity of the coolant purification system, i.e., the volume of coolant flowing through the filters per time unit, typically amounts to only a few percent of the total coolant flow through the reactor core. A portion of the coolant flow, known as blowdown, is continuously or periodically removed from the primary circuit, passes through cooling and filtration systems, and then the purified coolant is returned to the circuit. According to [6], [13], the nominal productivity of the purification system can vary in the range from 10 to 30 m^3/h, allowing a flexible response to changes in coolant quality and purification needs [6], [13].

The efficiency of the purification process is evaluated by purification coefficients, which indicate how many times the content of a specific impurity decreases after passing through the filtering element. For modern ion-exchange filters, these coefficients can reach 90–99% or higher for most dissolved ionic impurities. The efficiency of mechanical filters depends on their design and is characterized by the minimum particle size they can retain with high effectiveness [13].

Ion-exchange resins and other filtering materials sorb and accumulate significant amounts of radionuclides during operation. These are primarily corrosion activation products from structural materials (Co-58, Co-60, Mn-54, Fe-59) and fission products from nuclear fuel that may enter the coolant (Cs-137, I-131) [9], [12]. High levels of accumulated activity require the implementation and strict adherence to special radiation safety measures during all stages of system operation, maintenance, and especially during the replacement of spent filtering materials [1].

Radioactive substances accumulated on the filters generate heat due to radioactive decay. This residual heat release can significantly heat ion-exchange resins and other filtering materials, particularly when coolant flow stops through the filter or during their unloading. Therefore, resins must be heat-resistant, or systems and procedures must be provided to ensure their cooling [9].

Spent ion-exchange resins and mechanical filter elements are classified as radioactive waste. Their collection, transportation, processing, conditioning, and long-term storage or disposal must be carried out according to the special procedures and regulatory requirements to minimize impacts on personnel and the environment [1], [11].

Over time, as power units are operated and because of the increased requirements and safety standards for coolant purification efficiency, the reactor purification systems need modernization. Equipment is physically aging, while water treatment and purification technologies continue to develop [8], [9]. Therefore, this article is devoted to analyzing the current state of ion-exchange materials and justifying directions for ion-exchange filter modernization, which are the key elements of purification systems.

3. Formulation of the goal of the paper

The aim of this study is to determine the directions for modernizing ion-exchange filters of the coolant purification system of the WWER-1000 reactor, conduct a comparative analysis of known nuclear-grade cation resins, and calculate the parameters of cation exchange filters when using different types of resins.

4. Presentation and discussion of research results

4.1. Directions for ion-exchange filters modernization

An ion-exchange filter is a vertical cylindrical apparatus made from corrosion-resistant materials, designed for purifying the coolant from impurities (Fig. 1). The main components of the filter are the housing, upper and lower drainage-distribution devices (typically made as perforated plates or slotted caps), a layer of ion-exchange resin, loading and unloading hatches for fresh and spent resin, nozzles for inlet and outlet water, regeneration reagents, and air release, as well as devices for monitoring the quality of purified water and the resin characteristics. The drainage-distribution devices ensure uniform water flow distribution through the resin layer and prevent the loss of resin particles from the filter [13].

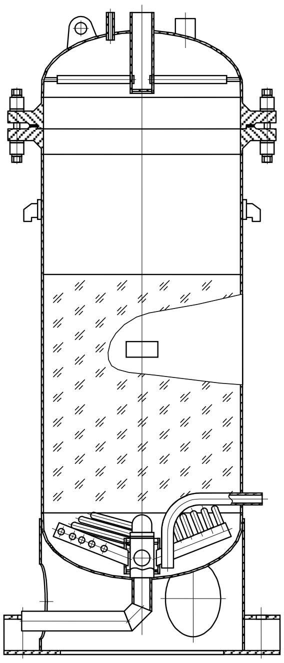

Fig. 1. Longitudinal cross-section of a cation exchange filter.

Contaminated water is fed into the filter's upper part, flows downward through the layer of ion-exchange resin where the ion-exchange process occurs, and purified water is removed from the filter's lower part. The type and properties of the ion-exchange resin and the filtration rate are the key factors influencing purification efficiency and filter cycle duration. The purification system at Ukrainian NPP uses nuclear-grade cation exchange resin AMBERLITE™ IRN77 H, which looks like translucent amber-colored spherical granules, and the strongly basic polystyrene gel anion exchange resin AMBERLITE™ IRN78 in hydroxyl form, which looks like gray spherical granules [14].

When the exchange capacity of the resin is exhausted, i.e., it becomes saturated with absorbed ions and can no longer effectively purify water, it should be regenerated or replaced. Regeneration is the restoration of the resin's exchange capacity by treating it with solutions of appropriate reagents. For example, cation resins in H^+ form are regenerated using hydrochloric acid (HCl) or sulfuric acid (H_2SO_4) solutions [9]. For ion-exchange filters in the primary circuit of WWER-1000 nuclear power plants, when the reagent is already exhausted and no longer suitable for regeneration, the spent resin is entirely replaced with fresh resin. The spent resin is solid radioactive waste that must be sent for specialized processing and disposal.

The efficiency of ion-exchange filters, particularly the duration of the filter cycle (the period of filter operation between regenerations or resin replacements), depends on several factors. The most significant factors are the properties of the ion-exchange resin, such as its type, exchange capacity, wear degree, and presence of contaminants; the content of impurities in the inlet water (higher impurity concentrations lead to faster resin exhaustion); coolant temperature (high temperatures can cause resin thermal degradation and reduce its exchange capacity); water flow rate (high flow rates may result in incomplete ion exchange due to insufficient contact time, while low flow rates may lead to inefficient use of the filter volume); coolant pH (affects the dissociation degree of the resin's ionogenic groups and the form of certain impurities in the solution); the presence of suspended solids and organic compounds (these can mechanically contaminate the resin layer, coat granules and block access to ionogenic groups, which reduces efficiency and increases hydraulic resistance); radiation impact (can cause resin degradation, structural changes and decrease in the exchange capacity and mechanical strength) [13], [15].

The authors analyzed known examples of ion-exchange filter modernization and innovations in water treatment, identifying the following key proposals.

- *Introduction of new ion-exchange materials and multilayer loading*: development, testing, and implementation of modern ion-exchange resins with improved characteristics, such as higher exchange capacity, enhanced selectivity for specific ions (e.g., cobalt or cesium ions), better mechanical strength, and greater thermal and radiation resistance [16]–[19]. This would extend the filter life and reduce the volume of liquid radioactive waste.
- *Improvement of filter design*: extending filter life by using more durable materials for the housing and its components; optimizing the internal filter structure to improve coolant flow hydrodynamics. This includes developing and applying more efficient drainage-distribution systems that ensure uniform flow distribution across the filter's cross-section and prevent the formation of stagnant zones or channels that reduce the efficiency of the resin layer [8], [9].
- *Improvement of control, management, and diagnostic systems*: implementing modern measuring technologies and automated control systems, including filters with integrated sensors that enable real-time monitoring of their operation and prediction of resource exhaustion. This allows for more precise and timely control of water-chemical regime parameters, the condition of filtering materials (e.g., exhaustion degree), and more effective control of the purification system [5], [9].
- *Optimization of blowdown-feedwater system for the primary circuit*: research for determining the optimal operating modes for the blowdown-feedwater system, which provides the required coolant quality while reducing the volume of blowdown water. This helps reduce the amount of liquid radioactive waste [9], [13].

4.2. Calculation of cation filter parameters using different ion-exchange resins

The authors have analyzed modern nuclear-grade ion-exchange resins, such as Lewatit® MonoPlus S 108 H, Purolite® NRW100, and DIAION™ SKN1, including their physicochemical properties and potential application in cation filters [17]–[19]. A comparative analysis of the physicochemical properties of nuclear-grade ion-exchange resins is presented in Table 1.

Table 1. Characteristics of ion-exchange resins.

Parameter	Unit	AMBERLITE^{tm} IRN77 H	Lewatit MonoPlus S 108 H	Purolite® NRW100	DIAION™ SKN1
Uniformity coefficient	-	<1.2	1.05(+/- 0.05)	1.1(+/- 0.05)	1.2(+/- 0.05)
Average granule diameter	mm	< 0.3 (0.2 %) > 1.180 (3%)	0.65(+/- 0.05)	0.8(+/- 0.05)	0.7(+/- 0.05)
Total exchange capacity	g-eq/L	> 1.9	2.0	1.8	1.7
Maximum water content	%	49-55	47-53	45-50	54
Maximum operating temperature	°C	120	120	120	120
Specific acid amount for regeneration	g-eq/L	6.21	2	6	4
Operating flow rate	m^3/hour	< 60	< 60	< 40	< 40

Lewatit MonoPlus S 108 H is a strong-acid cation exchange resin that is universal for water demineralization at industrial steam generators and purification systems, and for mixed filters combined with anionites. It provides low organic carbon content and resistance to oxidation, which is especially important for the nuclear industry. Thanks to its specialized manufacturing process, the resin exhibits exceptional chemical, osmotic, and mechanical stability, ensuring low leaching even at high temperatures, in the presence of oxidants, or during external regeneration [17].

Purolite® NRW100 is a strong-acid cation exchange resin with exceptional chemical and mechanical stability, which ensures its durability under challenging conditions, such as high temperatures or oxidant impact. Its monodisperse structure with minimal content of fine particles reduces hydraulic resistance and promotes uniform regenerant flow, thereby improving the efficiency of hydrochloric acid during regeneration. Its resistance to oxidation and low leaching level make it suitable for nuclear industry applications [18].

DIAION™ SKN1 is a strong-acid cation exchange resin specifically developed for the nuclear industry, particularly for coolant purification, radioactive waste processing, and purification of spent fuel storage pool systems, where high purity and low organic carbon content are necessary. The resin is chemically and mechanically stable at high temperatures and radiation. The resin's exchange capacity loss is only 2–5% per year with proper operation, making it cost-effective for long-term use [19].

The authors calculated the cation exchange filter parameters for different resins, including operational exchange capacity, duration between regenerations and acid amount for regeneration. The results of the filter parameter calculations using AMBERLITE™ IRN77 H, Lewatit MonoPlus S 108 H, Purolite® NRW100, and DIAION™ SKN1 resins are presented in Table 2. The formulas in Table 2 use the following labeling: D is the filter diameter; h is the height of the filtration zone; k_f is the coefficient of ionite filling with H^+ ions; E_t is the total exchange capacity; W is the coefficient of ion filling; d_{ion} is the resin grain diameter; C_{cat} is the average total cation concentration in the resin; k_{ef} is the regeneration efficiency coefficient; k_{pr} is the coefficient of incomplete utilization of the protective layer; H_{bf} is the water hardness before the filter; H_{af} is the water hardness after the filter; n_{if} is the number of ion-exchange filters; W_a is the specific acid amount.

Table 2. Parameters of cation exchange filters for different ion-exchange resins.

Parameter	Formula	AMBERLITE™ IRN77 H	Lewatit Mono Plus S 108 H	Purolite® NRW100	DIAION™ SKN1
Filter surface area, m^2	$f = \frac{\pi \cdot D^2}{4}$	0.785	0.785	0.785	0.785
Total volume of cation exchanger in the filter, m^3	$V_{cat} = f \cdot h$	0.942	0.942	0.942	0.942
Height of the protective filtration layer, m	$h_{pr} = 0.11 \cdot W^{0.5} \cdot d_{ion}^2 \cdot \log(C_{cat})$	0.0754	0.088	0.134	0.103
Equilibrium exchange capacity, $\frac{\text{g-eq}}{\text{m}^3}$	$E_e = (1 - k_f) \cdot E_t$	1881	1900	1782	1649
Working exchange capacity, $\frac{\text{g-eq}}{\text{m}^3}$	$E_w = k_{ef} \cdot E_e \cdot \left(1 - (1 - k_{pr}) \cdot \frac{h_{pr}}{h}\right)$	1647.18	1652.5	1512.95	1423.6
Number of regenerations per year	$n = \frac{Q \cdot (H_{bf} - H_{af}) \cdot 10^3 \cdot 24}{V_{cat} \cdot n_{if} \cdot E_w}$	22.572	22.5	24.57	26.12
Duration between regenerations, days	$T = \frac{1}{n}$	16.17	16.22	14.859	13.98
Acid amount for regeneration, kg	$Q_a = \frac{E_w \cdot W_a \cdot V_{cat}}{1000}$	6.21	6.23	8.555	5.367

Comparative analysis of the operational exchange capacity (Fig. 2), the duration between regenerations (Fig. 3), and the acid amount for regeneration for different cation exchange resins (Fig. 4) is presented below.

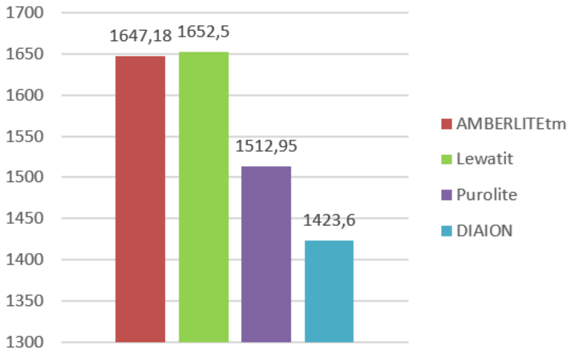

Fig. 2. Operational exchange capacity of cation resins.

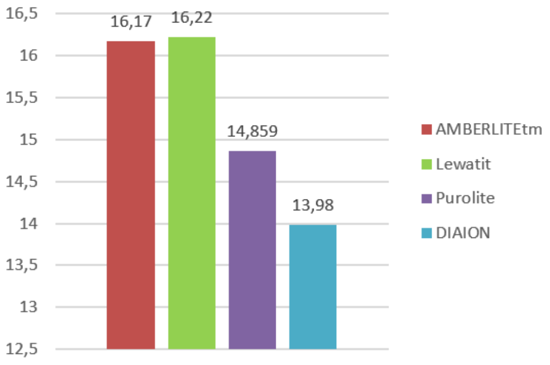

Fig. 3. Duration between regenerations for cation resins in days.

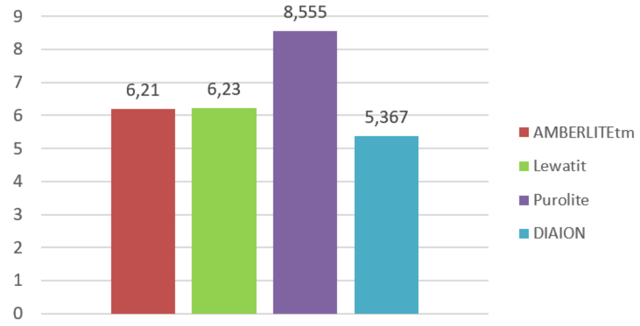

Fig. 4. Acid amount for regeneration of cation resins.

Analyzing the calculation results, the authors have concluded that the Lewatit® MonoPlus S 108 H resin offers advantages over the AMBERLITE™ IRN77 H resin, as it has a higher operational exchange capacity and a longer duration between regenerations.

Therefore, additional studies were conducted for the cation resin Lewatit® MonoPlus S 108 H. For this resin, the authors have analyzed the impact of the filter diameter within the range of 0.7 to 1.2 m on the filter's operational parameters. The calculation results are presented in Figures 5 and 6.

Based on the calculation results, the following conclusions were made:

- Increasing the filter diameter reduces the time between regenerations, increases acid consumption per regeneration, and requires modifications to the existing filter design, which is economically unfeasible.
- Increasing the height of the ion-exchange layer in the filter increases the resin's operational exchange capacity, positively affecting its productivity and efficiency; however, the costs for regenerating such a filter increase slightly. Therefore, for decisions regarding filter modernization, an additional economic analysis is necessary, considering the cost of acid amount for regeneration and the total expenses associated with modifying the filter design.

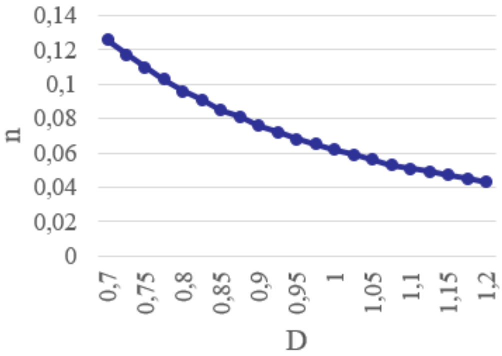

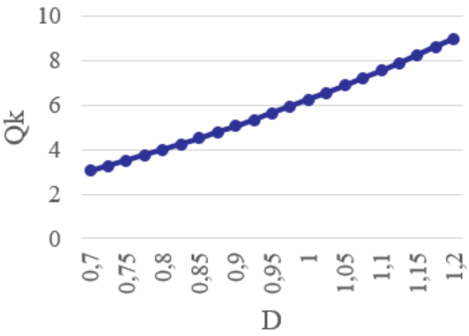

Fig. 5. Dependence of the number of regenerations on filter diameter.

Fig. 6. Dependence of acid amount for regeneration on filter diameter.

The authors also analyzed the impact of the operational filtration height within the range of 0.8 to 1.5 m on the filter's characteristics. The calculation results are presented in Figures 7 – 9.

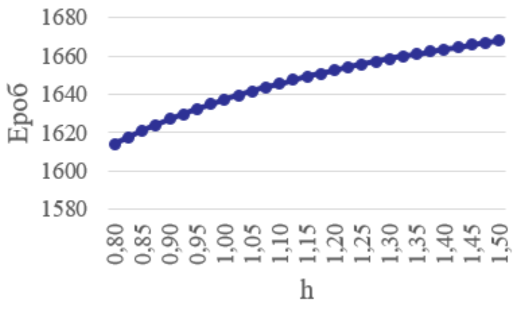

Fig. 7. Dependence of operational exchange capacity on the height of the working filter zone.

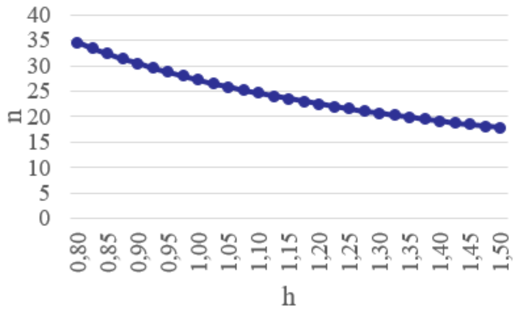

Fig. 8. Dependence of the number of regenerations per day on the height of the working filter zone.

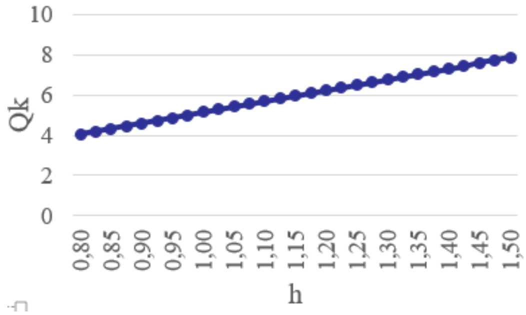

Fig. 9. Dependence of acid amount for regeneration on the height of the working filter zone.

5. Conclusion

The paper presents the operational features of ion-exchange filters used for purifying the coolant of the primary circuit of the WWER-1000 reactor, which play an essential role in enhancing the efficiency, safety, and cost-effectiveness of nuclear power plant operation. The directions for cation exchange filters modernization have been determined: using new ion-exchange resins; multilayer loading; reducing the volume of radioactive waste through optimized regeneration; using filters that do not require regeneration; extending the filters' service life by using more durable materials for housings and components; optimizing hydrodynamic regimes; implementing automated control and remote management systems, etc.

The nuclear-grade ion-exchange resins, such as Lewatit® MonoPlus S 108 H, Purolite® NRW100, and DIAION™ SKN1, were analyzed, including their physicochemical properties and potential for filter modernization. Cation exchange filter parameters, including operational exchange capacity, duration between regenerations, and acid amount for regeneration, were calculated. It was determined that the Lewatit® MonoPlus S 108 H resin provides a higher exchange capacity (2 g-eq/L), a longer duration between regenerations (22 regenerations per year), and a lower cost, making it suitable for replacing the existing AMBERLITE™ IRN77 H resin as part of filter modernization. The impact of the filter diameter within the range of 0.7–1.2 m and the height of the working filter zone within the range of 0.8–1.5 m on its performance was also analyzed, highlighting the need to balance increased productivity with regeneration costs.

References

[1] Safety of Nuclear Power Plants: Commissioning and Operation. Specific Safety Requirements No. SSR-2/2 (Rev. 1). (2016) Vienna: IAEA.

[2] NP 306,2,145-2008. Nuclear Safety Rules for Reactor Installations of Nuclear Power Plants with Pressurized Water Reactors. Approved by Order of the State Nuclear Regulatory Committee of Ukraine dated April 15, 2008 No. 73. Registered with the Ministry of Justice of Ukraine on June 9, 2008 by No. 512/15203. Available from: https://zakon,rada,gov,ua/laws/show/ z0512-08#Text.НП 306,2,145-2008. Available from: https://zakon.rada.gov.ua/laws/show/ z0512-08#Text (accessed on August 22, 2025)

[3] SOU NAEK 191:2020. Engineering, scientific and technical support. Water-chemical regime of the primary circuit of nuclear power reactors of the WWER-1000 type. Technical requirements. Quality assurance methods. Approved by order of SE NAEK Energoatom 23.09.2020 No. 755.

[4] IAEA Safety Standards No. SSG-13. Chemistry Programme for Water Cooled Nuclear Power Plants. 2011. Available from: https://www.iaea.org/sites/default/files/23/02/draft_ds525.pdf (accessed on August 22, 2025)

[5] Lister, D., Uchida, S. (2015). Determining water chemistry conditions in nuclear reactor coolants. *Journal of Nuclear Science and Technology*, **52(4)**, 451-466. doi: 10.1080/00223131.2014.973460

[6] Maltseva, T.V., Lukashyn, S.O., Shyshuta, A.M., Bakanov V.V. (2024). Water chemical regime of Ukrainian nuclear power units: national and international requirements, technical features and improvements. *Nuclear and radiation safety*, **1(101)**, 59-68. https://doi.org/10.32918/nrs.2024.1(101).06

[7] Semerak, M. M., Lys, S. S., & Yurasova, O. H. (2018). Analysis of the main means for ensuring the water-chemical regime of the NPP. *Scientific Bulletin of UNFU*, **(28(6)**, 81-83. https://doi.org/10.15421/40280615

[8] Pornima Vijayan, P., Chithra, P. G., Anjana Krishna, S. V, Ansar, E. B, & Parameswaranpillai, J. (2022). Development and Current Trends on Ion Exchange Materials. *Separation & Purification Reviews*, **53(1)**, 40–60. https://doi.org/10.1080/15422119.2022.2149413

[9] Spiro D. Alexandratos. (2021). Trends in ion exchange: Analysis of the literature. *Reactive and Functional Polymers*, **169(1)**, 1-10. DOI: 10.1016/j.reactfunctpolym.2021.105066

[10] Kritsky, V. G., Berezina, I. G., Rodionov, Yu. A., Stjazkin, P. S. (2005). Influence of water chemistry transients on fuel assemblies reliability. Structural behaviour of fuel assemblies for water cooled Reactors. IAEA-TECDOC-1454. *Proceedings of a technical meeting.* Cadarache, France, 22–26 November 2004. Vienna: IAEA, 75-86.

[11] SenGupta, A.K. (2017). Ion Exchange in Environmental Processes: Fundamentals, Applications and Sustainable Technology. Wiley. doi: 10.1002/9781119421252

[12] Alexandratos, S. D. (2008). Ion-Exchange Resins: A Retrospective from Industrial and Engineering Chemistry Research. *Industrial & Engineering Chemistry Research*, **48(1)**, 388-394. doi: 10.1021/ie801242v

[13] Kardasevych, O. (2003). Water regimes of thermal and nuclear power plants. Odesa: ONPU Publishing House.

[14] Fisher scientific. Amberlite IRN-77, ion exchange resin, nuclear grade. Available from: https://www.fishersci.ca/shop/products/amberlite-irn-77-ion-exchange-resin-nuclear-grade-thermo-scientific/p-4408669 (accessed on August 22, 2025)

[15] IAEA. Application of Ion Exchange Processes for Treatment of Radioactive Waste and Management of Spent Ion Exchangers. Available from: https://www.iaea.org/publications/6221/application-of-ion-exchange-processes-for-treatment-of-radioactive-waste-and-management-of-spent-ion-exchangers (accessed on August 22, 2025)

[16] Balashevska, Y., Balashevskyi, O., Gerliga, V., Kuba, I., Kostenko, V., Korsun, D. (2024). Challenges and Progress in Spent Ion-Exchange Resin Management at NPPs: A Perspective from Ukraine. *Nuclear and Radiation Safety*, **2(102)**, 14-24. doi: 10.32918/nrs.2024.2(102).02

[17] Fiche Informations Produit LEWATIT® MonoPlus S 108 H. Available from: https://www.lenntech.com/Data-sheets/Lewatit-MonoPlus-S-108-H-FR-L.pdf (accessed on August 22, 2025)

[18] Ecolab. Purification Technologies. Purolite CriticalResin NRW100. Available from: https://www.purolite.com/product?normalizedName=nrw100 (accessed on August 22, 2025)

[19] Product Data Sheet DIAION TM SKN1. Available from: https://www.diaion.com/en/products/ion_exchange_resins/strongly_acidic_cation/data_sheet_sk/pdf/skn1.pdf (accessed on August 22, 2025)

Аналіз катіонітових смол для очищення теплоносія реактора ВВЕР-1000

Галина Матіко, Назар Зосимчук

Національний університет «Львівська політехніка», вул. С. Бандери, 12, Львів, 79013, Україна

Анотація

У статті розглянуто фільтрувальне обладнання для очищення теплоносія реактора ВВЕР-1000, яке відіграє важливу роль у підтримці оптимального водно-хімічного режиму, зниженні радіоактивного забруднення обладнання та продовженні терміну служби компонентів реакторної установки. Досліджено особливості експлуатації іонообмінних фільтрів та визначено напрямки їх модернізації. Проаналізовано конструкцію та характеристики катіонітового фільтра, визначено фактори, які впливають на ефективність роботи фільтрів, зокрема заміна іонообмінних смол та оптимізація процесу регенерації. Виконано порівняльний аналіз іонообмінних смол ядерного класу, таких як Lewatit MonoPlus S 108 H, Purolite® NRW100 та DIAION™ SKN1. Обґрунтовано можливості їх застосування для модернізації катіонітових фільтрів. Проведено розрахунки параметрів катіонітового фільтра при застосуванні різних іонообмінних смол, зокрема робочої обмінної ємності, тривалості між регенераціями та витрати кислоти на регенерацію фільтра. Встановлено, що оптимальним варіантом для застосування у катіоніовому фільтрі є смола Lewatit MonoPlus завдяки вищій обмінній ємності (2 г-екв/л), довшій тривалості між регенераціями (22 регенерації на рік) та низькій ціні.

Ключові слова: реактор ВВЕР-1000; теплоносій; система очищення; катіонітовий фільтр; регенерація; іонообмінна смола.

ENERGY ENGINEERING AND CONTROL SYSTEMS

Volume 11, Number 2, 2025

Circulation Flow of Polyacrylamide Aqueous Solution between Coaxial Cylinders with Smooth Surfaces

Vadym Orel, Bohdan Pitsyshyn, Vadym Fasuliak[*]

Lviv Polytechnic National University, 12 Stepana Bandery St., Lviv, 79013, Ukraine

Received: October 07, 2025. Revised: October 31, 2025. Accepted: November 07, 2025.

Abstract

A mixer with coaxial arrangement of inner and outer circular cylinders with smooth surfaces is considered. During the mixer operation, a circulating flow is formed between the cylinders with the same conditions of motion along the entire length of the annular gap. The smooth surfaces of the inner and outer vertical cylinders reduce the possibility of the polymer solution destruction as an agent for reducing hydraulic resistance due to the high speed of rotation of the inner cylinder and/or the outer cylinder. The hydrodynamics of the mixing process of an aqueous solution of polyacrylamide (PAA) with a mass concentration of 100 ppm in the gap between the cylinders, the inner one of which was rotating, were estimated by the dependence of the power criterion N_P on the modified Reynolds criterion Re_m. The mixing of the aqueous solution of PAA occurred in a laminar mode with a decrease in N_P at a certain fixed value of Re_m compared to water.

Keywords: coaxial cylinders; rotor with smooth surface; power number; Reynolds number.

---

1. Definition of the problem to be solved

In mixers intended for the preparation of emulsions and related heterogeneous systems, the efficiency of the mixing process is significantly increased by broadening the spectrum of operating fluid velocities within the recirculating flow. Under a coaxial configuration of the stator and rotor, an annular gap is formed between the elements, ensuring uniform hydrodynamic conditions along its entire length (Fig. 1) [1]. A principal advantage of the proposed design, in comparison with conventional mixers, lies in the substantially enlarged active area of the lateral surface of the working element.

The stator diameter of the installation was $D = 0.142$ m, while the rotor diameter was $d = 0.113$ m, with a height of $H = 0.133$ m (Fig. 2). The aspect ratio of the rotor diameter was $\Gamma_d = 0.796$, and the width of the annular gap was $b = 0.0145$ m. These values were determined according to the following relationships:

$$\Gamma_d = \frac{d}{D}, \tag{1}$$

$$b = \frac{D-d}{2} = \frac{D}{2}\cdot\left(1-\Gamma_d\right). \tag{2}$$

---

[*] Corresponding author. Email address: vadym.y.fasuliak@lpnu.ua

This paper should be cited as: V. Orel, B. Pitsyshyn, V. Fasuliak. (2025). Circulation flow of polyacrylamide aqueous solution between coaxial cylinders with smooth surfaces. *Energy Engineering and Control Systems*, Vol. 11, No. 2, pp. 93 – 98. https://doi.org/10.23939/jeecs2025.02.093

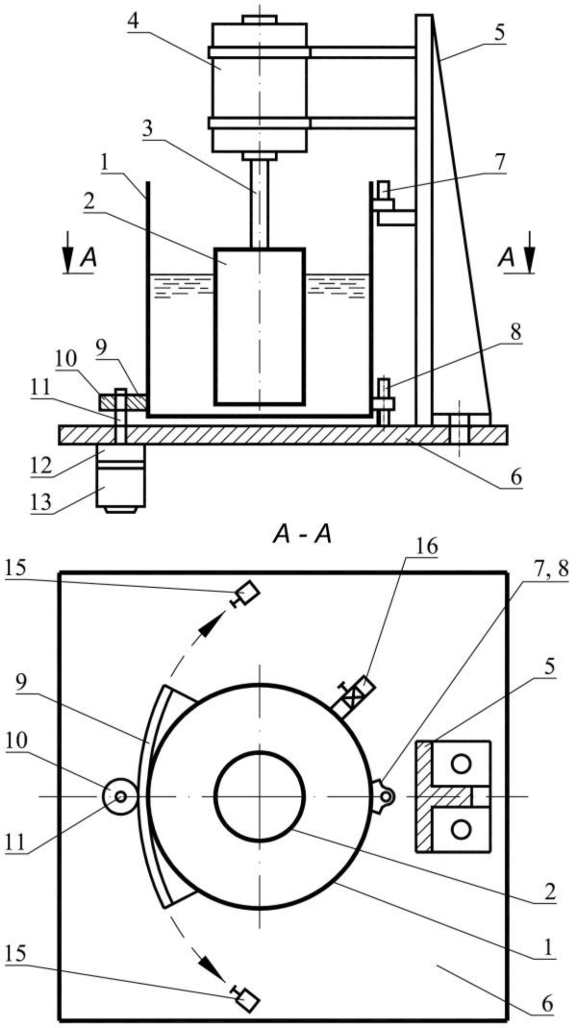

Fig. 1. Scheme of the mixer with coaxial cylinders:
1 – outer cylinder-stator; 2 – inner cylinder-rotor; 3 – drive shaft; 4 – electric motor; 5 – riser; 6 – plate;
7, 8 – suspension; 9 – part of the gear sector; 10 – gear wheel; 11 – shaft; 12 – reducer; 13 – reverse electric motor;
14, 15 – winding pole limit witches; 16 – outlet pipeline.

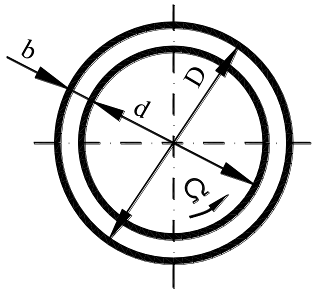

Fig. 2. Scheme of coaxial arrangement of cylinders.

2. Analysis of the recent publications and research works on the problem

Flow between rotating cylinders depends, in particular, on surface conditions [2]. The rotor, serving as the working body of the mixer, had a smooth surface.

The mixing process can be intensified by increasing the active area of the rotor's lateral cylindrical surface, for example, by introducing surface roughness. Thus, when the outer cylinder with a diameter of $D = 0.140$ m rotated relative to the stationary inner cylinder with a diameter of $d = 0.120$ m and a height of $H = 0.150$ m, a polyethylene oxide solution (Polyox WSR-301) at a concentration of 20 ppm rapidly lost its rheological properties. Both cylinders were roughened by machining longitudinal and transverse grooves on their surfaces, forming closely spaced tetrahedral pyramids with an apex angle of approximately 60° and a height of 0.00125 m (Fig. 3). In this case, the geometric similarity ratio of the rotor diameter was $\Gamma_d = 0.857$, and the width of the annular gap was $b = 0.010$ m [3].

The static pressure generated by a screw pump, positioned vertically in an open tank contained an aqueous solution of polyethylene oxide (Polyox FRA-1368-A-01) at concentrations ranging from 12.5 ppm to 100 ppm, initially increased to a maximum value and then gradually decreased to a minimum. The screw rotated relative to a stationary smooth cylinder. The screw protrusions had a pitch of 0.0016 m and a height of 0.0075 m (Fig. 4). In this configuration, the width of the annular gap was b=0.0005 m [4].

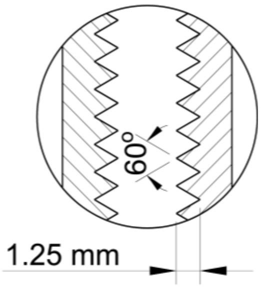

Fig. 3. Scheme of formation of rough surface of coaxial cylinders.

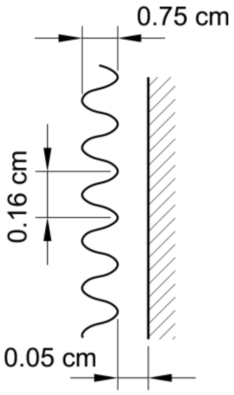

Fig. 4. Scheme of the formation of helical protrusions on the screw surface.

Although the mixing process is less intensive when the rotor and cylinder have smooth surfaces, the flow of a polymer solution through the annular gap between roughened cylinders may lead to its degradation under the action of shear stresses. Moreover, this degradation is irreversible [5]. But even with the flow in the annular gap with a width of $b = D/28$ between smooth cylinders, the polymer solution can be destroyed due to the high rotation speed of the outer cylinder [6].

The goal of this paper is to investigate the circulation flow of liquid between coaxial cylinders with a smooth rotor.

3. Presentation and discussion of the research results

An aqueous solution of polyacrylamide (PAA) with a concentration of $C = 100$ ppm by mass was examined. For its preparation, an 8% technical gel (Technical Specifications 6-01-1049-92) with a molecular weight of $1.8 \cdot 10^6$ was used. The concentration was determined based on the content of anhydrous PAA in the solution, calculated as $C = 0.0001$ kg PAA/kg. This fluid exhibits shear-thinning behaviour, which is described by Oswald's law

$$\tau = m \cdot \dot{\gamma}^n \tag{3}$$

with flow consistency index $m = 0.0027$ Pa·s^n and flow behaviour index $n = 0.83$. To determine the flow consistency index and flow behavior index, a rotational viscometer VSN-3 was used.

The molecular weight was calculated from the Mark-Houwink equation [7]:

$$[\eta] = 3.73.10^{-4} \cdot M^{0.66} \tag{4}$$

by the value of the intrinsic viscosity $[\eta]$ in a 0.1N $NaNO_3$ solution at a temperature of 30 °C. The intrinsic viscosity was $[\eta] = 5.0$ dl/g, it was determined by the standard method using a Bischof viscometer with a capillary diameter of 0.0006 m.

The hydrodynamic equation for mixing processes [8] for our case has the following form

$$N_P = f(\mathrm{Re}_m, \Gamma_d, \Gamma_H), \tag{5}$$

where N_P is the power number defined as follows[8], [9]

$$N_P = \frac{P}{\rho \cdot N^3 \cdot d^5}, \tag{6}$$

where P is the power (W); ρ is the fluid density (kg/m^3); N is the number of rotor revolutions (s^{-1}); Re_m is the Reynolds number for mixing [8], [9]

$$\mathrm{Re}_m = \frac{\rho \cdot N \cdot d^2}{\mu}, \tag{7}$$

where μ is the dynamic viscosity (Pa·s); Γ_H is the aspect ratio of the stator height

$$\Gamma_H = \frac{H}{D}. \tag{8}$$

In the studies, the temperature of water and PAA aqueous solutions was 26 °C. The fluid density for PAA aqueous solution was determined using a pycnometer and for water it was determined depending on the temperature. The dynamic viscosity for water was determined depending on the temperature.

Since the stator diameter in the experimental setup is constant, and the rotor in this experiment has the same height and diameter, the aspect ratio of the stator height $\Gamma_H = 1.077 = \mathrm{const}$ and the aspect ratio of the rotor diameter $\Gamma_d = 0.796 = \mathrm{const}$. Therefore, the hydrodynamic equation for mixing processes can be rewritten as [8], [9]

$$N_P = a \cdot \mathrm{Re}_m^k, \tag{9}$$

where a is the coefficient; k is the exponent.

Mixing occurs under laminar flow region with a slope of −1.0 (Fig. 5). For PAA aqueous solution, in comparison with water, a reduction in the N_P value is observed at a given fixed value of Re_m. For example, at $\mathrm{Re}_m \approx 57{,}000$, the relative change is $\Delta N_P/N_P = 77.1\%$. The relative change was determined as:

$$\frac{\Delta N_P}{N_P} = \left[1 - \frac{(N_P)_s}{(N_P)_w}\right] \cdot 100, \tag{10}$$

where $\frac{(N_P)_s}{(N_P)_w}$ is a criterion characterizing the hydrodynamic efficiency of PAA aqueous solutions of a given concentration, and the indices s and w correspond to PAA aqueous solutions and water, respectively.

In this case, the values of the N_P decrease with increasing Re_m for both water and PAA aqueous solutions. Furthermore, for identical Re_m values, lower N_P values are consistently observed for PAA aqueous solutions compared to water. This behavior corresponds to the dependence $C_F = f_1(\mathrm{Re}_b)$ [10], where C_F is the friction coefficient in the annular gap between the cylinders [11], defined as

$$C_F = \frac{G}{\mathrm{Re}_b^2}, \tag{11}$$

where G is the relative torque on the rotor; Re_b is the Reynolds number based on the gap width b (m).

The relative torque on the rotor is defined as follows

$$G = \frac{\rho \cdot G}{\mu^2 \cdot H}; \tag{12}$$

The Reynolds number based on the gap width is calculated according to the following formula

$$\mathrm{Re}_b = \frac{\rho \cdot \left(\Omega \cdot \frac{d}{2} \right) \cdot b}{\mu}, \tag{13}$$

where Ω is the rotational speed of rotor (rms), defined as

$$\Omega = 2\pi \cdot \mathrm{N}. \tag{14}$$

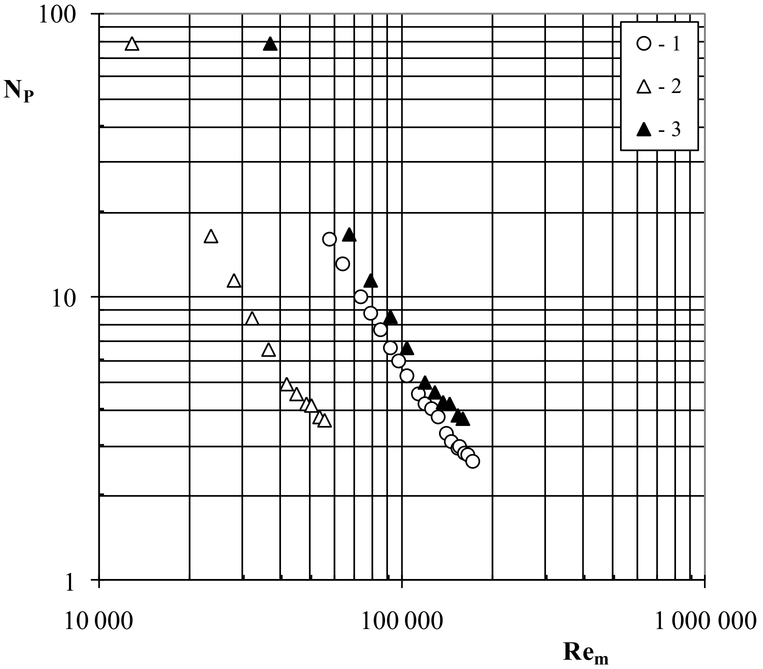

Fig. 5. Dependence of the power number on the Reynolds number for mixing for water (1) and for PAA aqueous solutions (2, 3), with calculations performed for the PAA aqueous solution (2) and for water (3).

Mechanical blade mixers operating in laminar regimes mix only those liquid layers directly adjacent to the blades [8]. But a mixing using a three-blade marine impeller operating at rotational speed of 75 rpm was achieved of minimal degradation of Magnafloc 5250 aqueous solution with a concentration of 100 ppm [12]. At low Reynolds numbers the PAA at a concentration of 80 ppm by weight can be mixed in a simple flow in a curved channel. As a solvent for the polymer was used a solution of 65% saccharose and 1% NaCl in water [13].

PAA aqueous solutions with concentrations up to 100 ppm may still be regarded as Newtonian fluids, albeit with increased viscosity [14]. Therefore, calculating the N_P and Re_m numbers using specific gravity and kinematic viscosity, as for water, makes it possible to determine the actual (technical) values of these criteria in comparison with water. Thus, for PAA aqueous solution at identical values of Re_m, the N_P value is slightly larger (approximately 1.26 times) than that for water. In this case, the relative change is $\Delta N_P/N_P \approx -26\%$. This behaviour resembles the dependence $C_F = f_2(\mathrm{Re}_b)$ [15].

4. Conclusion

For a mixer with coaxial arrangement of the inner and outer cylinders, the roughness of their surfaces is justified. Their smooth surface reduces the possibility of degradation of drag reducing polymers due to the high speed of rotation of the inner cylinder and/or the outer cylinder.

Mixing of an aqueous solution of polyacrylamide with a mass concentration of 100 ppm in the gap between the circular cylinders, the inner one of which was rotating, occurred in a laminar mode with a decrease in the power number at a certain fixed value of the Reynolds number for mixing compared to water.

References

[1] Cherniuk, V. V., Pitsyshyn, B. S. (2019). Mixer. UA Patent No. 120181. (Retrieved on September 25, 2025) (in Ukrainian)

[2] Bilgen, E., Boulos, R. (1973). Functional Dependence of Torque Coefficient of Coaxial Cylinders on Gap Width and Reynolds Numbers. *Journal of Fluids Engineering*, 95 (1), 122–126. https://doi.org/10.1115/1.3446944

[3] Belokon, V., Kalashnikov, V. (1971). Polymer Additives and Turbulent Friction near Rough Surfaces. *Nature. Physical Science,* **229**, 55–56. https://doi.org/10.1038/physci229055a0

[4] Kuo, J. T., Kovasznay, L. S. G. (1981). Drag Reducing Polymer in Helicoidal Flow. *Journal of Fluids Engineering*, **103(4)**, 491–496. https://doi.org/10.1115/1.3241757

[5] Anisimov, I. A., Mironov, B. P. (1980). Irreversibility of degradation of polymer solutions. *Journal of Engineering Physics*, **38**, 141–142. https://doi.org/10.1007/BF00861867

[6] Kalashnikov, V. N. (1998). Dynamical similarity and dimensionless relations for turbulent drag reduction by polymer additives. *Journal of Non-Newtonian Fluid Mechanics*, **75(2-3)**, 209–230. https://doi.org/10.1016/S0377-0257(97)00093-1

[7] Kargin, V. A. (Ed.) (1972). Polymer Encyclopedia. Vol. 1. Soviet Encyclopedia, Moscow. (in Russian)

[8] Boiko, V. S., Samoichuk, K. O., Tarasenko, V. H., Zahorko, N. P., Tsyb V. H. (2019). Processes and devices. Hydromechanical processes: Textbook. Dmytro Motornyi Tavria State Agrotechnological University, Melitopol. (in Ukrainian)

[9] Holland, F. A., Bragg, R. (1995). Fluid Flow for Chemical Engineers. Second Edition, Edward Arnold, London.

[10] Orel, V. I., Pitsyshyn, B. S., Popadiuk, I. Yu. (2019). Use of the mixer of modern construction for preparation of the polyacrylamide water solution in the Taylor-Couette flow. *Scientific Bulletin of UNFU,* **29 (9)**, 121–125. (in Ukrainian) https://doi.org/10.36930/40290921

[11] Bhambri, P., Fleck, B. (2016). Drag reduction using high molecular weight polymers in Taylor-Couette flow. *International Journal of Mechanical and Production Engineering Research and Development*, **6 (1)**, 59–72.

[12] Rowin, W. A., Sanders, R. S., Ghaemi, S. (2018). A recipe for optimum mixing of polymer drag reducers. *Journal of Fluids Engineering*, **140 (11)**, 111402-1–111402-10. https://doi.org/10.1115/1.4040109.

[13] Groisman, A., Steinberg, V. (2001). Efficient mixing at low Reynolds numbers using polymer additives. *Nature*, **410**, 905–908. https://doi.org/10.1038/35073524

[14] Zhuk, V. M. (1999). Regulation of the charge of a liquid in pipelines by introduction in a flow hydrodynamical active additives (PhD dissertation). Rivne. (in Ukrainian)

[15] Pitsyshyn, B. S., Orel, V. I. (2008). Application of a cylindrical rotor mixer for the preparation of polymer solutions for use in fire extinguishing. *Bulletin of Lviv Polytechnic National University: Theory and Building Practice*, **627**, 172–178. (in Ukrainian)

Циркуляційна течія водного розчину поліакриламіду між коаксіальним циліндрами з гладкими поверхнями

Вадим Орел, Богдан Піцишин, Вадим Фасуляк

Національний університет «Львівська політехніка», вул. С. Бандери 12, м. Львів, 79013, Україна

Анотація

Розглянуто змішувач з коаксіальним розташуванням внутрішнього та зовнішнього круглих циліндрів з гладкими поверхнями. При роботі змішувача між циліндрами утворюється циркуляційна течія з однаковими умовами руху по усій довжині кільцевого проміжку. Гладкі поверхні внутрішнього та зовнішнього вертикальними циліндрів зменшують можливість деструкції полімерного розчину як агента зменшення гідравлічного опору через велику швидкість обертання внутрішнього циліндра або/та зовнішнього циліндра. Гідродинаміку процесу перемішування водного розчину поліакриламіду (ПАА) з масовою концентрацією 100 ppm в проміжку між циліндрами, внутрішній з яких обертався, оцінювали залежністю критерію потужності N_P від модифікованого критерію Рейнольдса Re_m. Перемішування водного розчину ПАА відбувалося за ламінарного режиму зі зменшенням N_P за певного фіксованого значення Re_m порівняно з водою.

Ключові слова: коаксіальні циліндри; гладкий ротор; критерій потужності; критерій Рейнольдса.